

Methods to Enhance Nuclear Magnetic Resonance Sensitivity at High Magnetic Field

Présentée le 7 mai 2021

Faculté des sciences de base
Laboratoire Leenaards-Jeantet d'imagerie fonctionnelle et métabolique
Programme doctoral en physique

pour l'obtention du grade de Docteur ès Sciences

par

Claudia Christina ZANELLA

Acceptée sur proposition du jury

Prof. F. Mila, président du jury
Prof. R. Gruetter, directeur de thèse
Prof. C. Laustsen, rapporteur
Prof. J. H. Ardenkjær-Larsen, rapporteur
Prof. S. Kozerke, rapporteur

Résumé

La technique bien établie de IRM a un rôle important dans la recherche médicale de nos jours. La recherche moderne pousse les limites et les possibilités de cette méthode versatile. Le focus de cette thèse était l'amélioration de la sensibilité RM.

L'hyperpolarization du gaz ^{129}Xe est utilisée pour étudier les maladies pulmonaires et la perfusion cérébrale. Quand l'hyperpolarisation se fait à l'intérieur d'un polariseur conçu pour la PDN de dissolution le niveau de polarisation atteint de nos jours est limité à quelques pour cents. Un but de cette thèse était de contourner cette limitation en investigant l'effet de modulation de la fréquence des micro-ondes sur des systèmes de spins différents. Une augmentation de polarisation nucléaire de ^{129}Xe , par rapport à la polarisation sans modulation, de jusqu'à 220% a été atteint (de 3.5% à 11.2%). Une corrélation entre des temps de relaxation électronique T_{1S} courts (5 - 21 ms) a été observée. Des simulations du système électronique ont confirmé, que la modulation de fréquence peut être une méthode efficace pour augmenter la polarisation dans des matrices ayant de courts T_{1S} ou lors de l'utilisation de radicaux avec de grandes largeurs de ligne.

Une matrice PDN peut être hyperpolarisée en utilisant des radicaux non persistants générés par l'irradiation avec des rayonnements UV. Ces radicaux libres ont l'avantage de ne pas persister pendant la dissolution. Une solution hyperpolarisée est générée qui n'a pas besoin d'être filtrée. Lorsque les précurseurs recherchés jusqu'à présent n'étaient pas toxiques et n'interféraient pas avec le métabolisme, ils fournissaient des polarisations basses. Deux nouveaux précurseurs endogènes, α -cétovalérianate (αkV) et α -cétobutyrate (αkB), ont été investigués et utilisés pour l'étude *in vivo* du métabolisme cardiaque. La polarisation en état liquide de substrat métabolique glucose a augmenté de 13.3% à 16.3% avec du αkB par rapport au pyruvate. $[1-^{13}\text{C}]$ butyrate a été polarisé à 12.1% (αkV) et 12.9% (αkB). Le métabolisme cardiaque de $[1-^{13}\text{C}]$ butyrate hyperpolarisé a montré une incorporation du marquage dans une grande gamme de métabolites. Cette étude a démontré le potentiel d'utiliser ces radicaux

UV endogènes comme agents de polarisations en obtenant une solution de polarisation élevée sans radicaux libres.

Par ailleurs, la méthode d'IRM nécessite des antennes RF qui génèrent un champ B_1^+ homogène. La SRM dépend d'une efficacité B_1^+ et d'une sensibilité élevée. Deux antennes ^1H construites sur mesure, une antenne de selle et une antenne cage d'oiseaux, ont été investiguées par rapport à leur sensibilité ainsi que leur homogénéité et efficacité de champ magnétique B_1^+ pour des applications à haut champ (600 MHz). L'antenne de selle a été caractérisée avec une efficacité B_1^+ et un S/N plus élevés de 54% et de 20% respectivement, par rapport à l'antenne cage d'oiseaux. L'utilisation d'une antenne de selle pour l'imagerie CEST de glycogène a donné un coefficient de variation d'asymétrie MTR de 5.2% sur une région homogène de 11 mm de diamètre. L'antenne de selle était un bon compromis dû à une excitation globalement homogène et une sensibilité élevée. Elle était utilisée avec succès pour imager la distribution de glycogène dans le muscle *in vivo*.

Cette thèse s'est concentrée sur l'amélioration de la sensibilité RM. Ceci a pu être accompli dans des différentes situations en utilisant une antenne RF adaptée, en implémentant une méthode PDN qui profite des propriétés des électrons ou encore en développant des précurseurs nouveaux pour l'IRM hyperpolarisé *in vivo*.

Mots clés

Résonance magnétique (IRM) à haut champ, polarisation dynamique nucléaire (PDN), ^{129}Xe PDN, modulation de fréquence des micro-ondes, radicaux non persistants, radicaux UV, α -cétovalérianate, α -cétobutyrate, $[1-^{13}\text{C}]$ butyrate hyperpolarisé, antenne de selle, antenne cage d'oiseaux passe-haut, glycogène CEST

Zusammenfassung

Die weitverbreitete Technik der Kernspinresonanz (MR) nimmt heutzutage einen hohen klinischen Stellenwert ein. Moderne Forschung verschiebt stetig die Grenzen der möglichen Anwendungen dieser vielseitigen und nicht-invasiven Technik. Der Fokus dieser Arbeit lag in der Verbesserung der Sensibilität von MR Methoden.

Hyperpolarisiertes Xenon-Gas wird zur Erforschung von Lungenkrankheiten oder Hirnperfusion verwendet. Falls Hyperpolarisation mit Hilfe eines Dissolution-DNP Polarisierers erfolgt, sind die heutzutage erreichbaren Polarisationswerte tief. Ein Ziel dieser Arbeit war es, die Xenonpolarisation durch Mikrowellen-Frequenzmodulation zu erhöhen und die Auswirkung auf unterschiedliche Spinsysteme zu untersuchen. Die Xenonpolarization konnte mit dieser Methode um bis zu 220% gesteigert werden (von 3.5% auf 11.2%). Ultrakurze Elektronenspin- T_1 von 5 ms wurden gemessen und korrelierten mit Polarisationssteigerung dank Frequenzmodulation, unabhängig vom Grad der Deuterierung des Lösemittels. Simulationen des Elektronenspinsystems bestätigten, dass Mikrowellen-Frequenzmodulation durch verbesserte spektrale Diffusion eine effiziente Methode zur erheblichen Polarisierungssteigerung in Matrizen mit kurzen Elektronen- T_1 oder beim Gebrauch von Radikalen mit weiten Linienbreiten darstellen kann .

Alternativ können DNP Matrizen auch durch den Einsatz von nicht-persistenten Radikalen, die durch UV-Bestrahlung generiert wurden, hyperpolarisiert werden. Dies hat den Vorteil, dass nach Extraktion eine hyperpolarisierte Lösung ohne Radikale generiert wird. Für *in vivo* Applikationen fällt das Filtern der Radikale weg. Untersuchte nicht-persistente Radikale haben bisher entweder tiefe ^{13}C Polarisationen geliefert, enthielten toxische Substanzen im Endprodukt oder enthielten Substrate, die den Metabolismus beeinflussten. Deshalb wurden zwei neue endogene Ausgangsmoleküle, α -Ketovaleriansäure (αkV) und 2-Oxobutansäure (αkB) untersucht. Die Polarisierung des ^{13}C -markierten metabolischen Substrats Glukose wuchs von 13.3% auf 16.3% als das Ausgangsmolekül Pyruvat durch αkB ersetzt wurde. Herz-

metabolismus von $[1-^{13}\text{C}]$ Butyrat führte zur Markierung von etlichen Stoffwechselprodukten. Diese Studie zeigte das Potential von αkB and αkV für zukünftige Studien auf, dank ihrer endogenen Eigenschaft und den hohen erzielten Polarisationswerten.

Spulen werden zur Datenmessung benötigt und müssen den Anforderung der Bildgebung (MRI) oder Spektroskopie (MRS) genügen indem sie gleichförmige Transmittfelder B_1^+ erzeugen oder sensibel sind, respektive effiziente B_1^+ erzeugen. Zwei massgefertigte 600 MHz Spulendesigns, eine Sattelspule und eine Quadratur-Hochpass Vogelkäfigspule, wurden bezüglich dieser Kriterien im Bezug auf ultrahochfeld Anwendungen verglichen. Die Sattelspule lieferte nach voller FOV-Korrektur eine 54% höhere B_1^+ Effizienz und ein 20% höheres SNR als die Vogelkäfigspule. Die Anwendung der Sattelspule für glycoCEST eines gleichförmigen Phantoms führte zu einem MTR-Asymmetrievariationskoeffizienten von 5.2%. Insgesamt lieferte die Sattelspule einen guten Kompromiss zwischen einer global gleichförmigen Anregung und hoher Sensibilität. Sie wurde erfolgreich *in vivo* zur Abbildung der Glykogenverteilung von Skelettmuskulatur eingesetzt.

Der Fokus dieser Arbeit lag in der Weiterentwicklung von MR-Methoden, mit dem Ziel, die nukleare Sensibilität zu erhöhen. Die vorgeschlagenen methodologischen Lösungen wurden auf die experimentellen Begebenheiten massgeschneidert. Anpassungen der Methoden für ein breites Spektrum an Studien wurden diskutiert.

Stichwörter

Hochfeld Kernmagnetresonanz (MR), Dynamische Kernspinpolarisation (DNP), ^{129}Xe DNP, Mikrowellen-Frequenzmodulation, α -Ketovaleriansäure, 2-Oxobutansäure / 2-Oxobuttersäure, Nicht-persistente UV-Radikale, hyperpolarisiertes $[1-^{13}\text{C}]$ Butyrat, Sattelspule, Hochpass Vogelkäfigspule, Glykogen-CEST

Abstract

MR is a well-established technique routinely used in preclinical and clinical studies. This thesis focused on the improvement of sensitivity of different methods in MR.

Hyperpolarized ^{129}Xe gas is used for studying pulmonary disease or cerebral perfusion. When hyperpolarization is conducted inside a dissolution DNP polarizer, the achieved solid state polarization is currently limited to a few percent. One aim of this thesis was to counteract this bottleneck by investigating the effect of microwave frequency modulation for different spin systems. An increase in nuclear ^{129}Xe spin polarization by up to 220% (from 3.5% to 11.2%) was achieved compared to polarization obtained without frequency modulation. Electron spin-lattice relaxation times T_{1S} , as short as 5 ms, correlated directly with the gain in ^{129}Xe nuclear polarization due to microwave frequency modulation, irrespective of the solvent or its deuteration. Simulations of the electron spin system confirmed that microwave frequency modulation could be an efficient method to considerably enhance nuclear spin polarization in short T_{1S} matrices or in the presence of large linewidth radicals by promoting spectral diffusion.

DNP matrices can also be hyperpolarized through non-persistent radicals generated by UV-irradiation. They have the advantage of quenching upon dissolution, yielding a hyperpolarized solution with no need for radical filtration. Radical precursors researched up to date either yielded low ^{13}C polarization ($\lesssim 5\%$), contained toxic matrix components or interfered with metabolic processes. Therefore, the two novel endogenously-occurring precursors, alpha-ketoglutarate (αkV) and alpha-ketobutyrate (αkB) were investigated. Liquid state polarization of the metabolic substrate glucose increased to 16.3% using αkB compared with 13.3% obtained with pyruvate. $[1-^{13}\text{C}]$ butyric acid was polarized to 12.1% for αkV and 12.9% for αkB and used for *in vivo* hyperpolarized cardiac MRS. Hyperpolarized $[1-^{13}\text{C}]$ butyrate metabolism in the heart revealed label incorporation into a wide range of metabolites. This study demonstrated the potential of using UV-induced radicals generated

in the endogenously-occurring metabolites α kV and α kB as polarizing agents, enabling high polarization without requiring radical filtration for radical-free hyperpolarized MRI.

While MRI requires RF coils that generate high B_1^+ homogeneity, MRS strongly depends on high sensitivity and potentially high B_1^+ efficiency to allow for short-TE acquisitions. Two custom-made ^1H coils resonating at 600 MHz, a single-channel saddle coil and an 8-leg quadrature birdcage coil, were investigated with respect to those criteria for applications at ultra-high field (14.1 T). The saddle coil yielded a 54% higher transmit field efficiency with a 20% higher SNR compared to the birdcage coil after full-FOV corrections. Using the saddle coil in glycoCEST imaging of a homogeneous phantom resulted in an MTR asymmetry coefficient of variation as small as 5.2% over an 11 mm diameter ROI. Overall, the saddle coil provided a good compromise between globally homogeneous excitation and high sensitivity. Finally, it was successfully used to map skeletal muscle glycogen content *in vivo*.

This thesis focused on improving MR sensitivity by means of adequate custom-made RF coils as well as DNP through the implementation of a method capitalizing on the electronic properties and the development of novel endogenous precursors for *in vivo* hyperpolarized MRI.

Keywords

high field magnetic resonance (MR), dynamic nuclear polarization (DNP), ^{129}Xe DNP, dissolution DNP, microwave frequency modulation, non-persistent UV-radicals, α -ketovalerate, α -ketobutyrate, hyperpolarized $[1-^{13}\text{C}]$ butyrate, saddle coil, high-pass birdcage coil, glycoCEST

Contents

Résumé / Zusammenfassung / Abstract	i
List of Figures	xi
List of Tables	xv
List of Symbols	xvii
1 Introduction	1
1.1 Context	1
1.2 Aim of the thesis	3
1.3 Outline of the thesis	4
2 Magnetic Resonance and Dynamic Nuclear Polarization	7
2.1 NMR Sensitivity: Origin, Limitations, Selected Solutions	8
2.2 Hyperpolarization Techniques	12
2.3 The DNP Matrix	15
2.3.1 UV-generated Non-persistent Radicals	16
2.3.2 Current Efforts Targeting Translation to Clinical Standards	17
2.4 DNP Theory	18
2.4.1 Main Spin Interactions	18
2.4.2 The Total Spin Hamiltonian	22
2.5 The ESR Spectrum and Homogeneous Broadening	23
2.6 Hole Burning and Spectral Diffusion	26
2.7 Spin-Lattice Relaxation	28
2.8 Evolution of the Electron Spin Polarization	30
2.9 DNP Mechanisms	31
2.9.1 Solid Effect	31
2.9.2 Triple Spin Flips	33

2.10	Selected Application: Xenon Gas in Medical Imaging	36
3	Selected Principles in MR	39
3.1	RF Coils	40
3.1.1	The Radio-frequency Field and the Principle of Reciprocity	40
3.1.2	Bench Measurements	43
3.1.3	RF Losses	44
3.1.4	The Saddle Coil	45
3.1.5	The Birdcage Coil	47
3.2	Creating Contrast via CEST	49
3.2.1	Disentangling the Z-spectrum Architecture	53
3.2.2	Artifacts - B_0 Shift and B_1 Inhomogeneities	56
3.2.3	GlycoCEST of Hydroxyl Protons	58
3.2.4	State of the Research	59
4	Enhancing ^{129}Xe Spin Polarization in Short Electron T_1 Matrices via Microwave Frequency Modulation	61
4.1	Abstract	62
4.2	Introduction	63
4.3	Methods	65
4.4	Results	75
4.5	Discussion	88
4.6	Conclusion and Outlook	96
5	Hyperpolarized MRI with UV-induced Nonpersistent Radicals from Endogenously-occurring Precursors	99
5.1	Abstract	100
5.2	Introduction	101
5.3	Experimental	103
5.4	Results	110
5.5	Discussion	121
5.6	Conclusion	125
6	The Saddle Coil Design as Advantageous Solution for Preclinical MRI and MRS at Ultra-high Magnetic Field	127
6.1	Abstract	128
6.2	Introduction	129

6.3	Methods	132
6.4	Results	139
6.5	Discussion	147
6.6	Conclusion and Outlook	151
7	Conclusion, Perspectives, Outlook	153
7.1	Increasing Nuclear Polarization via Microwave Frequency Modulation	154
7.2	High ^{13}C Polarization for <i>in vivo</i> dDNP using Non-persistent Radical Precursors	155
7.3	Perspectives of a Versatile Coil Design	156
7.4	Overall Conclusion and Outlook of the Thesis	158
A	Hyperpolarizing ^{129}Xe matrices	159
A.1	ESR Spectra and T_{1S}	160
A.2	DNP Maxima and Frequency Modulation Parameters	162
A.3	Mixing Procedures	165
B	Residual B_0-field Considerations for <i>ex situ</i> Sublimation DNP and <i>in situ</i> dDNP	167
B.1	Motivation	168
B.2	Introduction	168
B.3	Methods	169
B.4	Results	175
B.5	Discussion	180
B.6	Conclusion and Perspectives	182
C	Expanding the Saddle Coil <> Birdcage Coil Comparison: Considering a High-pass 16-leg Quadrature ^1H Birdcage Coil	183
C.1	Motivation	184
C.2	Methods	184
C.3	Results	185
C.4	Discussion and Conclusion	190
D	5 T Polarizer Hardware Optimisations & Extensions	191
D.1	Excessive Helium Consumption	192
D.2	Further Testing, Repairs and New Implementations	194
	Bibliography	I

Acronyms	XXXIII
Acknowledgements	XXXVII
Communications	XXXIX
Curriculum Vitae	XLII

List of Figures

2.1	Zeeman splitting	10
2.2	Electromagnetic spectrum with typical transition energies	11
2.3	Chemical structures of TEMPO and OX063	15
2.4	Jablonski diagram of electronic states	17
2.5	Homogeneous and inhomogeneous ESR line broadening	24
2.6	Spectral diffusion and triple spin flips	26
2.7	Overhauser effect and cross relaxation	32
2.8	Coupled electron and nuclear spin system with transitions	33
2.9	Thermal mixing in the thermodynamic picture	35
2.10	SEOP and sublimation DNP in comparison	38
3.1	Current distribution along transverse resonators	45
3.2	Current paths within saddle coil	46
3.3	8-leg quadrature birdcage coil design	47
3.4	Generating contrast via CEST	50
3.5	Temporal evolution of two coupled spin populations	52
3.6	Z-spectrum architecture and parasite contributions	54
3.7	CEST acquisition and post-processing pipeline	57
4.1	Radical and solvent chemical structures	65
4.2	Design of custom-made glass cold finger	66
4.3	Schematics of xenon sample preparation procedure	66
4.4	Combined sample preparation set-up	67
4.5	Flip angle calibration and T_{1S} fitting	68
4.6	Flowchart of hardware and software modifications to implement microwave frequency modulation	70
4.7	Calibration of sensitivity-dependent frequency modulation amplitude	71
4.8	T_{1S} of TEMPO in presence and absence of xenon nuclear spins	76

4.9	TEMPO ESR spectra at DNP conditions	78
4.10	T_{1S} and ESR-FWHM dependence on nuclear spin concentration	79
4.11	Modulation amplitude dependent microwave frequency sweeps	79
4.12	Reproducibility of hyperpolarization over 47 hours	80
4.13	Frequency sweeps and DNP using fully protonated solvents	81
4.14	Frequency sweeps and DNP using deuterated solvents	83
4.15	T_{1S} -dependent polarization gain due to microwave frequency modulation	84
4.16	Hole burning under mono-chromatic microwave irradiation	85
4.17	Illustration of hole burning under modulated microwave irradiation	86
4.18	Hole burning at the positive versus negative DNP	87
4.19	Promoting efficient spin diffusion	89
5.1	Schematics of [1- ^{13}C]butyrate cardiac metabolism <i>in vivo</i> with down-stream label propagation	102
5.2	Timeline for the hyperpolarized dissolution DNP protocol at 7 T	104
5.3	Study design	105
5.4	UV-Vis absorption and X-band ESR	111
5.5	TEMPOL concentration calibration curve	112
5.6	Non-persistent radical generation time-course of αkB	113
5.7	UV-generated radical concentration calibration	113
5.8	[U- ^{13}C , U- ^2H]Glc microwave frequency sweeps	114
5.9	Hyperpolarized [U- ^{13}C , U- ^2H]Glc liquid state MRS	115
5.10	Hyperpolarized [1- ^{13}C]butyrate liquid state MRS	117
5.11	Early <i>in vivo</i> MR spectra	119
5.12	Hyperpolarized [1- ^{13}C]butyrate MRS of <i>in vivo</i> cardiac metabolism	120
6.1	Schematics of an 8-leg birdcage coil casing	133
6.2	Custom-built ^1H saddle and birdcage coil designs	134
6.3	CEST pulse sequence	138
6.4	Scattering parameters for loaded coils	140
6.5	Simulated and normalized B_1^+ maps	142
6.6	Transmit field map homogeneity of a 0.9 % saline phantom.	143
6.7	glycoCEST mapping using custom-made ^1H saddle coil	145
6.8	<i>In vivo</i> glycoCEST mapping	146
6.9	Control measurement	147
A.1	Solvent-dependent LOD-ESR with and without ^{129}Xe	160

A.2	Electron relaxation rates in protonated and deuterated matrices	161
A.3	ESR spectra of protonated and deuterated solvents	161
A.4	DNP sweep asymmetry	162
A.5	Modulation amplitude calibration at 139.9 GHz	163
A.6	Modulation amplitude calibration at 140.275 GHz	164
A.7	Calibration of modulation rate	164
A.8	Ultra-sonication and microwave frequency modulation to overcome magnetic stirring bottleneck	165
B.1	De-localized sublimation DNP: schematics of the procedure	171
B.2	Local magnetic field for delocalized sublimation DNP	172
B.3	<i>In situ</i> set-up for hyperpolarized MRS at 14.1 T after sample transfer from the adjacent 5 T polarizer	173
B.4	Magnetic field mapping of the 14.1 T MR scanner at EPFL	175
B.5	3D representation of magnetic field line mapping for the 5 T polarizer and the adjacent 14.1 T MR scanner at EPFL	176
B.6	<i>Ex vivo</i> hyperpolarized ^{129}Xe MRS at 9.4 T after cryogen-free extraction . .	177
B.7	[1- ^{13}C]NaPyr polarization enhancement due to frequency modulation	179
B.8	Transfer line crossings through filter panel of 14.1 T MR scanner	179
B.9	Summed <i>in vivo</i> hyperpolarized MR spectrum in rat liver after <i>in situ</i> transfer to 14.1 T	180
C.1	B_1^+ map simulations with slice- and ROI-dependent homogeneity analysis . .	186
C.2	B_1^+ homogeneity over increasing ROIs in phantom	187
C.3	MTR asymmetry coefficient of variation	187
C.4	MTR asymmetry and Z-spectra generated by a 16-leg birdcage coil and a saddle coil	188
C.5	<i>In vivo</i> glycoCEST MTR asymmetry maps of rat skeletal muscle	189
D.1	New single-walled transfer line extension	192
D.2	Custom-made dewar connection piece with helium level probe inlet	193
D.3	Microwave source power calibration and power limitation	195
D.4	90° E-plane bend connector	195

List of Tables

2.1	Characteristics and polarization of chosen spin species	10
3.1	glycoCEST imaging - overview of the state of research	59
4.1	Matrix-dependent T_{1S} of TEMPO	77
4.2	Impact of frequency modulation on sweep maxima, DNP and build-up time .	82
4.3	Simulated diffusion and hole burning parameters	86
5.1	Precursor-dependent UV-radical generation time constant and radical yield after 200 s of UV-irradiation	110
5.2	Positive and negative DNP maxima at 7 T	115
5.3	[U- $^{13}\text{C}_6$, U- $^2\text{H}_7$]Glc solid state build-up time constant and liquid state polar- ization	116
5.4	[1- ^{13}C]butyrate solid state build-up time constant and liquid state polarization	116
5.5	Chemical shifts observed in caridac MRS	118
5.6	Efficiency of αkV and αkB as precursors for non-persistent polarizing agents in context	123
6.1	Input and output parameters for loaded coils	141
B.1	Liquid state ^{13}C polarization and T_{1I} at 14.1 T	178
C.1	Data sheet for constructing the three ^1H volume coils at 600 MHz	185
C.2	Input and output parameters for all three loaded coils	186

List of Symbols

β	Inverse spin temperature
γ	Gyromagnetic ratio
δ	Hole width
Δ_{ESR}	Total width of ESR spectrum
$\Delta f_{\mu w}$	Frequency modulation amplitude
Δ_h	Width of homogeneous distribution
ϵ	Enhancement
ζ	Electromotive force
λ	Wavelength
μ	Magnetic moment
μ_0	Magnetic constant / vacuum permeability
ν_{FM}	Frequency of modulation
τ	Polarization build-up time
$\tau_{\mathcal{D}}$	Spectral diffusion transportation time
\mathbf{B}_0	Static magnetic field vector
B_1	Transmit magnetic field
$B_{\mu w}$	External microwave field
d	Coil diameter
\mathcal{D}	Spectral diffusion constant
\mathbf{g}	g-tensor
g_h	Homogeneous linewidth
g_N	Inhomogeneous linewidth of ESR spectrum
\hbar	Planck constant (in [J·s/rad])
I	Nuclear spin quantum number
k_B	Boltzmann constant
k_{ex}	Exchange rate

l	Coil length
m	Eigenvalue of spin state
M	Bulk magnetization
M_2	Second moment of a distribution
M_z	Longitudinal magnetization
n	Rung number
n_I	Nuclear spin density
\tilde{n}_S	Number of spin packets
N	Number of spins
NU	Non uniformity
p_0	Standard pressure
P	Polarization
Q	Quality factor
RU	Relative uniformity
S	Electron spin quantum number
S_{sat}	Saturated water magnetization
T	Temperature
T_0	Standard temperature
T_1	Spin-lattice relaxation time
T_2	Spin-spin relaxation time
TE	Echo time
TR	Repetition time
w	Resonance frequency
w_{0S}	Center of gravity of ESR spectrum
$w_{\mu w}$	Microwave irradiation frequency

Chapter 1

Introduction

1.1 Context

Nuclear Magnetic Resonance (NMR) is a well-established and non-invasive spectroscopic tool for studying structural and functional properties of molecules and their environment. Apart from its frequent use in chemistry to study morphology, it is also applied in medicine where it provides insights beyond structure and functionality, namely in metabolic studies [1]. In the latter case, the modality is referred to as Magnetic Resonance Imaging (MRI), respectively Magnetic Resonance Spectroscopy (MRS). While ^1H MR is the most conventional application, other nuclei (X-nuclei) are convenient to monitor metabolism or investigate regions of low ^1H density, as for instance the lung. ^{13}C is a low-gamma natural abundance isotope, which occurs in most metabolites. It therefore enables ^{13}C MRS studies of *in vivo* metabolic pathways and associated processes. The spectroscopic information can be combined with MRI to gain insights into anatomical information. ^{13}C MRS has the advantage of enabling tracer experiments, even though high doses of (costly) compounds have to be administered and long scan times are needed. Since NMR signal arises from the population difference of spin states, which are as small as a few parts per million (ppm) at physiological conditions at (pre-)clinical field strength, some applications inherently suffer from poor sensitivity. This is less of an issue for nuclei occurring at high concentrations, such as ^1H in biological tissue, but it is a strong inherent limitation for ^{13}C nuclei of low concentration metabolites. Several approaches address this drawback from various angles [2]. Some enhance the intrinsic NMR sensitivity by increasing the magnetic field strength, by looking at

a nuclear spin with a favourable gyromagnetic ratio or by employing polarization transfer methods. Post-processing and sequence-related approaches are frequently encountered. Alternatively, MR signal loss suffered during the signal generation or detection can be tackled by improving the RF coil design. The NMR signal can furthermore be boosted most efficiently through hyperpolarization, where out of equilibrium spin population distributions are generated through addition of external energy to the spin system.

Dynamic Nuclear Polarization (DNP) is a hyperpolarization technique which increases nuclear spin polarization of solid state samples at high magnetic field (several Tesla) and low temperatures (around one Kelvin) [3, 4]. This is achieved by embedding free radicals, containing unpaired electrons, into an amorphous DNP sample. The spins of the unpaired electrons are depolarized by introducing energy in the microwave range into the system. Electron spin polarization is then transferred to the nuclear spins. The rather recent innovation of dissolution Dynamic Nuclear Polarization (dDNP) enables the extraction of hyperpolarized samples for their transfer to an MR scanner while maintaining nuclear polarization enhancements by 4-5 orders of magnitude in liquid state and at room temperature [5]. Hyperpolarizing ^{13}C -labelled biomolecules and injecting them into living organisms enables the detection of low concentration metabolites and dynamic monitoring of real-time *in vivo* metabolism [6–10].

The vast amount of applications range from investigations of metabolic pathways [8, 9, 11–13] to human DNP trials [14–19]. To profit maximally from the DNP technique, prolonged duration of the hyperpolarized state and increased starting magnetization are sought after. A big effort is put into developing efficient hyperpolarization methods through sample matrix investigations (of the radical [20], the solvent [21] or additives [22]) or through methodological improvements of the polarizer hardware [23]. Using optimized dissolution pathways [24] and methods of transportation [25] minimize the loss of nuclear polarization during transfer from the polarizer to the MR scanner, thereby increasing the gain in liquid state sensitivity further. In this context, non-persistent radicals have been proposed [25] since they quench as soon as the hyperpolarized sample is heated to temperatures superior to 190 K, thereby obviating the need for radical scavenging or filtration prior to injection [26]. Up to date, a handful of different radical precursors have been researched and few *in vivo* studies have been conducted successfully with them.

The use of hyperpolarized ^{129}Xe gas is of interest when conducting MR lung imaging [27] or cerebral perfusion studies [28]. One method to produce hyperpolarized xenon gas is by using a conventional DNP polarizer that underwent minor modifications [29]. A major drawback

of the method is the currently encountered limited level of nuclear polarization achievable in solid state. A previously suggested approach to counteract this limit is microwave frequency modulation [30]. Its efficiency, however, is highly dependent on the matrix [23] and a substantial improvement of ^{129}Xe nuclear spin polarization is not a priori guaranteed.

Another crucial component that influences the sensitivity of an MR experiment is the RF coil. It creates the transmit magnetic field B_1^+ and detects the induced MR signal with a sensitivity that is determined by the principle of reciprocity [31]. While MRS requires high sensitivity and a potentially strong local B_1^+ [32], MRI depends more strongly on a globally uniform RF excitation. These constraints impose that surface coils, for instance, are more commonly used for spectroscopic applications and volume coils for imaging [33]. An optimal study design therefore requires that the intrinsic properties of the RF coil cover the needs of the specific application. At ultra-high magnetic field such as 14.1 T, non-uniform B_1^+ excitation is exacerbated [34], which poses a challenge for MRI applications [35]. The last chapter aims to provide a solution where various study-specific interests are aligned with the constraints imposed by the choice of the RF coil.

1.2 Aim of the thesis

This thesis focused on developing solutions to achieve enhanced sensitivity of magnetic resonance techniques at (ultra-)high magnetic field (5 T to 14.1 T). Several methods were applied to accomplish this aim, ranging from hyperpolarizing X-nuclei (^{13}C and ^{129}Xe) to refining conventional ^1H MR methods. The objective was to obtain increased sensitivity for three main aspects along an MR experiment, ranging from boosting the achievable polarization levels in solid state, over generating novel non-persistent radicals which yield high ^{13}C polarization for *in vivo* dissolution DNP to adapting a study-specific coil design.

The first goal was to enhance the spectral diffusion efficiency and to experimentally investigate its influence on nuclear spin polarization in a ^{129}Xe matrix with the aim to improve ^{129}Xe polarization levels. As a second objective, two novel precursors to generate non-persistent radicals for dissolution DNP were investigated for the first time, corresponding DNP samples were developed for their use in hyperpolarized ^{13}C -labelled MRS and their potential was demonstrated in *in vivo* cardiac MRS. A further major effort was put into identifying the respective inherent advantages of two volume coil designs to be able to propose a solution for

performing demanding applications in MRI and MRS at ultra-high magnetic field (14.1 T). Overall, various improvements to enhance MR sensitivity were suggested by experimentally studying the underlying mechanisms at play and by implementing novel methods.

1.3 Outline of the thesis

An introduction to principles of magnetic resonance and dynamic nuclear polarization is provided in **chapter 2**. It elaborates on basic spin physics mechanisms and interactions allowing for polarization transfer. The origin of non-persistent radicals created by UV light is introduced and the evolution of spin polarization under the influence of a strong microwave field and spectral diffusion is given. This theory provides the basis for the methodological developments of chapters 4 and 5. The foundations for chapter 6 are introduced in **chapter 3**, which addresses the underlying physics for signal induction and detection via RF coils. It focusses on the saddle and birdcage coil and describes the main sources of RF loss. Further, chemical exchange saturation transfer imaging is introduced with a short overview on Z-spectrum contributions and past work related to glycogen CEST.

Chapters 4 - 6 provide methodological solutions to either increase the NMR sensitivity of X-nuclei or to combine high MR sensitivity with a homogeneous transmit field for more traditional ^1H MR studies. The developments conducted aim at increasing the efficiency for translational DNP and yield a practical and capable solution for *in vivo* MR studies at ultra-high magnetic field. Improvements tackle several steps along a (hyperpolarized) MR experiment: from enhancing nuclear solid state polarization, over the discovery of novel endogenous DNP radical precursors to the use of a custom-designed RF coil. The underlying principle of all researched applications are based on polarization transfer methods creating contrast in MR. Further, the chapters stress how the introduced solutions can each be adapted to cater to the study-specific aims. Each chapter discusses extensively how results can be optimized by custom-designing the proposed implementations depending on the experimental conditions and primary study aim.

More specifically, **chapter 4** focusses on a method to boost solid state nuclear polarization prior to extraction of the sample for conducting hyperpolarized liquid state or *in vivo* NMR. The chapter analyses an approach to enhance nuclear spin polarization by modulating the frequency of the microwave irradiation. To this end, matrices of embedded nuclear ^{129}Xe

spins were considered. The electron spin-lattice relaxation time of TEMPO radicals were put into relation with the polarization enhancement to understand the impact of frequency modulation on the spin system. To bridge the transition from solid state DNP to hyperpolarized MR, a short optimization study was performed to maximize polarization conservation during the dissolution, respectively sublimation process. This was achieved by locally mapping the B_0 field distribution of the MR magnet and polarizer (**appendix B**).

Chapter 5 investigated another aspect to advance the field towards translational DNP. The focus of the chapter was on the investigation of two novel precursors for photo-induced non-persistent radicals. The two pyruvate analogues, alpha-ketobutyrate and alpha-ketovalerate were characterized for their use as endogenous nonpersistent radical precursors for hyperpolarized MRI. In that context, their reaction to UV light was researched and compared to the known reaction of pyruvate. The hyperpolarization experiments further benefited from the application of microwave frequency modulation, the method studied in chapter 4, to further enhance the solid state polarization of the ^{13}C labelled substrates prior to their use for measuring *in vivo* cardiac metabolism.

The focus of **chapter 6** was centred on simultaneously achieving optimal sensitivity as well as homogeneous transmit field coverage by choosing an adequate RF coil design for thermally polarized ^1H MR studies. Advantages and pitfalls of two established coil designs, a single-channel saddle coil and an 8-leg high-pass quadrature birdcage coil, were identified with the aim to use them for studies combining MRI and MRS at ultra-high magnetic field. Their performance for *in vivo* experiments was demonstrated on the example of glycogen CEST (glycoCEST) imaging of a rat thigh, further illustrated in **appendix C** by means of a 16-leg high-pass quadrature birdcage coil. Similarly to DNP, the working principle of CEST is based on saturation transfer mechanisms.

Finally, **chapter 7** summarizes the main achievements of this thesis. It provides a brief outlook and presents perspectives for potential future work.

Chapter 2

Magnetic Resonance and Dynamic Nuclear Polarization

This chapter starts with a short introduction of the origin of the NMR signal and the principle of hyperpolarization. Specific focus is put on the DNP sample, notably, on the radicals and the generation of non-persistent radicals, which forms the basis for [chapter 5](#). Subsequently, the main interactions occurring within a coupled system of electron-spins and nuclear-spins are identified. They are then used to determine the evolution of the electron spin polarization under the influence of an external microwave field. These derivations require the introduction of the ESR spectrum, the spin-lattice relaxation time and an electron spin polarization transfer mechanism called spectral diffusion. They form the basis of the experiments and simulations conducted in [chapter 4](#). Finally, an overview of the different mechanisms through which the transfer of polarization from electron to nuclear spins occurs is given. In a closing remark, the different uses of xenon gas in medical imaging are highlighted. They provide the rationale for the extensive effort put into the improvement of ^{129}Xe polarization.

2.1 NMR Sensitivity: Origin, Limitations, Selected Solutions

The spin quantum number is an intrinsic property of matter. The nuclear spin, denoted I in the following, can be either half-integer (fermions), integer (bosons) or zero. The principle of NMR is based on the interaction of a non-zero nuclear spin \mathbf{I} with an external magnetic field \mathbf{B}_0 . If a nuclear spin \mathbf{I} is exposed to an external magnetic field, its degenerate energy levels split into $(2I + 1)$ energy levels. This discretization of energy levels is referred to as the *Zeeman effect*. I is a multiple of $1/2$ since it is the combined spin of protons and neutrons inside the nucleus, each characterized by $I = 1/2$. The resulting spin states $|m_I\rangle$ are associated with a quantum number m_I ranging from $-I$ to I in steps of 1. These features hold equally true for an electron spin \mathbf{S} . Only spin $I = 1/2$ particles are considered in this thesis ([Table 2.1](#)), as is the case for the following description and schematics for the sake of simplicity.

The spin operators \mathbf{I} , respectively \mathbf{S} , determine the quantized magnetic (dipole) moment μ as

$$\begin{aligned}\mu_{\mathbf{I}} &= \gamma_I \hbar \mathbf{I}, \\ \mu_{\mathbf{S}} &= \gamma_S \hbar \mathbf{S}.\end{aligned}\tag{2.1}$$

The energy levels of the spin states are split by the Zeeman interaction with the energies of

$$\begin{aligned}E_m &= -\gamma_I \hbar B_0 m_I \\ &= \pm \frac{1}{2} \gamma_I \hbar B_0\end{aligned}\tag{2.2}$$

for $I = 1/2$ spins. The two energy levels considered here are referred to as *up* ($|m_I = +1/2\rangle \uparrow$) and *down* ($|m_I = -1/2\rangle \downarrow$) state. The energy required for spin transitions between energy levels to occur is given by $\Delta E = \gamma_I \hbar B_0 = \gamma_I w_0$.

For two energy levels with spin populations $N \uparrow$ (ground state) and $N \downarrow$ (excited state) such that the total number of spins N in the system is given by $N \uparrow + N \downarrow$, the relative population ratio can be described by the Boltzmann distribution as

$$\frac{N \downarrow}{N \uparrow} = e^{-\frac{\Delta E}{k_B T}}.\tag{2.3}$$

Considering an ensemble of spins, *thermal polarization* describes a purely macroscopic effect, determined by relative spin population difference between the Zeeman energy levels (Figure 2.1) as

$$\begin{aligned}P_{0I} &= \frac{N \uparrow - N \downarrow}{N \uparrow + N \downarrow} \\ &= \frac{\sum_{m=\pm 1/2} m e^{-E_m/k_B T}}{\sum_{m=\pm 1/2} e^{-E_m/k_B T}} \\ &= \tanh\left(\frac{\hbar \gamma_I B_0}{2k_B T}\right) \approx \frac{\hbar \gamma_I B_0}{2k_B T}.\end{aligned}\tag{2.4}$$

The last approximation assumes the high temperature limit where $\hbar \gamma_I B_0 = \hbar w_I \ll k_B T$, with k_B denoting the Boltzmann constant and T the absolute temperature ($[T]=\text{K}$). For nuclear spins, this holds even for $T = 1 \text{ K}$ due to the weak magnetic energy. An overview of polarization values at thermal equilibrium for the spins, temperatures and magnetic fields pertinent for this thesis are listed in Table 2.1.

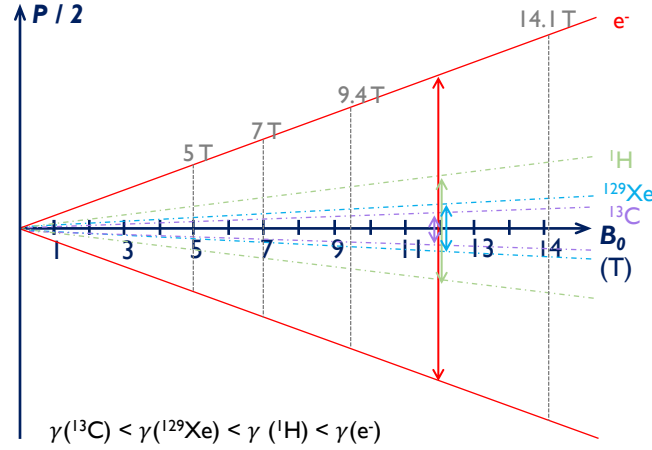


Figure 2.1: Polarization as function of static magnetic field strength (B_0) for the electron and different nuclear gyromagnetic ratios γ . The primary magnetic fields encountered in this thesis are 5 T, 7 T, 9.4 T and 14.1 T. Arrows illustrate the population differences of the energy levels at a given magnetic field. These differences translate directly to differences in polarization. Relative distances are not to scale.

Spin species	$\gamma/2\pi$ (MHz / T)	B_0 (T)	P at 1.1 K (%)	P at 4.2 K (%)	P at 293 K
e^-	-28024.952	5	-99.56	- 66.43	1.15 %
		7	-99.96	-80.78	1.61 %
1H	42.577	14.1	1.3	0.34	50 ppm
^{13}C	10.708	7	0.16	0.04	6 ppm
		9.4	0.22	0.06	8 ppm
^{129}Xe	-11.777	5	-0.12	-0.03	5 ppm
		9.4	-0.24	-0.06	9 ppm

Table 2.1: Nuclear and electronic characteristic parameters and polarization in different magnetic field strengths B_0 of 5 T, 7 T, 9.4 T, 14.1 T. All four spin species have a spin quantum number of 1/2. Temperature and B_0 values of importance in this thesis are used to calculate polarization under different conditions (using [Equation 2.4](#)).

While thermal fluctuations enable transitions between energy levels for individual spins even at thermal equilibrium, the Boltzmann distribution ensures a steady state of macroscopic thermal polarization. In the classical approach, the NMR signal is considered as a macroscopic representation of the microscopic nuclear spin ensemble and therefore directly proportional to the sum of the magnetic moments

$$\begin{aligned}\mathbf{M} &= \sum_{i=1}^{N_I} \mu_i \\ &= (N_{\uparrow} - N_{\downarrow}) \mu_I\end{aligned}\tag{2.5}$$

resulting in the macroscopic bulk magnetization \mathbf{M} . Using equations (2.1) and (2.4) yields

$$\begin{aligned}M_z &= N \frac{\gamma_I \hbar B_0}{2k_B T} \frac{2\gamma_I \hbar}{3} I(I+1) \\ &\stackrel{I=1/2}{=} N \frac{\gamma_I \hbar B_0}{2k_B T} \frac{\gamma_I \hbar}{2} \\ &= N P_I \mu_I \equiv M_0\end{aligned}\tag{2.6}$$

for spin 1/2 particles. Hence, NMR is based on relatively low energy transitions (Equation 2.4, Figure 2.2), in contrast to, for instance, X-ray spectroscopy. The reason for the low sensitivity of NMR becomes evident considering the low polarization at room or physiological temperature, even in the presence of ultra-high magnetic field. Considering for instance ^1H at 14.1 T, the polarization at room temperature (293 K) is only 50 ppm, equivalent to a population difference of 50 spins for an ensemble of 1 million spins. An important factor

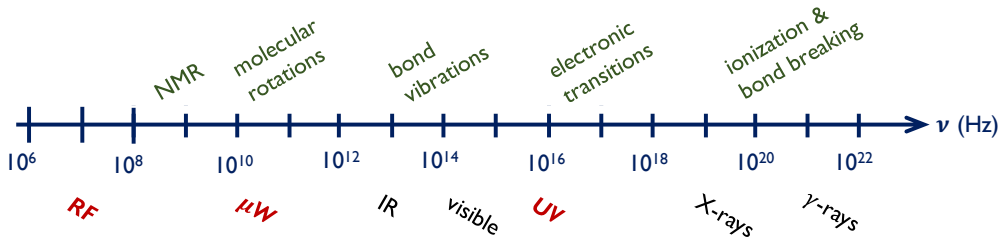


Figure 2.2: Electromagnetic spectrum with typical transition energies as a function of frequency (adapted from [36]). The effect of electromagnetic waves on matter can be of resonating, rotational (in liquid state), vibrational, electronic or ionizing nature depending on the energy-level spacing of the incident radiation [1]. The frequency involved in a certain photon transition determines the types of spectroscopy [1]. Transition energy ranges encountered in this thesis are in the radio-frequency (RF), microwave (μW) and ultraviolet (UV) range.

contributing to sensitivity in MR is therefore the concentration. However, the underlying mechanism limiting sensitivity in NMR is simultaneously the reason for the low-energy deposition during MR scans, giving it the advantage of being a non-invasive imaging tool.

A vast range of solutions exist to counteract the low sensitivity obtained from MR scans, ranging from optimized detection techniques (eg. RF coil, sequences) [2] to de-noising post-processing algorithms [37]. Some of them will be discussed in more depth in using Signal to Noise Ratio (SNR) considerations in subsection 3.1.1. However, a more powerful approach to enhance the MR sensitivity is related to changing the intrinsic nuclear magnetization through hyperpolarization. Different techniques exist to polarize nuclear spins beyond thermal equilibrium, namely Spin Exchange Optical Pumping (SEOP), dynamic nuclear polarization (DNP), the brute force approach and ParaHydrogen-Induced Polarization (PHIP). A short description of their underlying mechanisms is provided in the following chapter, whereas more emphasis is put on SEOP and DNP as they are more pertinent for this thesis.

2.2 Hyperpolarization Techniques

The most straight-forward technique to increase the thermal polarization given by Equation 2.4 is to maximize the magnetic field and to minimize the sample temperature. This approach is referred to as the *Brute Force* approach. Even though temperatures as low as 50 mK and magnetic fields as high as 16 T achieve a remarkable signal enhancement (for instance 80 % ^{13}C polarization at 1 T / 40 °C, after pre-polarization at 14 T and 2.3 K [38]), the longitudinal nuclear relaxation time T_1 at said conditions is in the range of hours to days which makes the method inefficient and poses experimental challenges related to maintaining constant sample temperature [38, 39].

Spin Exchange Optical Pumping (SEOP) is a two-step process first introduced by Happer et al. (1984) [40] to hyperpolarize nuclei of noble-gas atoms such as ^3He , ^{21}Ne , ^{83}Kr , ^{129}Xe or ^{131}Xe [41]. First, during the so-called 'optical pumping', circularly polarized laser light excites the **electrons** belonging to an alkali metal vapor, usually rubidium. The IR-regime of the laser light (few 100 nm -1 mm) thereby matches the wavelength required to excite the electrons. Then, during the 'spin exchange' step, collisions transfer the spin polarization from the valence electrons of the optically pumped alkali-metal atoms to the thermally polarized noble-gas **nuclear** spins. The method is rather powerful since it is able to produce

large volumes (in the order of litres at p_0, T_0) of highly polarized noble gas approaching the theoretical maximum ($> 90\%$) in a short amount of time ($\lesssim 1$ h) [42–45]. The high throughput is an indispensable criterion for using hyperpolarized ^{129}Xe gas in clinical pulmonary ventilation studies and makes SEOP the gold standard for hyperpolarizing xenon gas. As a drawback, a dedicated set-up is required which cannot hyperpolarize other nuclei of interest.

ParaHydrogen-Induced Polarization (PHIP) hyperpolarizes nuclear spins via the chemical reaction of hydrogenation, first introduced by Bowers and Weitekamp (1987) [46]. The hydrogen molecule H_2 occurs in the two possible configurations para-hydrogen (p- H_2) and ortho-hydrogen (o- H_2). The H_2 valence electrons can either be in the singlet state p- H_2 ($I = 0$) or in one of the triplet states of o- H_2 ($I = 1$). In the high temperature limit ($T \gtrsim 180$ K), the molecular states N_o and N_p at thermal equilibrium take a 25% p- H_2 versus 75% o- H_2 distribution, such that $N_o/N_p \rightarrow 3$. In the low temperature limit however, only spin states with low I are occupied such that $N_o/N_p \rightarrow 0$ and all spins occupy the p- H_2 state. At about 20 K and through chemical coupling (hydrogenation), this spin order is transferred within seconds to the (^{13}C -labelled) molecules of interest in NMR ($I \neq 0$) in the presence of a catalyst [47].

The last hyperpolarization technique is *Dynamic Nuclear Polarization (DNP)*. The theoretical framework for DNP was first formulated in 1953 by Overhauser [3] and experimentally demonstrated in the same year by Carver and Slichter [4]. In DNP, nuclear spins are hyperpolarized in a low temperature and high magnetic field environment. The driving force are unpaired electrons of free radicals embedded in the DNP sample, which are irradiated by microwaves. The electron spins are almost polarized to unity at thermal equilibrium in the range of 1 Kelvin and a few Tesla (cf. Equation 2.4). Under the influence of an externally applied microwave field, they are depolarized. The depolarization of the electron spin ensemble is then transferred to nearby nuclear spins (cf. section 2.9 for polarization transfer mechanisms), lifting the nuclear spin polarization beyond thermal equilibrium. This state is referred to as a hyperpolarized state. This way, the linear polarization dependence on the gyromagnetic ratio can be taken advantage of by transferring the intrinsically higher polarization of electron spins onto the nuclear spins of interest ($\gamma_e \gg \gamma_n$). As a consequence, the NMR signal is amplified by 4-5 orders of magnitude, yielding a tremendous gain in SNR. This enhancement factor ϵ is defined as the ratio between the hyperpolarized and the thermally polarized NMR signal integral, I_{hp} and I_{th} , respectively

$$\epsilon = I_{hp}/I_{th} \quad (2.7)$$

and yields the DNP polarization

$$\begin{aligned} P_I &= \epsilon \cdot P_{0I} \\ &= \epsilon \cdot \tanh\left(\frac{\gamma_I \hbar B_0}{2 k_B T}\right) \end{aligned} \quad (2.8)$$

by using Equation 2.4. The rather recent invention of dissolution DNP (dDNP) by Ardenkjær-Larsen et al. (2003) [5], allowed for taking the method of DNP to the next level: by rapidly dissolving the solid sample and extracting it from the polarizer, a hyperpolarized liquid is obtained. The extraction (and transfer to the MR scanner) should happen in the shortest amount of time possible to avoid massive loss in polarization due to short longitudinal relaxation times T_{1I} in liquid state. The hyperpolarized solution, providing a sensitivity enhancement of 4–5 orders of magnitude, can then be used in preclinical studies. This paved the way for *in vivo* hyperpolarized MR. Usually, nuclei occurring at low natural abundance are hyperpolarized. A popular target is ^{13}C , which exhibits a large chemical shift dispersion and forms the gist of most molecules implicated in metabolic processes. Hyperpolarized ^{13}C -enriched probes have enabled real-time imaging of metabolic pathways *in vivo* [6, 8, 9, 11, 12]. The main *in vivo* applications focus on probing cell metabolism and characterizing disease through detection of abnormal metabolic processes. A well-established and biocompatible target is ^{13}C -labelled pyruvate due to its long T_{1I} , the high polarization attainable, the absence of overlapping background signal and the pyruvate-to-lactate conversion mechanism. Recently, translation to human subjects was achieved successfully [14], with many studies demonstrating the potential of hyperpolarized MR for clinical applications [15–19]. To summarize, the dDNP experiment consists of the following major steps

1. **Sample preparation procedure:** generating a homogeneous solution containing a radical, the nuclei of interest and potentially a glassing agent. Experimental awareness: a well-chosen DNP sample is crucial to ensure efficient hyperpolarization (homogeneously mixed, glassing ensured, radical concentration adapted to the experimental conditions, etc).
2. **Substrate hyperpolarization at solid state:** applying microwave irradiation to the DNP sample at low temperatures and high magnetic field (typically at 1.05 - 1.5 K and 3.35 - 7 T).
3. **Dissolution and sample transfer:** dissolving the hyperpolarized solid sample and transferring the liquefied solution as fast as possible. Experimental awareness: Nuclear spin lattice relaxation limits the lifetime of the hyperpolarized state.

4. **Hyperpolarized MR scan:** Liquid state or *in vivo* MR scans are performed while the hyperpolarized state lasts (several seconds to a minute). In the case of clinical DNP, quality control must be performed prior to injection (^{13}C -labelled substrate temperature, pH, purity, residual radical concentration, etc).

Since the DNP sample is key in this thesis, it is discussed more elaborately in the following [section 2.3](#).

2.3 The DNP Matrix

The DNP matrix consists of a diamagnetic solid made of the nuclear spins of interest, potentially embedded in a solvent, and contains a low concentration (mM-range) of paramagnetic centres originating from the radicals embedded in it. Radicals refer to molecules with at least one unpaired valence electron. These unpaired electron spins drive the DNP process. They are found in rare earth and transition ions, highly reactive radicals (unstable) or stable ones to only name a few. Two frequently encountered spin 1/2 radicals are (2,2,6,6-Tetramethylpiperidin-1-yl)oxyl (TEMPO) and tris(4-carboxy-2,2,6,6-tetramethyl-1,3,5-trithienyl)methyl sodium salt (OX063) ([Figure 2.3](#)). While the stable ni-

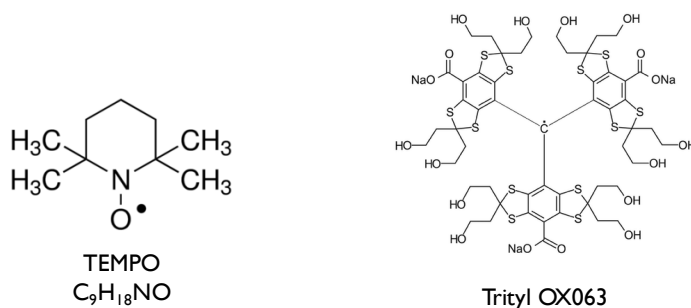


Figure 2.3: Chemical structures of two frequently used radicals in DNP: the broad line-width radical TEMPO (**left**) and the narrow line-width trityl radical OX063 (**right**). The position of the unpaired electron is indicated with a dot.

troxyl radical TEMPO is a well-established target in particle physics [48], it is also popular in dDNP due to its affordability and low physiological toxicity. OX063 is a more recently introduced and rather expensive trityl radical which has proven to be highly efficient for ^{13}C dDNP experiments [5, 49].

The sample matrix needs to be glassing to avoid accumulation of the paramagnetic centres in domains since such an inhomogeneous electron spin distribution leads to poor DNP efficiency [50, 51]. As will be discussed in the following (section 2.6), an efficient DNP process requires radicals to be homogeneously distributed with electrons randomly oriented along all directions. The amorphous arrangement of the lattice that is obtained during glassing avoids the long-range order of crystalline structures.

2.3.1 UV-generated Non-persistent Radicals

This chapter describes a rather specific class of radicals that is currently not commonly used in DNP sample formulations, namely non-persistent radicals. Their brief introduction is motivated by the key role they play in chapter 5. Typically, unpaired electrons of *persistent* radicals are used as polarizing agents. They have proven to be highly efficient for dissolution DNP [22, 52]. Their presence, however, poses a challenge for the translation to clinical applications: Free radicals may be toxic for living organisms so that they require scavenging or mechanical filtration to pass the quality-control step prior to injection [26]. While this step has been optimized and can be done fairly quickly nowadays, it still shortens the brief measurement window of the experiment, which is limited by the relaxation of the hyperpolarized state back to thermal equilibrium [8, 53]. Employing *non-persistent* radicals generated via Ultra-Violet (UV) light irradiation of particular precursor molecules may address this challenge. Organic molecules can undergo a transformation when irradiated with UV light ($\sim 10 - 400$ nm), thereby creating a stable radical at low temperature. Non-persistent radicals recombine into a diamagnetic and bio-compatible species (in small quantities) at 190 K [25, 54]. Their instant elimination during the dissolution process results in radical-free hyperpolarized solutions and the nuclear spin-lattice relaxation is no longer influenced by paramagnetic centres. Their good safety profile obviates the need for filtration of the endogenous radical precursor. Up to date, only three *in vivo* studies have measured metabolic processes by using UV-induced non-persistent radicals [55–57]. A group of such endogenous molecules are α -keto acids, two of which were investigated in chapter 5.

A short description of how such non-persistent polarizing agents are generated based on photo-reactive triplet states is given in the following. Customarily, electronic states of a molecule are represented by the Jablonski diagram [58], which schematically plots energy levels against spin multiplicity (cf. Figure 2.4). The orbitals of a molecule in the ground

state S_0 are filled with two electron spins. The electrons spins are anti-parallel and the total spin of the singlet state is zero. Upon UV-irradiation, one of the electrons is excited into the first (previously unoccupied) excited state. In the case of α -keto acids, for instance, non-persistent radicals can be generated by photo-excitation at 300 - 350 nm [59–61]. Through intersystem crossing, a non-radiative process, an intermediate triplet state (paramagnetic) can be populated. This state has a lifetime between several μ s up to half a minute, during which the molecule is chemically reactive and forms radicals. Possible mechanisms for radical formation are electron transfer or hydrogen abstraction. Afterwards a decay to the ground state S_0 occurs via phosphorescence. The non-degenerate triplet states are called zero-field states since they are present even in the absence of an external magnetic field and are caused by valence electron spin-coupling (fine-splitting). This kind of intersystem crossing is an indirect process requiring spin-orbit coupling.

2.3.2 Current Efforts Targeting Translation to Clinical Standards

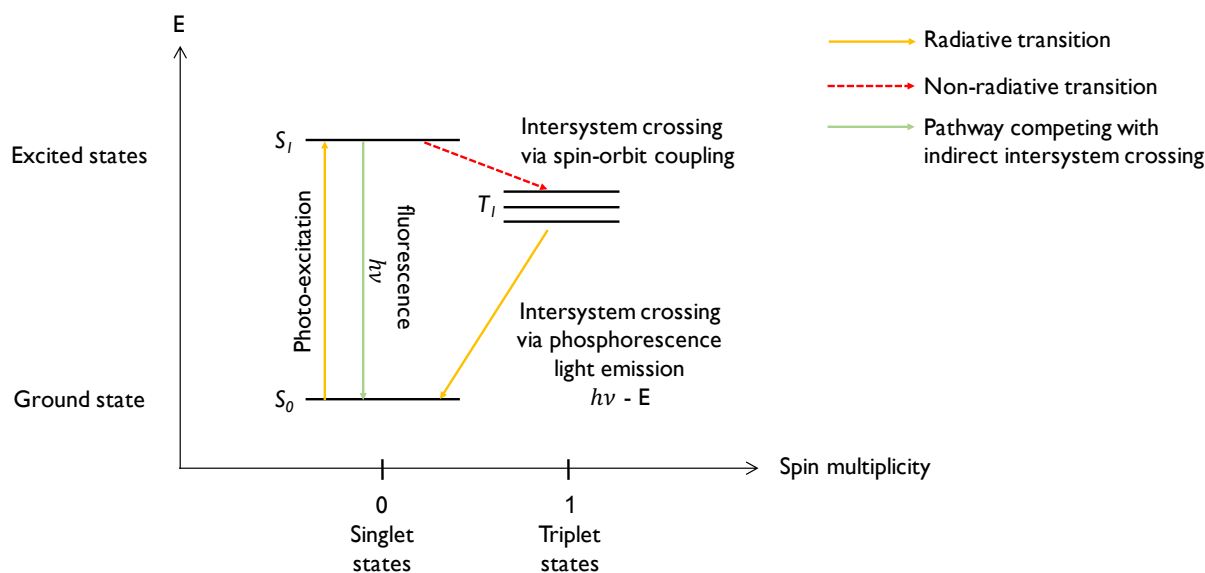


Figure 2.4: Jablonski diagram representing the electronic states of a photo-active molecule. Creating UV-radicals for DNP is based on the principle of photo-excited reactive triplet states. Arrows indicate transitions between the states. Intersystem crossings caused by spin-orbit coupling is a non-radiative transition pathway leading to the population of the triplet state. This pathway is an indirect one and experiences competition from direct fluorescence transitions between singlet states.

Current endeavours in DNP include the simplification of the hyperpolarized substrate delivery and quality control, the reduction of the delay encountered between hyperpolarization and injection, improved robustness of the hardware and injection process. Further efforts target an increasing number of substrates available for human DNP, which is currently almost exclusively focused on hyperpolarized pyruvate, with some exceptions such as hyperpolarized xenon. Furthermore, it would be advantageous to replace bolus injections by continuous substrate administration. Several approaches address the question of establishing the DNP technique for clinical standards, for instance by enabling hyperpolarized MR scans off-site. In this context, storage and transport of hyperpolarized substrates over long periods of time (hours and even days), for instance via non-persistent radicals or polarizing solids¹, are currently being investigated.

2.4 DNP Theory

The following chapter describes the most pertinent interactions encountered in a DNP matrix, as well as the resulting Electron Spin Resonance (ESR) spectrum. For the following derivations, the sample matrix is considered to consist of a single electron and nuclear spin species of spin 1/2 each, with $\gamma_S < 0$ and $\gamma_I > 0$. The theoretical framework further assumes the high temperature approximation limit [64].

2.4.1 Main Spin Interactions

In [section 2.1](#) the electron was introduced as an electrically charged particle which interacts with an external static magnetic field \mathbf{B}_0 ($\parallel \mathbf{e}_z$). This was done for the case of a free electron. To explain the ESR spectrum more fully, this description is developed further for an electron inside a sample matrix.

The energy of an electron with magnetic moment $\mu_S = \hbar \gamma_S \mathbf{S}$ in a magnetic field \mathbf{B} is

¹Polarizing solids refer, for instance, to Silica-based hybrid polarizing solids (HYPSO), a porous network architecture of solids containing the radical TEMPO with the advantage of providing a homogenous DNP matrix free of toxic components [62]. Hyperpolarizing porous polymers (HYPOP) are made of pores of free radicals and were found to improve repeatability and increase hyperpolarization lifetimes up to days [63].

linked to the Hamiltonian

$$\begin{aligned}
 \mathcal{H}_S &= -\mathbf{B} \cdot \mu_S \\
 &= -\hbar \mathbf{B} \cdot \gamma_S \cdot \mathbf{S} \\
 &= -\hbar \omega_{0S} \cdot \mathbf{S}.
 \end{aligned} \tag{2.9}$$

The magnetic field \mathbf{B} includes the externally applied static magnetic field B_0 and perpendicular to it a microwave field $\mathbf{B}_{\mu w}$ as well as the internal fields produced by adjacent particles. The main contribution is the *electron Zeeman interaction* given by

$$\tilde{\mathcal{H}}_S = \mu_B \mathbf{B}_0 \cdot \mathbf{g}_S \cdot \mathbf{S}, \tag{2.10}$$

with the g-tensor \mathbf{g}_S and the Bohr magneton μ_B . This term constitutes the predominant interaction characterizing the ESR spectrum (for $\mathbf{S} = 1/2$, \mathbf{B}_0 in the order of a few T). The g-tensor arises from the interaction of the electron spin \mathbf{S} with the superposition of \mathbf{B}_0 and the internal fields. Considering a DNP sample, the electron spin is no longer isolated such that the expectation value of \mathcal{H}_S , namely the electron Zeeman energy, becomes anisotropic. It is determined by the g-tensor asymmetry due to the orientation-dependent (internal) paramagnetic centres in the external static magnetic field. In the simplified assumption of a free electron, the g-tensor is isotropic with diagonal values of 2.0023193.

Assuming a monochromatic microwave frequency $w_{\mu w}$, the externally applied microwave field ($\parallel \mathbf{e}_x$)

$$\mathbf{B}_{\mu w} = 2 \mathbf{B}_{1,m} \cos(w_{\mu w} t) \tag{2.11}$$

contributes to the total Hamiltonian in [Equation 2.9](#) as

$$\mathcal{H}_{\mu w} = -\mathbf{B}_{\mu w} \cdot \mu_S, \tag{2.12}$$

according to [\[64\]](#). The interaction of the microwave field with the nuclear spins is not considered since the microwave frequency $w_{\mu w}$ is three orders of magnitude too high to interact with the nuclear spins (for instance $w_{\mu w} = 140$ GHz at 5 T versus $w_{0I} = 212$ MHz for ^1H).

In exact analogy, the nuclear Zeeman interaction caused by the coupling between the nuclear spin \mathbf{I} with \mathbf{B}_0 is given by the Zeeman energy of a single nuclear spin ([Equation 2.2](#)), assuming isotopic coupling for simplicity (i.e. $g_I = \text{cst}$), as

$$\begin{aligned}
 \mathcal{H}_I &= \hbar \omega_{0I} \cdot \mathbf{I} \\
 &= \mu_{BI} g_I \mathbf{B}_0 \cdot \mathbf{I}
 \end{aligned} \tag{2.13}$$

to the total spin Hamiltonian. The nuclear Zeeman interaction is 2 – 3 orders of magnitude weaker than the electron Zeeman interaction, depending on the nucleus involved.

The next class of interactions regards mutual spin-spin coupling. The electron spin magnetic moment μ_S induces itself a magnetic field at the location of the nuclear spin \mathbf{r}_I

$$\mathbf{B}_S(\mathbf{r}_{SI}) = -\frac{\mu_0}{4\pi} \left(\frac{\mu_S}{r_{SI}^3} - 3 \frac{(\mu_S \mathbf{r}_{SI}) \mathbf{r}_{SI}}{r_{SI}^5} \right). \quad (2.14)$$

The distance between the nuclear spin position and the electron spin is given by \mathbf{r}_{SI} . The nuclear spin located within this magnetic field generated by the electron spin feels a nuclear Zeeman interaction due to $\mathbf{B}_S(\mathbf{r}_{SI})$

$$\begin{aligned} \mathcal{H}_{SI} &= -\mathbf{B}_S(\mathbf{r}_{SI}) \cdot \mu_I \\ &= -\hbar \gamma_I \mathbf{B}_S(\mathbf{r}_{SI}) \cdot \mathbf{I} \\ &= \hbar \mathbf{S} \cdot \mathbf{A} \cdot \mathbf{I} \end{aligned} \quad (2.15)$$

which causes splitting of Zeeman levels. The tensor \mathbf{A} is referred to as *hyperfine* tensor in case that the nuclear spin is influenced by an electron spin of the same radical molecular group (contact interaction; negligible in DNP) and *super-hyperfine* tensor otherwise. For the latter, the electronic wave function can be approximated by a delta function and the super-hyperfine interaction becomes

$$\mathbf{A}_{\text{SHF}} = \frac{\mu_0}{4\pi} \hbar \gamma_S \gamma_I \left(\frac{1}{r_{SI}^3} - 3 \frac{\mathbf{r}_{SI}^2}{r_{SI}^5} \right) \quad (2.16)$$

which is the form a dipolar interaction. It causes hardly perceptible smoothing of the ESR spectrum and can be disregarded for coarse interpretation of the spectra due to the small coupling strength for increasing distances \mathbf{r}_{SI} . The hyperfine tensor is proportional to $\gamma_S \gamma_I |\psi(0)|^2$ with $\psi(0)$ the electronic spin density probability at \mathbf{r}_I . [Equation 2.15](#) shows that the hyperfine interaction observed in ESR spectra can be discussed independently of the external magnetic field.

Through the same mechanism do also nuclear spins cause a nuclear Zeeman interaction at the site of other nuclear spins as

$$\begin{aligned}\mathcal{H}_{II} &= -\mathbf{B}_I(\mathbf{r}_{II}) \cdot \mu_I \\ &= \hbar \mathbf{I} \cdot \left[\frac{\mu_0}{4\pi} \hbar \gamma_I^2 \left(\frac{1}{r_{II}^3} - 3 \frac{\mathbf{r}_{II}^2}{r_{II}^5} \right) \right] \cdot \mathbf{I}\end{aligned}\quad (2.17)$$

presuming nuclear spins of the same species with an average distance \mathbf{r}_{II} separating them. In the absence of dipolar coupling, all nuclear spins would resonate at their nuclear Larmor frequency w_{0I} . Considering dipolar interaction, though, nuclear spin resonance frequency can take any value in $w_{0I} \pm \gamma_I B_I$. This nuclear dipolar interaction is at the source of nuclear spin diffusion which transfers nuclear spin polarization between nuclear spins. The energy-conserving mechanism of that reverses two spin states simultaneously is referred to as *flip-flop* transition. The inverse relationship between the strength of the interaction and the cube of the distance between nuclei limits the transport of polarization almost exclusively to neighbouring nuclear spins.

Due to the 2 – 3 orders of magnitude lower concentration of electron spin compared to nuclear spins in DNP samples, the average distance between two electron spins r_{SS} is considerably bigger than the range of the wave function $\psi(\mathbf{r}_S; t)$ describing the position of a single spin. It is therefore a justified approximation to replace the wave function by $\delta(\mathbf{r} - \mathbf{r}_S)$ and to assume the electron spin to be located at its center \mathbf{r}_S . This assumption leads immediately to the analogue *electron dipolar interaction*

$$\begin{aligned}\mathcal{H}_{SS} &= -\mathbf{B}_S(\mathbf{r}_{SS}) \cdot \mu_S \\ &= \hbar \mathbf{S} \cdot \left[\frac{\mu_0}{4\pi} \hbar \gamma_S^2 \left(\frac{1}{r_{SS}^3} - 3 \frac{\mathbf{r}_{SS}^2}{r_{SS}^5} \right) \right] \cdot \mathbf{I}\end{aligned}\quad (2.18)$$

with $\mathbf{r}_{SS} = \mathbf{r}_S - \mathbf{r}_{\tilde{S}}$ denoting the approximated distance between two electron spins S and \tilde{S} . Similar flip-flop transitions as mentioned during the discussion of the nuclear dipolar interaction also occur between electron spins. These terms are responsible for enabling electron-spin polarization transfer during the thermal mixing mechanism (cf. [section 2.9](#)).

2.4.2 The Total Spin Hamiltonian

The total spin Hamiltonian describing a system of N_S electron spins and N_I nuclear spins therefore consists of the contributions from the Zeemann interactions, dipolar interactions and the coupling to the microwave field as

$$\mathcal{H} = \mathcal{H}_S + \mathcal{H}_I + \mathcal{H}_{\mu w} + \mathcal{H}_{SS} + \mathcal{H}_{II} + \mathcal{H}_{SI} \quad (2.19)$$

with

$$\mathcal{H}_I = -\hbar w_{0I} \sum_{k=1}^{N_I} I_z^k. \quad (2.20)$$

To resolve the total Hamiltonian of a spin ensemble with $N_I \gg N_S$ analytically, the interaction terms are truncated. During truncation several cross-terms can be neglected without suffering loss of accuracy. The simplified contributions to the Hamiltonian are

$$\begin{aligned} \mathcal{H}_{SS} &= \frac{\hbar}{2} \sum_i^{N_S} \sum_{j \neq i}^{N_S} D_{zz}^{ij} S_z^i S_z^j + \frac{1}{4} D_{+-}^{ij} (S_+^i S_-^j + S_-^i S_+^j), \\ \mathcal{H}_{II} &= \frac{\hbar}{2} \sum_k^{N_I} \sum_{l \neq k}^{N_I} C_{zz}^{kl} I_z^k I_z^l + \frac{1}{4} C_{+-}^{kl} (I_+^k I_-^l + I_-^k I_+^l), \\ \mathcal{H}_{SI} &= \hbar \sum_i^{N_S} \sum_k^{N_I} A_{zz}^{ik} S_z^i S_z^k + \frac{1}{2} A_{z-}^{ik} S_z^i I_+^k + \frac{1}{2} A_{z+}^{ik} S_z^i I_-^k, \end{aligned} \quad (2.21)$$

with $S_{\pm} = S_x \pm iS_y$ and $I_{\pm} = I_x \pm iS_y$. In this form, the equations illustrate nicely how the various interactions contribute to the shape of the ESR spectrum. The $(S_+^i S_-^j + S_-^i S_+^j)$ -term describes spin *flip-flops*, where an electron spin in the up-state flips an electron in the down state and both take the opposite configuration (cf. [Figure 2.6](#)). The ESR lineshape consists conceptually of *spin packets* (elaborated in [section 2.5](#)). The first term of \mathcal{H}_{SS} leads to a shift in ESR resonance frequency of the spin packets, therefore contributing in a major way to the shape of the ESR spectrum. Similarly, the $(I_+^k I_-^l + I_-^k I_+^l)$ -terms represent nuclear spin flip-flops. In the frame of reference rotating at $w_{\mu w}$ the remaining contributions write

$$\mathcal{H}_S = \hbar (w_{0S} - w_{\mu w}) \sum_{i=1}^{N_S} S_z^i, \quad (2.22)$$

$$\mathcal{H}_{\mu w} = \hbar w_{1m} \sum_{i=1}^{N_S} S_x^i. \quad (2.23)$$

Equation 2.19 includes all relevant interactions in our spin system with the exception of the spin-lattice interaction. Atoms embedded in a matrix are subjected to thermal vibrations about their equilibrium position, the so-called lattice vibrations². Spin coupling to the lattice causes spin-lattice relaxation of P_I and P_S and will be treated in section 2.7.

2.5 The ESR Spectrum and Homogeneous Broadening

Dipolar contributions arising from mutual electron spin interactions, mutual nuclear spin interactions and electron-nuclear spin interactions cause homogeneous line-broadening. Only the first and last interaction contribute to the ESR spectrum, though, since the ESR spectrum is a tool to study the system of unpaired electron spins. Practically speaking, the concept works in a similar way to NMR, except that the electron spins are excited instead of the nuclear spins (cf. chapter 4 for a short description on the working principle).

The inhomogeneously broadened ESR spectrum of spin 1/2 particles at $\mathbf{B}_0 \sim \mathcal{O}(T)$ is dominated by the g-tensor anisotropy due to the electron Zeeman interaction and the hyperfine interaction. The g-tensor anisotropy depends on the random³ orientation of the paramagnetic centres in \mathbf{B}_0 . Further, the hyperfine interaction by definition depends on the structural features of the molecular group to which the interactions electron and nuclei belong. Both of these static (time-independent) shifts in w_S lead to considerable differences in resonance frequencies of the electron spins, even within a homogeneous sample and constant \mathbf{B}_0 , as is illustrated by the ESR spectral width which spans several hundred MHz for broad-line radicals at DNP conditions. The super-hyperfine interaction and dipolar electron interaction, on the other hand, cause fluctuations (i.e. time-dependent contribution) of w_S . They are responsible for the homogeneous broadening of the so-called *spin packets*. The experimental ESR spectrum is a convolution of the homogeneous and inhomogeneous contributions, which is illustrated schematically in Figure 2.5. The g-tensor anisotropy causes broadening proportional to \mathbf{B}_0 , however the shifts in w_S due to the hyperfine interaction are independent of \mathbf{B}_0 .

In the following, the total envelope (or line shape) of the ESR spectrum is described through the so-called *spectral density function* $g_N(w)$ such that $g_N(w)dw$ is the probability

²In the thermodynamic picture such thermal vibrations, respectively the lattice (vibrations), are also referred to as the system's *heat bath*.

³Contrarily to crystals, where the crystal axes fix the orientation of the principal axes of the g-tensor, glassing matrices (as aspired in DNP samples) contain randomly oriented paramagnetic centres.

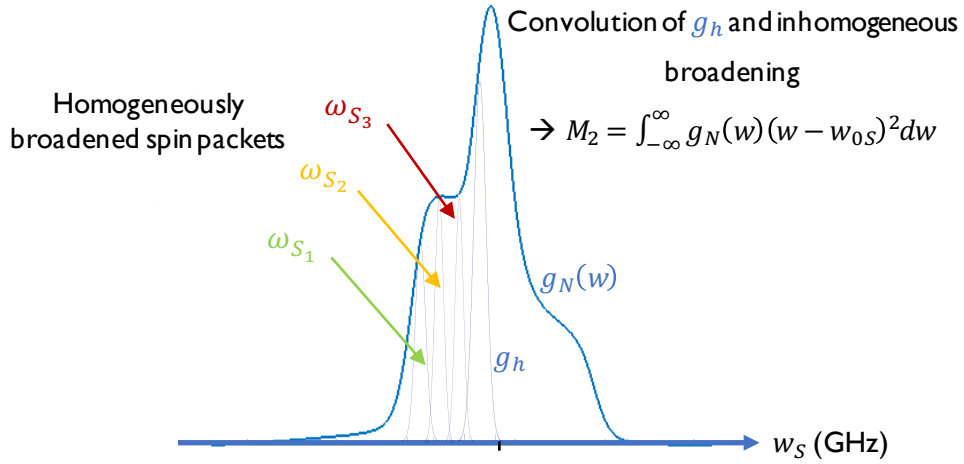


Figure 2.5: Schematic explanation of homogeneous and inhomogeneous line-broadening of the ESR spectrum. The inhomogeneously broadened envelope $g_N(w)$ contains the homogeneously broadened spin packets defined by their respective center frequencies w_{S_1} , w_{S_2} and w_{S_3} . The ESR lineshape was acquired from a 50 mM TEMPO dissolved in 2-methyl-1-propanol sample at X-band and liquid nitrogen temperature.

for an electron spin resonating between w and $w + dw$. The normalized ESR spectrum

$$\int_{-\infty}^{\infty} g_N(w) dw = 1 \quad (2.24)$$

with center of gravity w_{0S} at

$$w_{0S} = \int_{-\infty}^{\infty} w \cdot g_N(w) dw \quad (2.25)$$

is described by the second moment of the ESR spectrum g_N

$$M_2 = \int_{-\infty}^{\infty} g_N(w) \cdot (w - w_{0S})^2 dw. \quad (2.26)$$

To find the average width of a homogeneously broadened spin packet g_h , the mutual interaction between electron spins \mathcal{H}_{SS} is considered. The first moment $M_{1,SS}$ of g_h is proportional to the electron spin polarization P_S and represents a shift of g_N while the second moment

$M_{2,SS}$ describes the spectral density of g_h such that

$$M_{2,SS} - M_{1,SS}^2 = (1 - P_S^2) M_2. \quad (2.27)$$

In the case of full saturation, $P_S \rightarrow 0$ holds. It is assumed that homogeneous line broadening is caused purely by dipolar interactions D_{zz}^{ij} of the N_S electron spins S_i and S_j , $i \neq j$, separated by r_{ij} . Inserting the Van Vleck formula for dipolar broadening [65] yields

$$\begin{aligned} M_{2,SS} &= \sum_{i \neq j}^{N_S} \left(\frac{1}{2} D_{zz}^{ij} \right)^2 \\ &= \left[\frac{1}{4} \frac{\mu_0}{4\pi} \frac{\hbar \gamma_S^2}{r_{ij}^3} (1 - 3 \cos^2(\theta_{ij})) \right]^2 \end{aligned} \quad (2.28)$$

with the angle θ_{ij} between the vector \mathbf{r}_{ij} and the direction of \mathbf{B}_0 . The correction factor $1/2$ was added to account for counting the same interaction twice ($D_{zz}^{ij} = D_{zz}^{ji}$). In a DNP matrix, the spins are embedded in a glassy matrix and therefore randomly oriented, such the bracket expression can be integrated over all directions from 0 to π . Further, DNP samples work with low concentration of electron spins ($\mathcal{O}(10^{19})$ spins/cm³) such that an average distance r_{SS} between the electron spins was assumed. The Poissonian distribution was used to describe the probability of finding another electron spin within a sphere $4/3\pi r_{SS}^3$. Using the electron spin density per unit volume n_S , the average spin packet width writes

$$\begin{aligned} \Delta_{h,SS} &= \sqrt{M_{2,SS}} \\ &= 2 \sqrt{\frac{4\pi}{5} \frac{\mu_0}{4\pi} \gamma_S^2 \hbar n_S} \end{aligned} \quad (2.29)$$

for dipolar broadening. The contribution of the electron-nuclear dipolar broadening to the ESR spectrum has been derived in an analogue manner [66]

$$\Delta_{h,SI}^2 = \frac{11}{32} \frac{1}{0.556} \frac{\mu_0^2}{(4\pi)^2} \gamma_S^2 \gamma_I^2 \hbar^2 n_I^2. \quad (2.30)$$

The nuclear dipolar interaction can be derived accordingly and will take the same form, with the exception of the normalization factor.

2.6 Hole Burning and Spectral Diffusion

Without energy supply through an external source the equilibrium electron spin polarization P_S^0 at DNP conditions is close to unity (Table 2.1). Upon microwave irradiation at the monochromatic frequency $w_{\mu w}$, electron spins resonating close to $w_{\mu w}$ are subjected to a change of polarization due to the absorbed energy from the microwave field. The subsequent ESR signal change is referred to as *saturation* of the electron spin polarization P_S due to electron spin depolarization. This phenomenon leads to *hole burning* of the ESR spectrum, meaning that electron spins resonating at the frequency of irradiation $w_S = w_{\mu w}$ are depolarized (cf. simulations conducted in chapter 4, Figure 4.16 for representation of mechanism). The dipolar electron spin coupling transports the electron spin polarization P_S across the ESR spectrum through *spectral diffusion* (Figure 2.6). The underlying mechanism of spectral diffusion are the *flip-flop transitions* where a depolarized electron flips back to its equilibrium state by depolarizing another electron spin that resonates at a frequency close by. This mechanism is mathematically described by the $(S_+^i S_-^j + S_-^i S_+^j)$ -term in the dipolar

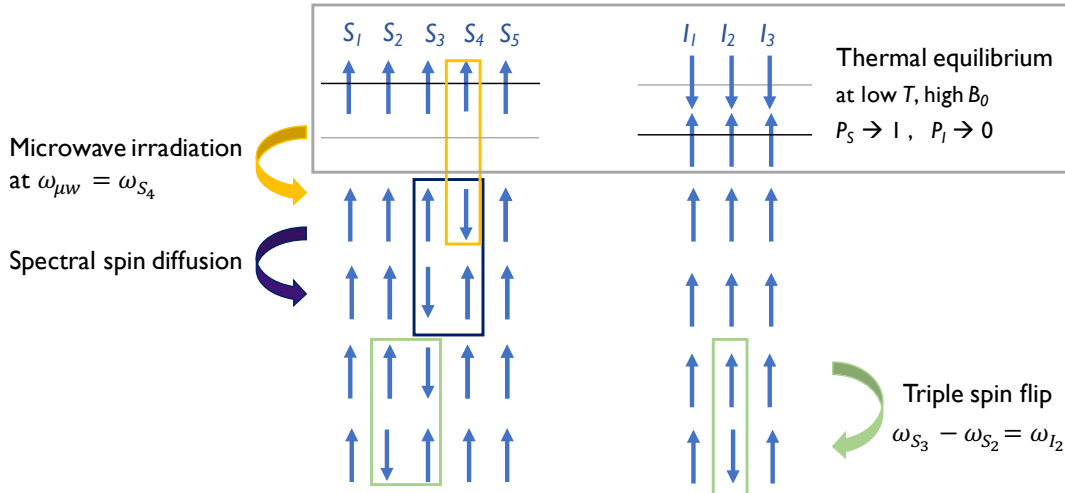


Figure 2.6: Schematic representation of spectral diffusion via spin flip-flops and triple spin flips. At DNP conditions, the electron spin S pool is polarized close to unity ($P_S \rightarrow 1$) and the nuclear spin I pool close to zero ($P_I \rightarrow 0$) (cf. Table 2.1). This situation is represented by the respective populations of the two energy levels (**top**) with the electron spin excited state being the up-state by convention. For the sake of simplicity only the pertinent energy levels are drawn to illustrate the polarization transport mechanisms. Triple spin flips involving two electron spins and a nuclear spin I are encountered if the DNP mechanisms thermal mixing and cross effect take place (cf. section 2.9). No temporal causality is implied: over the course of a DNP experiment, spin flips due to microwave irradiation at $w_{\mu w}$ can occur simultaneously with triple spin flips or spectral diffusion.

electron spin-spin Hamiltonian in Equation 2.21. It therefore also transports the saturation across the ESR spectrum, causing broadening of the hole with time.

To describe the spectral diffusion equation, the electron spin flip-flop transition rate W_{SS}^{ij} is introduced. The rate equation describing the evolution $P_S(w_S)$ is given by

$$\frac{\partial P_S(w_S)}{\partial t} = -W_{SS}^{ij} [P_S(w_S) - P_S(w_{\tilde{S}})] \quad (2.31)$$

By summing over all neighbouring spins resonating at $w_{\tilde{S}}$ and presuming an average dipolar interaction (Equation 2.28), the evolution of polarization writes

$$\begin{aligned} \frac{\partial P_S(w_S)}{\partial t} &= \pi M_2 g_N(w_S) \frac{\partial^2 P_S(w_S)}{\partial t^2} \int w^2 g_h(w_S) dw \\ &= \pi (M_2)^2 g_N(w_S) \frac{\partial^2 P_S(w_S)}{\partial t^2} (1 - P_S(w_S)^2). \end{aligned} \quad (2.32)$$

The diffusion equation should describe a random walk of spin flips across the ESR spectrum since a spin at frequency $w_S + dw$ is just as likely to be flipped as a spin resonating at $w - dw$. From the diffusion equation

$$\frac{\partial P_S(w_S)}{\partial t} = \mathcal{D}(w_S) \frac{\partial^2 P_S(w_S)}{\partial t^2} \quad (2.33)$$

one finds the spectral diffusion constant (with $[\mathcal{D}] = \text{Hz}^3$) for a given electron spin resonance frequency w_S

$$\mathcal{D}(w_S) = \pi (M_2)^2 (1 - P_{0S}^2) g_N(w_S). \quad (2.34)$$

$\mathcal{D}(w_S)$ depends on the initial spin polarization P_{0S} at thermal equilibrium, the normalized ESR lineshape and -width. The characteristic time

$$\tau_{\mathcal{D}} = \frac{\Delta_{ESR}}{4 \mathcal{D}(w_{0S})} \quad (2.35)$$

is required to transport the depolarization across the whole width Δ_{ESR} of the ESR spectrum via spectral spin diffusion.

2.7 Spin-Lattice Relaxation

One crucial kind of interaction that was disregarded in the derivation of the total spin Hamiltonian (Equation 2.19) is the spin lattice interaction. It does, however, provide a non-negligible contribution to the evolution of the electron spin polarization in time. To fully describe broadening of ESR hole burning due to spectral diffusion, this contribution needs to be included. In the following, electron and nuclear spin-lattice relaxation is introduced.

The inverse temperature dependence of the spin polarization (Equation 2.4) tells us that cooling of a spin system leads to increased polarization. Since cooling purely describes a reduction in thermal atomic motion about the equilibrium position and does not directly act on the electron spin, there needs to exist another mechanism coupling the spins to the thermal motion, respectively the lattice. This coupling is given by the *spin lattice interaction*. Three mechanisms of spin lattice relaxation were discovered, namely the direct and the Raman process [67, 68] and later the Orbach process [69]. The Orbach and Raman processes involve coupling of an electron spin to two phonon modes. The latter is a process which heavily depends on temperature but not on w_{0S} . This is the opposite behaviour of what is observed for the direct process, where hardly any temperature-dependence is found. In the following, only the direct process is considered since it is the predominant process for temperatures below ~ 3 K, as encountered at DNP conditions. The direct process describes the coupling of a single electron spin to a single phonon mode. Thereby, the electron spin is flipped as the lattice absorbs or emits a phonon with the energy $\hbar w_S$ (i.e. relaxation requires phonon modes resonating at $w_{ph} = w_{0S}$). In the case of our spin 1/2 particle, the direct spin lattice relaxation is given by

$$\frac{1}{T_{1S}} \propto w_{0S}^5 \cdot \coth\left(\frac{\hbar w_{0S}}{2 k_B T}\right) = \frac{w_{0S}^5}{P_{0S}} \quad (2.36)$$

In case the electron spin system is not considered as an isolated entity, the presence of hyperfine coupling changes the w_{0S}^5 -dependency of the electron spin relaxation rate to w_{0S}^3 . Up to date, the fundamental processes often times still do not fully explain experimental data, such as the T_{1S} -dependence on the radical concentration found in a TEMPO-butanol matrix [70].

Similarly to electron spins, nuclear spins are maintained at thermal equilibrium with the lattice through spin-lattice relaxation. The mechanism of relaxation can either be governed by direct spin lattice relaxation or thermal mixing. In the following, direct relaxation is

assumed to be the dominating process at liquid helium temperatures. The time scale of direct spin lattice relaxation is determined by the characteristic time T_{1I} such that

$$\frac{\partial P_I}{\partial t} = -\frac{1}{T_{1I}} P_I. \quad (2.37)$$

The rate equation is solved by an exponential evolution

$$P_I = P_{0I} e^{-t/T_{1I}} \quad (2.38)$$

which relaxes towards the thermal polarization $P_{0I} = \tanh(\hbar w_I/2 k_B T)$. To describe T_{1I} , a few simplifications are made. First, the model describing nuclear relaxation presumes a simultaneous flip of an electron and a nuclear spin. Starting from the minimal Hamiltonian describing a system of one electron spin and one nuclear spin, applying truncation (as in [subsection 2.4.2](#)) and assuming the lattice (modes) to be at thermal equilibrium at all times (in the thermodynamic picture of a heat bath), one finds

$$\frac{1}{T_{1I}} = \frac{1}{T_{1S}} \frac{[A_{z+}/2]^2}{w_{0I}^2} (1 - P_S P_{0S}). \quad (2.39)$$

Nuclear spin lattice relaxation is driven by the hyperfine interaction with an electron spin, which causes the A_{z+} -dependence. Furthermore, T_{1I} is proportional to the electron relaxation rate. However, it is independent of the mechanism dominating the electron spin relaxation. Finally, in the absence of an external energy source (microwaves switched off) and at high B_0 and low temperatures, one finds $P_S \rightarrow P_{0S} \lesssim 1$ such that the bracket-expression tends towards zero and the nuclear spin lattice relaxation time increases significantly. The spin-lattice relaxation time also increases with an increasing external magnetic field and decreasing temperatures due to the B_0/T -dependence of the thermal polarization ([Equation 2.4](#)). The same holds true for electron spins with the same reasoning. Alternatively, the nuclear spin-lattice relaxation time can also be calculated as a function of observables [\[71\]](#)

$$\frac{1}{T_{1I}} = \frac{N_S}{N_I} \frac{\gamma_S}{\gamma_I} \left(\frac{\Delta_I}{B_0} \right)^2 \frac{1}{T_{1S}} (1 - P_{0S}^2) \quad (2.40)$$

with the nuclear linewidth Δ_I .

2.8 Evolution of the Electron Spin Polarization

To describe the electron spin polarization $P_S(w_S, t)$ during a DNP experiment, the combined action of the continuous-wave microwave field, spin diffusion and T_{1S} relaxation have to be taken into account. The evolution of the electron spin polarization considering all three contributions can be written as [64]

$$\frac{\partial P_S(w_S, t)}{\partial t} = -\pi w_{1m}^2 h(w_S - w_{\mu w}) P_S(w_S, t) + \mathcal{D}(w_S) \frac{\partial^2 P_S(w_S, t)}{\partial w_S^2} - \frac{1}{T_{1S}} (P_S(w_S, t) - P_{0S}) \quad (2.41)$$

with the homogeneous line-shape $h(w_S - w_{\mu w})$ for a spin packet centred at w_S and $w_{1,m}$ originating from the microwave irradiation $\gamma_S |\mathbf{B}_{1,m}|$ (Equation 2.11). The thermal polarization P_{0S} is given by Equation 2.4, which sets an upper limit on $P_S(w, t)$, $\forall t$. For monochromatic irradiation, $w_{1,m}$ is much smaller than the homogeneous linewidth due to the fluctuating fields. In the following, it is assumed that homogeneous line broadening is predominantly caused by dipolar electron spin interaction. Since the average homogeneous linewidth is several orders of magnitude smaller than the full inhomogeneous ESR linewidth⁴, the homogeneous lineshape $h(w_S - w_{\mu w})$ can be approximated by $\delta(w_S - w_{\mu w})$. For long saturation at t_0 such that the system is in steady state, $\partial P_S / \partial t \rightarrow 0$. The boundary condition $P_S(w_{\mu w}, t_0) = 0$ holds for complete saturation upon microwave irradiation. Resolving Equation 2.41 under those assumptions yields the electron polarization

$$P_S(w_S, t_0) = P_{0S} \left[1 - \exp \left(\frac{-|w_S - w_{\mu w}|}{\sqrt{\mathcal{D}(w_{\mu w}) T_{1S}}} \right) \right] \quad (2.42)$$

under the influence of microwave irradiation and accounting for spectral diffusion and electron spin-lattice relaxation. The equation demonstrates that the further away from $w_{\mu w}$ the spin packets resonate, the less they contribute to hyperpolarizing nuclear spins. The exponential dependence on $w_S - w_{\mu w}$ burns a hole of the width $\sqrt{\mathcal{D}(w_{\mu w}) T_{1S}}$ into the ESR spectrum at $w_S = w_{\mu w}$.

⁴For instance, the spin packet width for TEMPO radicals in ethanol at DNP conditions is in the order of 100 kHz - 1 MHz while the total ESR spectral width is ~ 400 MHz [72].

2.9 DNP Mechanisms

Several mechanisms exist which transfer polarization of the electron spin ensemble to the nuclear spins. The mechanisms depend on sample-dependent variables such as γ_N , T_{1S} , T_{2S} , T_{1I} , T_{2I} , nuclear and electron spin concentrations or radical ESR line-width and -shape. The variables are not only inter-dependent but depend also on the external magnetic field strength and temperature. Making deductions on the prevalent mechanism from studies conducted under different experimental conditions are therefore not straightforward. The equilibrium nuclear polarization at different microwave frequencies $P_I(w_{\mu w}, t_{\infty})$ and the polarization build-up time τ are two observables which hold information on which mechanism dominates the evolution of polarization in a given spin system.

At the origin of DNP is the discovery of the *Overhauser Effect (OE)* [3]. The OE refers to the transfer of spin polarization between two coupled spins. Initially an unpaired electron spin and a nuclear spin were considered, as needed for DNP. Shortly afterwards the nuclear OE involving two nuclear spins was described (Figure 2.7). The Solomon equations, based on two nuclear spin species, describe how saturation is transferred from one spin pool to another, such the first pool returns to thermal equilibrium while the second one gets saturated [74]. It was demonstrated experimentally that metals [4] as well as insulators containing paramagnetic impurities [75] can be used as polarizing agents (the so-called solid effect). In the following, a short introduction into three possible mechanisms labelled solid effect, cross effect and thermal mixing is given; a detailed review can be found elsewhere [76]. The first mechanism is based on a two spin system, the second considers a three spin system and the last a many particle system with triple-spin flips.

2.9.1 Solid Effect

In the Solid Effect (SE), a single electron spin is coupled via dipolar interaction to a single nuclear spin. The energy difference between the ground and excited state is much larger for the electron spin compared to the nuclear spin (cf. Figure 2.8). The polarization transfer therefore happens via zero-quantum and double-quantum transitions in a three step process. Since zero-quantum and double-quantum transitions are 'forbidden', the probability of microwave energy flipping an electron spin is low.

The spin system is irradiated with microwaves at a frequency $w_{\mu w}$ slightly off-resonance with respect to the electron spin resonance w_S . The difference in frequency thereby corresponds to the nuclear spin resonance frequency w_I , such that $w_{\mu w} = w_S \pm w_I$. The incident microwave energy is absorbed (with a small probability) which excites the electron spin from the ground state to the first excited state. To ensure energy conservation, a **simultaneous** nuclear spin flip into the nuclear ground state has to occur. This distinguishes the SE from the Overhauser effect. The electron spin relaxes back to its ground state after T_{1S} ($\ll T_{1I}$). It thereby releases a *phonon* into the lattice. Lattice vibrations or phonon modes can be understood as an ensemble of coupled harmonic oscillators. The coupling ensures that the lattice imposes one characteristic T_1 over the whole sample. In the following, hyperpolarizing at $w_{\mu w} = w_S + w_I$ is denoted *negative DNP* since nuclear spins are forced to populate a higher energy level, causing the polarization to become negative. The resonance frequency

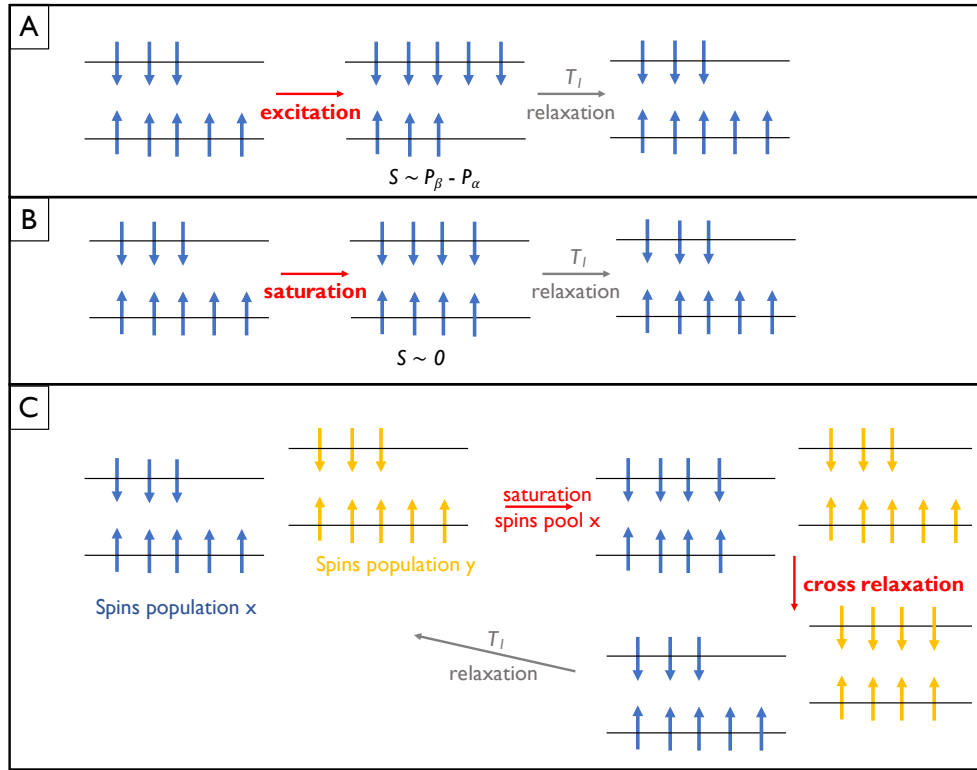


Figure 2.7: Overhauser effect (OE) and cross-relaxation mechanism illustrated on the example of two nuclear spin species. **A)** Conventional signal detection in NMR through spin system excitation. **B)** Thermal equilibrium state is reached through continuous irradiation. Saturation can be transferred, for instance through spin flips (as in DNP) or between molecules through proton exchange, as in CEST. **C)** Example of cross relaxation encountered in the nuclear OE. Transfer of saturation mediated by dipolar coupling, i.e. in the absence of proton exchange. Adapted from [73].

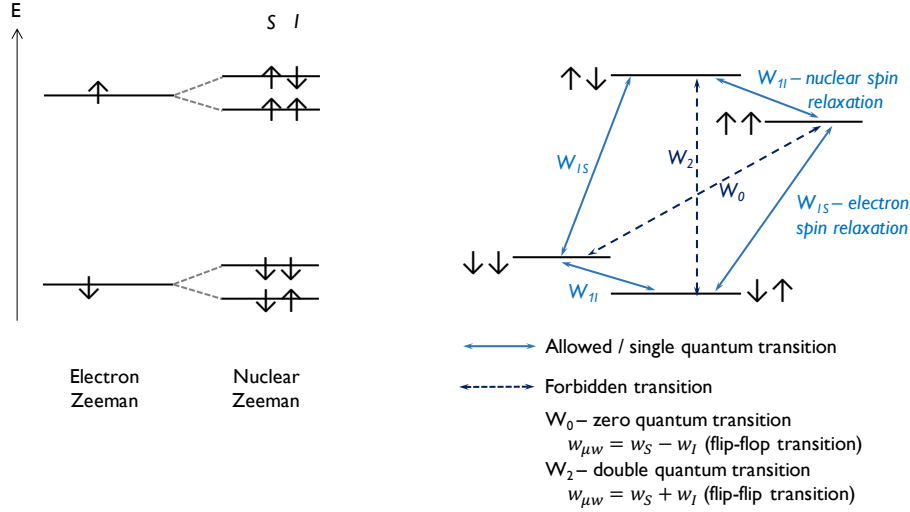


Figure 2.8: Energy levels and transitions of a coupled electron spin (S) - nuclear spin (I) system. In a good approximation, the starting polarizations are $P_S = 1$ and $P_I = 0$ in thermal equilibrium. The energetic separation of the electronic states are much bigger than the one of the nuclear states (**left**). Single quantum and double quantum transitions are so-called 'forbidden' transitions that can be stimulated upon microwave irradiation at $w_{\mu w} = w_S - w_I$ and $w_{\mu w} = w_S + w_I$, respectively. Forbidden transitions are pumped by microwave irradiation at the positive and negative DNP frequency. The system relaxes back into its ground state via electron and nuclear spin relaxation given by the transition rate W_{1S} and W_{1I} , respectively (**right**).

$w_{\mu w} = w_S - w_I$ is referred to as *positive DNP*. The positive and negative DNP are therefore separated by $2w_I$. An overall DNP frequency sweep results from a superposition of the different transitions. At dDNP conditions, usually other mechanisms are predominant for low gamma nuclei, where 'allowed' spin transitions occur.

2.9.2 Triple Spin Flips

The *Cross Effect (CE)* originates from allowed single quantum transitions, contrarily to the SE. Since those are first order transitions they are much more probable to occur. The CE requires three spins to be involved in polarization transfer, a nuclear spin and two dipolarly-coupled electron spins such that the energy-conserving conditions $w_n = w_{S_2} - w_{S_1}$ is fulfilled. Such a *triple spin flip* is schematically illustrated in Figure 2.6. Both, TM and the CE rely on triple spin flips that arise from the hyperfine coupling between electron and nuclear spins. TM can be seen as a generalization of the CE in the picture of a thermodynamic many-particle system.

Thermal Mixing (TM) is the dominant mechanism in samples with a high electron spin concentration and therefore strong dipolar interaction. Those dipole interactions were neglected in the description of the CE and SE. The evolution of a spin system under strong microwave irradiation was described by Redfield (1955) [77]. The Provotorov equations integrated the mean dipole-dipole coupling energy during the cross-relaxation processes [78]. If the spectral diffusion rate is faster than the electron spin-lattice relaxation rate, then the electron spin system reacts as one entity to the applied microwave field. To account for the collective coupling of electron spins to nuclear spins, DNP can be understood in the *thermodynamic picture* using a many-particle system. This approach is based on spin temperature theory in contrast to previous models which consider discrete quantum transitions of isolated spins. The concept of the spin temperature T_S is introduced such that

$$\beta = \frac{\hbar}{k_B T_S} \quad (2.43)$$

is the inverse spin temperature. The polarization P is given by the ratio between the nuclear Zeeman energy (magnetic energy) and the Boltzmann energy as

$$P = \frac{1}{2} \gamma B_0 \beta_S \quad (2.44)$$

in the high temperature limit. At thermal equilibrium, the spin temperature T_S is given by the temperature of the heat bath, respectively the lattice T_L . Practically speaking, the lattice temperature T_L is given by the cryostat temperature. It determines the thermal polarization through $P_{th} = \hbar \omega_{0I} / (2k_B T_S)$. The thermodynamic description works with the analogy that polarized electron spins take the role of a coolant inside a fridge and that the microwaves are the driving power to cool the system down. In a dielectric solid as used for DNP, the nuclear spin system has long relaxation times T_{1I} and is therefore well isolated from the lattice. If T_S differs considerably from T_L , the system is out of equilibrium. Saturation of the spins then causes heating while hyperpolarization results in cooling according to $P \propto 1/T_S$ (cf. [Figure 2.9](#)). Heat dissipating into the liquid helium bath corresponds to the dissipation of energy into the lattice. Leakage is governed by T_1 relaxation of the electron and nuclear spins and *leakage* is defined by

$$\eta = \frac{1}{2} \frac{N_I T_{1S}}{N_S T_{1I}}. \quad (2.45)$$

The Provotorov-Borghini equations describe the evolution of the electron and nuclear 'energy reservoirs', whereas nuclear spin-lattice relaxation occurs due to the presence of paramagnetic centres in the original Borghini equations [79]. A crucial assumption in Borghini's model was the full saturation of the electron spin packets at $w_S = w_{\mu w}$ due to the microwave field,

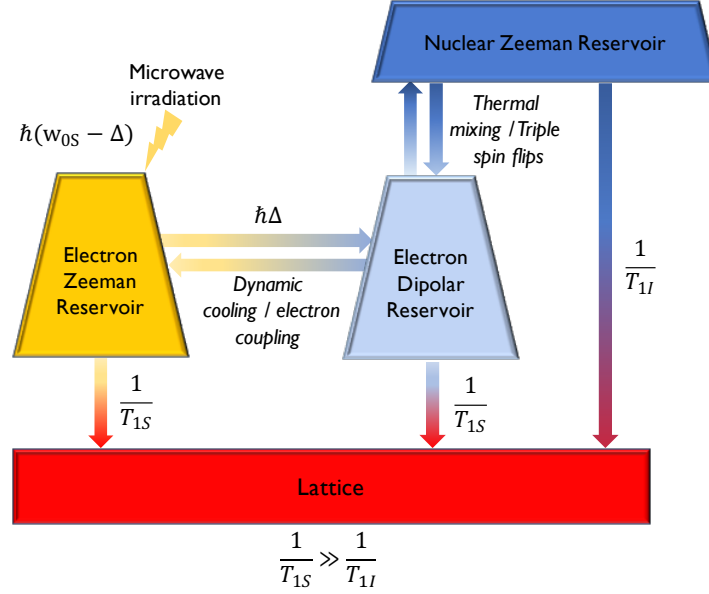


Figure 2.9: Schematics representing the mechanism of thermal mixing in the thermodynamic picture. The two step process involves dynamic cooling of the electron spins to the same spin temperature T_S (Redfield theory, Provotorov equations), followed by thermal mixing during which nuclear spins acquire the same temperature T_S through triple spin flips (Borghini model). At the source of the process is the microwave irradiation at the slightly off-resonance frequency $w_{\mu w} = w_{0S} - \Delta$.

resulting in $P_S(w_{\mu w}) \rightarrow 0$. Using equations (2.43) and (2.7), the enhancement of the nuclear spin polarization is given by

$$\epsilon = k_b T_L \beta_I \quad (2.46)$$

presuming strong coupling of the nuclear spin reservoir to the lattice. Practically speaking, the electron spin-lattice relaxation rate $1/T_{1S}$ decreases fast with increasing temperature such that insufficient cooling of the DNP sample space leads to considerable leakage. In this case, DNP will only take place under the influence of a strong microwave field. Even though the electron spins are already polarized to almost unity at 2 K, DNP is usually performed at temperatures below 2 K to avoid substantial leakage.

2.10 Selected Application: Xenon Gas in Medical Imaging

The use of xenon gas is well established in medical imaging. Xenon exhibits high physiologic compatibility since it does not cause any neurotoxic side effects [80]. The radiopharmaceutical ^{133}Xe is used in single photon emission computed tomography (SPECT) for cerebral blood flow measurements and pulmonary ventilation studies [81]. A most promising feature of xenon is its ability to induce anaesthesia and to serve as a neuroprotectant [82–85]. Acute brain injury caused by, for instance, stroke or trauma is often followed by secondary injury involving notably glutamate excitotoxicity. Xenon inhibits the propagation of oxidative stress-mediated signal cascades by inhibiting glutamate-induced overstimulation [86, 87]. Even though xenon is chemically inert, it still exhibits lipophilic behaviour due to a highly polarizable electron cloud and subsequent spontaneous dipole formation. Hence, easy solubility in lipids facilitates the binding of xenon to glycine sites of N-methyl-D-aspartate (NMDA) receptors or TREK-1 channels [88–90], a process which is at the source of the neuroprotective and anaesthetic properties of xenon gas. Due to the binding of xenon to said glycine sites, the neurotransmitter glutamate no longer acts on those targets, which obviates apoptosis in neuronal tissue. It is this antagonistic action at the glycine binding site that induces anaesthesia and explains the underlying process of neuroprotection by blockage of excitotoxic pathways by competing with the co-agonist glycine [91–93]. The idea has been brought forward to use ^{129}Xe MRI as a *theranostic* (therapeutic and diagnostic) tool, combining neuroprotection with ischemic injury evaluation [94]. Further, the strong affinity of xenon for hydrophobic regions allow the noble gas to diffuse freely through the blood-brain barrier, which has lead to xenon being the gold standard for cerebral perfusion imaging [95, 96].

Hyperpolarized ^{129}Xe is notably able to assess pulmonary diseases that are not caused by ventilation defects but instead, for instance, by pulmonary vascular occlusions or interstitial thickening [97]. A recent study on discharged COVID-19 patients demonstrated the utility of hyperpolarized ^{129}Xe in evaluating impairment of the lung function, which could not be identified using computed tomography [98]. The study found a longer blood-gas exchange function and a high rate of ventilation defects while the pulmonary micro-structure seemed to have made a full recovery. Xenon MRI was capable of not only qualitatively but also quantitatively monitor disease progression and help in diagnosing the nature of the functional impairment [98].

Apart from the convenient physiologic properties of xenon, also its intrinsic physico-chemical features make it a potent probing agent for MRI. The chemical shift of xenon spans >200 ppm in bio-compatible conditions [99], rendering it highly responsive even to hardly-perceptible changes in its local environment. Understanding the chemical shifts *in vivo* and differentiating the presence of xenon gas in the airspace, the interstitial barrier or red blood cells, is of great interest. Furthermore, no background signal contaminates the observed MR signal, so that smallest changes can be detected, which might remain undetected by many other molecules.

The surge of hyperpolarization sparked an interest in hyperpolarizing ^{129}Xe for MR imaging [100–102]. Nobel gases and therefore xenon can be hyperpolarized via Spin Exchange Optical Pumping (SEOP) (cf. [section 2.2](#)). ^{129}Xe hyperpolarized via SEOP was extensively used in clinical applications to conduct MR lung imaging [19, 27, 103–105], research brain perfusion [106, 107], Alzheimer’s disease [108] or conduct HyperCEST [109, 110]. The latter describes a molecular imaging method taking advantage of the fast exchange between free xenon atoms dissolved in a solvent and ^{129}Xe embedded in cages. An alternative method to hyperpolarize ^{129}Xe was proposed using a dissolution DNP polarizer. Hyperpolarized xenon can be extracted via sublimation DNP, a procedure largely identical with dissolution DNP except for the adaption of the output line to allow for the extraction of a gas [29]. [Figure 2.10](#) illustrates the respective advantages of each method: While SEOP allows for generating high polarization in a short amount of time and with sufficient throughput, it also requires a specialized hardware set-up that cannot hyperpolarize many other nuclei of interest, such as ^{13}C . This is the strong point of DNP, which has the disadvantage that the produced ^{129}Xe polarization cannot compete with results obtained with SEOP. Chapter 4 therefore focusses on implementing and researching a method to increase the solid state ^{129}Xe polarization inside a dissolution DNP polarizer.

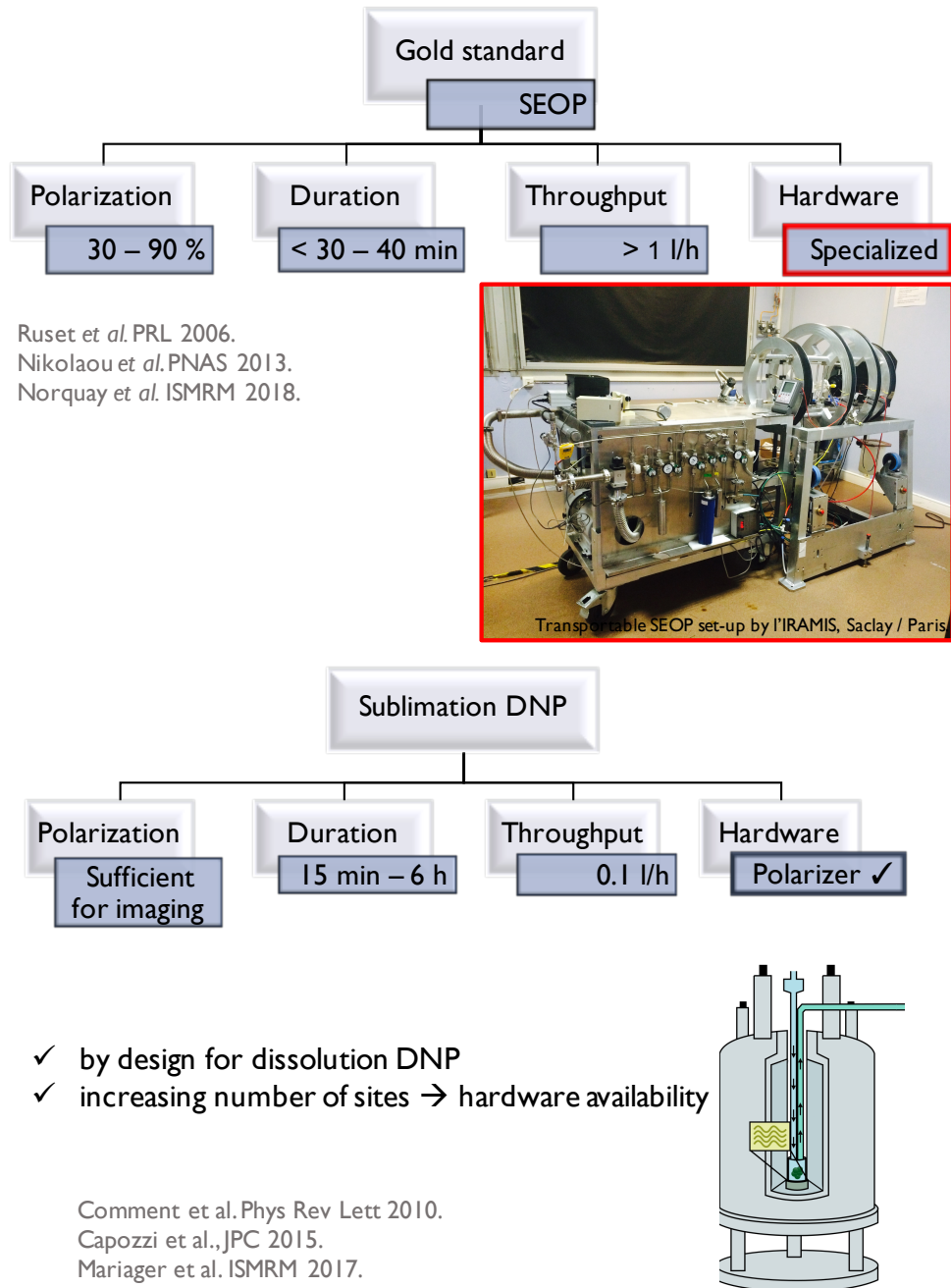


Figure 2.10: Spin Exchange Optical Pumping (SEOP) and sublimation DNP in comparison.

Chapter 3

Selected Principles in MR

This chapter provides the basis for the experiments conducted in [chapter 6](#). RF coils are introduced with focus on the principle of reciprocity, the created radio-frequency field, signal-to-noise ratio considerations and RF losses. The two volume coils investigated later on, an ultra-high field saddle coil and quadrature birdcage coil, are presented. As application of the volume coils, CEST imaging of glycogen is conducted in [chapter 6](#). The mechanism of contrast creation via CEST and different sources of CEST signal contributions are identified. Finally, an overview of research conducted with glycoCEST imaging is given and current endeavours of the scientific community targeting bottlenecks in the CEST method are briefly addressed.

3.1 RF Coils

RF coils are a vital component in an MR experiment, not only for data acquisition but also for signal creation based on excitation. RF coils can intrinsically function in a dual-mode, namely the Transmit mode (TX) and Receive mode (RX) mode. During transmission an oscillating transmit field is generated to 'tip' spins away from equilibrium state (classically speaking), whereas an oscillating magnetic field created by the excited spins is detected in receive mode. Naturally, simultaneous implementation of the two modes is not feasible. The following chapter elaborates on the underlying principle of reciprocity [31].

3.1.1 The Radio-frequency Field and the Principle of Reciprocity

The working principle of the **transmit** coil is based on **Ampère's law**. The current density \mathbf{J} ($[\mathbf{J}] = \text{A/m}^2$), created by the current I passing through the wires of the coil, induces the transmit magnetic field \mathbf{B} according to

$$\frac{1}{\mu} \oint_C \mathbf{B} \, dl = \iint_S \mathbf{J} \, d\mathbf{S} = I, \quad (3.1)$$

with the permeability μ , a loop C enclosing the current path and the surface S enclosed by the loop C . The **receive** part of the coil works based on **Faraday's law of induction**, which described the interaction of a time-varying magnetic field with an electric circuit to

induce an electromotive force ξ

$$\xi = \oint_{\tilde{C}} \mathbf{E} d\mathbf{l} = - \iint_{\tilde{S}} \frac{d\mathbf{B}}{dt} d\mathbf{S} \quad (3.2)$$

in a conductor. \mathbf{E} denotes an electric field and the electromotive force ξ a voltage difference. According to the principle of reciprocity, formulated by Hoult and Richards (1976) [31], the local receive sensitivity is directly proportional to the generated transmit field per unit current I at this location.

The time-varying magnetic field varies in space, thereby generating nodes and maxima. By definition, nodes and maxima follow a $1/2$ -wavelength $\lambda/2$ periodicity, which depends on tissue properties (the speed of light in tissue c , respectively the relative dielectric constant or relative permittivity of the tissue ϵ_r) and the B_0 -dependent nuclear Larmor frequency w_0 as

$$\lambda = \frac{c}{w_0} = \frac{1}{\sqrt{\epsilon_r}} \frac{c_0}{w_0}, \quad (3.3)$$

with the speed of light in vacuum c_0 . In the case of tissue (presuming, for example, an ϵ_r of 50 for a 0.9% saline solution), a wavelength λ of 7 cm is found at 14.1 T, such that a node / maximum occurs every 3.5 cm. This is a dimension comparable to the Region Of Interest (ROI) in preclinical studies. The occurrence of nodes and maxima determine regions of constructive and destructive interference. Overall, the spatial dependence of the magnetic field leads to image shading. RF simulation tools provide numeric solutions to the Maxwell equations, even for non-trivial, situation-specific geometries.

In order to detect signal in NMR, nuclear spins are excited by an external magnetic field \mathbf{B}_1 at the Larmor frequency ($w_0 = \gamma B_0$). \mathbf{B}_1 consists of two circularly polarized components \mathbf{B}_1^+ and \mathbf{B}_1^- with amplitudes $B_{1,max}/\sqrt{2}$ rotating in opposite directions. B_1^+ , component describing transmission, and B_1^- , component describing reception, are composed of the complex-valued transverse field components B_x and B_y according to

$$B_1^+ = \left(\frac{B_x + iB_y}{2} \right) \quad (3.4)$$

$$B_1^- = \left(\frac{B_x - iB_y}{2} \right)^*. \quad (3.5)$$

The transmit field B_1 can be circularly polarized or linearly polarized. Circular polarization

is created by two linearly polarized fields with a 90° phase-shift. The ideal circular polarization of the B_1 field is perturbed upon coil loading and the resulting elliptic polarization is thus characterized by a non-uniform B_1 magnitude distribution.

An optimal coil design aims for maximum efficiency and homogeneity of the circularly-polarized magnetic field in transmit mode and for a high coil sensitivity in receive mode. A measure of sensitivity is the ratio between the induced signal voltage and the standard deviation of the received noise voltage, which corresponds to the Signal to Noise Ratio (SNR). Hoult and Richards (1976) [31] proposed to measure 90° pulse lengths at constant input power, which yielded a direct measure of the SNR. This method allowed for efficiencies of different coil configurations to be compared directly, owing to the *Principle of reciprocity*: TX and RX characteristics of a coil need to correspond, thus the B_1 field generated within the sample per unit current I determines the coil sensitivity. The resistance of the coil determines the noise component and therefore the SNR. Concretely, the induced electromotive force ξ is governed by the transmit field \mathbf{B}_1 (induced by the unit current I) at the position of a magnetic dipole \mathbf{m} as [31]

$$\xi = -\frac{\partial}{\partial t}(\mathbf{B}_1 \cdot \mathbf{m}). \quad (3.6)$$

After application of a 90° pulse, which flips the macroscopic nuclear magnetization \mathbf{M}_0 into the xy-plane, it follows

$$\begin{aligned} \xi &= - \int_{\text{sample}} \frac{\partial}{\partial t}(\mathbf{B}_1 \cdot \mathbf{M}_0) dV_s \\ &= - \int_{\text{sample}} \frac{\partial}{\partial t}[(B_1)_{xy} M_0 \cos(w_0 t)] dV_s \\ &\approx w_0 K (B_1)_{xy} M_0 V_s \cos(w_0 t) \end{aligned} \quad (3.7)$$

whereas $(B_1)_{xy} \perp B_0$ and the transmit field inhomogeneity constant K being close to unity. The approximation is only valid in the case of highly homogeneous transmit fields over the integration volume V_s , such that $(B_1)_{xy} \approx \text{cst}$, $\forall (x, y, z) \in V_s$. The last proportionality follows from the magnetization Equation 2.6, where $M_0 \propto w_0$. Therefore, the induced signal scales with the square of the Larmor frequency, respectively the square of the gyromagnetic ratio. Hence, Equation 3.7 illustrates the decrease in observable magnetization for low-gamma X-nuclei or for low abundance isotopes compared to ^1H MR studies. Thermal movement of charged particles such as electrons causes fluctuating electric fields which results in the so-called Johnson-Nyquist noise or thermal noise. Random thermal noise can originate from

the geometry-dependent coil resistance, the sample or RX circuit components. The SNR increases with the magnetic field as $B_0^{7/4}$. Early equations were found to only provide an order of magnitude of the SNR [111] and the experimental resistance is often higher compared to the theoretical value [31]. The SNR was formulated by Webb (2012) [112] as

$$SNR \propto [\gamma_I B_0] \underbrace{\left[\frac{B_1}{I} \right] \underbrace{\frac{\hbar^2 \gamma_I^2 B_0}{4 k_B T_{sample}} N}_{\propto M_0}}_{\propto \xi, \text{ equ. (3.7)}} \left[\frac{1}{V_{noise}} \right]. \quad (3.8)$$

representing, in order, the dependence on (i) the excitation frequency, (ii) the so-called *coil sensitivity* as magnetic field produced per unit current, (iii) the total Zeeman energy over the whole sample and (iv) random noise from coil and sample. Different approaches to increase the SNR become apparent from Equation 3.8. They include improving the coil sensitivity, respectively B_1 , increasing the Larmor frequency w_0 , increasing energy level differences and thus net magnetic polarization, reducing thermal noise, choosing a larger Volume Of Interest (VOI) to measure a higher number of spins, reducing the receiver bandwidth or reducing T_{coil} (eg. cryo-coils). Other factors can be tweaked as well to achieve a relative SNR increase, such as adapting sequence-related parameters (eg. averages, increasing TR or decreasing TE etc.). Another approach researched in chapter 6 is adapting the choice of the RF coil. While volume coils allow for imaging a larger Field Of View (FOV) and create more homogeneous transmit fields, surface coils are advantageous with respect to high SNR and transmit field efficiency in a ROI in coil proximity.

3.1.2 Bench Measurements

The coil can be tested and its performance evaluated on the bench prior to the actual NMR experiment. Thereby, the RF power transmitted by or reflected from the coil is plotted as a function of frequency. For this, the coil can be connected through a coupling network to a network analyzer or, more affordable alternatives, to an oscilloscope or two pick-up loops. One quantitative measure of a coil's characteristics is the quality factor \mathcal{Q} , which is defined as the ratio between the peak stored energy and the energy dissipated per cycle. For an inductor, this translates to

$$\mathcal{Q} = \frac{w \cdot L}{R}, \quad (3.9)$$

yielding how much energy can be stored in the coil (via inductance) per dissipated energy via coil resistance (losses). Increased resistance leads to decreased \mathcal{Q} , which is seen in a

broadening of the probe-sensitivity curve. Thus, the peak sharpness of the resonance curve is a possible way of measuring Q . Ideally, the only source of loss (because unavoidable) would be the interaction of the magnetic near field with the fraction of the sample within the ROI.

3.1.3 RF Losses

The electromagnetic field generated by an RF coil consists of the Far Field (FF) and the Near Field (NF). In the latter, currents are induced in any conductive component within the reach of the NF, such as the sample. These losses cannot be avoided and contribute to the noise without adding to the signal. These sources of loss are increasingly important in high conductivity environments, i.e. with increasing B_0 and for *in vivo* experiments. The FF does not serve any purpose for signal detection and its losses due to electromagnetic radiation should be minimized. The RF coil is therefore subjected to several sources of loss due to

1. **Magnetic interactions** in NF: The fluctuating transmit field generated during transmission induces eddy currents in any conductor. Non-zero conductivity means loss of the transmitted power in the conductive materials (Maxwell) and therefore SNR decrease during signal detection due to the principle of reciprocity. Naturally, signal detection relies on this magnetic interaction between the B_1 -field and the sample and can thus not be avoided.

Experimental awareness: Optimal coil design ensures that the interaction cross-section is limited to the ROI.

2. **Electric interactions** in NF: These electric (stray) fields, mainly created by the presence of capacitors, arise from potential differences of coil components. The dissipative currents give rise to displacement currents in dielectrics, which again decrease the SNR.

Experimental awareness: The dimension of the RF coil should approach the ROI dimension.

3. **Em radiation** in FF: Loss of electromagnetic energy into the FF due to radiative losses R_{rad} , which scale with the square of the Larmor frequency.

Experimental awareness: Power deposition into the FF can be circumvented in 2 ways: (i) Avoiding wire length dimensions in the range of the em wavelength through capacitive segmentation. Radiative losses are hence especially problematic at high B_0 or

for large coils. (ii) Shielding the coil which simultaneously prevents interfering external fields.

In the unloaded state, losses consist of R_{rad} and R_{coil} , due to circuitry components and capacitors. In the loaded state, sample (or tissue) losses R_{load} are added to the overall RF losses.

3.1.4 The Saddle Coil

The saddle coil and the birdcage coil belong to the family of transverse resonators. They have a cylindrical geometry and produce a transmit field B_1^+ perpendicular to their main longitudinal axis, defined along \mathbf{e}_z and therefore along \mathbf{B}_0 in the MR scanner. Current flowing along the mantle of the cylinder (of length l and diameter d) is at the source of the B_1^+ field. To produce a homogeneous transmit field, the amplitude distribution of the current flowing along the cylinder needs to follow a cosine distribution (ideal case cf. [Figure 3.1](#)). The amplitude of the total current I circulating in the cylinder half-shell is

$$I = \int_{-\pi/2}^{\pi/2} i(\theta) d\theta. \quad (3.10)$$

It is antisymmetric in the yz -plane but symmetric in the xz -plane. Owing to the cylindrical

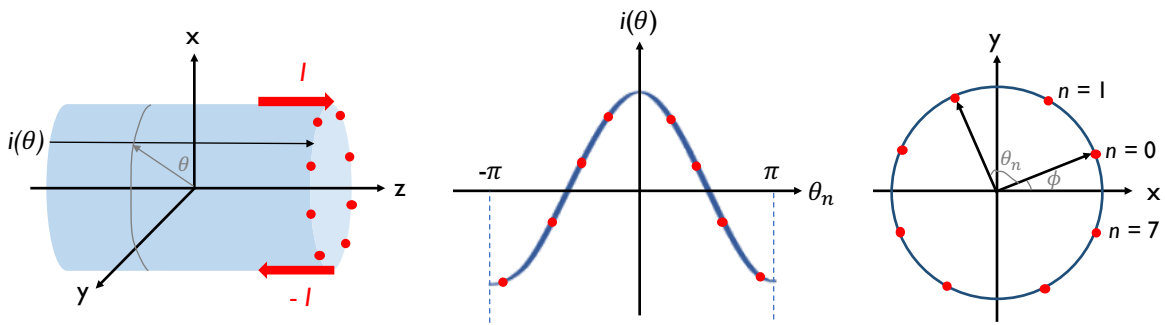


Figure 3.1: Current distribution along transverse resonators of cylindrical shape. A transverse field is created along the y -axis by an (ideally) cosine current amplitude distribution. Each half-shell of the cylinder is driven by an externally fed current I . Exemplary representation of the current distribution $i(\theta)$ in the rungs of an 8-leg birdcage coil (red dots, only one end ring represented).

symmetry, the resulting magnetic field therefore cancels out along the x -axis and is created

along the y-axis according to

$$B_y = \frac{2\mu_0}{\pi} \frac{l}{d\sqrt{l^2 + d^2}} \int_{-\pi/2}^{\pi/2} i(\theta) \cos(\theta) d\theta \quad (3.11)$$

Those equations hold in the theoretical ideal transverse resonator where the cosine-distribution can be reproduced with arbitrary precision and is not distorted by asymmetries.

In the case of the saddle coil the cosine distribution is only coarsely approximated and the magnetic field created by the wires on each half-shell of the cylinder (Figure 3.2) is given

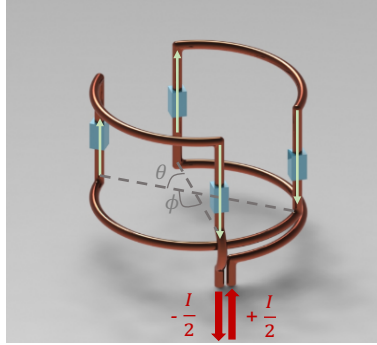


Figure 3.2: Current paths within a saddle coil. Two wires with equal direction of current flow are spanned by the angle θ .

by

$$\begin{aligned} B_y &= \frac{2\mu_0 I}{\pi} \frac{l}{d\sqrt{l^2 + d^2}} \left(1 + \frac{d^2}{d^2 + l^2} \right) \cos(\theta/2) \\ &= 2B_1^+ \end{aligned} \quad (3.12)$$

Maximum homogeneity within the saddle coil is obtained for $\theta = 60^\circ$ [113]. The bracket expression in Equation 3.12 arises from accounting for the return path of the current via the end arcs. Return path contributions cancel out for the B_x and B_z contributions and add up for the B_y contribution. Considering only the contributions of the wires along the half-shells (i.e. without the return path contributions), B_y adopts its maximal value of $2\mu_0 I \cos(\theta/2)/\pi$ for $l \rightarrow \infty$ and vanishes for $l \rightarrow 0$. For an infinitely long cylinder, the transverse field is furthermore perfectly identical in any slice along the main axis. The return path contributions cause the created transverse field intensity to increase with d/l . Short coils therefore see a large contribution to B_y from the return path in contrast to an infinitely long coil where $d/l \rightarrow 0$. Since B_y consists of contributions from the wires along the z-axis and the return

paths, l/d can be optimized to maximize B_y . The maximum B_y amplitude at the center was found for $l/d = 2$ [113], whereas highest homogeneity over the full coil volume requires $l/d = 1.661$ [114]. In practice, a sufficiently large wire thickness should be chosen to reduce resistive losses and saddle coils of large dimensions¹ can be capacitively segmented. The saddle coil design is frequently used for gradient coils or as RF coil with small diameter (a few mm) at high resolution NMR. It is rarely applied in (pre-)clinical studies where bigger coil geometries are required, in which case Alderman-Grand or birdcage coils are preferred.

3.1.5 The Birdcage Coil

Another example of the family of homogeneous coils is the birdcage coil first introduced by Hayes et al. (1985) [33]. In the following, the high-pass birdcage coil is introduced. The birdcage coil approximates the cosine distribution better than saddle-like designs and is intrinsically set-up to be driven in quadrature mode, which is advantageous in terms of SNR. However, it entails a higher dependence of the field homogeneity on the coil design and an increased complexity related to the tuning, especially in the case of multiple tuning. A picture of a home-built 8-leg birdcage coil design is given in Figure 3.3. It illustrates

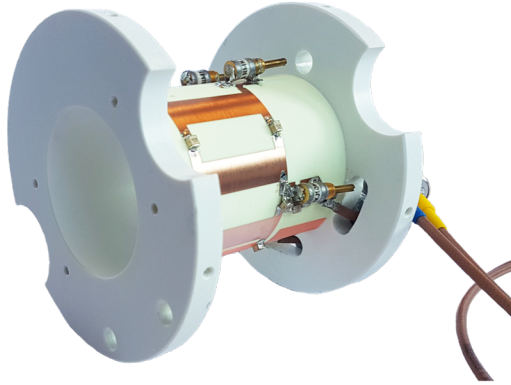


Figure 3.3: Illustration of a quadrature birdcage coil design with $2N = 8$ legs or rungs. This custom-made coil was used for the measurements conducted in chapter 6.

the arrangement of $2N$ identical conductors - the rungs - in form of a linear network which are interconnected by two end-rings. They are arranged on the surface of a cylinder or radius $d/2$ with equal inter-rung spacing s and a total length l . The presence of a current source creates propagating waves in the network, which can interfere constructively to form

¹such that the total wire length exceeds $\lambda/10$ at a given magnetic field

a standing wave. The $2N$ resonant modes created herein correspond to the waves' stationary states. The combined action of the $2N$ conductors, respectively their leg currents, create the magnetic RF field in their midst. A current I_n flows in each rung $n = 0, 2N-1$. It follows a cosine function according to [33, 115, 116]

$$\begin{aligned} I_n &= I(2N) \cos(\theta_n + \phi) \\ &= I_0 \cos(\pi kn/N + \phi) \end{aligned} \quad (3.13)$$

with θ_n defining the angle of rung n with respect to the phase π and frequency modes $k = 1, N$. A visual representation in the case of $2N = 8$ is given in Figure 3.1 (whereas $i(\theta)$ corresponds to I_n). By convention, the first end-ring mode is the $k = 0$ mode, resonating at the highest frequency, and the $k = 1$ mode is the targeted mode for maximum B_1^+ homogeneity (for the high-pass birdcage coil). In the coordinate system where the magnetic field created is along the y-axis, the angle ϕ is defined by the geometry of the coil as $\phi = \pi/2N$. Integrating Equation 3.11 gives the amplitude of the magnetic field aligned with the y-axis as

$$\begin{aligned} B_y &= \frac{2\mu_0 I}{\pi} \frac{l}{d\sqrt{l^2 + d^2}} \left(1 + \frac{d^2}{l^2 + d^2}\right) \zeta \\ &= 2B_1^+ \end{aligned} \quad (3.14)$$

with the rung-dependent geometry factor ζ

$$\zeta = \frac{\sum_{n=0}^{N/2-1} \cos^2(\pi(2n+1)/(2N))}{\sum_{n=0}^{N/2-1} \cos(\pi(2n+1)/(2N))}. \quad (3.15)$$

The proportionality factor ζ ranges from 0.707 for $2N = 4$, identical to the value found for the saddle coil, to $\zeta \rightarrow 0.785$ for $N \rightarrow \infty$. Notably, this implies that the 4-leg birdcage coil can be regarded as a saddle coil with suboptimal angular aperture α of 180° instead of 120° [113]. B_1^+ created in the center of the saddle coil (Equation 3.12) is stronger than the one created by the birdcage coil, assuming the case of optimized angular aperture. B_y is maximal at the center if a ratio l/d of $\sqrt{2}$ is respected. The magnetic field contributions along x and z cancel out. The higher N , the closer the approximation of a perfect cosine distribution of the current. It has been shown that the created B_1^+ field is more sensitive to deviations from the cosine-distribution for coils with a lower number of rungs [117]. This was explained by a better averaging of the current errors if N increased.

The resonant mode of interest is pre-tuned by using fixed capacitors on both end rings in between the rungs. The addition of those capacitors distorts the ideal cosine-current distribution and their capacitance and positioning should therefore be chosen to ensure maximal symmetry. Even manufacture-related deviations from the indicated capacitance values can lead to asymmetry effect. Further sources causing asymmetric current distributions and therefore transmit field inhomogeneities are geometric imprecisions. Also the presence of the soldering metal impacts the circuit since it locally increases the thickness of the endrings, therefore decreasing the inductance locally. Those contributions all add up and lead to perturbed resonance modes, i.e. degenerate modes split and coupling between the two quadrature modes is amplified. Practically speaking, this can render the choice of the right resonance frequency difficult. Variable capacitors can replace some of the fixed capacitors on the lower end-ring to be able to manually fine-tune and -match the coil as a function of the load. Furthermore, adding an isolation capacitor results in better decoupling between the two quadrature modes. Using first-order perturbation theory, Tropp (1991) [118] showed that placing two variable capacitors at $\pi/4$ with respect to the isolation capacitor almost perfectly eliminated splitting. However, capacitance values were required to not deviate by more than 7-8 % from the fixed birdcage capacitances, otherwise the splitting would not be avoided.

3.2 Creating Contrast via CEST

Chemical Exchange Saturation Transfer (CEST) refers to the use of exchangeable protons to create contrast in MRI [119]. Chemical exchange of protons is a dynamic process that increases MR sensitivity of low concentration metabolites. Applications of CEST range from pH mapping over enzyme activity monitoring to cell labelling and *in vivo* studies conducted in brain, cartilage or muscle [73, 120–124].

Exchangeable labile protons (or solutes) bound within the structures of metabolites, are labelled by applying long Radiofrequency (RF) pulses at the resonance frequency of the metabolite of interest. Through chemical exchange the saturated protons switch sites with bulk water protons, leading to a well observable change in water magnetization along \vec{e}_z . This indirect detection method thus relies on intermolecular saturation transfer. Solute concentrations are several orders of magnitude lower than the one of the water pool. Hence, visible change in macroscopic water z-magnetization requires repeated exchange as well as reoccurring frequency-selective RF saturation of the same solute protons (Figure 3.4). A

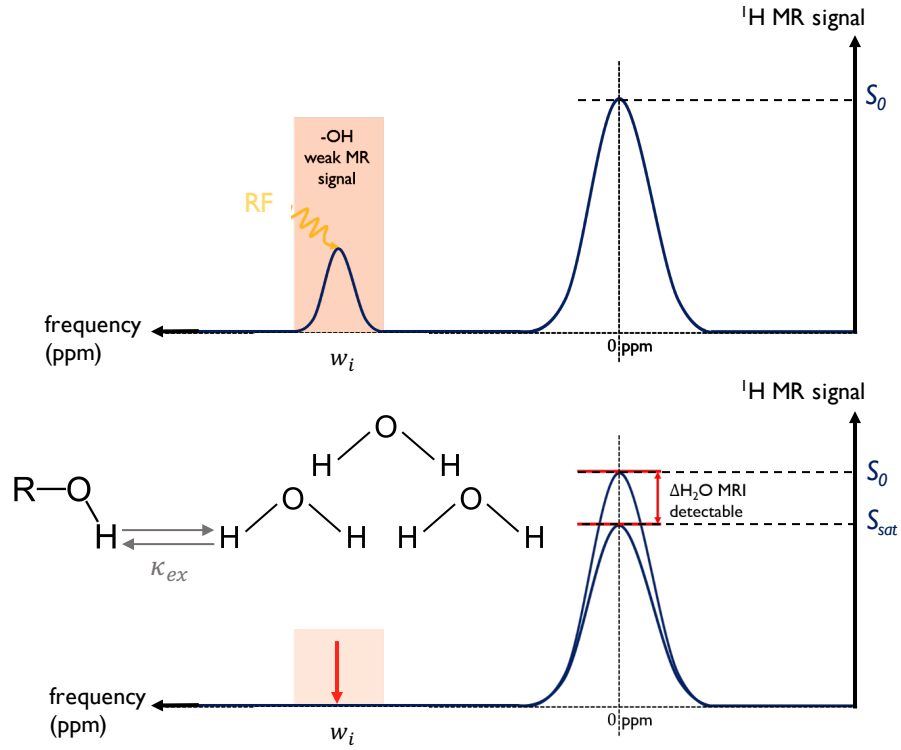


Figure 3.4: Generating contrast via CEST. The generation of CEST contrast is illustrated on the example of a solute containing mobile protons within a hydroxyl group (-OH). The ^1H signal of the solute pool is several orders of magnitude lower than the MR signal of free water protons (S_0) and such that MR sensitivity is not sufficient for satisfactory direct saturation. Applying RF pulses at the site of the mobile solute protons (w_i) leads to saturation of the solute peak. They exchange sites with protons in the water pool through chemical exchange which leads to saturation of the water signal (S_{sat}). This subsequent measurable change in signal is denoted CEST effect.

sufficiently fast proton exchange rate k_{ex} is therefore indispensable. On the other hand, facing too high exchange rates implicates difficulties in saturating the solute protons entirely, which decreases the observable bulk water magnetization change. Calibrating the duration of saturation is necessary to ensure steady state is reached. In general, the exchange rate k_{ex} varies between solute protons, respectively depends on the spectral distance between the exchanging pools. Therefore, a classification is defined based on their chemical shift δ with respect to free water protons, namely the slow exchange regime $k_{ex} \ll \delta$, the intermediate exchange regime $k_{ex} \sim \delta$ and the fast exchange regime $k_{ex} \gg \delta$. The type of molecule, pH and temperature influence the exchange rate [125], whereas k_{ex} can be in the order of some Hz in the case of amides [126] up to several 10^4 Hz for hydroxyls [127]. Solutes belonging to the fast exchange regime are characterized by broader Lorentzian resonances in the CEST spectrum compared to the ones in the slow exchange regime.

CEST imaging is classified into two mayor categories, namely diamagnetic CEST (diaCEST) and paramagnetic CEST (paraCEST)². While diaCEST agents can be both, exogenous or endogenous compounds, paraCEST agents are exclusively exogenous. ParaCEST agents contain ions that cause the ligand protons to exhibit huge chemical shifts. The advantage of diaCEST agents, on the other hand, is that no metallic compound needs to be injected as is the case for paraCEST agents. Therefore, non-toxicity and hence straightforward translation to *in vivo* studies are easier to accomplish. However, diaCEST agents have the disadvantage of exchanging protons belonging to -OH or -NH groups already present in cells and tissue: They resonate usually well within 10 ppm of the water resonance making detection challenging since they are at risk of direct saturation. Spill-over competes with the CEST effect and decrease the specificity to the underlying biochemical exchange processes [128]. For the same reason is ^1H MRS not useful for the detection of such resonances, considering that water suppression would be needed.

Mathematically, the CEST effect can be modelled by the Bloch-McConnell equation system [129–131]. The spin population of a water pool coupled the spin population of a solute pool – a so-called ”two-pool” system – with respective equilibrium magnetizations $M_{0,w}$ and $M_{0,s}$ is considered (Figure 3.5). Forward and backward exchange rates conserve the ratios

²Even though recently an extended method of categorization relating to the type of the exchanging species including, for example, molecular exchange (eg. hyperCEST) has been suggested [121].

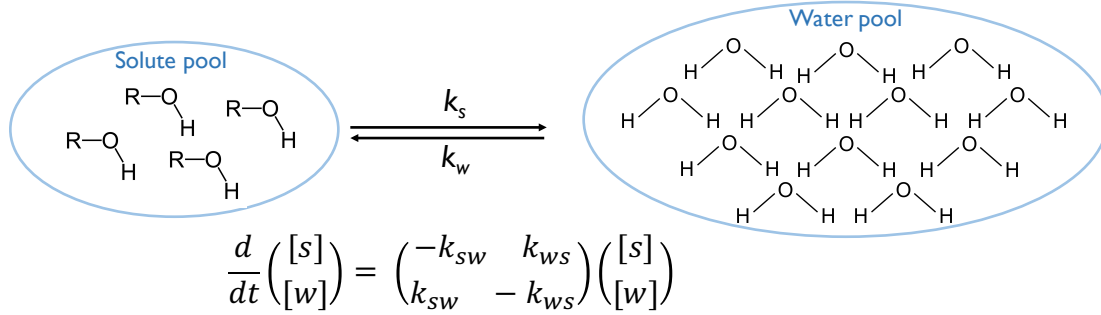


Figure 3.5: Temporal evolution of a system of a solute pool (s) coupled to a water pool (w) with concentrations $[s]$, $[w]$ and exchange rates k . Example of exchanging protons belonging to a hydroxyl group -OH.

$$\begin{aligned} \frac{k_{0,w}}{k_{0,s}} &= \frac{M_{0,s}}{M_{0,w}} \\ &= \frac{n_s \cdot [s]}{n_w \cdot [w]} \end{aligned} \quad (3.16)$$

with number of protons per molecule n , pool concentrations $[s]$, $[w]$ and the proton exchange rates $k_{w,s}$ denoting the proton exchange from the water pool to the solute pool and vice versa for $k_{s,w}$. The Bloch-McConnell equations describe the temporal evolution of $M_{0,s}$ and $M_{0,w}$ under RF irradiation in the absence of dipolar coupling [129, 132, 133]

$$\frac{d}{dt} \begin{pmatrix} M_{xw} \\ M_{yw} \\ M_{zw} \\ M_{xs} \\ M_{ys} \\ M_{zs} \end{pmatrix} = \begin{pmatrix} -k_{ws} & \Delta w_w & 0 & k_{sw} & 0 & 0 \\ \Delta w_w & -k_{ws} & -w_1 & 0 & k_{sw} & 0 \\ 0 & -w_1 & -k_{ws} & 0 & 0 & k_{sw} \\ k_{ws} & 0 & 0 & -k_{sw} & \Delta w_s & 0 \\ 0 & k_{ws} & 0 & \Delta w_s & -k_{sw} & -w_1 \\ 0 & 0 & k_{ws} & 0 & -w_1 & -k_{sw} \end{pmatrix} \begin{pmatrix} M_{xw} \\ M_{yw} \\ M_{zw} \\ M_{xs} \\ M_{ys} \\ M_{zs} \end{pmatrix} - \begin{pmatrix} M_{xw}/T_{2,w} \\ M_{yw}/T_{2,w} \\ (M_{0,w} - M_{zw})/T_{1,w} \\ M_{xs}/T_{2,s} \\ M_{ys}/T_{2,s} \\ (M_{0,s} - M_{zs})/T_{1,s} \end{pmatrix} \quad (3.17)$$

in the rotating frame of reference (x,y,z) with spin-lattice and spin-spin relaxation times T_1 and T_2 and using $\Delta w_j = w_{RF} - w_j$, $j = w, s$. In other words, it describes a probability per unit time for magnetization to be transferred from one pool to another. For CEST, $[s] \ll [w]$ holds, which justifies the assumption of negligible backward exchange of saturated protons since $k_w \ll k_s$. The Bloch equations can further be modified to include dipolar cross-relaxation terms, yielding the Bloch-Solomon equations used to describe Nuclear Overhauser Effect (NOE) in mathematical analogy to the Bloch-McConnell equations [74]. The concept is

much the same as the original Overhauser effect introduced in [section 2.9](#) but with the cross-relaxation rate between forbidden single- and double-quantum transitions now corresponding to the exchange rates. Similarly, two proton pools are considered instead of a pair of an electron and nuclear spin coupled by dipolar interaction. The Bloch-McConnell equations were further extended to model 3 pools and generalized for multi-pool systems, especially of interest in the case of paramagnetic CEST agents which often contain more than a single type of labile proton [\[132\]](#). MATLAB-compatible toolboxes have been implemented to conduct such simulations [\[134\]](#) and several approaches for solving the Bloch-McConnell equations numerically [\[135\]](#) and analytically [\[123\]](#) have been developed, catering to the requirements of the specific applications. They include, but are not limited to, the steady-state approximation ($\sum_i \sum_j dM_{i,j}/dt \rightarrow 0$, $i = x, y, z, j = w, s$), the strong saturation pulse approximation respectively full saturation limit ($w_{eff} \gg k_{s,w}$) [\[136\]](#) and in the large-shift limit ($w_s \gg w_w$) [\[137\]](#) the weak saturation pulse approximation (no direct saturation of water pool, on-resonance with solute pool $\Delta w_s = 0$) [\[138, 139\]](#). The Proton Transfer Ratio (PTR) for a given saturation time t_{sat}

$$PTR = \frac{M_{0,w} - M_{z,w}(t_{sat})}{M_{0,w}} \quad (3.18)$$

can subsequently be calculated (from the solutions extracted from the Bloch-McConnell equations) within those limits. They will, however, not hold outside of their validity range³. A related, frequently-encountered parameter is the Magnetisation Transfer Ratio (MTR), which in its full-saturation limit corresponds to the PTR calculated in the large-shift limit [\[138, 139\]](#). Similarly, several validity limits apply to the MTR and various case distinctions have been proposed [\[123\]](#). Current research furthermore targets the accelerated acquisition of CEST spectra, which can take up to an hour and more if not optimized [\[140, 141\]](#). The calculation for MTR asymmetry is introduced in the following chapter ([Equation 3.20](#)).

3.2.1 Disentangling the Z-spectrum Architecture

One possible method to evaluate CEST contrast is the so-called Z-spectrum [\[142\]](#). Z-spectra are generated by sweeping an RF pulse over a range of irradiation frequencies w_i (offsets), symmetric with respect to the water resonance frequency w_{H_2O} . The resulting water signal $S(w_i)$ is calculated for each saturation offset over a chosen ROI. It is then normalized by an unsaturated signal S_0 , respectively for a saturation far from the water resonance. By

³For instance, the often-referred to PTR calculated in the large-shift limit (ideal case) by Zhou et al. (2004) [\[138, 139\]](#) is likely to be a poor approximation for glycoCEST imaging with higher power pulsing.

plotting the signal intensities at their respective offset frequency, a dip in the Z-spectrum indicating the CEST effect appears at the site of the exchanging protons. Z-spectra are, by convention, plotted from positive to negative offsets (left to right). The water peak is redefined at 0 ppm, unlike the convention of 4.7 ppm used in MRS.

Several competing mechanisms unrelated to chemical exchange can simultaneously occur and their pathways often coexist, unintentionally contributing to contrast and thereby precluding quantification of metabolite concentrations. If they are not accounted for, the resulting CEST effect is either over- or underestimated or not detectable altogether. To illustrate in all detail the complex interactions of these parasite contributions, their origin as well as mathematical, experimental or post-processing methods to account for them is beyond the scope of this thesis and can be found elsewhere [120, 123, 139, 143]. Nevertheless, three major contributions superimposing the CEST contrast in Z-spectra (Figure 3.6) are briefly described in the following.

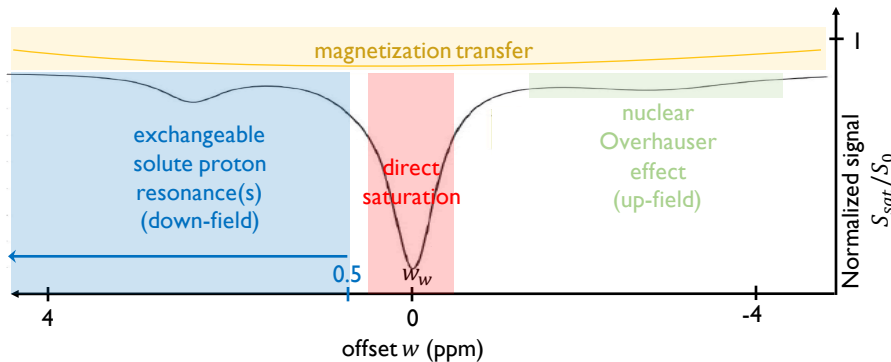


Figure 3.6: Schematics of Z-spectrum architecture consisting of the solute resonance peak of interest and parasite contributions from Direct Saturation (DS), Magnetization Transfer (MT) and Nuclear Overhauser Effect (NOE). The exchangeable protons generating contrast in CEST resonate down-field from water (redefined at 0 ppm). DiaCEST agents resonate closer to the water peak than paraCEST agents and are therefore more prone to being affected by direct water saturation, respectively spillover.

At clinical magnetic field strength, the solute protons of endogenous amides, amines and hydroxyls resonate close to the water frequency. The free water protons therefore experience undesirable Direct Saturation (DS) from the RF pulse instead of displaying loss of magnetization due to the CEST effect. DS cannot be completely avoided since the RF pulse bandwidth is finite. The subsequent influence of DS of water protons on the solute pool is referred to as spillover. The DS spectrum follows a Lorentzian lineshape with Full Width Half Maximum

(FWHM) [73]

$$FWHM_{H_2O} = \frac{\gamma_I B_1}{\pi} \sqrt{\frac{T_1}{T_2}}. \quad (3.19)$$

The contribution of DS becomes therefore more pronounced at stronger saturation amplitudes B_1 .

Furthermore, *in vivo* Z-spectra contain contamination from NOE, causing magnetization change up-field from w_{H_2O} [120, 144, 145]. NOE occurs due to polarization transfer between nuclear spins via cross-relaxation. Here, polarization transfer is not linked to physical proton exchange but occurs due to dipolar coupling and is thus almost exclusively limited to nearest neighbours (cf. Equation 2.17). Saturation is transferred from one spin pool to another, such the first pool returns to thermal equilibrium while the second one gets saturated [74] (Figure 2.7). In liquid state, however, the effect is not detectable in proton spectra since it is averaged out due to fast molecular tumbling of small molecules. Yet, molecular motion is reduced in macromolecules and even more so in semi-solid tissue as for instance cell membranes, such that an observable effect arises [73].

Similarly, asymmetric Magnetization Transfer Contrast (MTC) occurs due to fast transfer of NOE, mediated by the dipolar coupling of nuclear spin diffusion across a molecule. The effect is only detectable if the spin diffusion rate exceeds the longitudinal proton relaxation rate. Magnetization is then transferred from the proton pool of mobile macromolecules to free water protons [120, 146]. The macromolecular resonances - in the range of dozens of ppm and therefore broader than NOE-based contributions - broaden the spectrum and lead to signal reduction.

Quantitative evaluation of the CEST effect faces different pitfalls related to inter-study comparison and system-dependent parameters that influence the absolute CEST effect, such as pH, temperature, B_1 of the RF pulse etc. A popular method is the calculation of asymmetry of the two wings of the Z-spectrum regarding the frequency of free water protons. Symmetric contributions to the Z-spectrum can be eliminated by conducting this point-to-point subtraction called MTR asymmetry [147]

$$MTR_{asym}|_{w_i} = \frac{S_{sat}(-[w_i - w_{H_2O}]) - S_{sat}(w_i - w_{H_2O})}{S_0}. \quad (3.20)$$

This method quantifies in a discrete manner the spectral asymmetry with respect to the water resonance frequency w_w by conducting a point-wise subtraction of signal intensities

at equal offsets from w_w . As a consequence, symmetric contributions are cancelled out, as is the case for DS [148], providing that an RF saturation pulse of symmetric envelope was implemented. However, the nature of the subtraction implies that asymmetric contributions, for instance due to the NOE, are not taken into consideration. Alternatively, the Z-spectrum can be considered as a superposition of effects with Lorentzian lineshapes. Thereby, fitting of multiple Lorentzian contributions accounts for a more thorough description [149].

3.2.2 Artifacts - B_0 Shift and B_1 Inhomogeneities

Saturation patterns, MR sequences and post-processing-correction approaches, which cater to the needs of the specific application, have been developed and discussed [120, 121, 123, 124, 150, 151]. The following chapter concentrates on briefly presenting and discussing some pertinent ones. MTR asymmetry analyses are highly sensitive to magnetic field inhomogeneities. These inhomogeneities are further exacerbated at ultra-high field, so is the MTR asymmetry sensitivity. The presence of significant B_0 inhomogeneities causes not only attenuated CEST contrast but also broadened MTR asymmetry. B_0 correction remains indispensable irrespective of the shim quality, especially when asymmetry approaches are used to evaluate the CEST effect. Several approaches have been developed. While some are post-processing algorithms others require an additional scan. The most common ones include 1) Simultaneous mapping of water shift and B_1 (WASABI), which can be conducted within a mere minute [152] 2) Water Saturation Shift Referencing (WASSR), where the time-consuming dense sampling around 0 ppm can be omitted [153] 3) ΔB_0 mapping by dual-echoes based on TE differences 4) higher-order polynomial fit of the Z-spectrum with voxel-wise maximal saturation determination [126] 5) global minimum search of fitted Lorentzian line-shape [149]. While method 3) is time-consuming, the first method hardly prolongs the scan duration and methods 4) and 5) even work directly with the acquired Z-spectrum. Finally, WASSR is a low energy deposition method and can thus be acquired quickly, also in clinical settings.

Not only CEST contrast but also the contribution of NOE is highly B_1 -dependent. Implementing B_1 correction approaches improve the CEST data reliability [137, 154]. Proposed methods include the double-angle method [155, 156], which requires an additional scan to create a B_1 field map thereby increasing the total scan time and WASABI, which is fairly quick [152]. Especially for studies monitoring relative changes in CEST effect, does B_1 cor-

rection become indispensable to exclude mistakenly interpreting B_1 deviations for changing solute concentrations. A possible pipeline to evaluate the CEST effect considering various corrections is displayed in Figure 3.7.

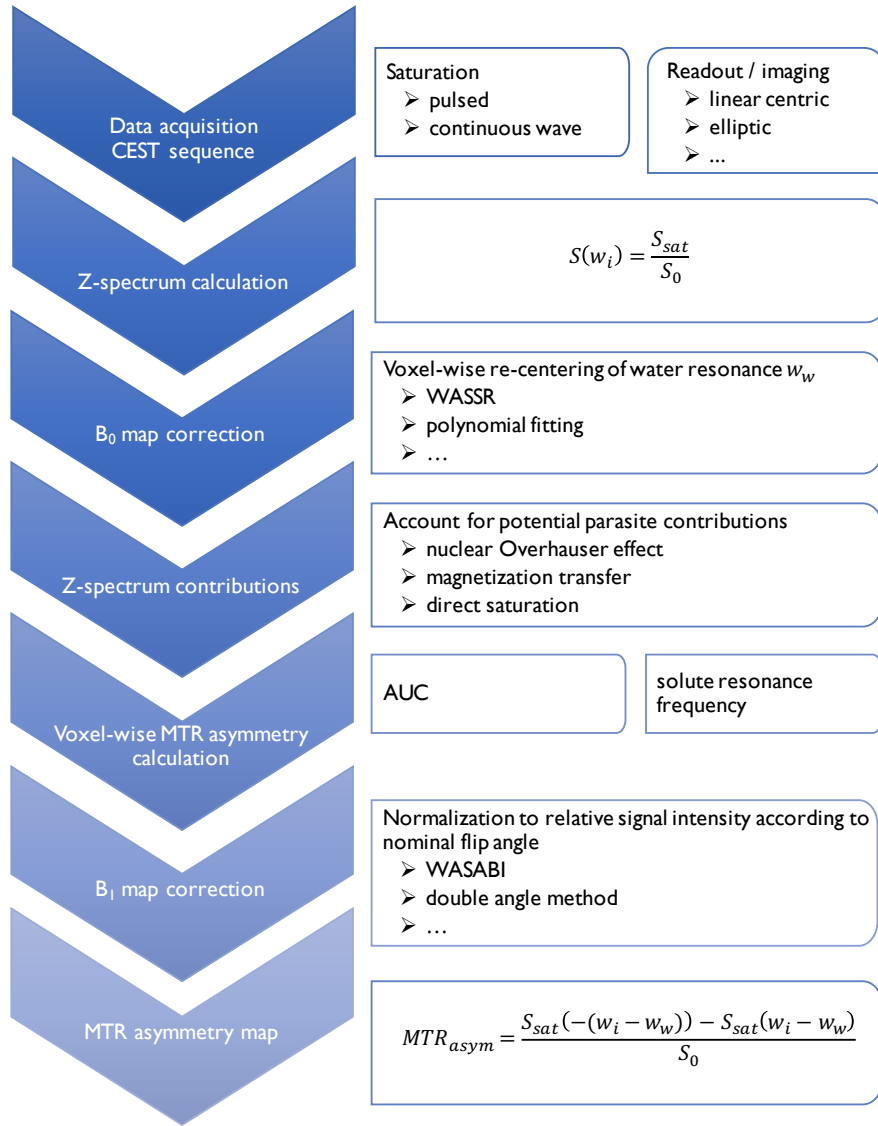


Figure 3.7: Suggested pipeline from data acquisition to MTR asymmetry map, including calculations to disentangle Z-spectrum architecture or to account for B_0 shift and B_1 inhomogeneities.

3.2.3 GlycoCEST of Hydroxyl Protons

In vivo glycogen detection via CEST would enable the study of physiologic and pathological conditions by another method than the currently used gold standard ^{13}C MRS, which is not globally available on clinical MR systems. GlycoCEST applications further include glycolysis-related metabolic disorders, responsiveness to insulin and other abnormal glycogen storage such as type 2 diabetes and obesity [122]. Reliable glycogen detection relies on short TE due to its extremely short T_2 [32], with T_2 in H_2O reported between 29 ms at 11.7 T [157] to 38 ± 3 ms at 8.4 T [158]. The hydroxyl protons of glycogen (-OH group) resonate around 1 ppm down-field from water, hence extremely close to the water resonance $w_{\text{H}_2\text{O}}$. Hydroxyl protons are in the intermediate to fast exchange regime since their chemical shift δ is much smaller than their exchange rate $\kappa_{ex} \sim \mathcal{O}(10^3 - 10^4)$ Hz, which requires high power pulsing to be selective enough while avoiding DS [127]. While selectivity can theoretically be achieved with long pulse widths and small B_1 , the exchange of proton limits the available time during which they can be saturated. This fast exchange regime is suboptimal for CEST imaging since it entails a broad line-shape and complicates selective RF irradiation. Yet, as the -OH groups are embedded within the complex structure of glycogen molecules they suffer loss of mobility. As a consequence, the exchange rate decreases. Further, the chemical shift δ increases with the static magnetic field. This puts less constraints on the pulse bandwidth, leading to easier fulfilment of the spectral selectivity condition and can therefore decrease unwanted DS [125]. The nuclear magnetization lifetime T_{I1} increases with B_0 , thereby prolonging the time interval during which saturation transfer via proton exchange can take place. Several glycoCEST studies (*in vivo* and / or *ex vivo*) were successfully performed in magnetic field strengths as low as 3 T [153, 159–161] (cf. Table 3.1 for overview). Previous studies were sensitive to the CEST effect created by low glycogen-concentration (> 10 mM) in phantoms [159, 160] as well as high-concentration environments (50 - 300 mM) such as liver and skeletal muscle (calf and thigh) [125, 153, 159–163]. However, cerebral glycoCEST was not performed up to date, nor do phantom measurements display the necessary sensitivity to reliably detect the CEST effect created by concentrations < 10 mM.

3.2.4 State of the Research

Even though CEST is among the more recent MRI techniques, it is a rapidly evolving field. As mentioned, unfolding the Z-spectrum architecture is of particular interest and major efforts are put into correcting for and disentangling parasite contributions unrelated to chemical exchange. While DS and magnetization transfer effects can be accounted for by employing symmetry corrections and multiple irradiation pulses, this does not hold for other contributions, such as the ones originating from the nuclear Overhauser effect. The aspiration is to work towards reliable detection of low concentration metabolites resonating close to the water resonance frequency with high spectral and temporal resolution, ideally at clinical field strengths. Another key objective of the CEST community relates to inter-study comparison. Sequence-related parameters such as saturation pulse duration t_S and transverse field strength B_1 affect the measured (absolute) CEST effect. Thus, quantification – relating the CEST effect directly to solute concentrations – remains one of the prevailing challenges.

Table 3.1: Overview over previous work conducted on glycoCEST imaging in chronological order [125, 153, 159–163]. Experimental conditions specify whether the study was conducted *in vivo*, in phantoms or in volunteers. Further, some of the essential parameters determining the CEST effect are noted, namely the magnetic field, the organ and hence the estimated (or measured) glycogen concentration and the position at which glycoCEST was detected.

Exp. Cond.	Organ	B_0 T	glycogen concentration mM	CEST effect resonance ppm	Study	Year
Phantom / perfused liver (mouse, fed)	Liver	4.7 / 9.4	200 (phantom) 200-300 (perf. Liver, fed)	0.5-1.5	Van Zijl et al.	2007
Bovine liver phantom / human	Calf muscle	3	200 (phantom) / ~50-100 (calf)	0-2	Kim et al.	2009
Human	Skeletal muscle, calf	7	~ 200-300	1	Dula et al.	2013
Phantom / human	Skeletal muscle, thigh	3	20-200 (phantom)	0.5-1.5	Clark et al.	2016
Human	Liver	3	~200-300	0.5-1.5	Deng et al.	2016
Rat	Skeletal muscle, thigh	14.1	~50-100	0.5-1.5	Vinckenbosch et al.	2018
Phantom / Human	Skeletal muscle, calf	3	10-200 (phantom) / ~200-300 (calf)	0.5-1.5 (max and integral)	Simegn et al.	2020

Chapter 4

Enhancing ^{129}Xe Spin Polarization in Short Electron T_1 Matrices via Microwave Frequency Modulation

Partially adapted from:

*Zanella, C.C., Lê, T.P., Radaelli, A., Hyacinthe, J.-N., Grütter, R., Capozzi, A.
Microwave Frequency Modulation Enhances Solid-state ^{129}Xe Polarization in Ultra-short Rad-
ical T_{1,e^-} Matrices. (Tentative title)
Manuscript in preparation.*

Contribution

The contribution of Claudia C. Zanella consisted of data acquisition, data analysis, data interpretation and preparing initial manuscripts.

4.1 Abstract

Hyperpolarized xenon gas is used in clinical MR trials to study, for instance, cerebral perfusion and pulmonary diseases. To ensure high MR sensitivity, maximal nuclear solid state polarization is aspired to. However, in solid state matrices where the spectral diffusion time is high compared to the electron spin-lattice relaxation time, the spectral diffusion is not rapid enough to spread the microwave-induced reduction of electron spin polarization across the ESR line. In this case, the efficiency of the hyperpolarization process is dampened, limiting the achievable nuclear . To counteract this inefficiency, modulation of the microwave frequency was implemented. This method allowed for an increase in polarization levels by up to 220 % (from 3.5 % to 11.2 %) for xenon spins embedded in solvents doped with the broad-linewidth radical TEMPO compared to the polarization obtained in the same sample without applying microwave frequency modulation. The results of solid state DNP experiments further indicated that ^{129}Xe polarization levels were predominately limited by the characteristic electron spin-lattice relaxation rate $1/T_{1S}$, rather than the hyperfine broadening of the TEMPO ESR line-shape. The radical T_{1S} in xenon-embedded matrices was extremely short, considering the given experimental conditions, with relaxation times ranging from 5.0 ± 0.4 ms to 21.0 ± 0.2 ms depending on the solvent. For the five samples investigated, the enhancement in polarization upon modulating the microwave frequency was found to be correlated to T_{1S} . The evolution of the electron spin polarization under the combined influence of an external microwave field, spectral diffusion and simultaneous spin-lattice relaxation was anticipated by performing spin system simulations. The characteristic time to spread the electron spin saturation across the whole ESR spectrum (of 355 - 450 MHz full width) was estimated between 0.1 - 1 ms, depending on the sample. The effect of hole burning was simulated for a mono-chromatic microwave frequency as a function of the hole width burnt into the ESR spectrum. The same effect was illustrated for the polychromatic case. A homogeneous spin packet width of 1.4 MHz was found. Hence, modulation of the microwave frequency by 150 MHz engaged over 100 spin packets directly, instead of just a single spin packet as for monochromatic microwave frequency irradiation. The results corroborated that modulating the microwave frequency leads to higher initial electron spin depolarization and subsequently higher nuclear ^{129}Xe polarization. Even though the impact of frequency modulation ranged from hardly perceptible polarization changes to downright boosting nuclear polarization, the method was in no studied case disadvantageous (assuming an appropriately chosen input wave function).

4.2 Introduction

The noble gas xenon has been extensively used in medical imaging due to its advantageous physico-chemical features (cf. [section 2.10](#) for an elaborate overview). The surge of hyperpolarization sparked an interest for hyperpolarizing ^{129}Xe for clinical MR imaging, with applications ranging from pulmonary studies [[19](#), [27](#), [103–105](#)] to researching brain perfusion [[106](#), [107](#)] and Alzheimer’s disease [[108](#)]. Most recently, the use of hyperpolarized ^{129}Xe to study the disease progression of COVID-19 has demonstrated its value for lung function monitoring, which could not have been assessed using, for instance, computed tomography [[98](#)]. The conventional method for hyperpolarizing noble gases such as xenon is SEOP (cf. [section 2.2](#)). Using SEOP, enriched xenon (86 % ^{129}Xe) was hyperpolarized up to 35 % while providing an appreciable throughput rate of 1.8 l/h [[44](#)]. Depending on the system, even higher polarizations have been reported, however, usually at the price of lower throughput rates [[42](#), [164](#)].

An alternative method to hyperpolarize ^{129}Xe was proposed using a generic dissolution DNP polarizer. This way of hyperpolarizing ^{129}Xe has the advantage of avoiding the need for specialized hardware such as a SEOP set-up, since slight modifications to a dissolution polarizer suffice. Modifications include, for instance, tuning the saddle coil of the DNP insert to the ^{129}Xe resonance frequency or putting an adequate disposition for xenon gas collection in place. In previous studies, xenon was hyperpolarized to 5 – 7 % in solid state, extracted via sublimation DNP [[29](#)] and used to conduct *in vitro* hyperpolarized MR imaging at a remote location [[66](#), [165](#)]. The throughput rate of hyperpolarized gas was rather low ($\mathcal{O} \sim 0.1$ l/h at 760 mm Hg, 20° C), even though adequate hardware modification were suggested to increase this throughput remarkably to 3 l/15 min [[29](#), [166](#)]. Xenon gas was liquefied and admixed to TEMPO-doped solvents [[29](#), [66](#)]. Alternatively, UV radicals could be used to hyperpolarize the heterogeneous xenon matrix [[167](#)] or powder impregnation using HYPISO structures can be considered [[62](#)]. Enriched xenon (70 % ^{129}Xe) was furthermore hyperpolarized in a clinical GE SpinLab with a fluid path system and measured at a remote 9.4 T MR scanner [[168](#)]. Hence, the research published up to date demonstrated successful hyperpolarization of xenon gas using generic polarizers, however, authors suggested that further steps needed to be taken to increase the currently achievable xenon polarization.

One method to enhance the DNP performance is to modulate the external magnetic field under continuous wave microwave irradiation [[169](#)] or to replace the monochromatic

microwave frequency with modulation¹ of the irradiation frequency in a static external magnetic field [30, 170–173]. The efficiency of this method being sample- and set-up-dependent, it is not an *a priori* powerful tool for any given radical or experimental condition (B_0, T). Previous studies showed that frequency modulation had a positive effect on ^1H , ^2H , ^{13}C and ^{29}Si nuclear spin polarization at DNP conditions when using radicals with a broad Electron Spin Resonance (ESR) spectral width in the range of a few 100 MHz [30, 170–173]. Broad linewidth radicals are for instance nitroxide radicals, such as the commonly used free radical TEMPO. The use of polychromatic microwave frequencies was also suggested for systems at higher temperatures (~ 50 K) that were characterized by short electron spin-lattice relaxation times T_{1S} of TEMPO around 1 ms (estimated) [172]. For increasing temperatures from 6 K to 50 K the T_{1S} of TEMPO² was found to decrease from 108 ms to 500 μs [174] and for TEMPOL³ from 170 ms to 3 ms [175]. At dDNP conditions, a TEMPO⁴ T_{1S} of 310 ms [176] and a TEMPOL⁵ T_{1S} 106 ms [177] were reported.

The study reported in the following chapter aimed to increase the solid state ^{129}Xe polarization achieved inside a conventional polarizer by applying microwave frequency modulation. Furthermore, solid state experiments were conducted to determine if a correlation between electron spin lattice relaxation time and change of ^{129}Xe polarization due to the application of microwave frequency modulation was measurable. The efficiency of microwave frequency modulation was studied for different ^{129}Xe matrices doped with TEMPO. To explain the observed change in nuclear spin polarization when modulating the microwave frequency, the behaviour of the unpaired electrons of free TEMPO radicals was studied. The electron spin system was investigated through (i) direct T_{1S} measurements and (ii) simulations of the evolution of the electron spin polarization. The electron spin relaxation time T_{1S} of unpaired TEMPO electrons was measured by conducting Longitudinal Detection (LOD)-ESR measurements at DNP conditions (5 T, 1.15 K). Spin system simulations evaluated the combined effect of strong microwave irradiation, spectral diffusion and spin-lattice relaxation on the theoretical evolution of the electron spin polarization. Based on the simulations, the spectral diffusion constant and the fraction of directly depolarized spins were calculated. The width of the hole burnt into the ESR spectrum was used to understand the boosting effect that microwave frequency modulation had on ^{129}Xe polarization.

¹Applying microwave frequency modulation will in the following also be referred to as using polychromatic irradiation frequencies.

²Using 40 mM TEMPO in DMSO/ H_2O , measured at 3.4 T.

³Using 40 mM TEMPOL in DMSO/ H_2O , measured at 3.4 T.

⁴Using 5 mM TEMPO in glycerol- H_2O , measured at 1.55 K.

⁵Using 50 mM TEMPOL in glycerol- d_8 - H_2O , measured at 6.7 T, 1.15 K.

4.3 Methods

4.3.1 The Xenon DNP Sample Matrix

To study different sample matrices, three protonated solvents with increasingly long carbon chains were studied, namely ethanol (EtOH, C_2H_6O), 2-methyl-1-propanol ($C_4H_{10}O$) and 2-methyl-1-pentanol ($C_6H_{14}O$) (Figure 4.1). Furthermore, the two deuterated equivalents

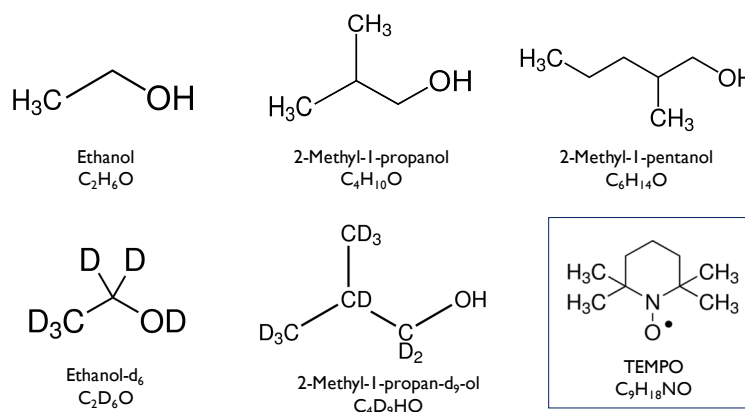


Figure 4.1: Paramagnetic centres induced in the sample matrix in form of TEMPO radicals and chemical structures of the 2/4/6-carbon alcohols used as solvents in their protonated and deuterated forms.

ethanol- d_6 (fully deuterated, hexadeuteroethanol) and 2-methyl-1-propan- d_9 -ol (partially⁶ deuterated) were also used for sample preparation. The solvents were doped with the radical TEMPO (2,2,6,6-tetramethyl-piperidine-1-oxyl), which is a popular inexpensive and stable nitroxyl radical for *in vivo* applications due to its low biological toxicity [178]. Cooled-down xenon (natural ^{129}Xe isotope abundance of 26.44 %, Sigma Aldrich, Buchs, Switzerland) was admixed to the doped solvent in its liquid state by means of a tubing⁷ system connected to a custom-made glass cold-finger (Figure 4.2) and a bath of melting ethanol ice. Concretely, this was achieved by implementing the steps described in the following and illustrated schematically in Figure 4.3. After having dissolved 50 mM TEMPO in 500 μl of solvent, the solution was added to the glass cold finger, which was connected to the tubing system and flushed with xenon gas to evacuate the air (Figure 4.3). The targeted ^{129}Xe concentration was calculated

⁶All protons replaced by deuterons except for the proton on the -OH group.

⁷The tubing described in Figure 4.2 was replaced by a fluid-path system of smaller total volume later on [179, 180]. The sample mixing did not change conceptually.

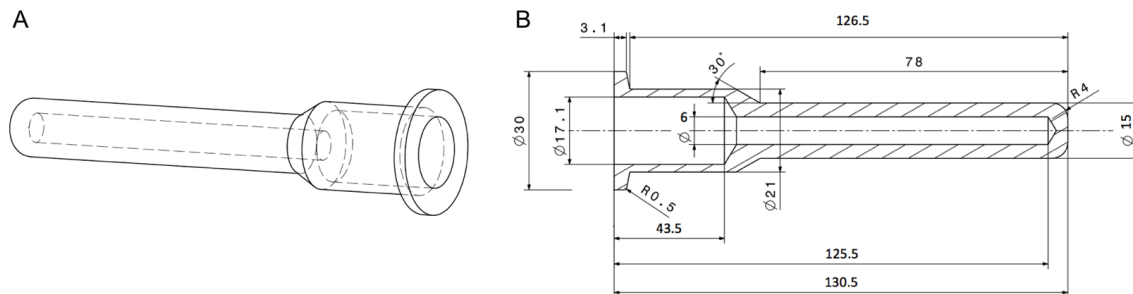


Figure 4.2: (A) Schematic drawing and (B) Drawing to scale of glass cold-finger of 10 ml volumetric capacity. Dimensions given in mm.

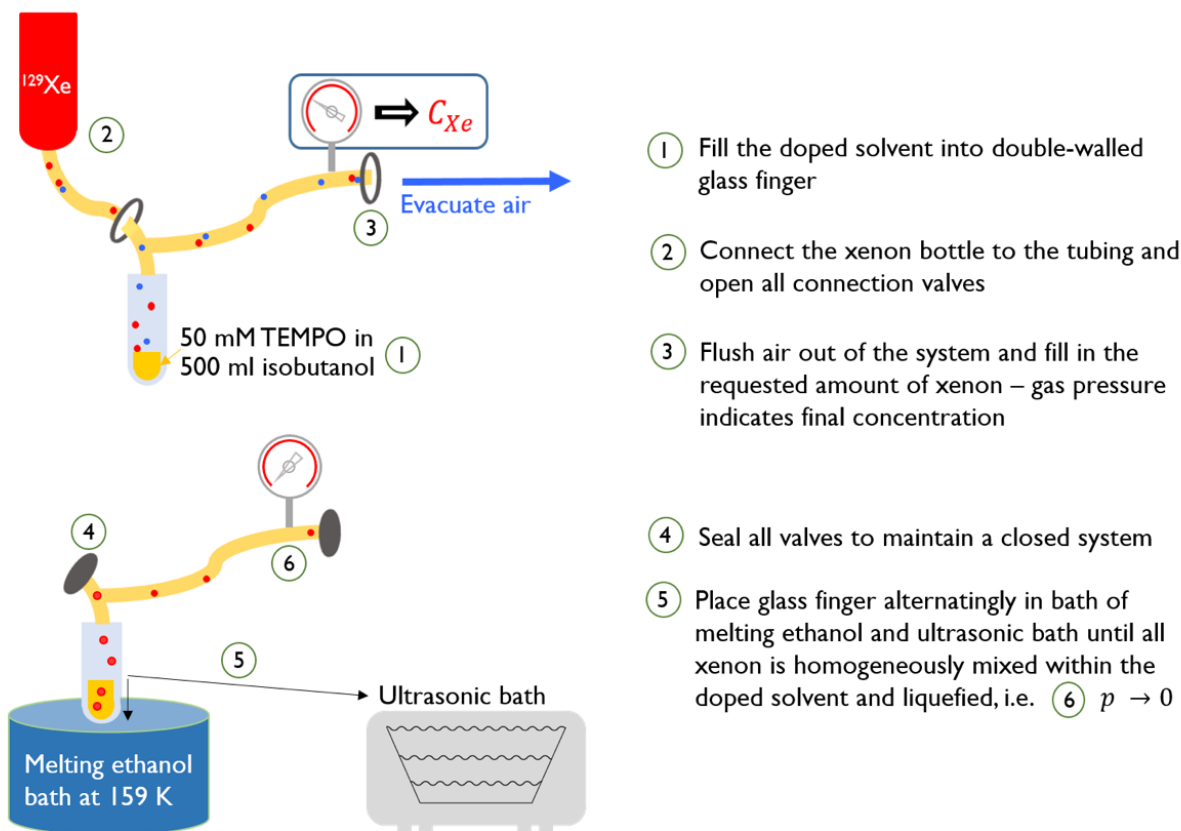


Figure 4.3: Schematics of the xenon sample preparation procedure (similar to a set-up described previously [181]). Solidification of the gas into an amorphous glassing matrix was achieved by attempted a bath melting ethanol ice.

as a function of the total system volume and the xenon gas pressure. The pressure in the closed system was controlled via a pressure gauge. The xenon concentrations were chosen to remain below the solubility threshold of 1.5 M, 5 M and 8.2 M for ethanol, 2-methyl-1-propanol and 2-methyl-1-pentanol, respectively [66]. The same solubility thresholds were



Figure 4.4: Sample preparation set-up combining ultra-sonic mixing and melting ethanol bath for mixing.

chosen for deuterated solvents as for their protonated counterparts. Liquefaction of the gas in an amorphous glassing matrix was achieved by emerging the cold finger in a bath of melting ethanol-ice (Figure 4.4). The bath was prepared by cooling ethanol down using liquid nitrogen (LN_2), all the while avoiding an excessive drop in temperature leading to solidification of the solvent. The target temperature of the melting ethanol bath being $\sim 159 \text{ K}$ (-114°C at p_0), it coincided well enough with the xenon melting point at 161 K (-112°C at p_0) to liquefy the xenon gas. This allowed for a short-lived state in which two liquids could be mixed using magnetic stirring or ultra-sonication (Skymen ultrasonic cleaner, AC220-240 V, 50 Hz, 35 W power). Once the xenon gas was fully embedded in the solvent, judging by the absence of solid xenon snow at the bottom of the vial (visual evaluation), LN_2 was used to flash freeze the sample.

4.3.2 LOD-ESR

To measure longitudinal electron-spin relaxation times T_{1S} and ESR spectra at DNP conditions, Longitudinal Detection (LOD)-ESR measurements were conducted at 5 T and 1.15 K. The design of the LOD-ESR set-up was initially inspired by Granwehr et al. (2007) [176] and modified by Capozzi et al. (2018) [179]. For samples without xenon the glass cold finger was not needed for mixing and 15 beads of $6 \mu\text{l}$ volume each were directly frozen in LN_2 and transferred to the smaller vial. A description of the vial design, sample handling and loading procedure can be found elsewhere [179], as can details on the methodology [182]. For samples containing xenon, the sample was prepared as initially described in the cold finger

and the maximally transferable amount of sample shreds were transferred into the vial.

Microwaves were switched OFF (0 W output power) and ON (55 mW output power, fulfilling ESR saturation condition locally) with lock-in demodulation frequencies of 0.5 Hz and 5 Hz for measuring T_{1S} and ESR spectra, respectively. T_{1S} was calculated from monitoring the signal induced in the coil by the electron spins. The coil hereby acted as a pure receive coil, with the out-of-equilibrium spins originating from the microwave energy instead of transmit pulsing, as usually in DNP. The full evolution of the induced signal was sampled in steps of 1 ms during 0.5 s. The signal curve was fitted to

$$S = A(e^{-t/T_{1S}} - e^{-t/\tau_C}), \quad (4.1)$$

with amplitude A and coil constant τ_C , allowed for the extraction of the characteristic electron spin-lattice relaxation time (Figure 4.5 right). The coil constant indicates the characteristic time constant of the system when driven with a square wave. Fitting errors of the iterative non-linear least squares method were reported. The ESR spectrum g_N was sampled over the fully operational microwave frequency range of [139.5; 140.5]GHz in steps of 5 MHz. ESR spectra were obtained by plotting the signal intensity, which is proportional to the number of spins resonating at a set frequency, as a function of the sampling frequency. Spectra were then normalized to the maximally measured signal amplitude of the corresponding modulated frequency sweep and spectral widths were calculated from the square root of the M_2 -values (according to Equation 4.8). To quantify the expected reduction in ESR linewidth due to

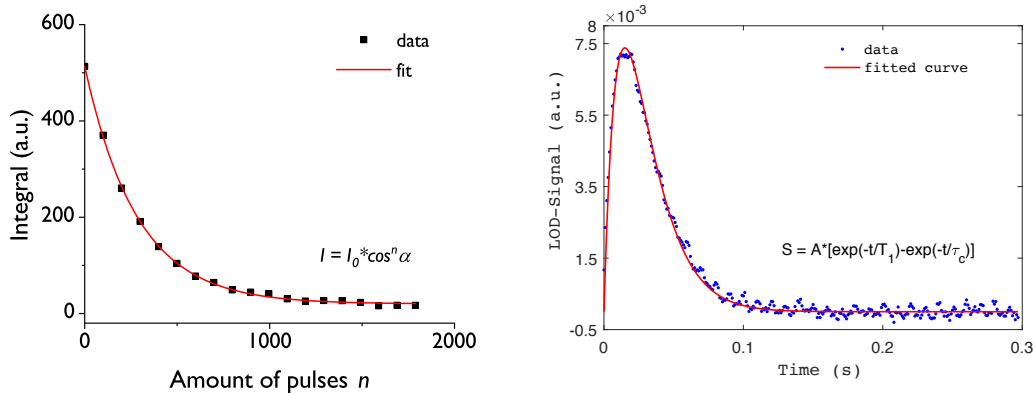


Figure 4.5: Methodology: Flip angle calibration conducted in $t \ll T_{1I}$ to neglect relaxation during fitting procedure (**left**). Flip angle was calibrated to be 4.4° for polarization build-up monitoring. Fitting the LOD signal to extract the electron spin-lattice relaxation time T_{1S} (**right**).

deuteration of the solvent, the contribution of the nuclear-electron dipolar interaction was calculated for deuterated and protonated ethanol according to [Equation 2.30](#)

$$\Delta_{h,SI} = \sqrt{\frac{11}{32}} 0.55^{-3} \frac{\mu_0}{4\pi} \gamma_S \gamma_I \hbar n_I. \quad (4.2)$$

with γ_I of 42.577 MHz/T and 6.53 MHz/T and a nuclear spin density n_I of $6.51 \cdot 10^{22}$ spins/cm³ (from [\[66\]](#)) and $7.36 \cdot 10^{22}$ spins/cm³ in protonated and deuterated EtOH, respectively.

4.3.3 Microwave Frequency Modulation

To be able to excite a larger portion of the ESR spectrum, the microwave source (ELVA-1, VCOM-06/140/0.5/50-DA) was modified to allow for frequency modulation. A priori, microwave frequency modulation can be implemented on any existing polarizer, requiring minor modifications to the hardware and software. The microwave source was altered so that frequency stabilization of the output frequency could be manually disabled, namely the Digital-to-Digital output was modified to allow for Digital-to-Analog conversion. This enabled the input of a time-dependent function, therefore generating a polychromatic frequency output ([Figure 4.6](#)). Communication between the different units (source, waveform generator, PC) was controlled in LabView (National Instruments, USA). For the following experiments, a sinusoidal wave was generated through an arbitrary waveform generator (Tektronix Inc, USA) as proposed previously [\[183\]](#), even though a different input function such as a step function or triangular function would be possible. The software was then adapted to allow for manual control of the frequency modulation amplitude $\Delta f_{\mu w}$ (defined as the hole modulation width, cf. [Figure 4.6](#)) and the rate of modulation ν_{FM} . A feedback loop was implemented to avoid microwave frequency drift. Build-up time and polarization levels were investigated as a function of modulation frequencies $\nu_{FM} = 10$ Hz, 100 Hz, 1 kHz, 5 kHz, 10 kHz and modulation amplitudes $\Delta f_{\mu w}$ between 11 MHz and 150 MHz.

4.3.4 Sensitivity Calibration

The Voltage Controlled Oscillator (VCO) unit could be operated for voltages U between 0 - 10 V, depending on the required frequency modulation amplitude. However, the dis-

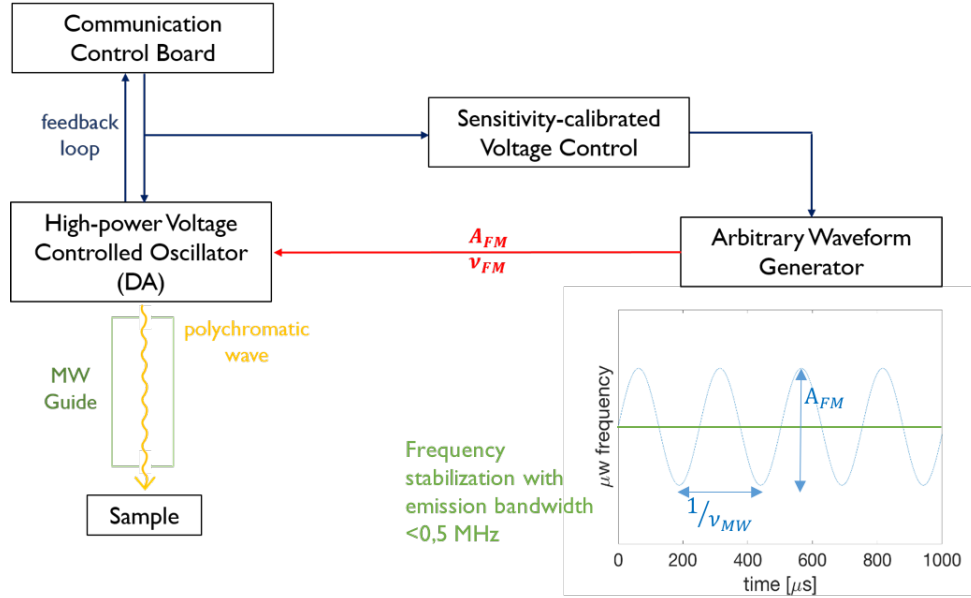


Figure 4.6: Hardware and software modifications required for implementation of microwave frequency modulation. Chain of commands: Red: voltage, blue: data flow, yellow: microwaves. DA: Digital-to-analog control.

crepancy of the zero-crossing positions in frequency sweeps acquired without FM and with a 150 MHz nominal modulation amplitude (as well as a discrepancy with the LOD-ESR maximum) revealed that the actual frequency modulation amplitude depended on the center frequency (Figure 4.7 A,B). To account for this discrepancy, the frequency modulation span was calibrated for 1 V control voltage, yielding the input sensitivity S_i (Figure 4.7 C). The settings for future measurements were corrected according to the sensitivity curve obtained by a 5th degree polynomial fit by calculating the actual modulation amplitude $\Delta f_{\mu w}$ as

$$\Delta f_{\mu w} = S_i \cdot U. \quad (4.3)$$

For a given modulation amplitude in volt the corresponding modulation amplitude in MHz increased for increasing center frequencies. Corrected electron spin resonance frequencies resulted in a coherent overlap (Figure 4.7 D).

4.3.5 DNP

To monitor the nuclear polarization with small pulses α of 4.4° , a flip angle calibration was conducted by fitting the hyperpolarized signal decay upon rapid pulsing (100 pulses n of 20 μs pulse width, TR of 10 ms. Since the duration t of the train of hard pulses fulfilled

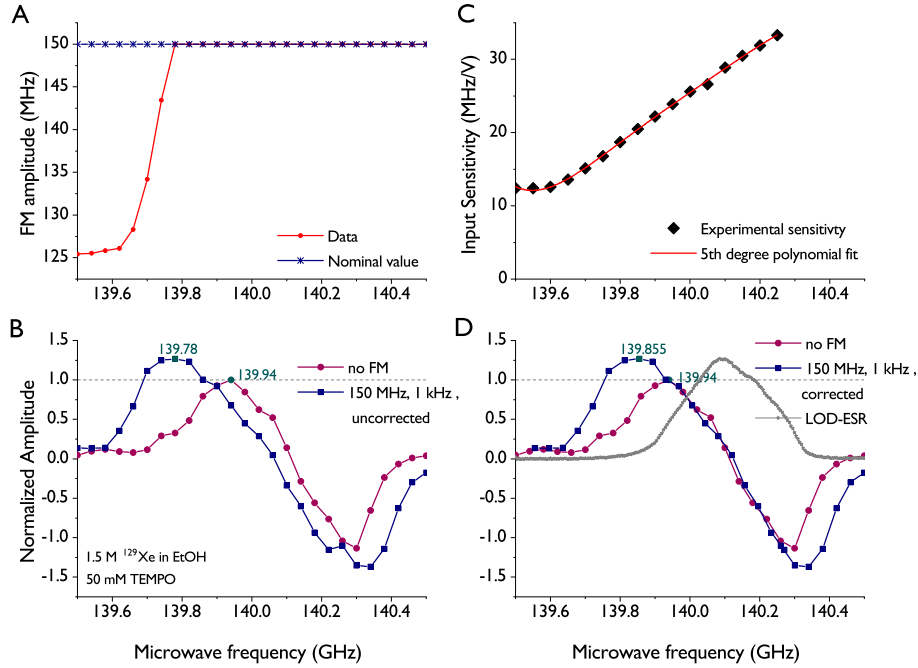


Figure 4.7: Sensitivity calibration of microwave frequency modulation. The nominal microwave frequency was calibrated to account for sensitivity-dependent modulation amplitudes. **A)** Resulting frequency modulation amplitude for 150 MHz nominal value as a function of the center frequency with resulting discrepancy of electron spin resonance frequencies (**B**). **C)** Calibrated correction function to account for discrepancy between nominal and actual modulation amplitude due to a center frequency dependent sensitivity of the input voltage. Several acquired data points were fitted with a 5th degree polynomial function to allow for a continuous correction of the input voltage. **(D)** Resulting corrected electron spin resonance frequencies.

$t \ll T_{1I}$, the nuclear relaxation was neglected and the integrated signal I was fitted to the function $f(x) = I_0 \cdot \cos^n(\alpha)$ (Figure 4.5 left).

Microwave frequency sweeps were conducted to determine the positive and negative DNP maxima at DNP conditions (5 T, 1.15 K), as well as their shift in position depending on the solvent and under the influence of frequency modulation. Samples were hyperpolarized during 10 minutes of irradiation at a given frequency and monitored using 4.4° flip angles. After each read-out, the polarization was destroyed with a train of hard pulses. Sweeps were conducted in 26 steps of 40 MHz between 139.5 GHz and 140.5 GHz, using 55 mW output power. Sweeps were acquired by applying (i) frequency stabilization for monochromatic irradiation and (ii) frequency modulation at a rate of 1 kHz and with an amplitude of 88 MHz.

To determine the effect of modulating the irradiation frequency, nuclear ^{129}Xe spin polarization was monitored using 4.4° hard pulses every 5 minutes. The optimal irradiation frequency was extracted from the frequency sweeps such that each sample was hyperpolarized at ideal conditions (within the parameters tested). The characteristic build-up time τ of the spin system was extracted by fitting the signal build-up data to a mono-exponential function. Samples were hyperpolarized for minimum of three build-up time constants to reach $\geq 95\%$ of the polarization plateau. Whenever possible, thermal nuclear polarization at equilibrium was measured by means of a single 30° hard pulse, applied after 5 hours at 1.15 K. This yielded the enhancement as the ratio of hyperpolarized and thermally polarized integrated NMR signal intensity I , taking the flip angle differences into account

$$\epsilon = \frac{\sin(30^\circ) I_{hp}}{\sin(4.4^\circ) I_{th}}. \quad (4.4)$$

Solid state polarization levels were calculated as the product of the enhancement and the theoretical thermal polarization calculated in [Equation 2.4](#) as

$$P_{hp} = \epsilon \cdot \frac{\hbar w_{0I}}{2k_B T}. \quad (4.5)$$

Control measurements were conducted over an extended period of time (47 h total) to check if the polarization build-up curves were reproducible if a sample was left undisturbed inside the polarizer. A xenon sample embedded in 2-methyl-1-propanol was hyperpolarized during 8200 s using the full 55 mW microwave output power and frequency modulation with a 40 MHz amplitude at a rate of 10 kHz. NMR signal levels were normalized to the initial polarization levels obtained immediately after loading ($t = 0$). The experiment was repeated after a waiting time t of 22 h and 47 h.

4.3.6 Spin System Simulations

Simulations were performed in MATLAB (The MathWorks Inc., USA) to quantify spin-system dependent parameters related to spectral diffusion, hole burning and electron spin polarization as a function of the microwave irradiation. The previously measured ESR spectrum, the T_{1S} and the frequency of the positive and negative DNP maximum were used as observables. The unpaired electrons in TEMPO radicals were characterized by $S = 1/2$

and $\gamma_S = -28\text{GHz}/T$. Further, the radical concentration of 50 mM fulfilled the condition $N_S \ll N_I$, that is a much smaller amount of electron spins $N_S \sim 3 \cdot 10^{19}$ spins/cm³ compared to nuclear spins $N_I \sim 1 \cdot 10^{21}$ spins/cm³. The homogeneous linewidth was much smaller than the inhomogeneous linewidth of the broad-line radical TEMPO. Therefore, the approximations made in chapters 2.5, 2.6, 2.8 are valid and the corresponding derivations were applied and extended. The following gives a brief reminder of the relevant equations (applied and adapted to the experimental conditions). The ESR spectrum g_N was normalized such that

$$\int_{w_{min}}^{w_{max}} g_N(w) dw = 1 \quad (4.6)$$

and used to calculate its center of gravity w_{0S}

$$w_{0S} = \int_{w_{min}}^{w_{max}} w g_N(w) dw \quad (4.7)$$

as well as its second inhomogeneous moment

$$M_2 = \int_{w_{min}}^{w_{max}} g_N(w) (w - w_{0S})^2 dw. \quad (4.8)$$

The ESR spectra were acquired between w_{min} of 139.5 GHz and w_{max} of 140.5 GHz. The spin polarization P_{0S} , initially close to unity ($P_{0S} = -0.9942$) at 1.15 K and 5 T, was assumed to be fully saturated locally (at $\omega_{\mu w}$) under the influence of a strong microwave field at the respective frequency ($P_{0S}(\omega_{\mu w}) \rightarrow 0$). This depolarization spreads across the ESR spectrum via spectral spin diffusion, burning a hole into the ESR spectrum. The spectral diffusion constant \mathcal{D} was calculated at the frequency of irradiation $w_{\mu w}$ as

$$\mathcal{D}(w_{\mu w}) = \pi (M_2)^2 (1 - P_{0S}^2) g_N(w_{\mu w}). \quad (4.9)$$

The resulting hole width δ burnt into the ESR spectrum as a result of microwave irradiation was calculated from

$$\delta = \sqrt{\mathcal{D}(w_{\mu w}) T_{1S}} \quad (4.10)$$

and the characteristic time $\tau_{\mathcal{D}}$ to spread the electron spin polarization across the full width

of the ESR spectrum Δ_{ESR} resulted from

$$\tau_{\mathcal{D}} = \frac{\Delta_{ESR}}{4 \mathcal{D}(w_{\mu w})}. \quad (4.11)$$

Δ_{ESR} was defined to be the span of frequencies where the signal exceeded 10 % of the maximum resonance signal. The number of spin packets \tilde{n}_S was calculated from the ratio of the total ESR width Δ_{ESR} and the average homogeneous linewidth Δ_{av} , which was derived previously [184]

$$\Delta_{av} = \frac{4}{5} \frac{\mu_0}{4\pi} \hbar \gamma_S^2 N_S \quad (4.12)$$

with the magnetic permeability constant μ_0 and the average distance between two adjacent electron spins r_{SS} presumed constant in a matrix where $N_S \ll N_I$, such that $r_{SS}^3 \propto 1/N_S$.

To simulate the combined effect of the external microwave field, the electron spin-lattice relaxation and the spectral spin diffusion on the electron spin system, the normalized electron spin polarization $P_S(w_S, t_0)$ was plotted against the resonance frequency w_S as

$$P_S(w_S, t_0)/P_{0S} = 1 - \exp\left(\frac{-|w_S - w_{\mu w}|}{\delta}\right) \quad (4.13)$$

at a time t_0 sufficiently long for saturation to have reached its steady state. The influence of the hole width δ was simulated for a δ of 1 MHz, 10 MHz, 100 MHz, 1 GHz and 10 GHz. The effect of hole burning on the normalized (measured) ESR spectrum was simulated as [64]

$$g_{N,\delta} = P_S(w_S, t_0) \cdot g_N(w_S) \quad (4.14)$$

and equally evaluated for increasing widths δ . The fraction of electron spins that were depolarized by $\mathbf{B}_{\mu w}$ was calculated as the Area Under Curve (AUC) of $g_{N,\delta}$.

The effect of microwave frequency modulation on the ESR spectrum was illustrated through simulations. In the case of modulating the frequency during a time t , the field $\mathbf{B}_{\mu w}$ derived in equation Equation 2.11 can be described by a polychromatic frequency evolution [169]

$$\mathbf{B}_{\mu w} = 2 B_{1,m} \cos\left(\int_0^t w_{\mu w}(\tau) d\tau\right). \quad (4.15)$$

The sinusoidal frequency modulation around the centre frequency w_c , with modulation amp-

litude $\Delta f_{\mu w}$ at a rate ν_{FM} was given by

$$w_{\mu w}(t) = w_c + \frac{\Delta f_{\mu w}}{2} T(t), \quad (4.16)$$

such that

$$T(t) = \sin(\nu_{FM} t + \phi_0), \quad (4.17)$$

with the initial phase ϕ_0 set to 0 for the sake of simplicity. As is custom, perfect saturation of the spin packets by the microwave field was presumed at all times ($P_S(w_{\mu w}) \rightarrow 0$). The saturation of a given spin packet due to spectral diffusion was assumed to be uncorrelated with the initial state of polarization. The continuously modulated microwave frequency was simulated as a discrete sweep over the spin packets covered by the modulation amplitude $\Delta f_{\mu w}$. The cumulated effect on the electron spin polarization was therefore calculated and simulated as a superposition of separately depolarized spin packets (Equation 2.42).

4.4 Results

Electron spin-lattice relaxation times T_{1S} were measured to be able to make an adequate choice for the rate of modulation ν_{FM} for subsequent frequency modulation sweeps and DNP. The T_{1S} of TEMPO radicals was 21.0 ± 0.2 ms, 17.2 ± 0.2 ms, 15.9 ± 1.4 ms, 9.8 ± 0.3 ms, 5.0 ± 0.4 ms in a xenon-embedded matrix of EtOH-d₆, EtOH, 2-methyl-1-propan-d₉-ol, 2-methyl-1-propanol, and 2-methyl-1-pentanol, respectively (Figure 4.8, Table 4.1). In doped solvents containing no xenon, the T_{1S} was 38 ± 0.2 ms, 44.5 ± 0.3 ms, 30.1 ± 1.8 ms, 26.4 ± 0.2 ms and 20.3 ± 0.2 ms for EtOH-d₆, EtOH, 2-methyl-1-propan-d₉-ol, 2-methyl-1-propanol, and 2-methyl-1-pentanol matrices, respectively. The T_{1S} was therefore consistently longer than in samples with xenon embedded. Thus, an increase in relaxation rates upon addition of xenon spins was observed for deuterated as well as protonated samples. Irrespective of the presence of xenon, radical T_{1S} for protonated samples was longest in a matrix of ethanol and shortest in a matrix of 2-methyl-1-pentanol (appendix Figure A.1). Deuteration of the sample matrix did not lead to considerable changes in T_{1S} (appendix Figure A.2).

To determine how the addition of xenon spins to the DNP matrix affected the electron spin system, the ESR linewidths were characterized with and without embedded xenon. Adding xenon to the matrix consistently decreased the ESR linewidths (Figure 4.9) but they

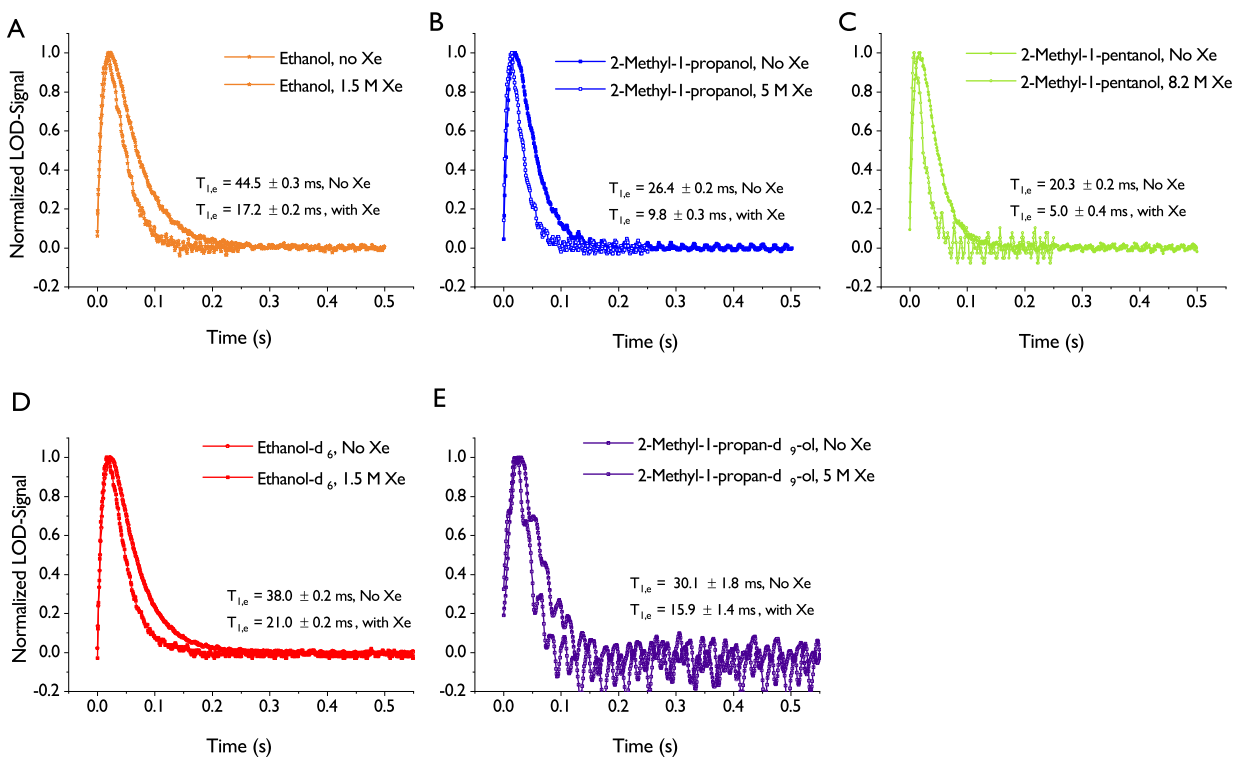


Figure 4.8: T_{1S} of TEMPO in presence and absence of xenon nuclear spins for the solvents (A) ethanol, (B) 2-methyl-1-propanol, (C) 2-methyl-1-pentanol, (D) ethanol-d₆ and (E) 2-methyl-1-propan-d₉-ol.

Table 4.1: Electron spin-lattice relaxation times T_{1S} of TEMPO for different xenon concentrations below or at the solubility threshold. Data was acquired under DNP conditions, namely at 5 T and 1.15 K. Corresponding spectra are plotted in [Figure 4.8](#).

	Xenon concentration (M)	T_{1S} (ms)
<i>2 – Methyl – 1 – propanol</i>	0	26.4 ± 0.2
	3.8	14.1 ± 0.3
	5	9.8 ± 0.3
<i>2 – Methyl – 1 – propan – d₉ – ol</i>	0	31.1 ± 1.8
	5	15.9 ± 1.4
<i>2 – Methyl – 1 – pentanol</i>	0	20.3 ± 0.2
	8.2	5.0 ± 0.4
<i>EtOH</i>	0	44.5 ± 0.3
	1.5	17.2 ± 0.2
<i>EtOH – d₆</i>	0	38.0 ± 0.2
	1.5	21.0 ± 0.2

remained in the broad linewidth regime, spanning between 355 MHz and 450 MHz. The ESR line centre of gravity was shifted by up to 30 MHz when changing the matrix solvent. Deuteration of the solvent EtOH further decreased the spectral width by 30 MHz ([appendix Figure A.3](#)). The width of the dipolar electron-nuclear spin broadening $\Delta_{h,SI}$ was calculated to be 2.88 MHz and 0.5 MHz for protonated and deuterated EtOH, respectively. Increasing the xenon concentration from 3.8 M to 5 M in a doped matrix of 2-methyl-1-propanol had no effect on the ESR full spectral width Δ_{ESR} or spectral width, which were consistently 425 MHz and 105 MHz, respectively ([Figure 4.10](#)). Meanwhile, the T_{1S} decreased from 14.1 ± 0.3 ms to 9.8 ± 0.2 ms ([Table 4.1](#)).

To research if modulation amplitudes were subjected to an upper boundary beyond which they would no longer increase nuclear spin polarization, modulation amplitude calibrations with $\Delta f_{\mu w}$ between 11 MHz to 150 MHz were performed ([Figures 4.11](#) and [A.5](#), [A.6](#) of [appendix A](#)). The modulation amplitude $\Delta f_{\mu w}$ of 150 MHz lead to a larger separation in positive and negative frequency sweep DNP maxima with respect to $\Delta f_{\mu w}$ of 88 MHz. It did, however, not entail an increase in polarization ([Figure 4.11](#)). Meanwhile, polarization levels were affected stronger when hyperpolarizing at the positive DNP compared to the negative DNP for comparable modulation amplitudes $\Delta f_{\mu w}$ ([appendix Figures A.5](#), [A.6](#)). Applying

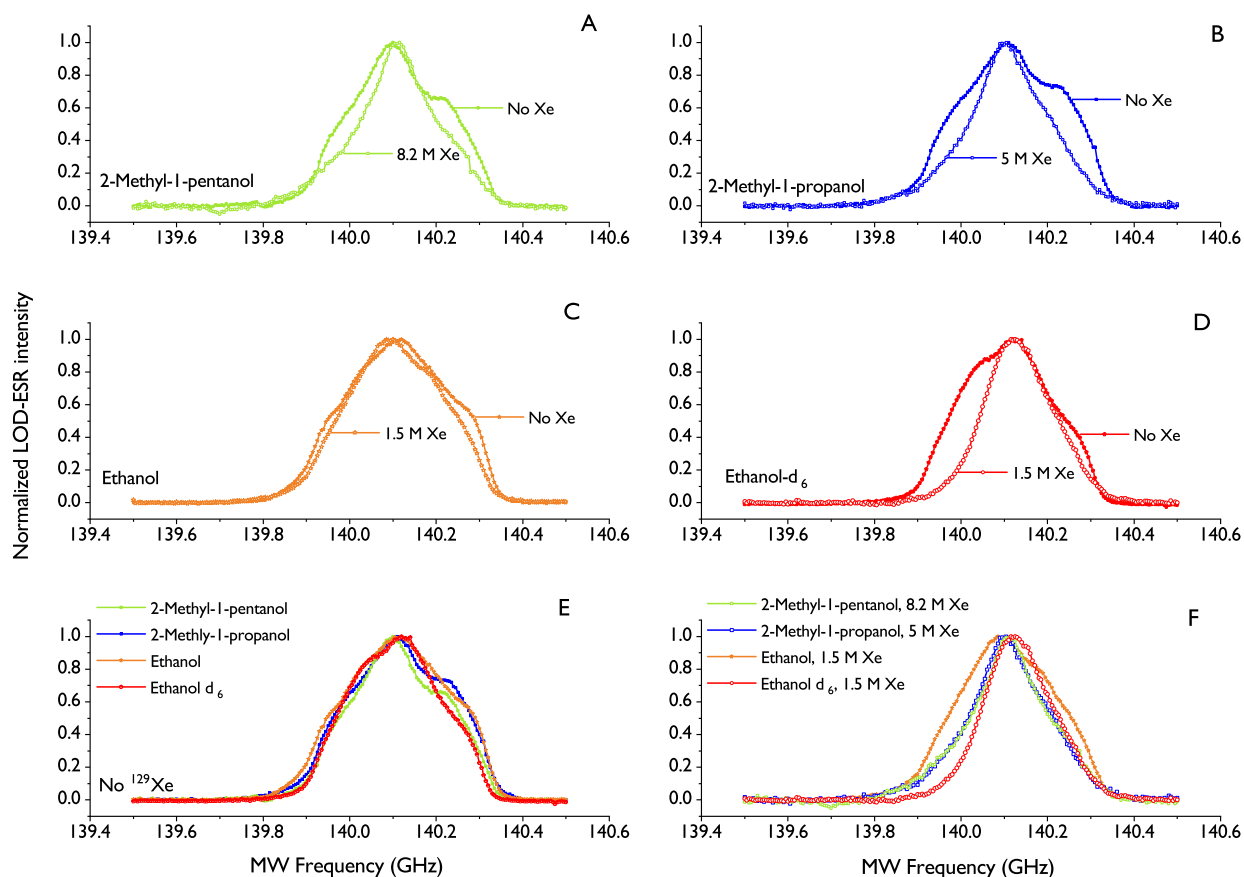


Figure 4.9: TEMPO ESR spectra with and without the addition of solidified xenon atoms at DNP conditions (5 T, 1.15 K), normalized to maximum integrated LOD signal. A constant electron spin density of $3.011 \cdot 10^{19}$ spins/cm³ was maintained throughout the samples. Xenon concentrations were maximized by choosing them at the solubility threshold.

microwave frequency modulation did not influence the DNP sweep zero-crossing (after applying sensitivity correction). Calibration of the rate of modulation showed that polarization increased with the modulation rate. While the increase in enhancement after 5.5 ks was considerable (44 %) when replacing the mono-chromatic microwave frequency with a 10 Hz modulation, the polarization increased only by 8 % when changing the modulation rate from 1 kHz to 10 kHz (appendix [Figure A.7](#)).

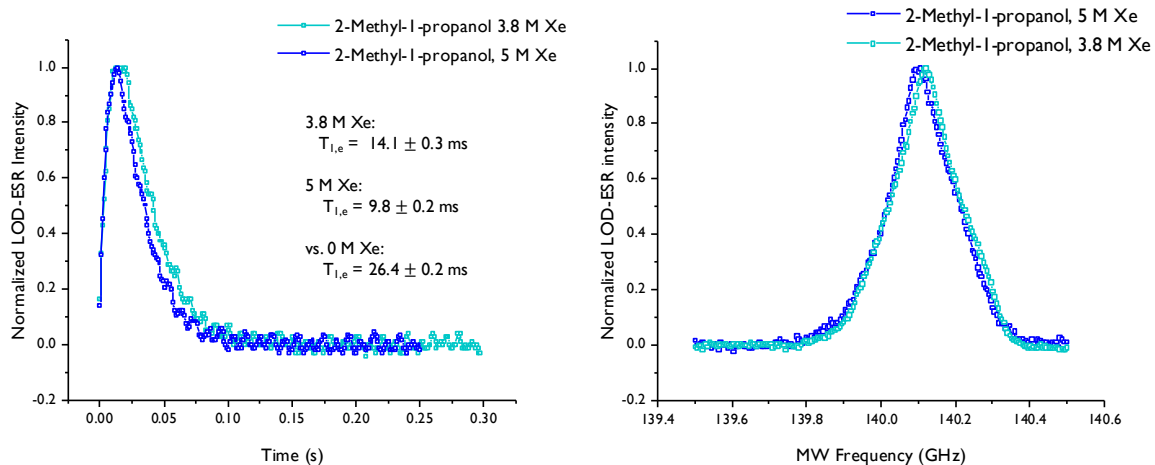


Figure 4.10: T_{1S} (**left**) and ESR-spectrum (**right**) dependence on nuclear spin concentration. While the electron spin-lattice relaxation rate increased with the xenon concentration, no effect on the ESR-lineshape was measured with Δ_{ESR} of 425 MHz unchanged.

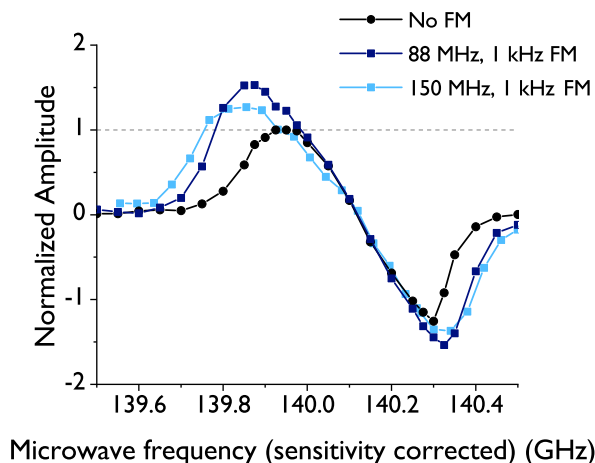


Figure 4.11: Exemplary frequency sweeps acquired from a 1.5 M xenon in TEMPO-doped ethanol matrix for modulation amplitudes of 0 Hz, 88 MHz, 150 MHz. The rate of modulation was kept constant at 1 kHz for a sinusoidal wave input. Sweeps are normalized to the non-modulated DNP maximum.

Control measurements conducted over an extended period of time demonstrated that the hyperpolarization process was not reproducible, neither in polarization level nor build-up time (Figure 4.12). The NMR signal, normalized to the initial polarization levels which were acquired upon sample loading at $t = 0$, dropped to 57.7 % and 52.9 % of the initial polarization level after a waiting time t of 22 h and 47 h. The build-up time τ decreased from 2.8 ± 0.2 ks to 1.9 ± 0.1 ks and 2.5 ± 0.1 ks after 22 h and 47 h, respectively.

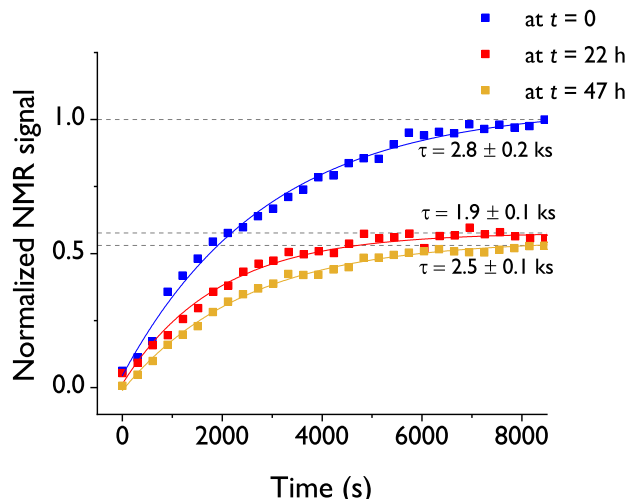


Figure 4.12: Testing reproducibility of the hyperpolarization process over 47 hours using the same sample. The same parameters were chosen as used for hyperpolarization: 40 MHz modulation amplitude with a rate of the frequency modulation of $(10 \text{ kHz})^{-1}$, 55 mW microwave output power with a 4.4° acquisition pulse every 5 minutes. The NMR signal was normalized to the initial polarization levels (acquired upon sample loading, $t = 0$) and dropped to 57.7 % and 52.9 % after $t = 22 \text{ h}$ and $t = 47 \text{ h}$. The build-up time τ decreased with increasing waiting time, similar to observations linked to suspected clustering (cf. explanation Figure A.8 and reported results from [185]). A matrix of 5 M xenon dissolved in 2-methyl-1-propanol and mixed by magnetic stirring was used.

Hyperpolarizing the samples at their respective optimal irradiation frequency (cf. Figures 4.13, 4.14 for detailed positions) yielded polarization levels of up to 6.9 % (non-modulated) and 14.5 % (modulated) for xenon spins embedded in a 2-methyl-1-propanol matrix. The highest gain in polarization levels due to utilization of microwave frequency modulation was recorded for 2-methyl-1-pentanol, where DNP enhancement increased by 220 %, boosting the polarization from $3.5 \pm 0.05 \text{ %}$ to $11.2 \pm 0.02 \text{ %}$ (Table 4.2). Irrespective of the sample composition, the use of frequency modulation lead to enhanced DNP. The maximum positive DNP was found at 140.085 GHz, 140.12 GHz and 140.115 GHz for EtOH, 2-methyl-1-propanol and 2-methyl-1-pentanol. Nuclear polarization was also enhanced by frequency modulation for xenon spins embedded in deuterated doped solvents, similarly to their protonated counterparts (Figure 4.14). Most samples displayed accelerated DNP build-ups when using frequency modulation (with the exception of the ethanol sample). Overall, an inverse linear relationship between decreasing electron spin-lattice relaxation times and relative polarization gain due to frequency modulation ($R_p = \epsilon_{FM}/\epsilon_{noFM}$) was found, such that $1/R_p \propto T_{1S}$ with coefficient of determination of $R^2 = 0.87$ (Figure 4.15).

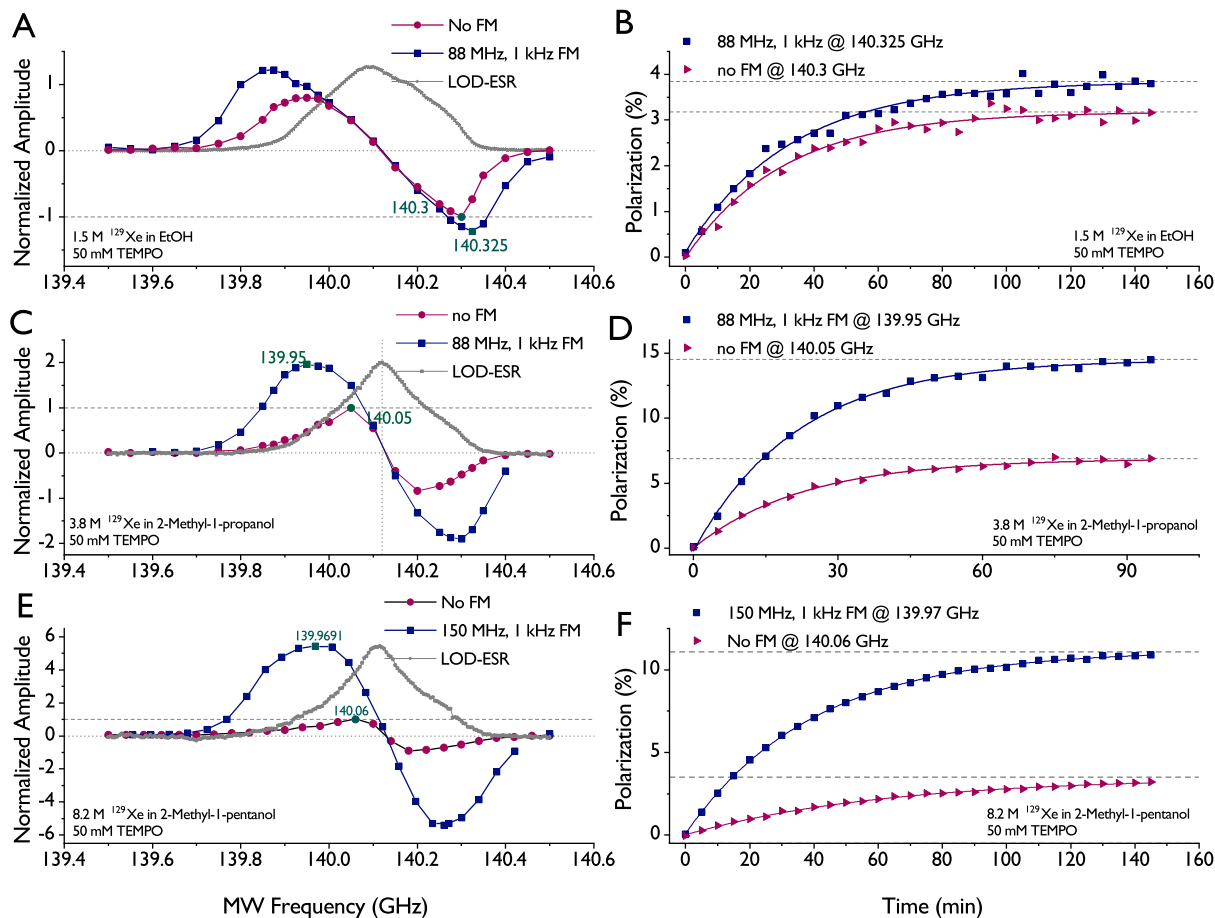


Figure 4.13: Frequency sweeps and DNP of nuclear xenon spins embedded in fully protonated solvent matrices of (A, B) ethanol, (C, D) 2-methyl-1-propanol and (E, F) 2-methyl-1-pentanol. The sample preparation method specifies the concentration of xenon in the final matrix and the melting ice used for cooling down the sample upon mixing. Microwave frequency sweeps acquired without (red) frequency modulation (FM) and modulating the irradiation frequency at a rate of 1 kHz (blue). Corresponding LOD-ESR spectra acquired under identical conditions are superimposed (grey). DNP build-up curves were acquired for microwave irradiation at optimal frequency with respect to relative enhancement (cf. Table 4.2). DNP curves were monitored during minimum three build-up time constants, which were extracted from mono-exponential fits (solid lines).

Table 4.2: Impact of frequency modulation on the position of sweep maxima in the frequency domain, on DNP after microwave irradiation at respective optimal frequency and on build-up time. Samples contained 50 mM TEMPO each. They were prepared directly in the vial and liquefied xenon gas was admixed in an external environment of alcohol ice (ethanol ice or 2-methyl-1-propanol-ice). Sweeps and hyperpolarization were conducted in identical conditions. DNP of 2-methyl-1-propan- d_9 -ol was normalized (values given in a.u.) since no thermal was acquired. Build-up times were extracted from mono-exponential fitting and fitting errors are reported. The gain in polarization due to the use of microwave frequency modulation is calculated compared to non-modulated hyperpolarization at optimal microwave frequency. Corresponding frequency sweeps and build-up curves are plotted in Figures 4.13 and 4.14.

Solvent	Sample preparation*	Microwave frequency modulation	Positive DNP Maximum (GHz)	Negative DNP Maximum (GHz)	Polarization (%)	Gain due to MW FM (%)	Build-up time (min)
2 – Methyl – 1 – propanol	3.8 M Xe, Methypropanol ice	no	140.05	140.20	6.9 ± 0.08	110	22.8 ± 1.1
		150 MHz, 1 kHz	139.95	140.30	14.5 ± 0.1		21.7 ± 0.7
2 – Methyl – 1 – propan – d_9 – ol	5 M Xe, EtOH ice	no	139.98	140.26	$0.55 \pm 0.01^{**}$	83	12.2 ± 0.9
		150 MHz, 1 kHz	139.85	140.34	$1.0 \pm 0.01^{**}$		9.4 ± 1.0
2 – Methyl – 1 – pentanol	8.2 M Xe, EtOH ice	no	140.06	140.18	3.5 ± 0.05	220	62.5 ± 2.2
		150 MHz, 1 kHz	139.97	140.26	11.2 ± 0.02		39.7 ± 0.4
EtOH	1.5 M Xe, EtOH ice	no	139.94	140.30	-	-	-
		150 MHz, 1 kHz	139.86	140.34	-		-
EtOH	1.5 M Xe, EtOH ice	no	139.95	140.30	3.2 ± 0.04	19	30.7 ± 2.1
		88 MHz, 1 kHz	139.88	140.33	3.8 ± 0.05		32.5 ± 1.7
EtOH – d_6	1.5 M Xe, EtOH ice	no	139.98	140.30	3.7 ± 0.03	5	15.2 ± 0.7
		150 MHz, 1 kHz	139.89	140.34	3.9 ± 0.03		10.5 ± 0.6

* incl. 50 mM TEMPO

** given in (a.u.)

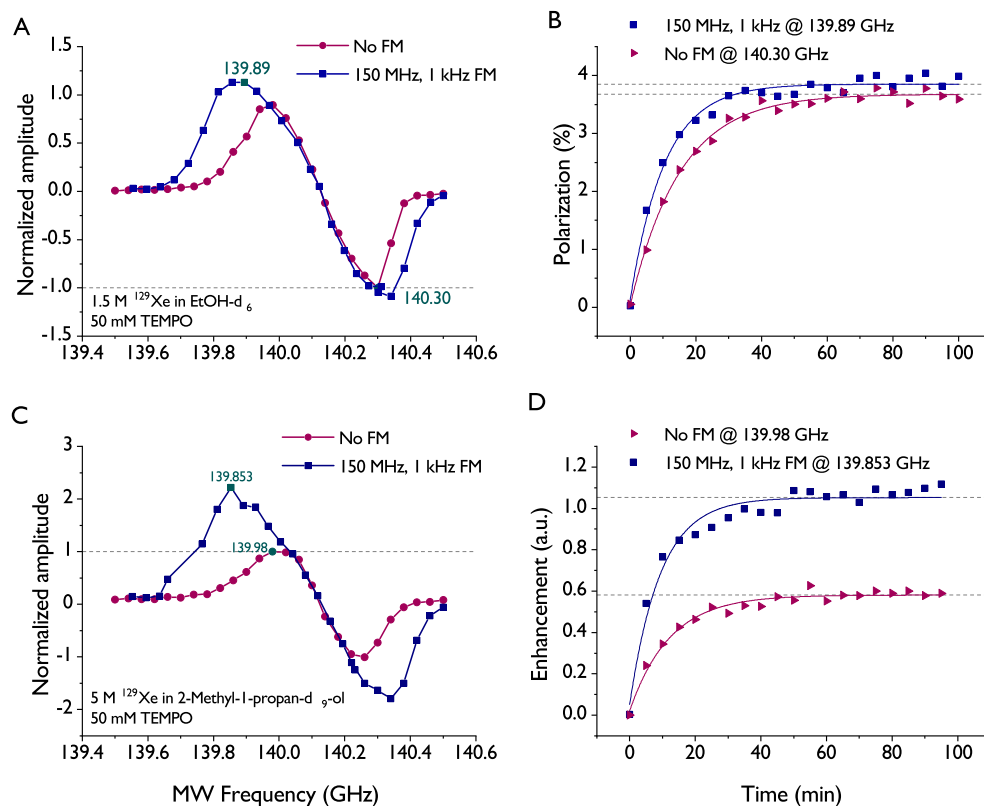


Figure 4.14: Frequency sweeps and DNP of nuclear xenon spins embedded in deuterated solvent matrices of (A, B) ethanol- d_6 and (C, D) 2-methyl-1-propan- d_9 -ol. Microwave frequency sweeps acquired without (red) frequency modulation (FM) and a 150 MHz modulation at a rate of 1 kHz (blue). DNP build-up curves were acquired for microwave irradiation at optimal frequency with respect to relative enhancement (cf. Table 4.2). DNP curves were monitored during minimum three build-up time constants, which were extracted from mono-exponential fits (solid lines).

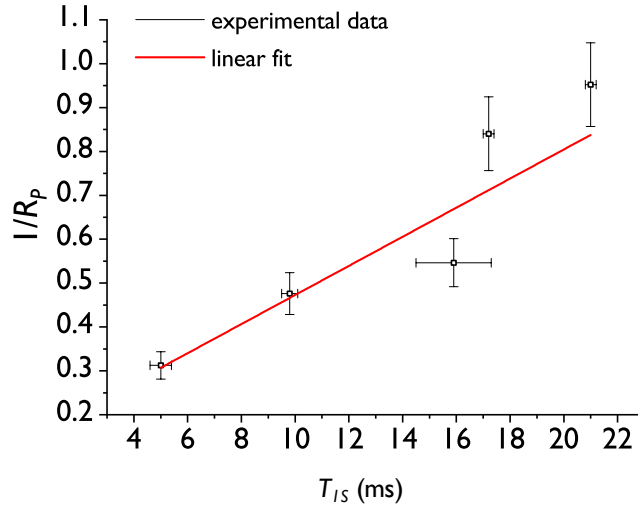


Figure 4.15: Inverse relationship between the ratio of polarization with and without frequency modulation ($R_p = \epsilon_{FM}/\epsilon_{noFM}$) and electron spin-lattice relaxation time T_{1S} . The fitting error on the T_{1S} and experimental measurement error on the NMR signal are given.

Simulations illustrated the cumulative impact of the microwave field ($\mathbf{B}_{\mu w}$), the electron spin-lattice relaxation (at the rate $1/T_{1S}$) and spin diffusion (with the characteristic constant \mathcal{D}) on the electron spin polarization (Figure 4.16). The fraction of electron spins depolarized by $\mathbf{B}_{\mu w}$ were 1.4 %, 6.3 %, 46.8 %, 90.9 % and 99.0 % for theoretical hole widths δ of 1 MHz, 10 MHz, 100 MHz, 1 GHz and 10 GHz, respectively. Simulations performed by using the acquired ESR spectra further revealed that actual hole widths were in the range of a few GHz (Table 4.3).

The average homogeneous linewidth due to electron dipolar coupling of nearest neighbours Δ_{av} was calculated to be $1.4 \cdot 10^6$ Hz for an electron spin density of $3.011 \cdot 10^{19}$ spins/cm³. This parameter was kept constant throughout the experiments and is therefore valid for all six matrix compositions tested. As already observed qualitatively in panel (F) of Figure 4.9, the full ESR width was largest when TEMPO was dissolved in EtOH (with 450 MHz) and narrowest in EtOH-d₆, where it was ~ 100 MHz narrower. Identical widths of 425 MHz were found for 2-methyl-1-propanol and 2-methyl-1-pentanol. Hence, the corresponding total amount of spin packets covered by the ESR lines ranged from 253 to 321 (Table 4.3). Figure 4.17 illustrates the hole burnt into the ESR spectrum of TEMPO embedded in 2-methyl-1-propanol for different theoretical hole widths δ under polychromatic microwave frequency irradiation.

To gain more information on the TEMPO-EtOH matrix used to investigate the impact of increasing frequency modulation amplitudes $\Delta f_{\mu w}$ (Figure 4.11), the ESR spectrum of said sample was used to perform spectral diffusion simulations (Figure 4.18). Irradiating the sample at the negative DNP ($w_{\mu w} = 140.3$ GHz) resulted in a hole width δ of 1.47 GHz with spectral diffusion constant of 126 MHz^3 . For monochromatic microwave irradiation at the positive DNP ($w_{\mu w} = 139.9$ GHz), the burnt hole was narrower by 320 MHz and the spectral diffusion was slower with $\mathcal{D}(w_{\mu w}) = 77 \text{ MHz}^3$.

Simulations further provided sample-dependent spectral diffusion parameters (Table 4.3). The spectral diffusion constant \mathcal{D} was fastest in the deuterated EtOH matrix with 32 MHz^3 and similar for 2-methyl-1-pentanol and 2-methyl-1-propanol with 326 MHz^3 and 330 MHz^3 . The characteristic time $\tau_{\mathcal{D}}$ to spread the electron spin saturation across the ESR spectral width was between 0.1 ms and 1 ms. The width of the holes burnt into the ESR spectrum were calculated to be in the GHz range.

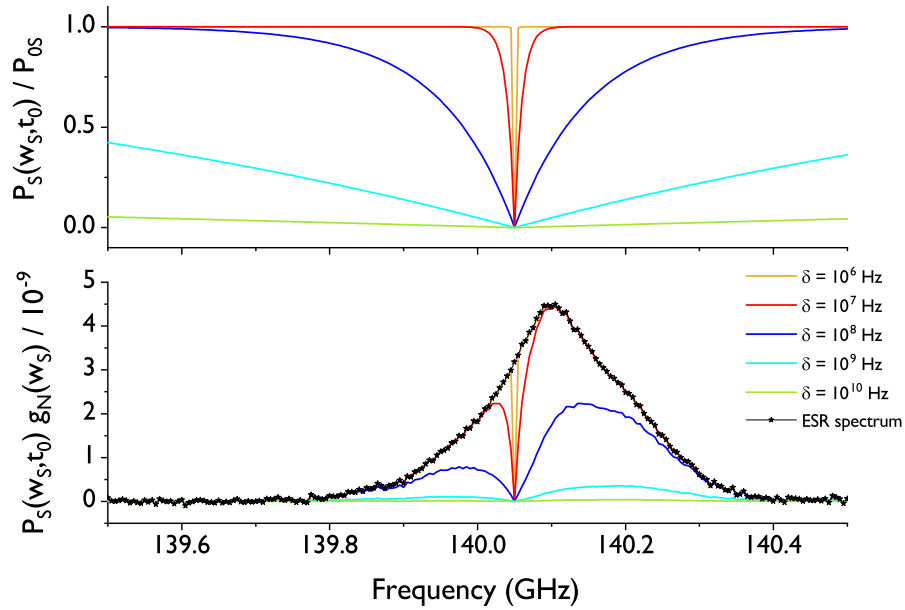


Figure 4.16: Hole burning under mono-chromatic microwave irradiation. The frequency-dependent decrease in electron spin polarization is illustrated for different hole widths δ ranging from 1 MHz to 10 GHz (**top**). The width of the hole burnt by microwave irradiation is matrix-dependent and increases with T_{1S} and \mathcal{D} , as given by Equation 4.10. Exemplary inhomogeneous ESR lineshape acquired from a 2-methyl-1-propanol matrix doped with 50 mM TEMPO and containing 5 M xenon gas. The resulting hole burnt into its spectrum for different magnitudes of δ (**bottom**). Legend entries apply to both graphs.

Table 4.3: Parameters extracted from the experimentally acquired ESR spectra (with embedded xenon atoms) and simulated diffusion and hole burning parameters. The extracted spin system parameters from left to right are the spectral width (square root of the second moment of the inhomogeneous ESR lineshape M_2), the ESR spectral center of gravity w_{0S} , the total ESR spectral width Δ_{ESR} (spanned by frequencies whose signal exceeded 10 % of the maximum resonance signal), the hole width δ , the characteristic time τ_D to spread the electron spin saturation across Δ_{ESR} , the spectral diffusion constant at the frequency of irradiation $\mathcal{D}(w_{\mu w})$ and the total number of spin packets \tilde{n}_S presuming an average homogeneous linewidth Δ_{av} . All parameters reported in this table presume mono-chromatic microwave irradiation at the frequency $w_{\mu w}$.

	$\sqrt{M_2}$ (MHz)	w_{0S} (GHz)	Δ_{ESR} (MHz)	δ (GHz)	τ_D (ms)	$\mathcal{D}(w_{\mu w})$ (MHz ³)	\tilde{n}_S
2 – Methyl – 1 – pentanol	102.7	140.107	425	1.28	0.14	326	303
2 – Methyl – 1 – propanol	103.2	140.106	425	1.80	0.14	330	303
EtOH	108.5	140.104	450	1.47	0.40	126	321
EtOH – d₆	83.9	140.134	355	0.83	0.97	32	253

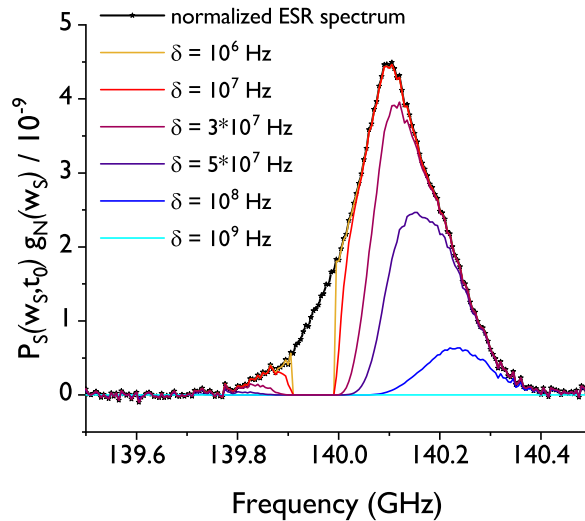


Figure 4.17: Illustration of hole burning effect under modulated microwave irradiation for a modulation amplitude $\Delta f_{\mu w}$ of 150 MHz. The same definition of $\delta^2 = \mathcal{D}(w_{\mu w}) \cdot T_{1S}$ was used, whereas $\mathcal{D}(w_{\mu w})$ was calculated at every spin packet center frequency covered by $\Delta f_{\mu w}$. The measured ESR spectrum of TEMPO embedded in a 2-methyl-1-propanol matrix containing 5 M xenon was used. Simulations assumed complete saturation of the spin packets at all times.

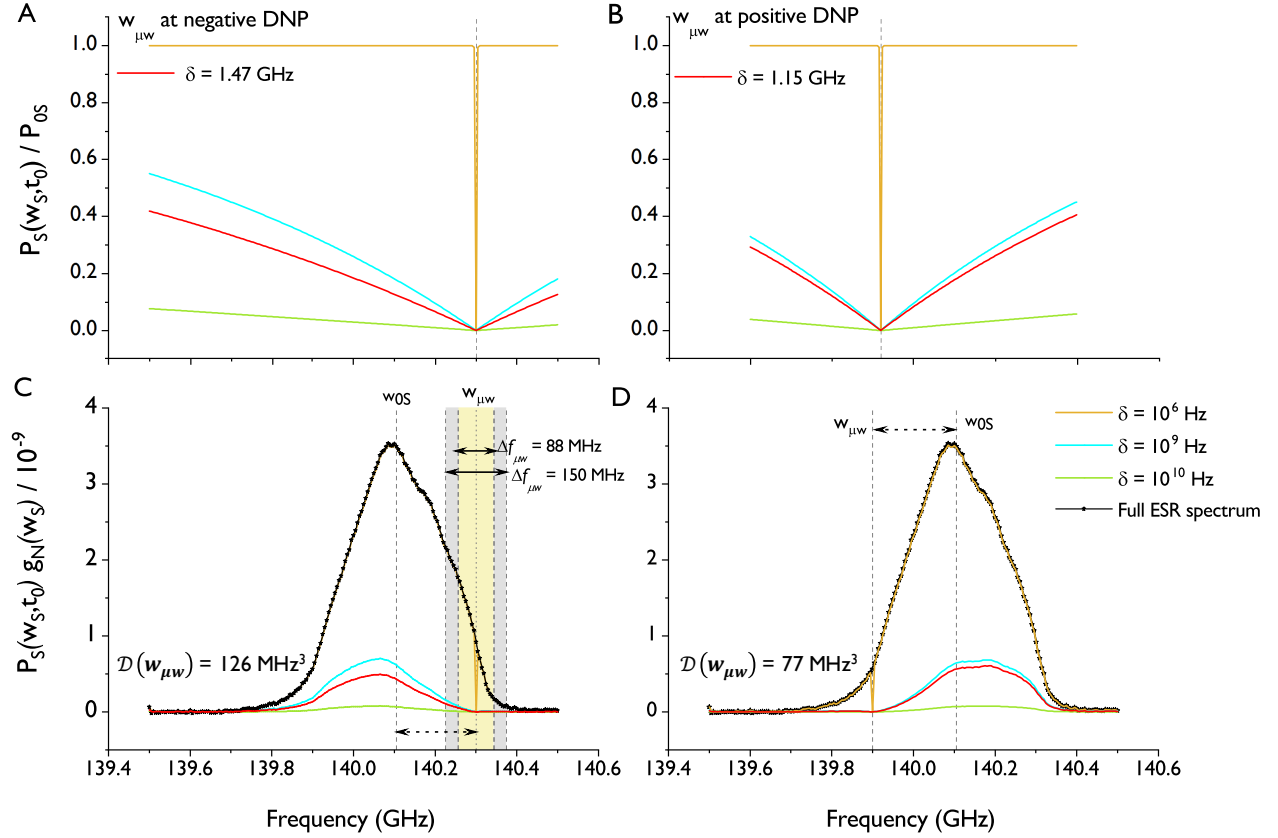


Figure 4.18: Impact of hole burning when mono-chromatic microwave irradiation is applied at the frequency of negative DNP (A,C) and positive DNP (B,D). The positive and negative DNP were found from Figure 4.11. The acquired ESR spectra of the TEMPO-EtOH-matrix were used to simulate the actual width of the hole burnt (red). Theoretical hole widths δ were added for comparison (orange, blue, green). To guide the eye, spin packets covered by a modulation amplitude $\Delta f_{\mu w}$ of 88 MHz (yellow) and 150 MHz (gray) are indicated by shading. In case of polychromatic irradiation, these areas would be shifted slightly towards the tails of the ESR spectrum to account for the optimized center frequency.

4.5 Discussion

This study found a linear dependence of the ^{129}Xe nuclear polarization enhancement due to microwave frequency modulation on the characteristic electron spin-lattice relaxation rate. The shorter the electron spin-lattice relaxation time T_{1S} , the higher was the polarization increase achieved by modulating the microwave frequency. Simulations illustrated how the observable macroscopic change in nuclear polarization was induced by an increasing fraction of electron spins being depolarized upon saturation by the modulated microwave field.

Generally speaking, depolarization is governed by an ensemble of three mechanisms, namely the combined effect of the microwave field, electron spin-lattice relaxation and the electron spin spectral diffusion. While microwave irradiation acted on *resonant electron spins*, defined as electron spins resonating in a close range of the irradiation frequency, spectral spin diffusion transported a part of this energy across the ESR spectrum to depolarize electron spins resonating further away from the excitation frequency. Ultimately, all the depolarized electron spins would release the absorbed energy to the lattice via relaxation. Assuming long saturation such that the ESR spectrum reached its steady state ($t \rightarrow t_0$), the polarization of electron spins decreased by a factor $\propto \exp(-T_{1S}^{-1/2})$ (Equation 4.13). Hence, a high degree of depolarization could be achieved for matrices containing radicals with characteristically long T_{1S} . Following the same logic, the extremely short⁸ T_{1S} between 5 ms and 21 ms measured for the xenon-TEMPO matrices used herein indicated poor overall saturation of the ESR line. Considering the mechanisms involved, the fast spin-lattice relaxation counteracted more efficiently the saturation caused by the combined action of the microwave field and spectral diffusion. A lower number of electron spins involved in triple spin flips would have resulted in a lower rate of nuclear spin diffusion, which would ultimately put an upper limit⁹ on the nuclear spin polarization. At monochromatic microwave irradiation, the microwave field engaged only a single spin packet directly since the spectral linewidth of the monochromatic microwave was 200 kHz and the frequency stability better than 0.5 MHz according to

⁸ Typical TEMPO T_{1S} reported were an order of magnitude higher, with 310 ms at 1.55 K, 6.7 T [176], 106 ms at 1.15 K, 6.7 T [177] in glycerol-(d₈)-H₂O, 108 ms [174] and 170 ms [175] at 6 K, 3.4 T in DMSO/H₂O. A shorter T_{1S} in the glassy DNP samples than, for instance, in crystalline structures could, however, be expected. The ~ 3.5 times higher T_{1S} in crystalline ethanol compared to a glass of ethanol was attributed to the higher local order in crystals which reduced the matrix sensitivity to the environment [186].

⁹Considering the experimental constraint $N_S \ll N_I$, the indirect process of nuclear spin diffusion is the driving force of inducing nuclear polarization. Only a small ensemble of nuclear spins within the so-called *diffusion boundary*, denoting nuclear spins in proximity of a depolarized electron spin, experiences polarization transfer through direct triple spin flips.

manufacturer specifications. Replacing the monochromatic microwave field by polychromatic irradiation of 150 MHz amplitude increased the number of spin packets directly engaged by the microwave field to 107. Modulating the microwave frequency thereby promoted spectral spin diffusion by involving a higher number of electrons spins, as schematically illustrated in [Figure 4.19](#). This explains why microwave frequency modulation had an increasingly positive impact on matrices with a higher spin-lattice relaxation rate, consistent with the experimental data. In the 2-methyl-1-pentanol matrix, which had the shortest T_{1S} with 5 ms, the gain in polarization due to frequency modulation was highest with 220 %. Furthermore, this was the protonated sample with the narrowest hole burnt by mono-chromatic irradiation. To sum

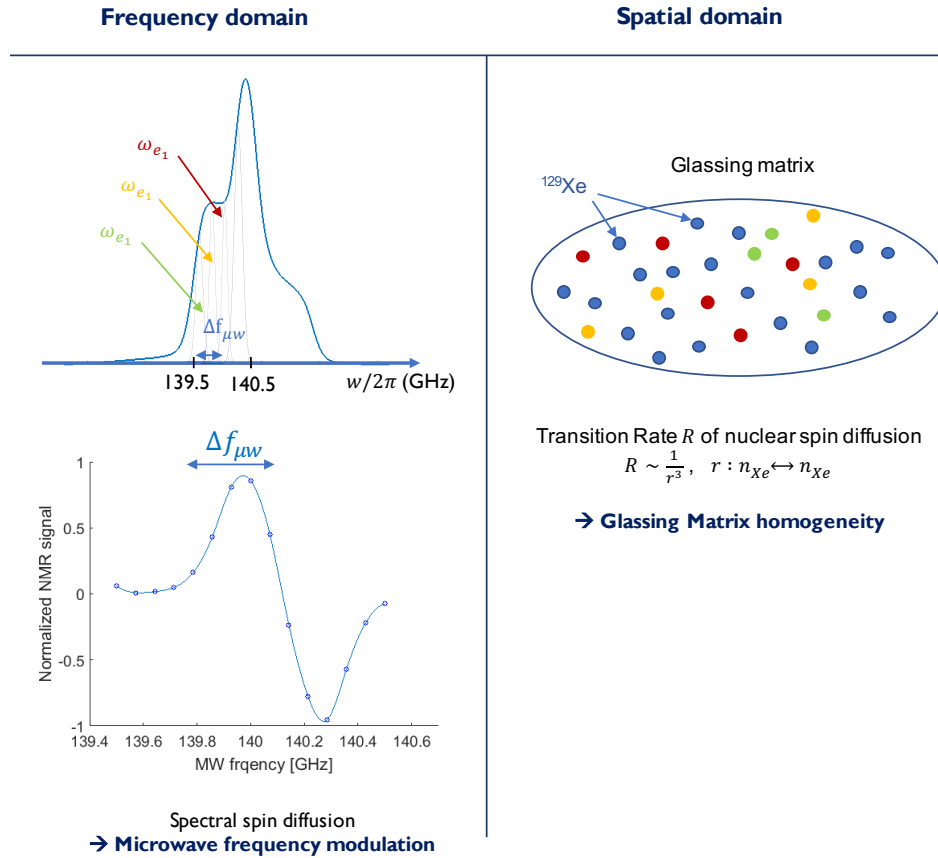


Figure 4.19: Schematics of two approaches promoting efficient spin diffusion. Electron spin spectral diffusion can be rendered more efficient if an increasing amount of electron-spin resonance frequencies are excited by microwave irradiation, i.e. more spin packets contribute to triple spin flips. The method of modulating the microwave frequency leads to a supplementary part of the ESR line being covered and additional spin packets being saturated (**left**). Meanwhile, the nuclear spin diffusion rate decreases with the third power of the distance between nuclear spins, hence requiring close spatial proximity of the spins for an efficient mechanism. This requires a globally homogeneous glassing matrix (**right**).

up, high enhancement was a consequence of a relatively broad-line radical ESR spectrum coupled with the short lifetime T_{1S} and efficient nuclear spin diffusion beyond the diffusion boundary.

Interestingly, the ESR linewidth was narrowest for 2-methyl-1-pentanol followed by 2-methyl-1-propanol and EtOH even though $1/R_P$ was highest in EtOH. Microwave frequency modulation was shown to have little effect on narrow linewidth radicals and radicals with long electron T_{1S} [23], such as the trityl radical OXO63 [49], but was shown to work well on larger linewidth radicals [30]. Yet, the full TEMPO linewidth, exceeding 355 MHz irrespective of the solvent, was in a range where further broadening did not predominantly determine the efficiency of frequency modulation. In the case of TEMPO, results are consistent with the enhancement due to microwave frequency modulation being governed by T_{1S} , rather than the ESR linewidth.

Modulating the irradiation frequency at a rate of 1 kHz proved to be an efficient mechanism to enhance polarization levels by up to a factor of 3.2. The relaxation rate needed to be inferior to the rate of modulation

$$\frac{1}{T_{1S}} \ll \nu_{FM} \quad (4.18)$$

to avoid significant electron spin-lattice relaxation while the microwave irradiation swept over the polychromatic frequencies. Therefore, the consistent increase in polarization due to frequency modulation that was observed for all solvent-matrices when modulating at a frequency superior to 1 kHz is coherent with the measured $T_{1S} \geq 5$ ms, \forall matrices. Furthermore, the amplitude of modulation $\Delta f_{\mu w}$ covered a significant part of the full TEMPO ESR line $\Delta_{ESR} \sim \mathcal{O}(400 \text{ MHz})$, roughly within [139.85; 140.3] GHz for any solvent investigated. Modulation amplitudes as small as 11 MHz had a positive effect on polarization levels since this corresponded to directly saturating eight spin packets instead of a single one. Those results are consistent with previous observations using $\Delta f_{\mu w}$ in the range of 2.5 % of Δ_{ESR} of TEMPOL [30]. The narrowing effect that solvent deuteration and xenon addition had on the ESR spectrum was reported previously [187, 188] and is briefly discussed in [subsection 4.5.1](#).

Microwave frequency modulation shifted the positive DNP peak towards lower MW frequencies and the negative DNP peak towards higher frequencies, unlike the zero-crossing which was not affected by modulation (figures¹⁰ 4.11, 4.18). The polarization enhancement

¹⁰All data discussed in this paragraph specifically applies to the doped EtOH matrix.

caused by modulation of the microwave frequency was higher at the positive DNP due to the ESR-line asymmetry of TEMPO (Figure 4.18): at monochromatic irradiation, the width of the hole burnt at the positive DNP was 1.15 GHz and therefore 320 MHz narrower than the hole burnt at the frequency of negative DNP. Frequency modulation had therefore a higher enhancement effect at the positive DNP. Furthermore, the $\sim 60\%$ higher coefficient of diffusion at the negative DNP entailed that more electron spins were depolarized. Therefore, monochromatic microwave irradiation saturated a more substantial part of the ESR line if applied at the negative DNP maximum compared to the positive DNP maximum. Subsequently, polarization levels were expected to be higher at the negative DNP, which was confirmed by the data (Figure 4.11). Further experiments confirmed that the polychromatic nature of modulated microwave beams affected the polarization build-up at the positive DNP stronger (appendix Figure A.6), producing higher enhancements than at the negative DNP (appendix Figure A.5). Moreover, no shift in the frequency sweep zero-crossings ν_C was detected when modulating the frequency. This can be explained by considering the origin of the zero-crossing, defined by the center of gravity w_{0S} of the electron spin distribution across the ESR spectrum. Since the input sine-function defines a symmetric distribution of frequencies around the center frequency, the zero-crossings were unchanged by polychromatic irradiation up to 150 MHz amplitude.

It was to be expected that modulation amplitudes were subjected to an upper boundary beyond which they would lead to a decrease in nuclear spin polarization, namely when the amplitude exceeded twice the distance between DNP maximum and zero-crossing (180 MHz in EtOH). In this case, negatively and positively hyperpolarized spins would partially compensate, thereby decreasing the macroscopic polarization. Yet, a slight decrease in nuclear polarization was already observed when increasing the modulation amplitude from 88 MHz to 150 MHz; A behaviour which was not initially expected – assuming perfect saturation at all times – since (i) the modulation amplitude was below the expected upper boundary and (ii) the rate of modulation of 1 kHz was one to two orders of magnitude faster than the spin-lattice relaxation rate in the studied matrix (58 Hz in EtOH). However, in the picture of discrete spin packets, the result indicated insufficient saturation of the spin packets contributing significantly, respectively an insufficient irradiation time per spin packet due to the great width of the ESR spectrum being covered. The characteristic time to spread the saturation across the whole width of the ESR spectrum via spectral diffusion was 0.4 ms and therefore inferior to the sinusoidal period of the modulation of 1 ms. Combined with the homogeneous spin packet width of 1.4 MHz, it follows that for a 150 MHz modulation amplitude, each spin packet was on average saturated directly by the microwave field during only 9 μs /period.

Spin-lattice relaxation took place on a much larger time scale ($1/\tau_D, 1/\nu_{FM} \ll T_{1S} \sim 17$ ms) so that it was neglected for this discussion in a first approximation. Therefore, for extremely large modulation amplitudes, the data suggests that spectral diffusion spreads faster than direct saturation. The saturation time per spin packet was small enough to enter a regime where the assumption of full saturation at all times may have lost its validity.

Efficient spectral spin diffusion was furthermore promoted by optimizing the matrix homogeneity, largely defined by the goodness of the amorphous glass and preparation procedure [189, 190]. Homogeneity of the sample matrix was found to impact polarization levels [191], build-up time [192] and even the predominant DNP mechanism [193]. The mechanism of phase separation caused by freezing has been described previously [194, 195] and was found to entail major drawbacks on polarization transfer efficiency [196]. Notably, clustering of ^{129}Xe spins necessarily leads to a higher median distance between resonant electron spins and nearby nuclear spins. By eliminating regions where nuclear spins accumulate in micro-clusters in the absence of unpaired electron spins, the previously described nuclear spin diffusion bottleneck delimiting regions of purely indirect polarization transfer can be avoided [192]. In pure xenon clusters, polarization was found to be propagated from the cluster boundary inward through nuclear spin diffusion, while the core of the cluster relaxed towards thermal equilibrium. Therefore, to mix the matrix homogeneously, an ultrasonic bath of melting ethanol or 2-methyl-1-butanol ice was used. Ultra-sonication is known to break up crystals by inducing vibrations into the system. Frequency modulated ultrasonic mixing was applied during mixing since it was found to avoid accumulation of microparticles suspended in a standing acoustic wave [197]. The results corroborated a more homogeneous mixing when using ultra-sonication compared to mixing via magnetic stirring (appendix Figure A.8). The data furthermore indicated that frequency modulation and homogeneous sample mixing were both methods to promote spectral diffusion (appendix Figure A.8). Nuclear dipolar coupling, which scales with the inverse of the third power of the distance r_{II} between two nuclear spins (Equation 2.17), transports polarization from nuclear spins in proximity to an electron to nuclear spins further away. As xenon concentrations were chosen according to the solubility threshold, the mean distance between two nuclear spins were solvent-dependent, hence, so was the nuclear dipolar coupling. The subsequent solvent-dependent efficiency of nuclear spin diffusion contributed to the matrix-dependent polarization levels and build-up time. Further, the results demonstrated a solvent-dependent spin-lattice relaxation time T_{1S} that can be increased by optimizing the sample matrix, as was previously demonstrated by replacing the solvent 2-methyl-1-propanol by $[1-^{13}\text{C}]\text{PA}$ which increased T_{1S} of Finland trityl in a xenon matrix by a factor of 4 [198].

Finally, simulations of the electron spin polarization showed that the most beneficial effect from modulating the microwave frequency can in general be expected when the external microwave field burns only a narrow hole δ into the ESR spectrum ($\delta \ll \Delta_{ESR}$). This can either apply to ultra-large linewidth radicals, to the case of low microwave power or poor power transmission, for short spin-lattice relaxation times T_{1S} or for slow spectral diffusion at the frequency of microwave irradiation $\mathcal{D}(w_{\mu w})$. The latter two criteria follow directly from the hole-width dependency on the square root of $[T_{1S} \cdot \mathcal{D}(w_{\mu w})]$ (Equation 4.10).

4.5.1 Effect of Deuteration and Xenon Addition on ESR Linewidth

DNP conditions involve temperatures below 4 K, at which T_{1S} relaxation is known to be governed by the direct relaxation process, where a single electron spin interacts with a single phonon mode. Adding xenon to the lattice would imperatively change the phonon distribution and therefore T_{1S} , as has been observed. This observation is consistent with previous publications, where the presence of xenon was shown to decrease the lifetime T_{1S} of Finland trityl from 152 ms to 98 ms at 6.7 T [198]. Introduction of xenon spins into the matrix furthermore reduced the ESR linewidth, indicating an interaction of the xenon atoms with the unpaired electrons of the radical precursor.

Since frequently used radical precursors are often well-dissoluble in liquid xenon [187], xenon was historically used as a solvent in ESR experiments. The effect of xenon on the ESR lineshape has therefore been researched previously and was attributed to large differences in the g-factor (deviating from the free-spin value) due to the combined action of (i) a charge transfer between 5p-electrons of xenon and the unpaired electrons of radicals [188] and (ii) an overlap interaction violating the Pauli exclusion principle [187]. Notably, this translates to a spin-orbit coupling exerted by the 5p-electrons of the noble that is stronger compared the coupling perceived by p-electrons for conventional solvents. The impact on the g-tensor was found to depend on the electron affinity of the radical precursor and would typically show a complex dependency on the radical structure and electronic configuration [187].

Deuteration of the EtOH matrix lead to a decrease in ESR linewidth. One of the effects contributing is the reduced hyperfine interaction of electron spins with deuterons compared to protons, as demonstrated in the linear dependence of the hyperfine tensor on the nuclear gyromagnetic ratio ($\gamma_d = 6.54$ MHz/T versus $\gamma_p = 42.57$ MHz/T) (Equation 2.16). The cal-

culated difference in ESR broadening attributed to this effect, $\Delta(\sqrt{M_{2,SI}})$, was however only 2.38 MHz and does therefore not by itself explain the observed decrease in ESR linewidth by 24.6 MHz. The interactions and g-anisotropy of a matrix of liquid xenon in the presence of ^1H and deuterium was again found to non-trivially depend on the electronic configurations and affinities of the matrix components [188].

It is interesting to note that there is a threshold beyond which a increased xenon concentration does not cause further narrowing of the ESR linewidth, while the $1/T_{1,S}$ continues to increase. As a future study it would be highly interesting to conduct a systematic study investigating the impact of increasing the xenon concentration on the electron spin system and to determine if a thresholding effect could be consistently observed.

4.5.2 Addressing Consistency Challenges and Limitations

Different freezing methods were found to change the distribution of 4-amino TEMPO radicals due to the formation of different polymorphs of the glass [195]. Further, significant changes to DNP profiles and enhancements were observed when a sample underwent annealing compared to rapid freezing [185, 195]. In this study, the acquisition of a complete data set (including LOD-ESR measurements plus frequency sweeps plus thermal and hyperpolarized measurements) was a time-consuming process, extending over several days (up to one week) for each sample. Measuring DNP immediately after sample loading ($t = 0$ h) resulted in higher DNP than identical measurements conducted after $t = 22$ h (P dropped to 57.7 % of the initial polarization), with a further polarization decrease to 52.9 % observed after $t = 47$ h (Figure 4.12). This observation was in perfect agreement with previous reports that ^{129}Xe polarization decreased by 58.1 %, from 5.3 % to 3.08 %, after 21.75 h (at 1.5 K, 5 T and hyperpolarized at the positive DNP) [185]. Due to the long time-scale of the measurements, the polarizer did not retain its 1.15 K during over-night experiments - especially under the continuous influence of microwave irradiation as the energy transferred inevitably lead to sample (space) heating. The exact temperature profile was unknown since the system was not set up to monitor temperatures superior to 30 K, a limit which was easily breached after a couple of hours, though. Kuzma et al. (2012) were able to relate the decrease in polarization to spontaneous cluster formation of xenon spins and atomic self-diffusion up to $0.7 \mu\text{m}$ due to annealing [185]. Naturally, thermal ^{129}Xe spin polarization was unaffected by such micro-scale processes, however, the polarization transfer process was found to suffer

reduced efficiencies due to spin diffusion boundaries, resulting in lower overall polarization levels. The consistency with the results reported herein indicates the occurrence of similar micro-scale process.

It is pivotal to be aware that the gaseous nature of ^{129}Xe (at T_0, p_0) asked for an exceptionally complex mixing procedure, unparalleled by conventional dDNP samples. The xenon sample preparation procedure was a highly empirical process in a minimally-controlled environment. First, only a few kelvins separated the ^{129}Xe melting point (161 K at p_0) from the solvent's freezing point (eg. 159 K for EtOH at p_0). Further, the system's conditions (temperature and pressure), which determined these phase-transitions, kept changing throughout the mixing procedure. This added a high degree of variability to the experiments, especially in terms of matrix-morphology-dependent parameters such as build-up time and maximally-achievable polarization levels. A rigorous solution would be to complete the current set-up with extensions that permit the control of pressure and temperature of the closed system at all times during the mixing procedure [199]. This would allow for reproducible exposure to temperature and pressure gradients and an equivalent amount of phase-transition steps between samples. Only then could an intra-study comparison between the efficiency of microwave frequency modulation for different solvents be conducted reliably. In the extreme case, the temporal evolution of the pressure inside the vial would remain reproducible between different experimental sessions. This process, however, is not only governed by the ambient temperature but also by the initial ^{129}Xe particle number and the combined volume of solvent and radical. The latter cannot be kept constant if constraints on the solubility-threshold are to be respected, unless a compromise on optimal polarization levels is accepted by choosing the lowest threshold as boundary condition for all samples. To conclude, even though a major effort could be put into a more complex sample-preparation set-up that consistently controls the temperature of the melting ice, respectively the pressure inside the vial, at no time can such a solution achieve intra-study comparability simultaneously with optimal sample compositions for all samples. A trade-off between comparability and maximally achievable polarization levels will remain.

Inter-study variability was furthermore added by hyperpolarizing sample flakes of varying surface and volume. Previous research has shown that pulverization of frozen xenon matrices increases polarization levels up to 100 % [199], due to an increased contact area between fragments and liquid helium bath, thus counteracting the observed overheating effect of microwave irradiation more efficiently [185]. Due to the nature of the mixing procedure involving a gaseous component, the sample matrix had to be extracted from the glass cold

finger by rapid heating. The extraction therefore yielded either one solid block of sample (up to 6 mm diameter x 10 mm length) or broken pieces of 2 - 3 mm diameter, or even pulverized fragments (≤ 1 mm diameter). Further, sample heating likely occurred throughout the experiments, as was previously deduced from simulations in identical conditions, namely hyperpolarization at 1.2 K, 5 T and 55 mW microwave power [200]. Combined with the production of different-sized sample flakes, this points towards another source of variability in polarization across samples.

Due to these sources of bias, reported ^{129}Xe polarization values should be treated with caution. A quantitative analysis comparing the gained enhancements due to microwave frequency modulation between different samples, respectively solvents, was therefore avoided.

Conclusively, factors limiting the polarization are (i) the lifetime T_{1S} , since it impacts the probability of a depolarized electron spin engaging a nuclear spin prior to its relaxation back to equilibrium and (ii) the hyperfine-mediated ESR line-width and -shape. Hence, the performance of the frequency modulation method will not only depend on the radical species but also on the experimental conditions. For instance, HyperSense polarizers operate at lower magnetic field of 3.35 T instead of 5 T, entailing a lower electron spin-lattice relaxation rate at equal temperature in a given experimental environment [182]. Due to the longer lifetime of T_{1S} , frequency modulation is expected to be less efficient at HyperSense conditions. Simultaneously, it was only due to microwave frequency modulation that ^{129}Xe nuclear spins could still be hyperpolarized to a detectable level at 6.7 T, 1.1 K [198], demonstrating the methodological dependence on external experimental conditions.

4.6 Conclusion and Outlook

This study aimed at increasing the available nuclear ^{129}Xe polarization in solid state. To this end, the effect of modulating the microwave irradiation frequency was investigated for different solvents. It was found that microwave frequency modulation lead to improved solid state ^{129}Xe polarization levels irrespective of the sample composition or solvent deuteration. Depending on the sample matrix, more than a 3-fold increase in ^{129}Xe polarization was achieved. Electron spin-lattice relaxation times were reported to range from 5 ms to 21 ms. They correlated with the efficiency to increase nuclear ^{129}Xe polarization via microwave frequency modulation. Simulations of the electron spin polarization yielded an average ho-

mogeneous spin packet width of 1.4 MHz while the width of the hole burnt into the ESR spectrum was calculated to be in the GHz-range.

Unavoidable repeated annealing, the degree of sample pulverization as well as varying glassing matrix homogeneity due to uncontrolled temporal evolution of pressure, temperature and the resulting phase-changes were all factors contributing to variability in polarization levels and build up time. Hence, while the effect of microwave frequency modulation on polarization levels was encouraging, a quantitative comparison between different samples was avoided for the sake of consistency. Generally speaking, the method of microwave frequency modulation has the potential of increasing nuclear polarization without entailing any drawbacks, assuming calibrated input parameters. Beneficial results can especially be expected for radicals with short T_{1S} , with large inhomogeneous linewidths Δ_{ESR} , at low concentrations, for experiments at high magnetic field or when inefficient spin diffusion is encountered. Microwave frequency modulation is therefore a most versatile tool, beneficial to a broad range of nuclei, radical precursors and applications.

Chapter 5

Hyperpolarized MRI with UV-induced Nonpersistent Radicals from Endogenously-occurring Precursors

Partially adapted from

Zanella, C.C., Capozzi, A., Yoshihara, H.A.I., Radaelli, A., Arn, L.P., Grütter, R., Bastiaansen, J.A.M.

Radical-free hyperpolarized MRI using endogenously-occurring pyruvate analogues and UV-induced nonpersistent radicals.

ArXiv preprint, arXiv:2006.14408, 2020.

Manuscript submitted to NMR in biomedicine, in revision.

Contribution

Claudia C. Zanella contributed to the data acquisition, data analysis and interpretation, initial manuscript preparation and manuscript revision.

5.1 Abstract

It was recently demonstrated that non-persistent radicals can be generated by UV-irradiation of metabolites, such as pyruvic acid (PA), enabling radical-free dissolution DNP. Although PA is endogenous, the presence of an excessive amount of PA may interfere with metabolic processes and may therefore not be suitable as polarizing agent for fatty acids, such as butyrate, or carbohydrates such as glucose. Thus, the aim of the study was to develop and characterize solutions containing endogenous biomolecules as alternative to PA for their use as non-persistent radical precursors for *in vivo* hyperpolarized MRI.

The metabolites alpha-ketoglutarate (α kV) and alpha-ketobutyrate (α kB), molecular analogues of pyruvate, were evaluated for their use as photo-induced non-persistent radical precursors and compared with PA. Their generated non-persistent radical yields following UV irradiation were studied with Ultra-Violet-Visible (UV-Vis) spectroscopy, quantified with ESR, and their efficiency as polarizing agents were determined in *in vitro* and *in vivo* dissolution DNP experiments at 9.4 T using either ^{13}C -labelled butyric acid or glucose.

Non-persistent radical formation of the precursors α kV and α kB was significantly influenced by addition of ^{13}C -labelled substrates. Using α kB increased the ^{13}C -labelled glucose liquid state polarization to 16.3 ± 1.3 % compared with 13.3 ± 1.5 % obtained with PA, and 8.9 ± 2.1 % with α kV. $[1-^{13}\text{C}]$ butyric acid polarization levels of 12.1 ± 1.1 % using α kV, and 12.9 ± 1.7 % using α kB were achieved. This was in a similar range than the $[1-^{13}\text{C}]$ butyric acid polarization observed when using trityl radicals (1.5 ± 0.2 % - 18.7 ± 0.7 %). Hyperpolarized $[1-^{13}\text{C}]$ butyrate metabolism in the heart revealed label propagation into $[1-^{13}\text{C}]$ acetylcarnitine, $[1-^{13}\text{C}]$ acetoacate, $[1-^{13}\text{C}]$ butyrylcarnitine, $[5-^{13}\text{C}]$ glutamate and $[5-^{13}\text{C}]$ citrate.

This study demonstrates the potential of α kV and α kB to be used as endogenous polarizing agents for *in vivo* radical-free hyperpolarized MRI owed to the encouraging *in vivo* MRS results and the high polarization levels achieved. Non-persistent radicals generated in endogenous metabolites pave the way to fast-tracked filtration and thus simplified quality-control testing in clinical applications.

5.2 Introduction

As introduced in [subsection 2.3.1](#), non-persistent endogenous radicals generated via UV light irradiation of particular precursor molecules may replace persistent radicals to avoid the need for filtration prior to injection. However, so far, only three *in vivo* studies have demonstrated the use of UV-induced non-persistent radicals to measure *in vivo* metabolic processes [55–57]. Several candidates were shown to be suitable precursors for UV-induced non-persistent radicals. Precursors used so far were a [butanol+phenol]-mixture [54], d₄-PA [201], (d₉)trimethylpyruvic acid [202] and [2-¹³C]PA [203]. Moreover, phenylglyoxylic acid [55] was found to be beneficial as polarizing agent for photosensitive metabolites. Yet, the achievable polarization was relatively low, at least at HyperSense conditions (3.35 T and 1.25 K). The precursor used in the most studies so far is Pyruvic Acid (PA) [56, 57, 179, 201], which achieved higher polarization than for instance phenylglyoxylic acid. Its presence, however, may interfere or even compete with metabolic processes that involve or are linked to pyruvate dehydrogenase activity [12, 204, 205]. Using PA as a polarizing agent for hyperpolarized MR experiments that study fatty acids, which are for instance of importance for metabolic cardiac studies since they constitute the main source of energy [7, 206, 207], may thus not be suitable. As much was demonstrated by the observed change in cardiac metabolism of hyperpolarized butyrate in the presence of co-injected pyruvate [12]. Therefore, it is of interest to find endogenously-occurring alternatives to PA for their use as non-persistent radical precursors for the measurement of short- or medium-chain fatty acid metabolism ([Figure 5.1](#)) with for example, hyperpolarized acetate [208–210], butyrate [12, 211–214] or octanoate [215]. Additionally, such alternatives may be beneficial for studies where glucose [216], lactate [217, 218] or alanine [219] are hyperpolarized and the formation of pyruvate is a metabolic product of interest.

Alpha-ketobutyrate (α kB, C₄H₆O₃) and alpha-ketovalerate (α kV, C₅H₈O₃) are two analogues of PA (C₃H₄O₃) that naturally occur in human blood [220, 221]. All three metabolites belong to the group of α -keto acids and display different biochemical properties [212, 221]. While α kB is an approximately 50% less efficient substrate of the enzyme Pyruvate Dehydrogenase (PDH) compared to PA, α kV is neither a substrate nor inhibitor of the enzyme [221] and is likely to be metabolized by a different enzyme than PDH. More detailed data for α kV and α kB substrate specificity for LDH (isoforms) can be found elsewhere [222, 223]. Notably, α kV is almost certainly not going to be a good substrate of Lactate Dehydrogenase (LDH) in the rat heart [224, 225]. Since α -keto acids have been shown to create radicals under UV-

irradiation [202], α kB and α kV are potential candidates of non-persistent radical precursors. Even though the enzymatic pathways of the novel radical precursors as well as the affinity of the enzymes LDH and PDH for α kB and α kV have yet to be proven *in vivo*, previous studies have demonstrated the potential interest in those alternative radical precursors [212].

The aim of this study was to characterize the endogenous pyruvate analogues α kV and α kB as novel non-persistent radicals following UV irradiation and to quantify their potential as endogenous polarizing agents for dissolution DNP. Effects of matrix composition on radical yields and polarization of ^{13}C -labelled butyric acid and glucose were quantified and a comparison was made with PA. In a proof-of-concept *in vivo* study it was investigated whether α kV and α kB could be used to measure cardiac metabolism of ^{13}C -labelled BA.

5.3 Experimental

A schematic overview displaying the timeline of the processes involved to conduct a single dissolution experiment is shown in Figure 5.2. Experimental parameters are specific to the set-up at EPFL and timings apply to dissolution experiments involving both substrates, $[1-^{13}\text{C}]\text{BA}$ and $[\text{U-}^{13}\text{C}, \text{U-}^2\text{H}]\text{Glc}$. Samples are hyperpolarized inside a 7 T polarizer at 1.05 K and subsequently automatically transferred to the adjacent 9.4 T MR magnet. Polarizer (**left**) and isocenter of the MR scanner (**right**) are approximately 4 m apart such that samples were pushed in ~ 3 s to the separator, thanks to the use of helium gas pressurized to 12 bar [24, 226]. Once the sample arrived inside the separator, the hyperpolarized pH-neutralized solution was injected as a bolus into the rodent and acquisition was triggered automatically [227]. The experimental study design is illustrated in Figure 5.3. Detailed explanations of the underlying motivation, the aim of individual experiments and data acquisition protocols is provided in the following chapter.

5.3.1 Sample Formulation and Preparation

All chemicals were ordered from Sigma-Aldrich (Buchs, SG, Switzerland). Different sample formulations were used depending on the type of experiment:

UV-Vis spectroscopy experiments were performed at room temperature on 100 mM of α kV, α kB or PA in glycerol-water for characterizing UV light absorption of the radical

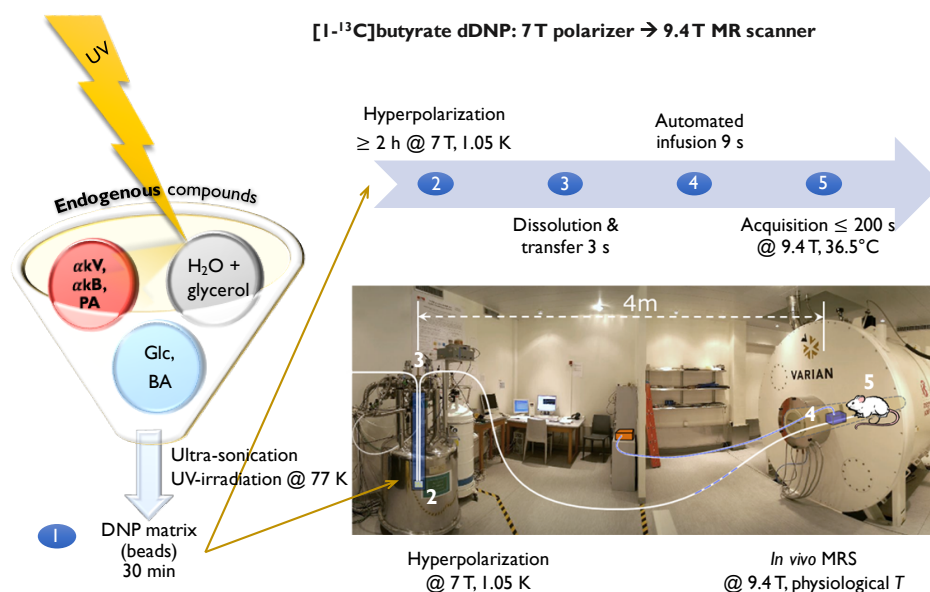


Figure 5.2: Timeline for the hyperpolarized dissolution DNP protocol at the 7 T polarizer. Protocol for *in vivo* dissolution DNP experiments of [1-¹³C]BA ([U-¹³C, U-²H]Glc experiments were conducted in analogy), hyperpolarized using UV-generated non-persistent radicals. Set-up corresponds to DNP hardware available at EPFL, LIFMET / CIBM.

precursors.

Electron Spin Resonance (ESR) was used to characterize the ESR line-shape and to quantify the concentration of the photo-induced radicals. ESR experiments were performed with 5 M solutions of αkV, αkB or PA in a glycerol:water (GW) 1:1 (v/v) mix. The ESR signal intensity was calibrated using six glycerol-water solutions with known TEMPOL concentrations between 0 mM and 100 mM. In a second series of experiments, 2 M unlabelled Glucose (Glc) or 5.7 M Butyric Acid (BA) was added to the glycerol-water mix. The amount of radical precursor was then empirically optimized to obtain 40 mM of non-persistent radicals after 200 s of UV irradiation, to ensure comparability between DNP experiments.

Empirical procedure for optimizing sample formulation: Sample formulations were empirically optimized to obtain 40 mM of non-persistent radical concentration and to simultaneously ensure satisfactory bead consistency. Choosing a target radical concentration of 40 mM was based on previous experience with broad linewidth radicals used to hyperpolarize ¹³C-labelled nuclei at 7 T [217]. The criterion of satisfactory bead consistency was important to allow for traditional sample loading and reproducible radical generation rates. In a first step, the maximum concentration of unlabelled Glc or BA inside glycerol-water

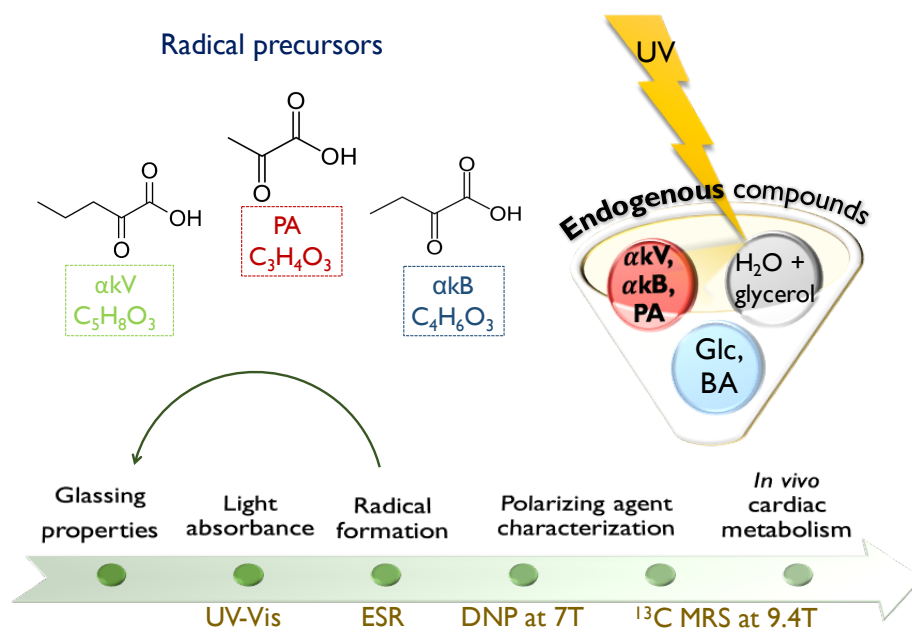


Figure 5.3: Study design. Overview over individual experimental steps involved in the study. Experiments follow the logical sequence linearly, except for the sample optimization protocol which requires several iterative steps.

was determined such that the solution still created glassy beads upon freezing droplets of it in liquid nitrogen (according to a visual assessment). This solution served as starting point for the subsequent iterative steps, where increasing volumes of radical precursors were added to reach the target value of 40 mM. A maximum of 10% of the irradiated beads were accepted to pulverize during UV-irradiation. If beads would not match the previous condition, glycerol-water (1:1, v/v) was added in an iterative process until one possible mix was found that yielded robust beads of 40 mM radical concentration. Reducing the glycerol: H_2O 1:1 (v/v) ratio resulted in deteriorated bead stability and pulverized beads mid-irradiation. A UV-irradiation time of 200 s was chosen for all further concentration calibrations, after having observed that several sample compositions yielded plateauing radical concentrations after ≤ 200 s of UV-irradiation and that a large number of beads did not resist 320 s of UV-irradiation without pulverizing.

Hyperpolarized ^{13}C MRS was performed on samples containing fully deuterated, fully ^{13}C -labelled glucose ($[U-^{13}C_6, U-^2H_7]Glc$) or $[1-^{13}C]$ -labelled butyric acid ($[1-^{13}C]BA$). After concentration optimization on samples prepared with non-labelled compounds, the amount of radical precursor was set to 5.7 M α kV, 4.1 M α kB and 1.6 M PA for $[U-^{13}C_6, U-^2H_7]Glc$ samples. Conversely, the radical precursor was set to 2.4 M α kV and 4.0 M α kB for $[1-^{13}C]BA$

samples. The latter were also used for *in vivo* measurements. To compare the polarization achieved by using the novel radical precursors with those obtained when using the popular and highly efficient trityl radicals, two additional samples were prepared. First, the trityl radical OX063 was used to hyperpolarize $[1-^{13}\text{C}]\text{BA}$ according to a previously published recipe by Ball et al. (2014) [211], however with a radical concentration of 25 mM, adjusted to the magnetic field of 7 T [228]. Further, 25 mM of Finland trityl were used to hyperpolarize the (non-irradiated) $\alpha\text{kB} + \text{BA}$ sample (concentrations as specified above).

5.3.2 Creating Non-persistent Radicals using UV Irradiation

To create non-persistent radicals, sample formulations described in the previous section were sonicated and degassed at 50°C for 20 minutes prior to pipetting 6 μl droplets and freezing them in liquid nitrogen to create a solid pellet. The frozen beads, were transferred to a quartz Dewar (Magnettech, Freiberg Instruments, Germany) filled with liquid nitrogen and irradiated with a broadband UV-lamp (Dymax BlueWave 200, Torrington, CT, USA) at maximum power (40 Wcm^{-2}) for a maximum of 200 s using a home-built irradiation setup [179]. In experiments aiming at investigating the time course of radical generation for αkV , αkB or PA ($n = 3$ per precursor), frozen beads were irradiated for a predefined duration of 20 s, 45 s, 70 s, 110 s, 150 s, 200 s, 320 s and the ESR spectrum was acquired at the end of each step.

5.3.3 Quantification and Characterization of Non-persistent Radicals

UV-Vis spectroscopy was performed to measure the light absorbance of the different radical precursors using a single beam UV-3100PC Spectrophotometer (VWR International) and a 1 mm pathlength quartz cuvette. UV light absorption of 100 mM αkV , αkB or PA in glycerol-water samples was measured from 280 – 600 nm in steps of 0.5 nm. Measurements were performed at room temperature since past studies showed no significant difference between absorbance spectra of PA solutions acquired at room- and liquid-nitrogen temperature [179].

ESR was used to determine the non-persistent radical concentration generated in the

samples after UV irradiation at liquid-nitrogen temperature. X-band ESR was performed at 77 K using a MiniScope MS 400 spectrometer (Magnettech GmbH, Germany). Spectrometer parameters were kept constant throughout all experiments. They were set to a sweep time of 20 s, 20 mT magnetic field range, 0.2 mT magnetic field modulation amplitude and 30 dB power attenuation. ESR experiments were performed on two 6 μ l beads for each sample formulation. Yet, viscosity-differences between the samples were considerable so that a correction factor was introduced for the concentration calibration: As the beads were extracted from the quartz Dewar, they were transferred to a pre-weighted microcentrifuge tube, which was then weighted again to determine the exact bead volume and correct the concentration calibration for it.

5.3.4 Hyperpolarization via DNP

All DNP experiments were performed in a 7 T custom-built polarizer. The sample cup was filled with 12 frozen UV-irradiated beads containing [U- ^{13}C , U- ^2H]Glc. Nuclear spins were hyperpolarized using a millimeter-wave source with digital control for frequency modulation, a 55 mW output power and a 1 GHz tuning range (Elva-1 VCOM-06/197/1.0/55-DD). Microwave frequency sweeps were performed to determine optimal hyperpolarization conditions in terms of microwave irradiation frequency and to quantify polarization build-up times using the three photo-induced non-persistent radicals. In the case of αkV , αkB and PA, microwave frequency modulated profiles were acquired at 4.2 K using a constant 40 MHz modulation amplitude and 5 kHz modulation rate for each microwave frequency step. The step size was 40 MHz for beads containing αkV or αkB , and 20 MHz for beads containing PA. For each frequency step, the sample was irradiated for 40 minutes during which the polarization build-up was monitored using a 2° hard pulse every 5 minutes. The y-axis value at each frequency point of the DNP sweeps corresponded to the polarization plateau measured at 4.2 K. The microwave frequency sweeps were performed with and without microwave Frequency Modulation (FM) to find the optimal microwave frequency and to quantify the effect of microwave FM on the DNP enhancement. They were normalized with respect to the positive DNP maximum measured without frequency modulation¹. In the case of the trityl radicals OX063 and Finland acid, sweeps were conducted at 1.05 K, with a step size of 10 MHz. No microwave frequency modulation was applied since it was expected to have a negligible effect

¹The microwave frequencies at which highest absolute polarization is achieved are referred to as positive DNP maximum and negative DNP maximum.

on polarization at said conditions.

The optimal conditions found in the previous experiments for a given set of frequency modulation parameters were used to hyperpolarize [U- ^{13}C , U- ^2H]Glc as well as [1- ^{13}C]BA for quantification of ^{13}C polarization levels in liquid state after dissolution and for the *in vivo* experiments. The ^{13}C -labelled metabolites were hyperpolarized at 1.05 ± 0.02 K for 2.5 hours (> 3 build-up time constants), with frequency modulated (40 MHz amplitude at a rate of 5 kHz) microwave irradiation at 196.69 GHz center frequency for αkV and αkB , and at 196.65 GHz center frequency for PA. Their polarization build-up was monitored using 2° RF excitation pulses every 5 minutes.

5.3.5 Dissolution DNP, Hyperpolarized ^{13}C MRS in Phantoms and *In Vivo*

Dissolution DNP Frozen hyperpolarized beads were dissolved using either 5.5 ml of D_2O or a phosphate buffered saline solution for liquid state *in vitro* and *in vivo* experiments respectively [24, 226]. The dissolved sample was automatically transferred to a separator/infusion pump located in a 9.4 T horizontal bore magnet (Agilent, Palo Alto, CA, USA) [227]. Hyperpolarized ^{13}C MR spectra were recorded within the pump using a dual $^1\text{H}/^{13}\text{C}$ volume coil starting 3 s after dissolution and using a 5° RF excitation pulse with 3 s repetition time (TR). After a complete decay of the hyperpolarized magnetization, a thermal equilibrium ^{13}C spectrum of the sample was acquired using a 90° RF excitation pulse, with a TR of 60 s and 64 averages. The enhancement ϵ was calculated as the ratio of the hyperpolarized and thermal signal peak integral, taking into account a correction for the RF excitation angle and number of averages. The remaining ^{13}C hyperpolarization after transfer was calculated as the product of the enhancement factor and the ^{13}C thermal equilibrium polarization at 293 K and 9.4 T, namely $P = \epsilon \cdot \tanh(\hbar\gamma_{\text{C}}B_0/2k_{\text{B}}T)$.

In vivo Hyperpolarized experiments were performed *in vivo* to demonstrate a proof of concept of the use of the novel polarizing agents to measure cardiac metabolism of hyperpolarized [1- ^{13}C]BA. *In vivo* experiments were conducted on altogether four male Wistar rats according to federal ethical guidelines and were approved by the local regulatory body. An-

imal physiology was monitored throughout the experiment and included tracking cardiac and respiration rhythms via a femoral artery catheter as well as tracking of the body temperature, which was maintained at a physiological level using a tubing system with circulating warm water. Details on the experimental set-up including a description of the isoflurane anesthesia were described previously [12, 57] and a similar volume of 62 μl $[1-^{13}\text{C}]\text{BA}$ was hyperpolarized. Frozen droplets of 10 M NaOH solution were added to the sample cup to neutralize the hyperpolarized solution during dissolution. Following an automated dissolution and transfer to the separator infusion pump [227], which was prefilled with 0.6 ml of phosphate buffered saline and heparin, 800 μl of the hyperpolarized solution was administered via a femoral vein catheter.

Hyperpolarized ^{13}C MRS MR data was recorded using a custom-made RF hybrid probe of $^1\text{H}/^{13}\text{C}$ -pair surface coils. Correct positioning of the coil on the chest of the animal in supine position was ensured using gradient echo ^1H MRI. FAST(EST)MAP shimming was performed until a ^1H linewidth of 30 Hz was achieved. Respiratory gated and cardiac-triggered MR acquisitions were performed using a ^1H -decoupled (WALTZ-16) [229] sequence with adiabatic 30° RF excitation pulses (BIR-4) [230] and a TR of 3 s. 8258 complex data points were acquired to sample a bandwidth range of 20.5 kHz. The first spectra acquired following injection, in which metabolic products are absent, were used to confirm the resonances identified in phantom experiments.

5.3.6 Data Processing and Analysis

To calibrate the radical concentration, the second integrals of the ESR signal intensity were calculated and plotted as a function of their known radical concentration. The corrected data was fitted to a linear function to obtain the concentration calibration curve. By means of the calibration curve, non-persistent radical generation time courses were plotted and fitted with a mono-exponential function to extract the radical generation time constant.

Statistical significance for polarization level difference obtained using αkB or αkV compared with PA were tested via an unpaired, 2-tail t-test assuming equal variance, with $p < 0.05$ considered significant.

In vivo spectra were post-processed in VnmrJ 3.2 (Agilent, Palo Alto, CA, USA) using 20 Hz line-broadening, baseline correction and drift correction. The SNR was calculated as the ratio of the highest signal intensity after phasing and the standard deviation of the noise over a region without metabolic or injected substrate resonances. All *in vivo* spectra where the $[1-^{13}\text{C}]$ acetylcarnitine resonance was visible were summed, corresponding to 10 consecutive spectra in the case of αkV , and 12 spectra in the case of αkB . Chemical shifts were assigned using $[1-^{13}\text{C}]$ acetylcarnitine as reference peak resonating at 173.9 ppm [12].

5.4 Results

To characterize structural changes and absorption characteristics of UV-light irradiation on the metabolites αkV , αkB and PA, UV-Vis and ESR measurements were performed: UV-Vis absorption spectra showed a $\sim 1.7\times$ higher absorbance for αkV compared with αkB or PA (Figure 5.4a). αkB and PA displayed nearly identical absorbance maxima in the UV range between 300 - 400 nm. Absorbance of all three metabolites peaked around a wavelength of 320 nm.

ESR performed on frozen samples prior to UV irradiation indicated the initial absence of unpaired electron spins in the matrices of glycerol-water mixed with 5 M of αkV , αkB or PA (data not shown). ESR spectra acquired after 200 s of UV irradiation demonstrated that free radicals of broad linewidth were generated within the frozen samples (Figure 5.4b-d). αkV and αkB showed a nearly identical ESR line-shape (Figure 5.4b,c), distinct to the one of PA (Figure 5.4d). The UV-irradiated beads displayed a yellowish tint upon visual examination,

Table 5.1: UV-induced radical generation time constants obtained from a mono-exponential fit to the time-dependent radical concentration curves and (maximum) radical concentrations obtained after 200 s of UV-irradiation. Sample formulations contained 5 M precursor dissolved in glycerol-water. Values represent the mean and standard deviation for $n = 3$ and the according data is plotted in Figure 5.4 e).

	Build-up time (s)	Maximal concentration (mM)
αkV	30.9 ± 5.1	41.6 ± 0.6
αkB	37.0 ± 5.2	56.1 ± 2.7
PA	46.5 ± 1.4	55.0 ± 1.9

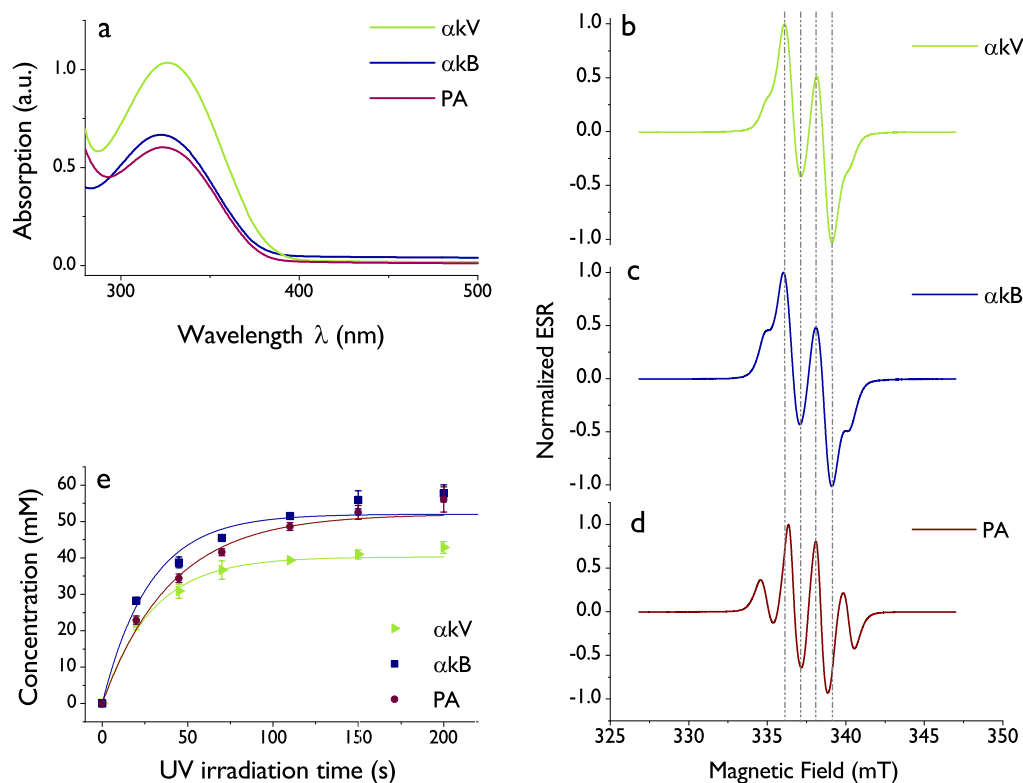


Figure 5.4: UV-Vis absorption spectra at room temperature and X-band ESR at 77 K. **a)** UV-Vis absorption spectra of 100 mM of radical precursor in glycerol-water using a 1 mm light path showing UV-light absorbance of α kV, α kB and PA. **b) c) d)** ESR spectra of the endogenous metabolites α kV, α kB and PA (5 M) at 77 K after 200 s of UV irradiation with a 40 Wcm^{-2} power UV-light source. Dashed reference lines to guide the eye. **e)** Radical generation time course of 5 M precursor in glycerol-water with respective mono-exponential fits. Concentrations were calculated using the linear TEMPOL calibration curve (Figure 5.5). Table 5.1 contains corresponding build-up times and maximum radical concentrations.

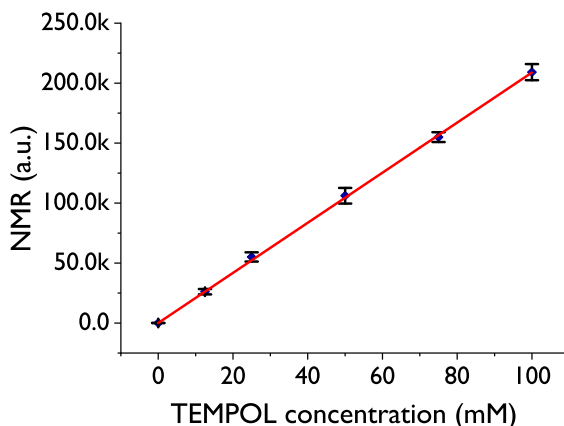


Figure 5.5: Concentration calibration curve of TEMPOL in glycerol-water (v/v 1:1) and linear fit ($R^2 = 0.999$, red) for $n = 4$ data sets. Data was acquired with X-band ESR at 77 K and subsequently used to quantify concentrations of UV-induced radicals.

in contrast to their initial colorless transparent appearance. Though, their transparency persisted.

The radical concentration calibration curve yielded the expected perfect linear relationship between NMR signal intensity and radical concentration (Figure 5.5). The slope of the calibration curve was found to be 2332 (for $2 \times 6 \mu\text{l}$, arbitrary units), which yielded the basis for non-persistent radical concentration calibrations. The production of non-persistent radicals as function of UV-irradiation time followed a near mono-exponential build-up. For the high-concentration samples a characteristic time constant (Figure 5.4e, Table 5.1) of 30.9 ± 5.1 s for αkV , 37.0 ± 5.2 s for αkB and 46.5 ± 1.4 s for PA was found. The maximum non-persistent radical concentrations were 41.6 ± 0.6 mM for αkV , 56.1 ± 2.7 mM for αkB and 55.0 ± 1.9 mM for PA. Irradiating the samples for 200 s resulted in plateauing radical concentration while avoiding pulverization of the beads due to excessive UV-irradiation.

To obtain transparent glassy beads that remained intact upon irradiation with UV-light, 4.1 M of αkB , for example, were found to yield the targeted 40 mM radical concentration upon 200 s of UV-irradiation after a mono-exponential build-up (exemplary build-up shown for αkB in Figure 5.6). Completing all calibrations, the 2 M Glc dissolved in glycerol-water were admixed with either 5.7 M of αkV , 4.1 M of αkB and 1.6 M of PA. These formulations yielded a non-persistent radical concentration of 41.5 ± 2.5 mM in αkV , 39.5 ± 2.3 mM αkB and 41.7 ± 2.0 mM in PA after 200 s UV irradiation (Figure 5.7). The BA sample contained final concentrations of 2.4 M αkV and 4.0 M αkB to generate a radical concentration of 40.0

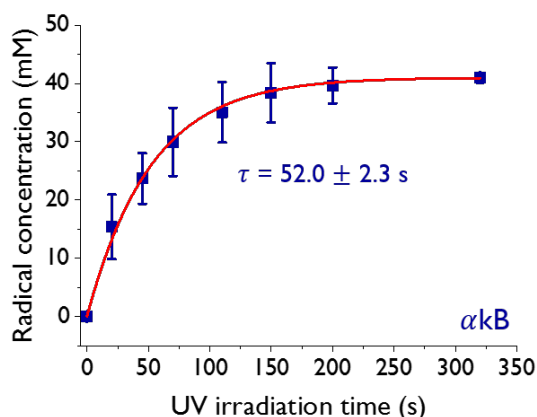


Figure 5.6: Non-persistent radical generation time-course of α kB calibrated to show absolute concentrations ($n = 4$). The build-up follows a mono-exponential function with characteristic time constant τ .

± 3.4 mM and 37.9 ± 5.7 mM.

To assess the effect of microwave FM, the ^{13}C nuclear polarization was measured as a function of the microwave frequency, which resulted in broadened sweeps upon frequency modulation. Modulation of the microwave frequency increased the DNP performance in terms of signal enhancement of hyperpolarized ^{13}C -labelled glucose by 100%, 50% and 30% for α kV, α kB and PA, respectively (Figure 5.8). The microwave frequencies of the modu-

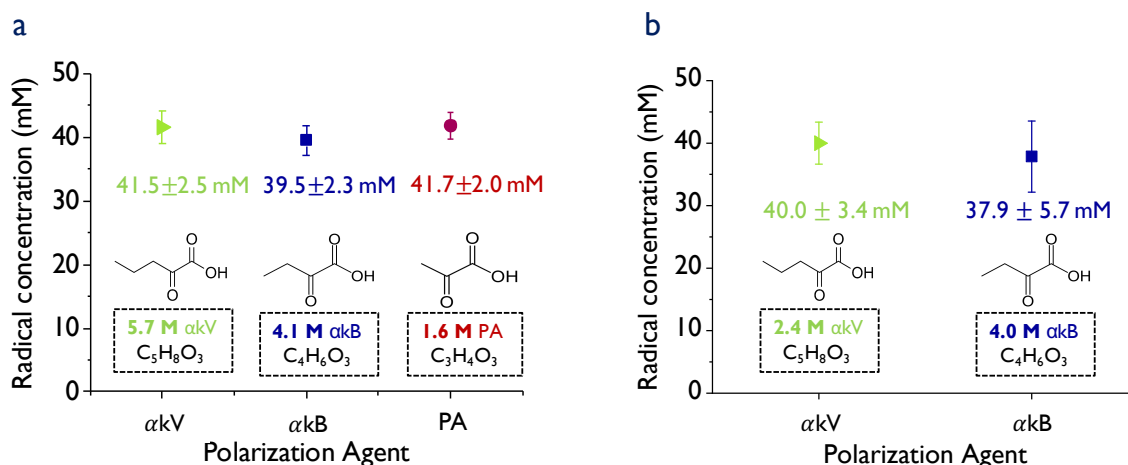


Figure 5.7: Sample formulations were optimized to obtain ~ 40 mM of non-persistent radicals after 200 s UV irradiation in **a)** $[\text{U-}^{13}\text{C}, \text{U-}^2\text{H}]\text{Glc}$ and **b)** $[1\text{-}^{13}\text{C}]\text{BA}$. Underlying chemical structures are illustrated for each non-persistent radical precursor, with the required concentrations indicated.

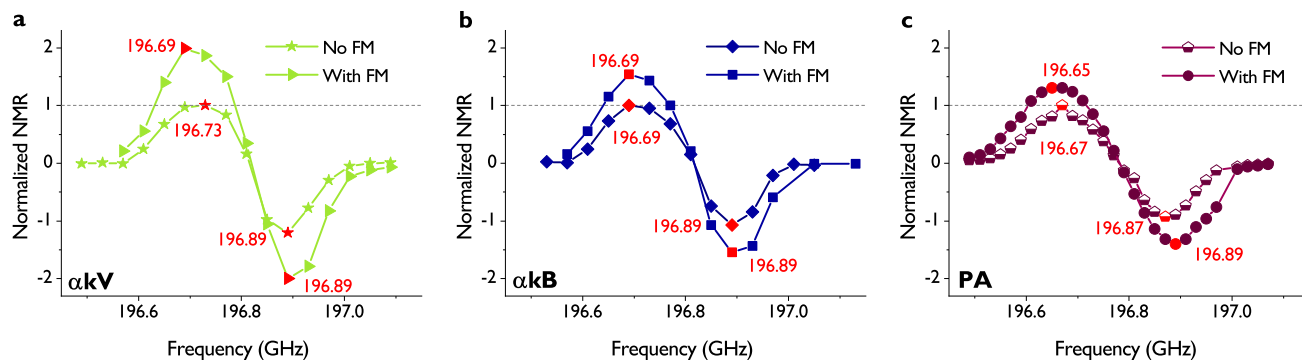


Figure 5.8: Hyperpolarized ^{13}C signal as a function of microwave frequency with and without the application of frequency modulation (FM). Formulations containing $[\text{U-}^{13}\text{C}, \text{U-}^2\text{H}]\text{Glc}$ in glycerol-water were hyperpolarized at 7 T and 4.2 K. FM was set to 40 MHz modulation amplitude at a frequency of 5 kHz. Microwave frequencies corresponding to observed positive and negative DNP maxima are reported in red and also in Table 5.2. Hyperpolarization was achieved using the UV radicals a) αkV , b) αkB and c) PA.

lated, positive DNP maxima were observed at $\nu = 196.69 \text{ GHz} / 196.65 \text{ GHz}$ for αkV and $\alpha\text{kB} / \text{PA}$, respectively (Figure 5.8, Table 5.2). Those for the negative DNP maxima were observed at $\nu = 196.89 \text{ GHz}$ for all three broad-linewidth precursors. Finland trityl was hyperpolarized at its positive DNP (196.67 GHz) where it showed a higher absolute DNP than at 196.77 GHz (negative DNP). OX063 was hyperpolarized at 196.7 GHz (positive DNP).

To determine the build-up time constants of nuclear magnetization, ^{13}C magnetization in solid state was measured as a function of microwave irradiation duration. The solid state build-up times of hyperpolarized $[\text{U-}^{13}\text{C}, \text{U-}^2\text{H}]\text{Glc}$ were $1.7\text{k} \pm 0.5\text{k s}$, $1.3\text{k} \pm 0.5\text{k s}$ and $1.6\text{k} \pm 0.5 \text{ k s}$ for αkV , αkB and PA, respectively (Table 5.3). Following dissolution, the liquid state (Figure 5.9) polarization for the C_{2-5} group of $[\text{U-}^{13}\text{C}, \text{U-}^2\text{H}]\text{Glc}$ were $8.9 \pm 2.1 \%$, $16.3 \pm 1.3 \%$ and $13.1 \pm 1.5 \%$ for αkV , αkB and PA, respectively. While $[\text{U-}^{13}\text{C}, \text{U-}^2\text{H}]\text{Glc}$ hyperpolarized with αkB showed significantly higher liquid state polarization than those hyperpolarized using PA ($p = 0.048$), there was no significant difference between PA and αkV ($p = 0.09$). The quantification of polarization levels on the C_1 and C_6 resonances of glucose did not alter the results (cf. Table 5.3).

Table 5.2: Microwave center frequencies at which positive and negative DNP maxima occur at 7 T. Microwave frequency sweeps (Figure 5.8) were conducted on $[U-^{13}\text{C}, U-^2\text{H}]\text{Glc}$ in glycerol-water samples for the UV-irradiated samples. The microwave frequency was swept using either mono-chromatic microwave irradiation or frequency modulation with 40 MHz modulation amplitude at a 5 kHz rate. For the Finland trityl sample, no frequency modulation was used.

	Microwave frequency modulation	Positive DNP Maximum (GHz)	Negative DNP Maximum (GHz)
αkV	no	196.73	196.89
	yes	196.69	196.89
αkB	no	196.69	196.89
	yes	196.69	196.89
PA	no	196.67	196.87
	yes	196.65	196.89
Finland trityl	no	196.67	196.77

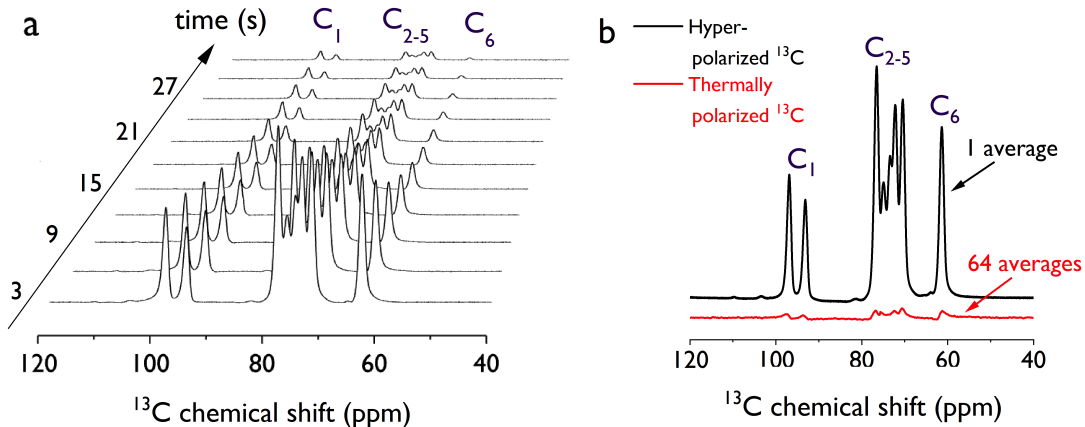


Figure 5.9: Hyperpolarized ^{13}C MRS of $[U-^{13}\text{C}, U-^2\text{H}]\text{Glc}$ sample formulations. **a)** Liquid state ^{13}C signal evolution of $[U-^{13}\text{C}, U-^2\text{H}]\text{Glc}$ hyperpolarized using αkB as polarizing agent. **b)** Hyperpolarized ^{13}C MR spectrum of $[U-^{13}\text{C}, U-^2\text{H}]\text{Glc}$ acquired 3 s after dissolution (top) and the thermally polarized ^{13}C spectrum (bottom). Acquisitions were performed at 9.4 T and $T = 20^\circ\text{C}$.

Table 5.3: Polarization build-up time constants at 7 T, 1.05 ± 0.02 K and liquid state polarization of the C_1 , C_{2-5} and C_6 resonances of $[U-^{13}C_6, U-^2H_7]Glc$ at 9.4 T, 20 °C. Liquid state enhancement was calculated as a ratio of hyperpolarized signal (rectangular RF excitation pulse of duration $\tau = 5 \mu s$, RF excitation angle $\alpha = 5^\circ$) and thermal signal (64 averages of $\alpha = 90^\circ$, TR = 60 s). Values show mean and standard deviation over $n = 3$ data sets.

$n = 3$	Build-up Time (s)	C_1 Glc liquid state polarization (%)	C_{2-5} Glc liquid state polarization (%)	C_6 Glc liquid state polarization (%)
αkV	$1.7k \pm 0.5k$	9.4 ± 3.0	8.9 ± 2.1	8.0 ± 2.8
αkB	$1.3k \pm 0.5k$	16.8 ± 0.4	16.3 ± 1.3	14.6 ± 1.7
PA	$1.6k \pm 0.5k$	13.9 ± 1.8	13.3 ± 1.5	11.5 ± 2.5
Conditions	7 T, 1.05 K	9.4 T, 293 K		

Table 5.4: Solid state build-up times at 7 T, 1.05 K are reported for $[1-^{13}C]$ butyrate. Room temperature liquid state enhancements, respectively liquid state polarization, were calculated after sample dissolution and transfer to a 9.4 T MR scanner. Mean and average values obtained from n data sets. Exemplary spectra hyperpolarized using the precursors αkV or αkB are shown in Figure 5.10.

	Build-up time (s)	n	BA liquid state enhancement (%)	BA liquid state polarization (%)	n
αkV	$2.1k \pm 0.3k$	4	$14.6k \pm 1.4k$	12.1 ± 1.1	3
αkB	$3.3k \pm 0.4k$	5	$15.6k \pm 1.7k$	12.9 ± 1.7	3
Trityl OX063	$0.8k \pm 0.3k$	3	$1.8k \pm 0.2k$	1.5 ± 0.2	3
Finland trityl	$1.7k \pm 0.3k$	3	$22.7k \pm 0.8k$	18.7 ± 0.7	3
Conditions	solid state: 7 T, 1.05 K		liquid state: 9.4 T, 293 K		

The solid state build-up times of hyperpolarized $[1-^{13}C]$ butyrate were $2.1k \pm 0.3k$ s and $3.3k \pm 0.4k$ s when hyperpolarized using αkV and αkB , respectively. Liquid state enhancement over thermal polarization at 9.4 T was $14.6k \pm 1.4k$ and $15.6k \pm 1.7k$ for αkV and αkB samples, respectively, which translated to liquid state polarization of $12.1 \pm 1.1\%$ and $12.9 \pm 1.7\%$ (Table 5.4). $[1-^{13}C]$ butyrate was hyperpolarized to $1.5 \pm 0.2\%$ and $18.7 \pm 0.7\%$ using the trityl radicals OX063 and Finland acid, respectively.

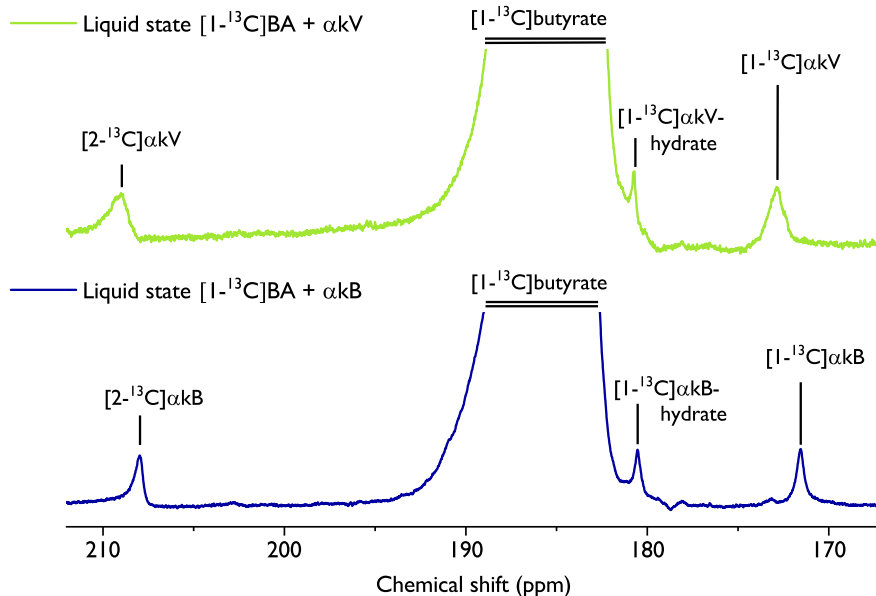


Figure 5.10: Liquid state ^{13}C MR spectra of $[1-^{13}\text{C}]$ butyrate hyperpolarized using αkV (top) and αkB (bottom) displaying the ^{13}C -labelled substrate and precursor resonances. Spectra were acquired 3 s post dissolution and were line-broadened with 20 Hz. Solutions were acidic because pH neutralization was not performed in these experiments.

The butyric acid liquid state nuclear relaxation times T_1 were 44.2 ± 0.8 s and 40.5 ± 1.8 s for αkV and αkB , respectively ($n = 3$). In these experiments, the natural abundance ^{13}C resonances of αkV and αkB could be identified as $[1-^{13}\text{C}]\alpha\text{kV}$ (at 172.9 ppm), $[1-^{13}\text{C}]\alpha\text{kV-hydrate}$ (at 180.7 ppm), $[2-^{13}\text{C}]\alpha\text{kV}$ (at 209.1 ppm), $[1-^{13}\text{C}]\alpha\text{kB}$ (at 171.9 ppm), $[1-^{13}\text{C}]\alpha\text{kB-hydrate}$ (at 180.6 ppm) and $[2-^{13}\text{C}]\alpha\text{kB}$ (at 208.4 ppm) (Figure 5.10). Note that the pH was not neutralized in these experiments, and the chemical shifts were different in pH-neutralized *in vivo* experiments (Table 5.5).

To assess the potential of αkV and αkB to investigate cardiac metabolism, hyperpolarized $[1-^{13}\text{C}]$ butyrate was injected in male Wistar rats. The first few seconds after injection of the hyperpolarized solution, metabolic products were not observable and the detected ^{13}C resonances could be identified as $[1-^{13}\text{C}]$ butyrate (at 184.8 ppm), and natural abundance resonances of $[1-^{13}\text{C}]\alpha\text{kV}$ (at 172.0 ppm), $[2-^{13}\text{C}]\alpha\text{kV}$ (at 208.7 ppm), $[1-^{13}\text{C}]\alpha\text{kB-hydrate}$ (at 178.1 ppm), $[1-^{13}\text{C}]\alpha\text{kB}$ (at 172.1 ppm) and $[2-^{13}\text{C}]\alpha\text{kB}$ (at 209.3 ppm). The resonance of $[1-^{13}\text{C}]\alpha\text{kV-hydrate}$ was not detected *in vivo*, further evidenced by its absence immediately after injection (Figure 5.11). Maximum *in vivo* SNR on ^{13}C BA was observed 12 s after dissolution, with a SNR of 1370 for αkV and 1780 for αkB . Cardiac metabolism of hyperpolarized $[1-^{13}\text{C}]$ butyric acid (Figure 5.12, Table 5.5) resulted in ^{13}C labeling of

[1-¹³C]acetylcarnitine (173.9 ppm), [1-¹³C]acetoacetate (176.0 ppm), [1-¹³C]butyrylcarnitine (176.4 ppm), [5-¹³C]glutamate (182.4 ppm), and [5-¹³C]citrate (179.8 ppm). Due to the shoulder of the nearby α kB-hydrate resonance, [5-¹³C]citrate could not be detected in the α kB experiment.

Table 5.5: Chemical shifts of observed metabolites in the heart after injection of pH-neutralized hyperpolarized [1-¹³C]butyrate *in vivo* using either α kV or α kB as polarizing agent (*in vivo* spectra displayed in Figure 5.12). [1-¹³C]acetylcarnitine was used as reference peak (*) and assigned to 173.9 ppm. The resonance of natural abundance [1-¹³C] α kV-hydrate was not detected in these experiments (see also Figure 5.11).

Metabolite	Chemical Shift (ppm)
natural abundance [2- ¹³ C] α kB	209.3
natural abundance [2- ¹³ C] α kV	208.7
[1- ¹³ C]butyrate	184.8
[5- ¹³ C]glutamate	182.4
[5- ¹³ C]citrate	179.8
natural abundance [1- ¹³ C] α kB-hydrate	178.1
[1- ¹³ C]butyrylcarnitine	176.4
[1- ¹³ C]acetoacetate	176.0
[1- ¹³ C]acetylcarnitine	173.9*
natural abundance [1- ¹³ C] α kB	172.1
natural abundance [1- ¹³ C] α kV	172.0

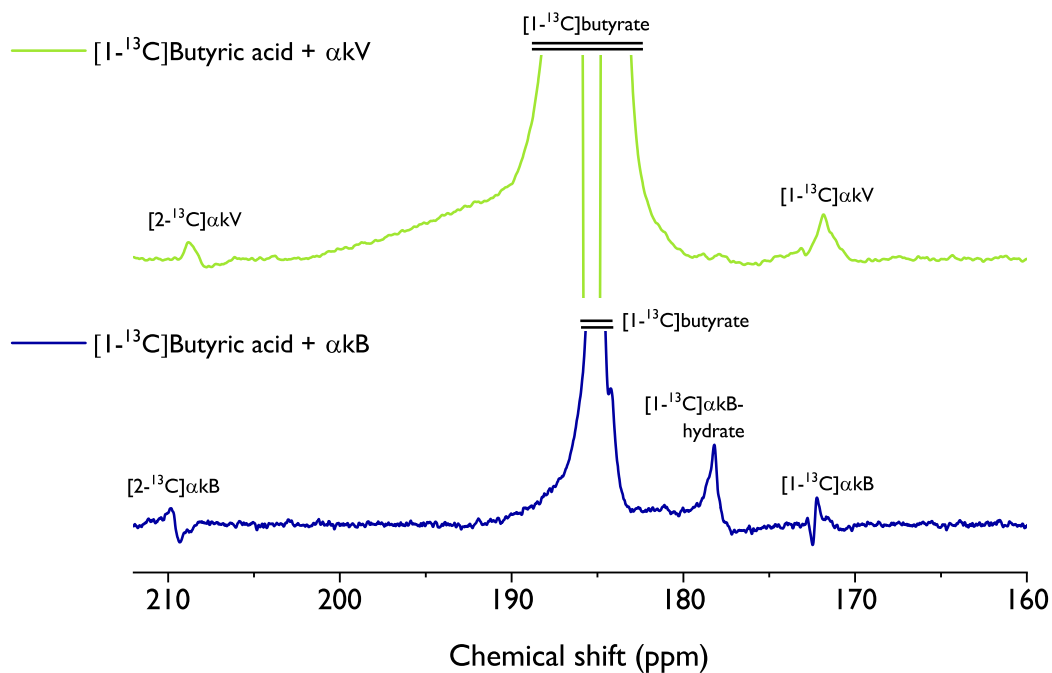


Figure 5.11: *In vivo* spectra acquired immediately after injection depict the injected ^{13}C labelled substrate and the natural abundance ^{13}C resonances of the polarizing agent αkV (top) and αkB (bottom). Metabolic products are absent in these spectra. Visible resonances are $[1-^{13}\text{C}]\text{butyrate}$, $[1-^{13}\text{C}]\alpha\text{kV}$, $[2-^{13}\text{C}]\alpha\text{kV}$, $[1-^{13}\text{C}]\alpha\text{kB-hydrate}$, $[1-^{13}\text{C}]\alpha\text{kB}$ and $[2-^{13}\text{C}]\alpha\text{kB}$. The resonance of $[1-^{13}\text{C}]\alpha\text{kV-hydrate}$ could not be detected.

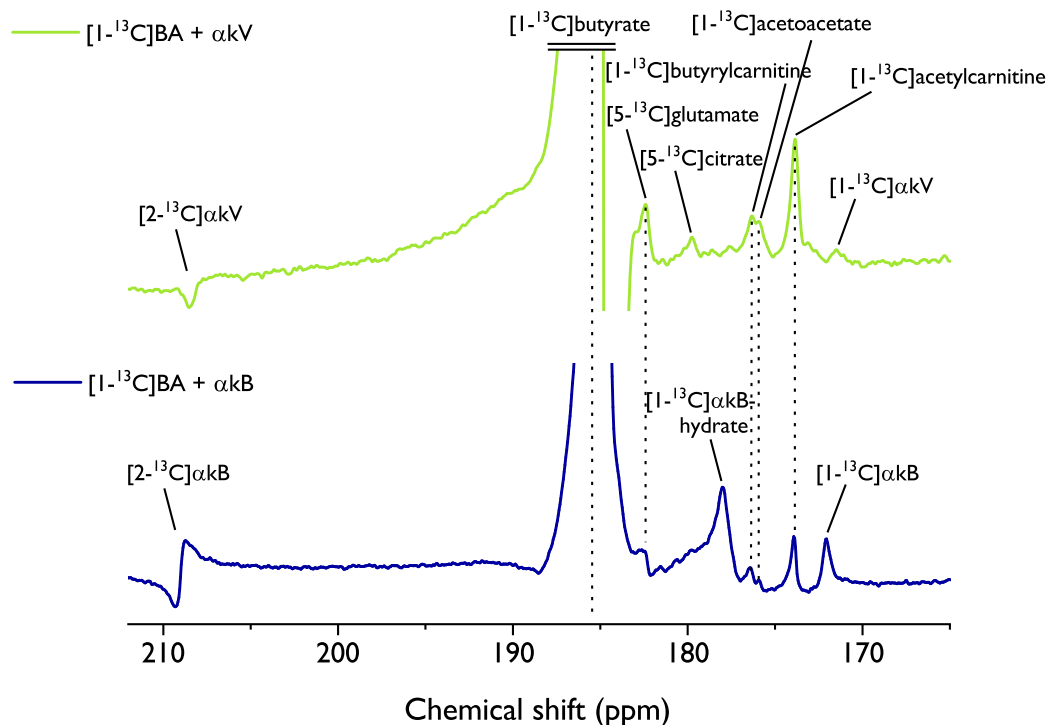


Figure 5.12: Summed *in vivo* spectra of cardiac metabolism in two male Wistar rats following the injection of a radical-free hyperpolarized $[1-^{13}\text{C}]$ butyrate solution. Hyperpolarization via DNP was performed at 7 T, 1.05 K using the UV-induced non-persistent radical αkV (top) and αkB (bottom). Spectra were acquired at 9.4 T and resonances where $[1-^{13}\text{C}]$ acetylcarnitine was visible were summed and line-broadened by a factor 20. This was the case for spectra acquired 22 - 51 s (αkV) and 18 - 51 s post-dissolution (αkB). Cardiac metabolism resulted in the detection of $[1-^{13}\text{C}]$ acetylcarnitine, $[1-^{13}\text{C}]$ acetoacetate, $[1-^{13}\text{C}]$ butyrylcarnitine and $[5-^{13}\text{C}]$ glutamate. $[5-^{13}\text{C}]$ citrate could not be detected in the αkB experiment, due to the proximity and phase of the αkB -hydrate resonance. The natural abundance resonances of the injected precursors αkB and αkV were also identified.

5.5 Discussion

This study showed that α kV and α kB can be used to generate non-persistent radicals for hyperpolarizing ^{13}C -labelled substrates, extending the method of radical-free dissolution DNP performed on mixtures containing only endogenously-occurring substances. Their potential as polarizing agents for *in vivo* metabolic studies was demonstrated in proof-of-concept experiments performed in the heart.

Although UV-irradiated α kV and α kB demonstrated virtually identical ESR line-shapes, their reaction to UV-light visibly differed (Figure 5.4). This was not only seen in the different UV-Vis absorption at low concentrations of 100 mM but also in their different radical yield at 5 M. Adding glucose or butyric acid further changed the reaction of each compound to UV light such that a specific sample formulation was required to achieve the targeted non-persistent radical concentration of 40 mM. The relation between non-persistent radical yield and precursor concentration was non-linear, which is consistent with previously reported results [179]. This posed a challenge during the iterative sample formulation process. The results illustrated that the sample formulation requires careful optimization in terms of UV-induced radical yield for each ^{13}C -labelled metabolic substrate, which is a non-trivial process.

Because the current work focused on the feasibility of α kV and α kB as non-persistent radical precursors, optimization of the sample formulation did not go beyond obtaining the targeting 40 mM non-persistent radical concentration in solid beads. Samples were not specifically optimized to maximize radical yield or achievable polarization, nor to minimize precursor concentration or UV-irradiation time. This resulted in the presence of larger α kV and α kB concentrations in the final sample formulation compared with PA. The empirical nature of the sample optimization procedure, plus the observation that radical yields in glycerol-water mixtures were comparable at high concentrations (Figure 5.4) indicate that there is significant room for improvement. Our experience with UV-irradiated non-persistent radical precursors and published work [57, 179] indicate that precursor volumes can be reduced when boosting radical yield or UV-light penetration. This may be achieved by using different glassing agents such as ethanol, by deuteration of the radical precursors, by changing the relative ratios of precursor to glassing agent, by adapting the UV irradiation time or changing the bead size.

The ESR experiments demonstrated the broad linewidth of the novel non-persistent rad-

icals, such that the previously researched method of microwave frequency modulation (cf. [chapter 4](#)) was applied to boost polarization. Indeed, microwave frequency modulation turned out to enhance nuclear polarization levels considerably, as expected [30, 169, 170], and contributed to the polarization results of up to 17 % and 13 % liquid state polarization for glucose and butyric acid, respectively. This was achieved with mixtures of purely endogenously-occurring metabolites and no added persistent radicals. In previous work using similar experimental conditions, UV-irradiated metabolite mixtures containing ^{13}C -labelled PA and BA were hyperpolarized to significantly lower levels (i.e. 3.3 ± 0.5 % - 5.2 ± 0.5 % for ^{13}C BA) [57]. The latter was a consequence of a less optimized sample preparation protocol, yielding a third of the radical concentration measured in this study, and the absence of microwave frequency modulation [57]. In the current study, a 40 times more powerful broad-band UV-light source was used compared to the previous study and glycerol-water was added to improve the DNP matrix. Although performed under different experimental conditions (cf. [Table 5.6](#)), previous studies using persistent radicals or non-endogenous non-persistent radicals reported polarization levels between 22.2 ± 2.1 % [216] and 30.1 ± 1.8 % [202] for glucose and 7 ± 2 % [211] to 28 ± 4 % [214] for butyric acid. Our own confirmation experiments yielded a butyric acid polarization of up to 19 % using trityl radicals such that the current results obtained with αkV and αkB are within a similar range and thus promising. It is probable that polarization may be further increased by optimization of the sample formulation or by a detailed investigation of the microwave frequency modulation. However, previously reported improvements of DNP performance may conflict with the UV performance and non-persistent radical generation: For example, using dimethyl sulfoxide (DMSO) as the glassing agent increased the DNP performance by more than 9-fold when polarizing ^{13}C -labelled BA [214]. However, UV-Vis and ESR measurements have shown the photosensitive nature of dimethyl sulfoxide and its unsuitability as a glassing agent for UV-induced non-persistent radical formulations using a broad-band UV source [55].

Ultimately, it is of interest to put the efficiency of the novel polarizing agents into context with existing ones. Yet, using inter-study comparisons of the polarization levels as a tool to do so entails pitfalls. A key factor to be considered is the widely varying experimental conditions across different studies, such as magnetic field strength at hyperpolarization and MR acquisition, sample space temperature in solid state, microwave source properties (output power, modulation-enabled) or sample matrix (cf. [Table 5.6](#)). While some factors such as solid state temperature during hyperpolarization will have a strong influence on the achievable liquid state polarization, other factors like the modulation of microwave frequencies might have a negligible to considerable impact depending on the radical properties. For example, $[\text{U-}^{13}\text{C}$,

Table 5.6: Inter-study comparison between liquid state (ls) polarization levels obtained for $[1-^{13}\text{C}]\text{BA}$ and $[\text{U}-^{13}\text{C}, \text{U}-^2\text{H}]\text{Glc}$. Experimental conditions list the (non-comprehensive) variability across studies. Non-persistent radical precursors as well as persistent trityl radicals were used. Current results are in the same order of magnitude as polarization levels obtained using persistent radicals.

	substrate	liquid state polarization	radical (precursor)	experimental conditions*	radical non-persistent	sample endogen.	study
1	$[1-^{13}\text{C}]\text{BA}$	$12.1 \pm 1.1 \%$, $12.9 \pm 1.7 \%$	αkV , αkB	55 mW MW output power (non-optimized MW FM for 1), $C_e = 40 \text{ mM}$ (1) / 25 mM (2,3), UV power = 40 W cm^2 , hp at 7 T, 1.1 K, MRS at 9.4 T	yes	yes	current
2	$[1-^{13}\text{C}]\text{BA}$	$1.45 \pm 0.15 \%$	Trityl OX063		no	no	current
3	$[1-^{13}\text{C}]\text{BA}$	$18.7 \pm 0.7 \%$	Finland acid		no	no	current
4	$[1-^{13}\text{C}]\text{BA}$	$3.3 \pm 0.5 \%$	PA	No MW FM, $C_e = 16 \text{ mM}$, no GW, UV source power = 20 W cm^2 , same B_0 , T than for (1) with hp at 7 T, 1.1 K, MRS at 9.4 T	yes	yes	Bastiaansen et al. MRM. 2018
5	$[1-^{13}\text{C}]\text{BA}$	$5.2 \pm 0.5 \%$	PA		yes	no (EtOH)	Bastiaansen et al. MRM. 2018
6	$[1-^{13}\text{C}]\text{BA}$	$7 \pm 2 \%$	Trityl OX063	Hp at 3.35 T, MRS at 11.7 T, 100 mW MW output power	no	no	Ball et al., MRM, 2014
7	$[1-^{13}\text{C}]\text{BA}$	3% – $28 \pm 4 \%$	Trityl OX063	Hp at 3.35 T, 1.4 K, <i>in vivo</i> MRS at 3 T, no MW FM, $C_e = 10 \text{ mM}$, optimized sample matrix	no	no	Flori et al., Spectrochim Acta A, 2018
8	$[\text{U}-^{13}\text{C}_6, \text{U}-^2\text{H}_7]\text{glc}$	$9.4 \pm 3 \%$ – $16.8 \pm 0.4 \%$	αkV , PA, αkB	cf. [1-3]	yes	yes	current
9	$[\text{U}-^{13}\text{C}_6, \text{U}-^2\text{H}_7]\text{glc}$	$22.2 \pm 2.1 \%$	Trityl	Hp at 7 T, 1.1 K, MRS at 9.4 T, no MW FM	no	no	Mishkovsky et al., Sci. Rep., 2017
10	$[\text{U}-^{13}\text{C}_6, \text{U}-^2\text{H}_7]\text{glc}$	$21.1 \pm 1.5 \%$ – $30.1 \pm 1.8 \%$	Trityl, (d_9 -)TriPA	Hp at 6.7 T, 1.1 K, optimized MW FM, UV pow. = 19 W cm^2 , $C_e = 20 - 40 \text{ mM}$, MRS at 9.4 T, not involved in metabolic pathways	yes ((d_9)-TriPA) no (trityl)	no	Capozzi et al., Angew. Chem. Int. Ed., 2019
11	$[\text{U}-^{13}\text{C}_6, \text{U}-^2\text{H}_7]\text{glc}$	$41 \pm 1 \%$	Trityl AH111501	Hp at 6.7 T, 1.1 K, MRS at 9.4 T, 50°C , MW FM without positive effect. Addition of 1 mM Gd^{3+}	no	no	Capozzi et al. J. Phys. Chem. Lett., 2019.

* List not comprehensive

$\text{U}-^2\text{H}]\text{Glc}$ hyperpolarized without frequency modulation at 7 T using trityl radicals OX063 [216] would likely not have exhibited significant liquid state polarization increase if microwave frequency modulation had been applied. This was explained by the narrow ESR linewidth and long electron T_{1S} at a magnetic field of 6.7 T [23]. On the other hand, $[1-^{13}\text{C}]\text{BA}$ hyperpolarized at the same field but using a broad line-width radical [57] might have profited from such a set-up.

Hyperpolarized BA has been used before as a probe to study short-chain fatty acid cardiac metabolism [12, 57, 211, 213, 214], with different results in terms of the amount of observed metabolites. In the current study, hyperpolarization of BA with αkV and αkB reached sufficient SNR to observe cardiac metabolism with a similar metabolic profile observed in previous studies using persistent radicals at high magnetic field [12, 211]. Since high magnetic field

allows for a better spectral resolution, it thus facilitates the resolved detection of metabolites such as ^{13}C labelled citrate and glutamate. However, B_0 inhomogeneities also increase, which complicates shimming procedures, especially around the heart. In the current study, the citrate resonance could not be reliably detected due to the shoulder of the neighboring $[1-^{13}\text{C}]\alpha\text{kB}$ -hydrate resonance. Conversely, the absence of $[1-^{13}\text{C}]\alpha\text{kV}$ -hydrate (Figure 5.12) enabled citrate detection when using αkV . Note that the concentration of αkV in the BA sample formulation (2.4 M) was much smaller compared to the one of αkB (4.0 M), which contributed to increased signal intensities of natural abundance αkB resonances compared with those of αkV . This can be appreciated when observing the relative signal ratio of $[1-^{13}\text{C}]\alpha\text{kV}$ or $[1-^{13}\text{C}]\alpha\text{kB}$ with $[1-^{13}\text{C}]\text{acetylcarnitine}$ (Figure 5.12).

Furthermore, $[1-^{13}\text{C}]\alpha\text{kV}$ -hydrate was detected in the non-pH-neutralized liquid state experiments compared with its absence in the pH-neutralized *in vivo* experiment. Meanwhile the signal intensity of the $[1-^{13}\text{C}]\alpha\text{kB}$ -hydrate resonance increased *in vivo* compared with the non-pH-neutralized liquid state experiment. This demonstrates the sensitivity of the proposed polarizing agents to pH and illustrates the importance of pH optimization.

The use of endogenous αkV and αkB may be a versatile alternative to PA for studying fatty acid metabolism or metabolic processes where pyruvate is a metabolic product. Based on the peak locations of the ^{13}C resonances of αkV and αkB , the potential detection of pyruvate as metabolic product would not be disturbed, especially in organs where B_0 inhomogeneities as well as motion-induced artefacts are reduced. Moreover, while the enzyme PDH does not have any affinity for αkV , it does have an affinity for αkB but oxidizes it at a much lower rate than PA [221]. This was partially confirmed in experiments using hyperpolarized ^{13}C -labelled αkB that showed a decreased ^{13}C -labelling of bicarbonate compared with PA [212]. Determining the *in vivo* affinity of PDH for hyperpolarized ^{13}C -labelled αkV , and potentially elucidating any metabolic interference of the proposed polarizing agents remains to be established. Nevertheless, radical-free dissolution DNP via the use of endogenous non-persistent radicals provides a benefit and may increase the duration of the hyperpolarized state by avoiding one filtration step in clinical applications. In addition, UV-induced radicals were reported to quench with increasing temperature [54] and recombine at a threshold of 190 K [25], providing an additional potential benefit of UV-induced radicals within αkV and αkB to produce transportable hyperpolarized ^{13}C -labelled substrates for hospitals at off-site locations.

5.6 Conclusion

To conclude, the endogenous α -keto acids α kV and α kB can be used as efficient endogenous non-persistent radicals following irradiation with UV light, achieving similar or higher ^{13}C polarization when compared with PA. Their ability to hyperpolarize glucose up to 17 % and butyrate up to 13 % was also made possible due to the enhancement gained by microwave frequency modulation. α kV and α kB are thus potential candidates for translational clinical hyperpolarized MRI, enabling high polarization without requiring radical filtration. Cardiac metabolism of ^{13}C labelled butyrate hyperpolarized with α kV or α kB manifested label propagation in a wide range of metabolites, demonstrating their potential as endogenous polarizing agents for *in vivo* radical-free hyperpolarized MRI.

Chapter 6

The Saddle Coil Design as Advantageous Solution for Preclinical MRI and MRS at Ultra-high Magnetic Field

Partially adapted from

*Zanella, C.C., Clément, J., Wenz, D., Lanz, B., Grütter, R.
Saddle Coil Design for MRI/MRS at 14.1 Tesla: A Favorable Alternative to the Quadrature
Birdcage Coil.
Manuscript in preparation.*

Contribution

This chapter is in preparation for submission to MAGMA and is currently being adapted according to co-author revisions. Claudia C. Zanella built both coils, contributed to the experimental design and data acquisition, performed data analysis, prepared the original draft and participated in the revision process.

6.1 Abstract

Performing MR experiments at high magnetic fields is of increasing interest for a vast amount of applications, ranging from X-nuclei MRS to CEST. This is motivated by the intrinsically enhanced SNR or the advantages provided by higher spectral dispersion. Increasing the static magnetic field, however, also entails challenges for MRI as well as MRS, such as increased transmit field inhomogeneity. When going to higher field strengths, the issue of non-uniform B_1^+ excitation, respectively non-uniform image intensity, has to be addressed: The choice of the RF coil impacts these parameters in a major way and ultimately determines the viability of the study.

The purpose of this study was to compare a single channel ^1H saddle coil with a high-pass 8-leg quadrature ^1H birdcage coil in the context of preclinical magnetic resonance imaging studies at 14.1 T. The custom-build coils were analyzed with respect to their performance for MR imaging or for their potential usage in combined spectroscopic studies. Their characteristics were evaluated with respect to transmit field (B_1^+) homogeneity over a large field of view, signal-to-noise ratio (SNR) and B_1^+ efficiency. Evaluation was conducted through electromagnetic field simulations, saline phantom measurements and *in vivo* imaging of a rat thigh muscle. As application, the performance of the saddle coil for CEST imaging of glycogen hydroxyl groups at ultra-high field was investigated.

Over a ROI of $11 \times 11 \times 2 \text{ mm}^3$, the transmit field efficiency was 54 % higher for the saddle coil than for the birdcage coil. The saddle coil was found to yield 20 % higher SNR without suffering substantial loss in transmit field homogeneity and was successfully used for *in vivo* glycoCEST mapping of skeletal muscle. The saddle coil was found to be a versatile alternative to the birdcage coil in terms of SNR, transmit field homogeneity, RF power requirements and potentially advantageous for combined MRS and MR imaging studies, such as CEST, where both, strong and homogenous B_1^+ are necessary.

6.2 Introduction

Magnetic resonance imaging and spectroscopy non-invasively enable unique insights not only in pre-clinical but also in clinical research. The RF coil, essential to RF signal creation and detection, must be adapted for each specific application to obtain optimal results. Any given magnetic field strength B_0 entails its advantages and challenges. Conducting pre-clinical research at ultra-high magnetic field imposes hardware constraints such as a reduced bore size compared to clinical MR scanners, since it becomes increasingly difficult to maintain B_0 homogeneity, and therefore scales research down to small-animal *in vivo* applications or *in vitro*/*ex vivo* data acquisition. Increasing B_0 furthermore exacerbates transmit field inhomogeneities due to decreasing transmit wavelengths and decreases the effective spin-spin relaxation time T_2^* . A further challenge at high magnetic field is the presence of additional RF coil capacitors that are introduced to reduce wavelength effects. A higher number of capacitors entails supplementary energy loss as well as increased interaction between capacitors [35]. One of the challenges associated with ultra-high magnetic field is therefore simplifying the coil design by reducing the amount of components [34]. Yet, the advantages of increasing magnetic field strength outweigh the drawbacks for answering a vast range of scientific questions [231]. High magnetic field is intrinsically advantageous in terms of increased spectral dispersion and enhanced SNR. Hence, methods linked to X-nuclei, phase-contrast, susceptibility-weighted (functional, etc) imaging and MRS profit from a high B_0 .

Another method profiting from high magnetic fields is CEST (introduced in [section 3.2](#)). Due to the decreased bulk water spin-lattice relaxation rate $1/T_{1,w}$, the lifetime of saturation stored in the water pool is prolonged. The sensitivity of CEST for low-concentration solutes is intrinsically much higher than the one of MRS since it relies on detecting changes of the more abundant water signal. Yet, being able to combine CEST imaging with ^1H MRS using the *same* RF coil could be useful to conduct ^1H MRS reference scans or a separate study simultaneously without changing animal or FOV positioning. In fact, one of the major challenges in CEST imaging today, namely the quantification of the CEST effect, can be resolved this way: The acquired CEST maps yielding relative metabolite distributions could be calibrated through localized ^1H MRS to calculate quantitative metabolite concentration maps over a large FOV. The idea of combining CEST MRI with ^1H MRS has received some attention in recent years, applying it to several metabolites such as lactate [232], creatine [233] and glycogen [234]. It was furthermore used for separated creatine and phosphocreatine quantification [235], simultaneous glycoCEST imaging and lipid level quantification [236] and global and

local quantification of the pulmonary gas exchange function in hyperCEST of ^{129}Xe [234]. Frequently, the Point RESolved Spectroscopy (PRESS) sequence was used to acquire spectra of exchangeable protons but alternatively accelerated sequences have been developed, which allow for simultaneous acquisition of CEST images and ^1H spectra to achieve quantitative CEST mapping [237, 238]. All these applications have in common, that they do not only require homogeneous transmit fields to create unbiased spatial CEST distribution maps but also high sensitivity to reliably quantify local metabolite concentrations, making the choice of an appropriate RF coil pivotal. For MRS, there is not only the question of the sensitivity but also the strength of the transmit field B_1^+ to achieve short enough RF pulses to have sufficient excitation bandwidth and allow for short-TE acquisitions, which typically produce spectra with higher SNR, increased sensitivity and reliability for metabolite detection and lower T_2 effects to correct for [32]. Glycogen, for instance, was reported to have an extremely short T_2 in H_2O between 29 ms at 11.7 T [157] and 38 ± 3 ms at 8.4 T [158], so that a short TE is advantageous for glycogen detection [32].

In CEST, solute protons are labelled by applying RF pulses at the resonance frequency of the metabolite of interest. Therefore, the nature of creating contrast via CEST entails an increased challenge for reliable detection of metabolites resonating close to the proton resonance frequency of water. Glycogen CEST (glycoCEST) in skeletal muscle, for instance, is a particularly challenging measurement in terms of SNR for several reasons: (1) the proximity of the glycogen hydroxyl group resonance frequency to the water frequency and (2) the limited fulfilment of the slow proton exchange regime condition [125]. (3) While glycogen concentration in liver was found to be approximately 200 - 300 mM [162], glycoCEST measurements estimated it to be much lower in rested skeletal muscle (human) with 50 - 100 mM [153]. The latter was confirmed in biopsy and ^{13}C studies [239]. According to studies on male Wistar rats including over a dozen subjects n , the resting skeletal muscle glycogen concentration was estimated to be 152.2 ± 7.7 mmol/kg dry weight ($n = 13$) [240], respectively 174.8 ± 6.7 mmol/kg dry weight ($n = 27$) [241]. Data therefore suggested that rat skeletal muscle contained 50 - 60 mM glycogen, similar to data found for humans [242]. The approximately 3 - 4 times smaller glycogen concentration found in skeletal muscle compared to liver adds an additional challenge for skeletal muscle glycoCEST. Cerebral glycoCEST would even need to be sensitive to metabolite concentrations an order of magnitude lower: glycogen content was reported to be around 3.5 mM in both, healthy volunteers [243] and sham and hypoglycaemic rat brain [244] and no higher than 5.6 mM [245]. Those studies were conducted using ^{13}C MRS, the gold standard for *in vivo* glycogen detection.

Spatial homogeneity of the RF field (B_1^+) over the ROI is indispensable for most imaging methods and also for CEST effect interpretation to avoid biased interpretation of relative metabolite concentration ratios. For applications requiring a highly homogeneous RF coverage, volume coils are advantageous with respect to surface coils, however at the cost of lower transmit field efficiency and receive sensitivity. Purely considering signal detection, a surface coil (array) would be preferable to the volume coil. A combined design using a volume coil in TX and a surface coil in RX would be ideal to profit maximally from their respective advantages. In practice, this conceptual 2-coil-model entails several pitfalls for small animal imaging at ultra-high field, such as the small-bore size and strong electrical coupling between the two coils, rendering it a less practical solution [246, 247]. Pre-clinical animal studies conducted at high field, such as 9.4 T or above, focus on ROIs in the range of several millimetres diameter. Saddle and birdcage coils are popular choices in MR microscopy and MR imaging at ultra-high field [248, 249]. Most uses of saddle coils were for *ex vivo* applications, for instance for microimaging at 600 MHz [35] or for DNP-NMR at 400 MHz [250]. Quadrature birdcage coils are more frequently chosen since they are known to yield highly homogeneous transmit fields in a large volume [33, 115, 251]. However, on the practical side, changes in loading have to be balanced by locally tuning the RF circuit using trimmer capacitors. At higher field strength, such as 14.1 T, and over a widespread range of loadings, their presence distorts homogeneity, which is a long-standing and well-known problem [246, 251].

MR imaging in our laboratory was thus far conducted with a 16-leg quadrature birdcage coil. The limiting factor in imaging studies requiring large flip angle pulsing was the maximally generated transmit power. Early on, insufficient transmit power limited the generation of 90° flip angles. An alternative coil design was therefore required to conduct reliable flip angle calibrations. Considering the interest in creating quantitative CEST metabolite concentration maps, it seemed appropriate to compare and discuss the performance of a single channel ^1H saddle coil with that of an 8-leg quadrature high-pass ^1H birdcage coil at ultra-high magnetic field for a relatively large FOV. The goal was to compare their respective advantages for a study, where high sensitivity for ^1H -MRS measurements and good B_1^+ homogeneity for ^1H imaging were simultaneously required. Notably, it was of interest to compare the transmit power required to create large flip angles. This comparison study was conducted through electromagnetic field simulations and phantom studies. Ultimately, the aim was to use the saddle coil for an *in vivo* application, namely *in vivo* glycoCEST imaging of a rat skeletal thigh muscle. Evaluation criteria in the present study included not only B_1^+ homogeneity, but also B_1^+ efficiency, sensitivity as well as practical considerations.

A supplementary study was furthermore conducted using a 16-leg quadrature high-pass ^1H birdcage coil, which theoretically displays increased transmit field homogeneity compared to the 8-leg birdcage coil. The results of the comparison of the 3 coils (including *in vivo* glycoCEST imaging) can be found in [Appendix C](#).

6.3 Methods

6.3.1 RF Coil Designs and Bench Verification

A **high-pass 8-leg ^1H birdcage resonator** driven in quadrature mode was custom-build ([Figure 6.1](#)). The coil was dimensioned to fit the 14.1 T (Agilent Technologies, Palo Alto, CA, USA) magnet bore and with the aim to accommodate a rat thigh (resulting in 50.6 mm diameter and inner rung length $l = 27$ mm). Circuit geometry was chosen with rung width $W = 9$ mm, endring width $W_r = 3$ mm and inter-rung spacing $s = 11$ mm. A shield of 100 mm diameter and 68 mm length was added to the RF coil. The frame was manufactured from ertalyte, a material which did not interfere with the NMR resonance at 600 MHz. Furthermore, ertalyte did not deform upon (moderate) heating caused by the RF pulsing such that deformation of the coil geometry and the entailed transmit field inhomogeneity could be avoided. Apertures inside the mounting flanges were added for RF coaxial cables, anaesthesia tubes, oxygen tubes as well as tapped holes to fix the shield to the coil body (cf. [Figure 6.1 a](#)). Detailed schematics to scale were drawn inside SolidWorks 2017 (Dassault Systems, France) ([Figure 6.1 b,c](#)). The body of the birdcage coil was then wrapped with a Printable Circuit Board (PCB) accommodating all necessary capacitors ([Figure 6.2 b](#)). RF signal in TX/RX modes was transmitted via 50 Ohm coaxial cables (Huber+Suhner, Switzerland), which were equipped with adequate cable traps tuned to 600 MHz by trimmer capacitors to eliminate unwanted common-mode currents. Coarse tuning and matching to meet the resonance condition at 600 MHz was achieved using ceramic chip capacitors C_t , C_m . Capacitor values were initially estimated to be 4.0 pF by the simulation tool Birdcage builder [252] and finally chosen as 4.3 pF (4R3D, 3x3 mm², American Technical Ceramics, USA) upon bench experimentation. Fine tuning and matching adjustments could retroactively be conducted through variable capacitors C_t^* , C_m^* , C_{iso}^* of 1–9 pF (Knowles Voltronics, USA).

The **single-turn single-channel ^1H saddle coil** was dimensioned to serve the same purpose as the birdcage coil, that is to conduct imaging of a rat thigh. This resulted in a diameter to length ratio of 34 mm / 22 mm. Choosing a somewhat smaller diameter was possible thanks to the more open design inherent to saddle coils compared to birdcage coils. The saddle coil was formed from silver plated copper wire. The design was adjusted to minimize radially dependent contributions to the central magnetic field B_1^+ by choosing an angular aperture of $2\pi/3$ [113]. Due to the small electromagnetic wavelength λ of the RF current in the silver plated conductor at 14.1 T, the total wire length exceeded $\lambda/10$. Therefore, the coil was capacitively segmented by 4 fixed capacitors [117] with nominal values of 2×2.2 pF and 2×1.8 pF. The corresponding capacitor pairs were placed diagonally from each other

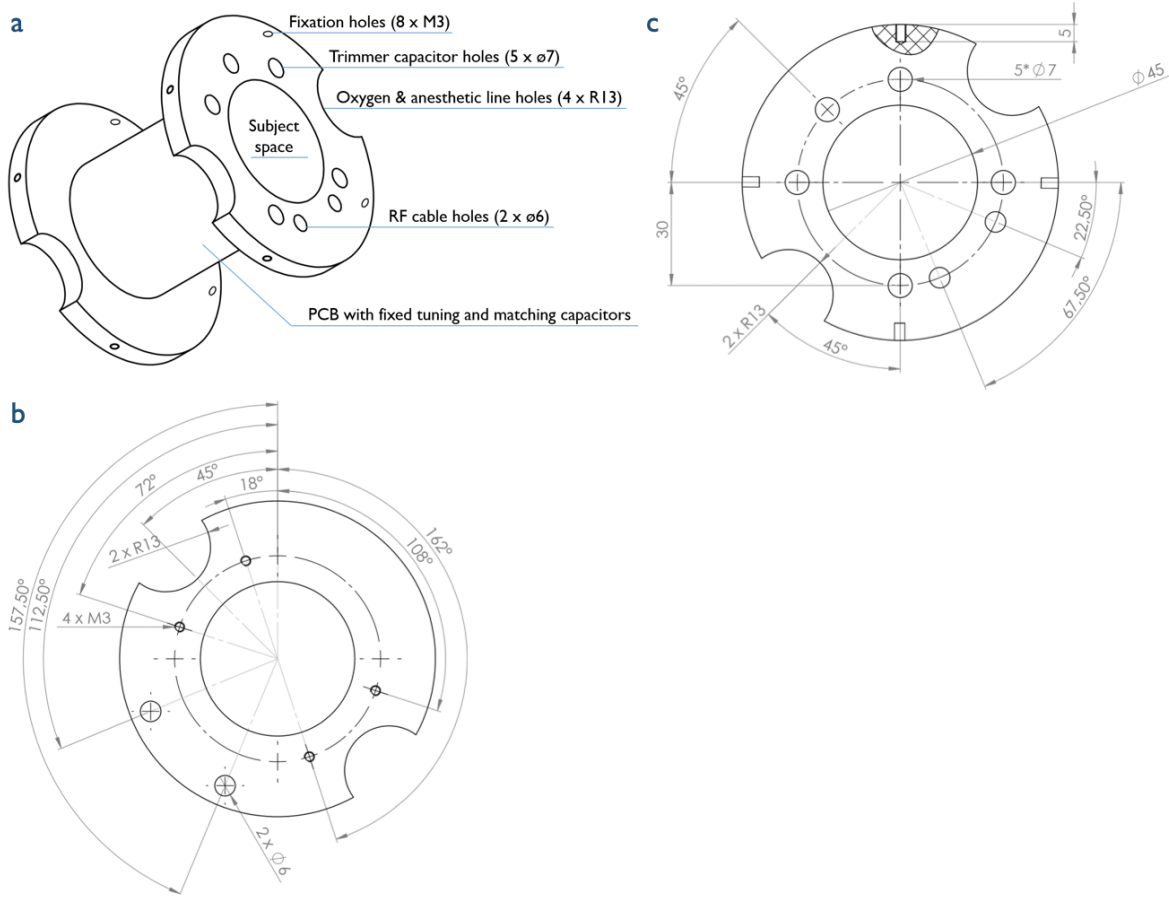


Figure 6.1: Schematics of the birdcage coil, including any dispositions to allow for *in vivo* imaging. Ertalyte was chosen as material to avoid deformation of the coil geometry upon potential heating. Designed in SolidWorks 2017 (Dassault Systems, France). SolidWorks and Sim4Life designs largely implemented by J. Clément. **a)** Semi-lateral view of the birdcage coil support frame. The coil was hand-crafted from a single piece of ertalyte. **b)** Back view. **c)** Front view, towards the source of the current.

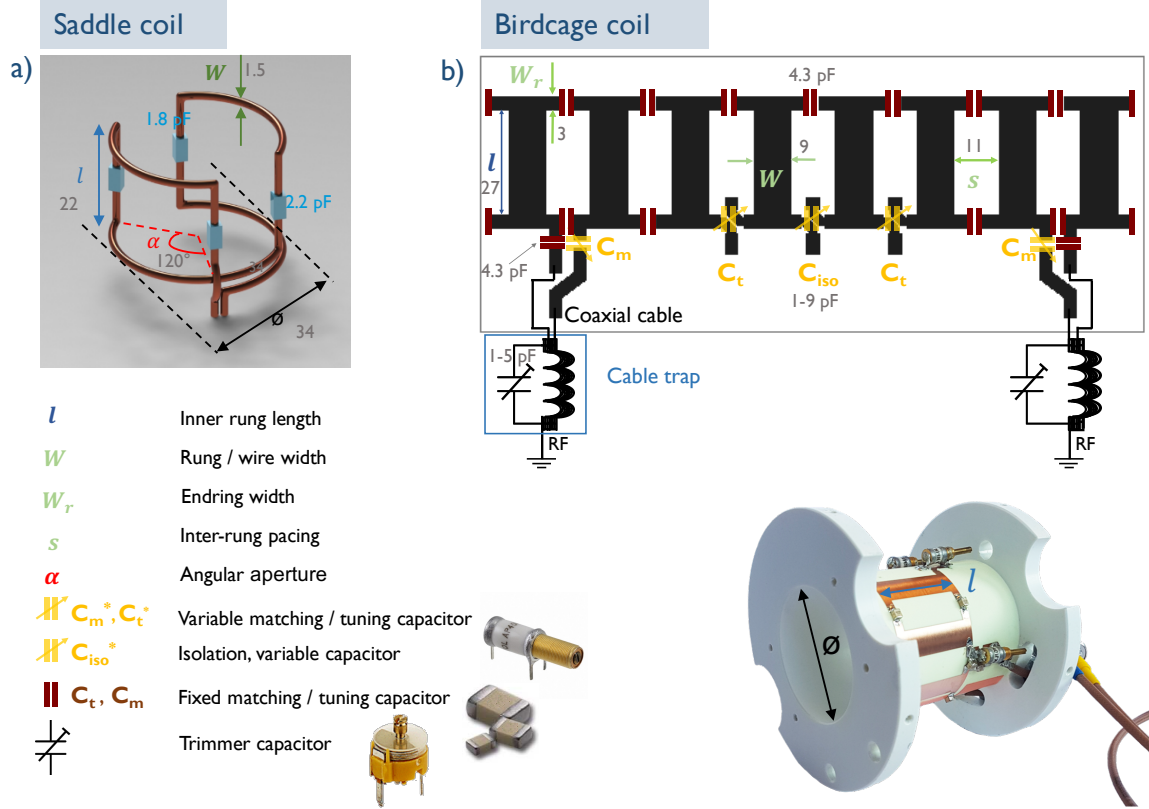


Figure 6.2: Saddle and birdcage coil designs. a) Single channel ^1H saddle coil. b) Design of PCB used for quadrature ^1H 8-leg birdcage coil, including CL cable trap circuit (**top**) and picture of final result (**bottom**). RF coil shield not shown. Values are given in millimetres unless otherwise indicated, distances are true to scale. Corresponding lengths and capacitor values are indicated in the figure and listed in table Table C.1.

(cf. Figure 6.2 a). Trimmer capacitors ($1-9$ pF) were added for fine tuning and matching. A data-sheet which lists the precise dimensions and capacitor values can be found in the appendix (Table C.1).

Quality factors for unloaded coils (Q_{ul}) and saline phantom loaded coils (Q_l) were measured on a 4-channel vector network analyzer (Agilent Technologies 5071C-ENA, USA). Full quality factors were measured by dividing the center frequency by the bandwidth measured at -7 dB [249, 253]. Calibration to a reference level of 0 dB attenuation was done using a short circuit.

6.3.2 Electromagnetic Field Simulations and Phantom Characteristics

To see whether there was a theoretical advantage to replacing the birdcage coil by a saddle coil with respect to transmit field homogeneity, electromagnetic field simulations were performed with the finite-difference time-domain (FDTD) based software Sim4Life 4.0.1 (ZMT AG, Switzerland). Birdcage models were based on the software-inherent BCAGE-module, with lumped elements located at identical positions as in the real coil design. An exact copy of the saddle coil, including introduction of capacitors due to segmentation, was designed in Solidworks 2017 (Dassault Systems, France) and imported to Sim4Life for simulation. Coaxial cables as well as cable traps were not included in the simulation. Simulations were conducted for loaded coils, containing the same 0.9 % saline phantom as for subsequent B_1^+ homogeneity MR experiments. The phantom was characterized by mass density ρ of 1004.6 kg/m³, relative permittivity ϵ_r of 49.85, with a cylindrical geometry of 15.7 mm inner diameter and 38 mm length. The phantom diameter was chosen to correspond to an adult rat thigh (ensemble of muscle, bone and fat). Simulated coil dimensions, angular alignment, capacitor positions and wire thickness were identical to their physical counterpart. RF coil segments and shield material were assumed to be perfect electric conductors, meaning that the intrinsic coil circuitry losses due to circuitry components and conductors were neglected. A resolution of 0.39 mm was chosen for saline phantom studies and for simulations. For the CEST experiments, the saline phantom was replaced by a 50 mM glycogen phantom (from bovine liver, Sigma-Aldrich) of the same dimension.

6.3.3 B_1^+ Homogeneity, Efficiency and Sensitivity at 14.1 T

Key performance indicators of both coils were then evaluated in an experimental context by choosing a phantom that mirrored the *in vivo* application of interest. The key assessment parameters were the transmit field homogeneity and efficiency as well as RF coil sensitivity over a large FOV.

SNR was calculated from the saline phantom data acquisition as $\text{SNR} = \langle S_{30^\circ} \rangle_{ROI} / \sigma(S_{0^\circ})$. $\langle S_{30^\circ} \rangle_{ROI}$ denotes the mean signal intensity obtained from a single slice GE image (TR / TE = 10000 / 2.6 ms, nominal excitation flip angle $\theta = 30^\circ$, FOV = 25 x 25 mm², data matrix = 64 x 64) over a cylindrical, central ROI of 11 mm diameter (ROI₁₁) and 2 mm

slice thickness. For an identical data matrix and FOV, $\sigma(S_{0^\circ})$ denotes the standard deviation over ROI₁₁ (containing 611 voxels) of a noise-only ($\sigma = 0^\circ$) acquisition. Gradient Echo (GE) imaging as well as the non-localized power calibration were conducted subsequent to B_0 shimming using the FAST(EST)MAP method [254, 255]. The measured SNR was corrected for the full coil FOV and number of channels: FOV correction was implemented by dividing the saddle coil SNR by the filling factor ratio between the two coils, thereby accounting for the different coil diameters. Furthermore, the birdcage driven in quadrature mode should provide an increased SNR by up to a factor of $\sqrt{2}$ (under perfect decoupling) as compared to single channel reception [117]. SNR was calculated for a single channel and normalized with respect to the saddle coil SNR.

Flip angle maps were acquired to allow for subsequent B_1^+ map calculation. The flip angle maps were computed using the double angle method, that is $\theta = \cos^{-1}(I_2/2I_1)$ [155, 156]. Two GE images with a nominal flip angle θ_1 and θ_2 yielded voxel-wise magnitude image intensities I_1 , respectively I_2 . The pulse sequence used Gaussian pulses, short echo time (TE) of 4.83 ms, θ_1 of 60° , 2 ms pulse duration, 128 x 128 data matrix, 25 x 25 mm² FOV and a slice thickness of 2 mm. A long repetition time (TR) of 20 s ensured that $TR > 5 \cdot T_{1,H_2O}$, thus eliminating T_1 -dependency on either flip angle map. Thresholding by zero-filling was applied to any voxel of signal intensity lower than 15 % of the maximal signal intensity in the image to eliminate regions containing only noise. B_1^+ maps were deduced from the flip angle maps using the voxel-wise calculation $B_1^+ = \theta / \gamma \tau \epsilon$, with the ¹H gyromagnetic ratio γ , the pulse duration τ and the normalized Gaussian pulse envelope correction factor ϵ of 0.413 .

B_1^+ **homogeneity** was evaluated with respect to the ROI-diameter and 2 different homogeneity metrics were used for quantification [256] (1) non-uniformity (NU) describing the ratio of standard deviation of B_1^+ to its mean, and (2) relative uniformity within 10 % deviation (RU), yielding the percentile number of voxels which deviate maximally by 10 % from the mean B_1^+ . In order to increase the robustness of the parameter RU, the mean B_1^+ was calculated as the average over 25 center voxels in the same axial slice.

The mean effective flip-angle θ over the excited slice was analyzed as a function of the axial slice position (parallel to \vec{B}_0). The nominal flip angle was calibrated to 30° in the center slice (position defined as 0 mm). A GE sequence with TR = 10 s, TE = 2.6 ms, FOV = 25 x 25 mm², matrix size = 32 x 32 and 2 mm slice thickness was used to acquire flip angle maps over 7 axial slices spanning 14 mm in total. Mean and standard deviation of voxel-wise flip-angles over an 11 mm diameter central ROI (147 voxels) were analyzed as a function of

slice position.

RF transmit field efficiency (B_1^+/\sqrt{P}) was evaluated by calibrating the input power P needed to generate a 90° flip angle in a given calibration volume. The input power (values as generated by the amplifier) was calibrated for localized (voxel size of $11.2 \times 11.2 \times 3 \text{ mm}^3$) and non-localized acquisitions (full coil FOV), using a STimulated Echo Acquisition Mode (STEAM) pulse sequence ($500 \mu\text{s}$ asymmetric 90° pulses, $\text{TE} = 2.8 \text{ ms}$, $\text{TR} = 4 \text{ s}$) [32, 257] and a single block pulse ($20 \mu\text{s}$ hard pulse), respectively. Non-localized acquisition data furthermore yielded B_1^+ maps. The comparison of transmit field efficiency using non-localized data was corrected for the full FOV of the coils to account for the higher power requirements to generate a 90° pulse in a bigger volume.

Temperature changes of the saline phantom and coil components were monitored upon high-power pulsing via four fibre optic temperature sensors (Neoptix, Canada) made out of ^1H MR-invisible PTFE Teflon to exclude excessive heating due to power deposition. These control measurements were conducted prior to *in vivo* experiments. Maximal realistic power conditions were achieved by using the maximally available transmit power of the 1 kW amplifier. A STEAM sequence generated high power pulsing during 15 minutes (TR of 4 s, τ of $500 \mu\text{s}$ each, voxel size = $5 \times 5 \times 5 \text{ mm}^3$).

6.3.4 Application of the Saddle Coil: *In Vivo* GlycoCEST Imaging

To confirm that the saddle coil would also yield satisfying results when used *in vivo* for a highly B_1^+ -sensitive sequence where furthermore selective pulsing is crucial, glycoCEST imaging of a rat thigh was conducted *in vivo*. The CEST sequence consisted of a train of Gaussian saturation pulses coupled to a segmented GE sequence for image acquisition [162, 163]. The modules of the used CEST pulse sequence are illustrated in Figure 6.3.

First, a 50 mM **glycogen phantom** ($\text{pH} = 7.16$, room temperature) was used to evaluate the saddle coil homogeneity upon CEST imaging by calculating a (voxel-wise) MTR asymmetry map according to Equation 3.20. Prior to performing MTR asymmetry calculations, B_0 and B_1 correction maps were applied on a voxel-wise basis: shifts in the water resonance frequency $w_{\text{H}_2\text{O}}$ due to local B_0 inhomogeneities were corrected for by referencing $w_{\text{H}_2\text{O}}$ to a B_0 map. Similarly, local discrepancies in nominal flip angles were accounted for by correcting the relative intensities using a B_1 reference map. MTR asymmetry maps were

calculated from the AUC over a frequency interval covered by the saturation pulse. Applying this method instead of using point-wise MTR values (at only one resonance frequency) was shown to smooth spatial metabolite distribution [125]. Performing such integration calculations accounts for several sources of line-broadening, namely (1) proton exchange-rates, (2) spin-spin relaxation times T_2 and (3) limited saturation pulse bandwidths. Therefore, a normalized integrated MTR asymmetry map was calculated, performing voxel-wise calculations of the MTR over offsets within $[1, 0.5]$ ppm (i.e. around the glycogen chemical shift). Acquisition was done with a nominal B_1^+ of $1.1 \mu\text{T}$, 6 s pre-saturation pulse train (206 pulses of 29 ms each) and a 540° flip angle α . The transmit offset was varied between -5 and +5 ppm around the water resonance frequency in 51 steps of 0.2 ppm, which were acquired in a randomized order. The sequence parameters were a $35 \times 35 \text{ mm}^2$ FOV, 64×64 matrix size, 20° nominal imaging flip angle. Linear centric k-space filling was used where central k-space lines were acquired prior to outer ones [258]. The mean and standard deviation over 25 center-voxels were calculated for the Z-spectra as well as the MTR asymmetry.

The *in vivo* rodent experiment was only conducted once phantom experiments yielded optimized sequence parameters (saturation duration t_s and nominal B_1^+) and distinct glycoCEST effect could be detected. Animal experiments were conducted according to federal and local ethical guidelines. The protocols were approved by the local regulatory body of the Canton de Vaud, Switzerland. In total, two female Wistar rats [259] were scanned, one using the saddle coil and one using the 16-leg birdcage coil (cf. Appendix C). The rat thigh of

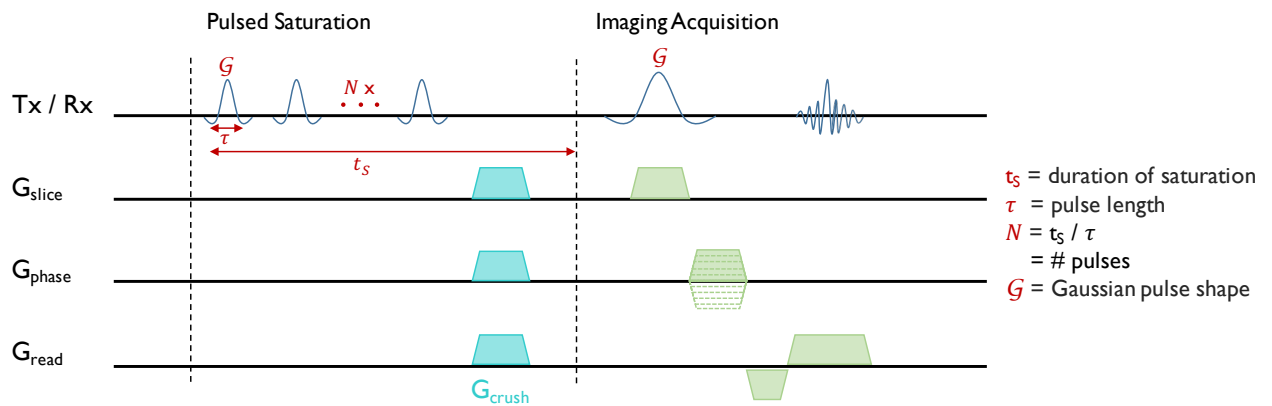


Figure 6.3: CEST pulse sequence consisting of 2 parts: (1) Pulsed saturation using a train of Gaussian pulses with $\alpha = 540^\circ$, $B_1 = 1.1 \mu\text{T}$, centric k-space filling, offset range $[-5; 5]$ ppm in 150 Hz steps acquired in randomized order and (2) Read-out with a segmented GE (Echo Train Length (ETL) = 4). The sequence was published [162] and programmed previously [163].

the first rat (250 g body weight) measured $12 \times 18 \text{ mm}^2$, therefore corresponding well to the phantom in size and loading. Anaesthesia was achieved with 1 - 2 % isoflurane in an air:O₂ (1:1) mix. The animal was positioned prone and head first. The body temperature was monitored via a rectal thermosensor and maintained at $38.0 \pm 0.5 \text{ }^\circ\text{C}$ via a water circulation tubing system for the duration of the experiment set-up and scan.

Muscular glycoCEST images of a rat thigh muscle were acquired with the sequence described above but with a FOV of $30 \times 30 \text{ mm}^2$, a matrix size of 32×64 , TR / TE = 16 ms / 1.91 ms and a saturation time of 10 s. The individual scans of the 53 saturation offsets between -7.5 and +7.5 ppm were acquired in a randomized order to avoid bias in saturation values in case of insufficient relaxation. Small reference samples of 50 mM glycogen and distilled H₂O were added in close proximity to the rat leg for controlling the sequence conduct. Finally, an *in vivo* structural image was acquired with the saddle coil using a fast spin-echo multi-slice (fSEMS) sequence with a 256×256 matrix size and TR / TE = 6000 ms / 40 ms, FOV of $30 \times 30 \text{ mm}^2$ and a single slice of 0.8 mm thickness.

6.4 Results

To ascertain satisfactory electronic coil properties, bench experiments were conducted yielding scattering parameters and the quality-factor (Q -factor) for the loaded coil. After having tuned the single saddle coil resonance and the 1st birdcage coil modes of each channel to 600 MHz, a matching of -37.1 dB for the saddle coil and -25.5 dB / -30.5 dB for the birdcage coil modes was achieved (Figure 6.4). The Q -factor ratio yielded $Q_{ul} / Q_l = 1.1$ and $Q_{ul} / Q_l = 2.7$ for birdcage and saddle coil, respectively.

To assess transmit and receive properties, SNR and transmit power were compared. After having added the corrections for number of channels and coil FOV - respectively loading - the saddle coil SNR measured in the 0.9 % saline phantom was about 20 % higher than the birdcage coil SNR (Table 6.1). To generate a nominal 90° flip angle, the saddle coil required 5 dB less RF power P than the birdcage coil for a localized STEAM acquisition and 6 dB less for a non-localized acquisition. The saddle coil was therefore found to yield higher receive sensitivity and higher transmit efficiency compared to the birdcage coil. Control experiments showed that high-power pulsing through the saddle coil increased the sample and RF components temperature by less than 0.5° C. The FOV-corrected RF transmit field efficiency for

non-localized acquisition (B_1^+/\sqrt{P}) was 54 % higher for the saddle coil than for the birdcage coil.

To gain a first insight into how the transmit fields of the coils compare, electromagnetic field simulations were conducted before proceeding to experimental data acquisition. Inside the center slice of the saline phantom, a higher transmit field homogeneity was found for the saddle coil than for the birdcage coil. This was the case for any central ROI diameter between 3.7 – 13.7 mm (statistics including 85 – 1137 voxels, cf. Figure 6.5). The non-uniformity of the saddle coil NU was 1.7 % for the largest analyzed $ROI_{13.7}$ (13.7 mm diameter) and no voxel deviated by more than 10% from the mean B_1^+ (relative uniformity $RU = 100$ %). The birdcage coil showed a $NU = 4.0$ % for the same $ROI_{13.7}$, with 4.6 % of all voxels subjected

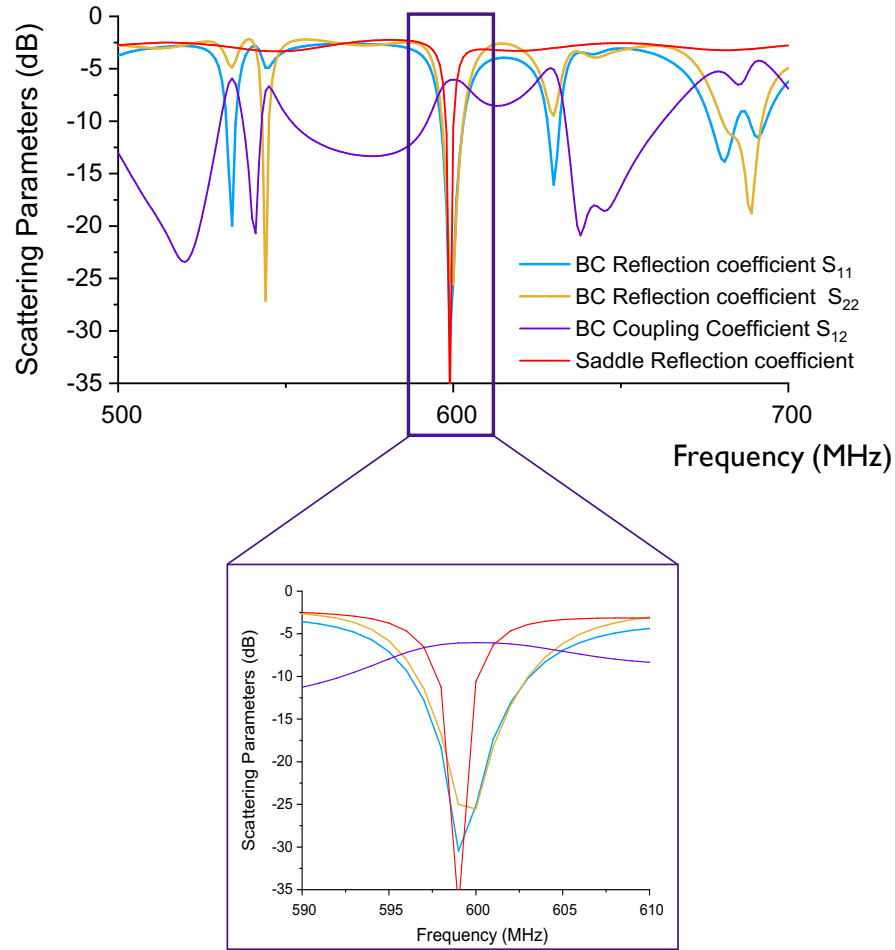


Figure 6.4: Scattering parameters for the loaded coils. Reflection and coupling coefficients show the different resonance modes. The latter only applies to the quadrature birdcage (BC) coil.

Table 6.1: Input and output parameters for coils loaded with the 0.9 % saline phantom. SNR values were normalized to the saddle coil SNR and corrected for the coil full FOV and number of channels. Statistics was done over a cylindrical ROI of 11 mm diameter and a thickness of 2 mm (single slice), which includes 611 voxels. The transmit power describes the system-specific amplifier output power needed to create a nominal 90° pulse for a localized and a non-localized acquisition scheme via $\tau = 500 \mu\text{s}$ asymmetric STEAM pulses and a $\tau = 20 \mu\text{s}$ hard pulse, respectively. Bench experimentation yielded Q -factor ratios for loaded coils.

	SNR, corrected	Transmit power, localized acquisition (dB)	Transmit power, non-localized acquisition (dB)	Q_{ul} / Q_l
Saddle coil	1 ± 0.1	58	23.5	2.7
8-leg BC coil	0.8 ± 0.1	63	29.5	1.1

to a B_1^+ that deviated by more than 10 % from the mean B_1^+ ($RU = 95.4 \%$). Homogeneity through several slices spanning 14 mm in total in axial direction (parallel to \vec{B}_0) indicated constant uniformity for both coils, whereas the saddle coil displayed a slightly higher uniformity with $NU = 1.0 \pm 0.1 \%$ vs. $NU = 2.7 \pm 0.1 \%$ for the birdcage coil (over ROI_{11} and spanning all slices in axial direction).

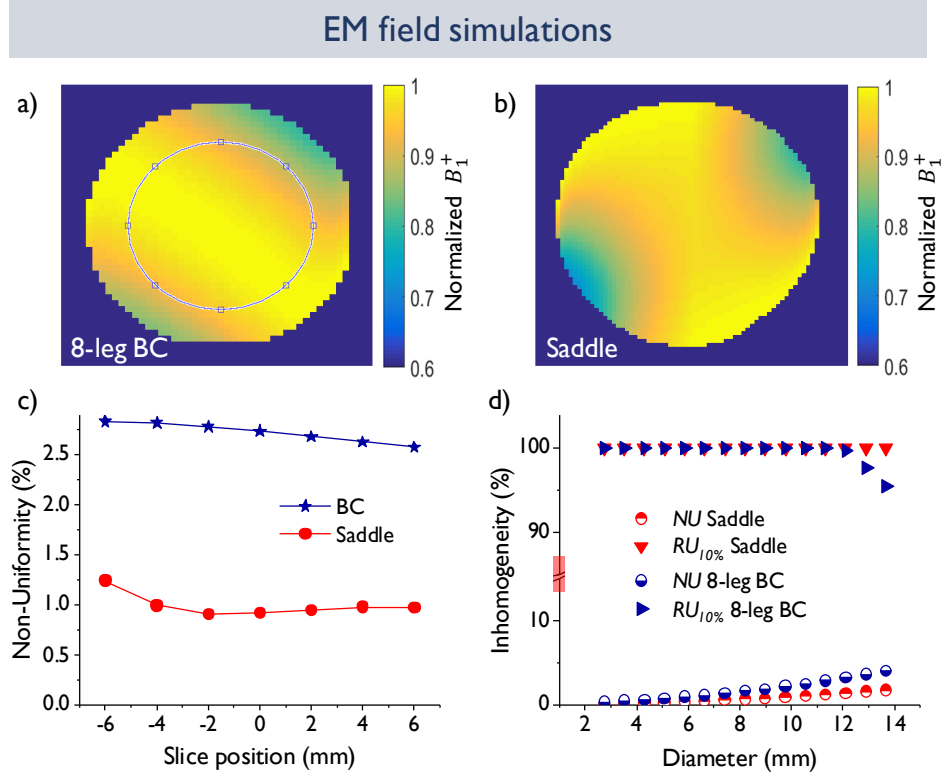


Figure 6.5: Simulated and normalized B_1^+ maps. B_1^+ maps from axial slices located in the central z-position (isocenter) generated by **a)** the 8-leg birdcage coil (BC) and **b)** the saddle coil. **c)** Dependence of NU on the slice distance from the isocenter. Statistics were calculated over an 11 mm diameter ROI (encircled in a), which is comparable to sizes required in rodent MR. **d)** NU and RU of the B_1^+ maps as a function of the ROI diameter. Note the cut of the y-axis.

To evaluate the transmit field generated by the custom-build coils, B_1^+ maps were acquired. A NU of 5.0 % and NU of 3.5 % were calculated for the saddle and the birdcage coil, respectively, in the same central ROI_{11} (Figure 6.6). Relative uniformity decreased compared to simulations to $RU = 91.1$ % and $RU = 97.7$ % for the saddle coil and the birdcage coil, respectively. The flip-angle dependency on the axial slice position showed a constant increase from $\theta|_{z=-6mm} = 20.4 \pm 1.0^\circ$ to $\theta|_{z=+6mm} = 33.6 \pm 1.1^\circ$ in an 11 mm diameter central ROI for the birdcage coil, for a flip angle calibrated to 30° in the center slice. The saddle coil

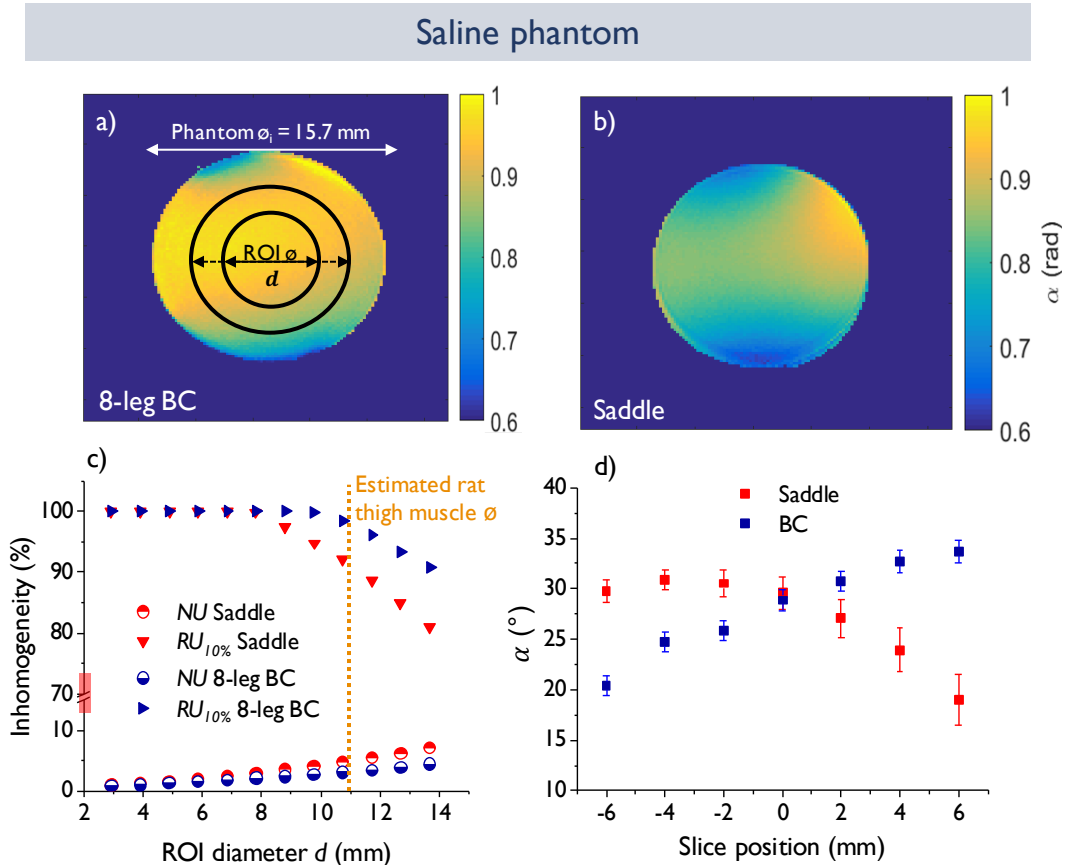


Figure 6.6: Normalized B_1^+ axial maps of a 10 ml 0.9 % saline phantom (inner diameter of 15.7 mm) generated by a **a)** 8-leg birdcage coil (BC) and **b)** saddle coil. B_1^+ maps were created using the double angle method. Circles illustrate ROI positioning chosen in c) for statistics. **c)** B_1^+ homogeneity was evaluated via RU and NU as a function of the ROI diameter. Note the cut of the y-axis. An estimated rat thigh muscle diameter is indicated as a reference for a 11 mm diameter **d)** Mean effective flip-angle θ over the excited slice as a function of the slice position in z-direction (parallel to \vec{B}_0) for a flip angle calibrated to 30° in the center slice (0 mm position). Error bars denote the standard deviation of the voxel-wise flip-angles over an 11 mm diameter central ROI (147 voxels). The scale is chosen such that the origin is in the isocenter and positive slice positions are in direction of the coil current source.

created constant flip angles over the first 4 slices in direction of the RF feed with $\theta|_{-6 < z < 0 \text{ mm}} = 30.2 \pm 0.6^\circ$ and only then gradually decreased to $\theta|_{z=+6 \text{ mm}} = 19.0 \pm 2.4^\circ$.

To assess the suitability of the saddle coil for an imaging method requiring highly homogenous transmit field as well as highly frequency selective pulsing, an *in vivo* glycoCEST experiment was conducted. The normalized MTR asymmetry maps of the glycogen phantom (Figure 6.7b) show a coefficient of variation of 5.2 % over ROI₁₁. The Z-spectrum and corresponding MTR asymmetries (mean values over 25 central voxels plotted in Figure 6.7a) displayed a standard deviation within the 25 voxels of < 1 % at any offset. The glycoCEST effect caused by the exchanging proton from the hydroxyl groups in glycogen was visible around 1 ppm. The MTR asymmetry map for the *in vivo* CEST image of a rat thigh showed the presence of glycogen over the whole rat thigh except for the bone (lower left corner in Figure 6.7c). Two resonance groups between [2.1, 1.7] ppm and [1, 0.5] ppm were visible from the MTR asymmetry of a single voxel in muscle (Figure 6.7d). This observation was representative for other voxels and the maximum MTR asymmetry over 12 voxel was 4.6 ± 1.2 % and 9.1 ± 1.2 % for the first and second resonance group (Figure 6.8).

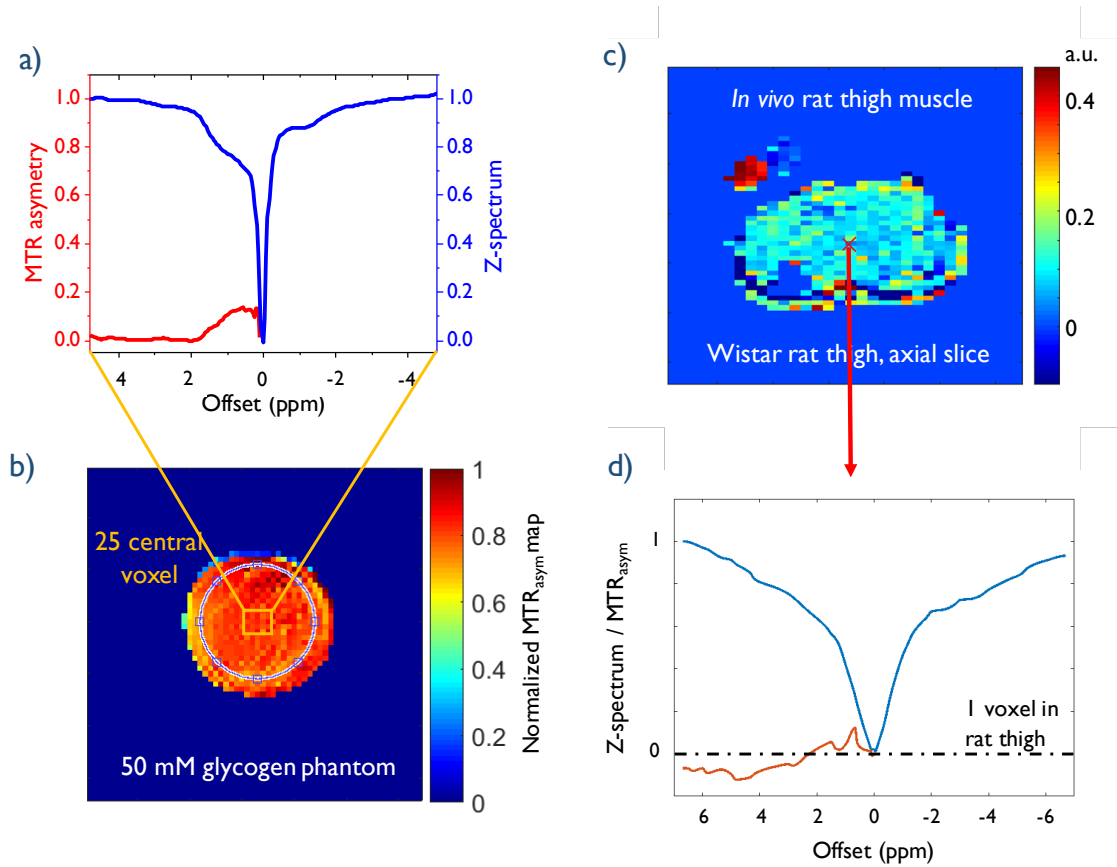


Figure 6.7: CEST imaging using a custom-made ^1H saddle coil. **a)** Normalized Z-spectrum (blue) and MTR asymmetry (red) spectra averaged over 25 central voxels (yellow square in b). **b)** Normalized MTR asymmetry map of the 50 mM glycogen phantom after magnetic field correction maps and voxel-wise summation of the MTR over $[1, 0.5]$ ppm, that is around the glycogen chemical shift. **c)** MTR asymmetry map of the muscle around the glycogen resonance $[1, 0.5]$ ppm with 2 reference samples: 50 mM glycogen and water. **d)** Normalized Z-spectrum and MTR asymmetry of 1 central voxel in muscle.

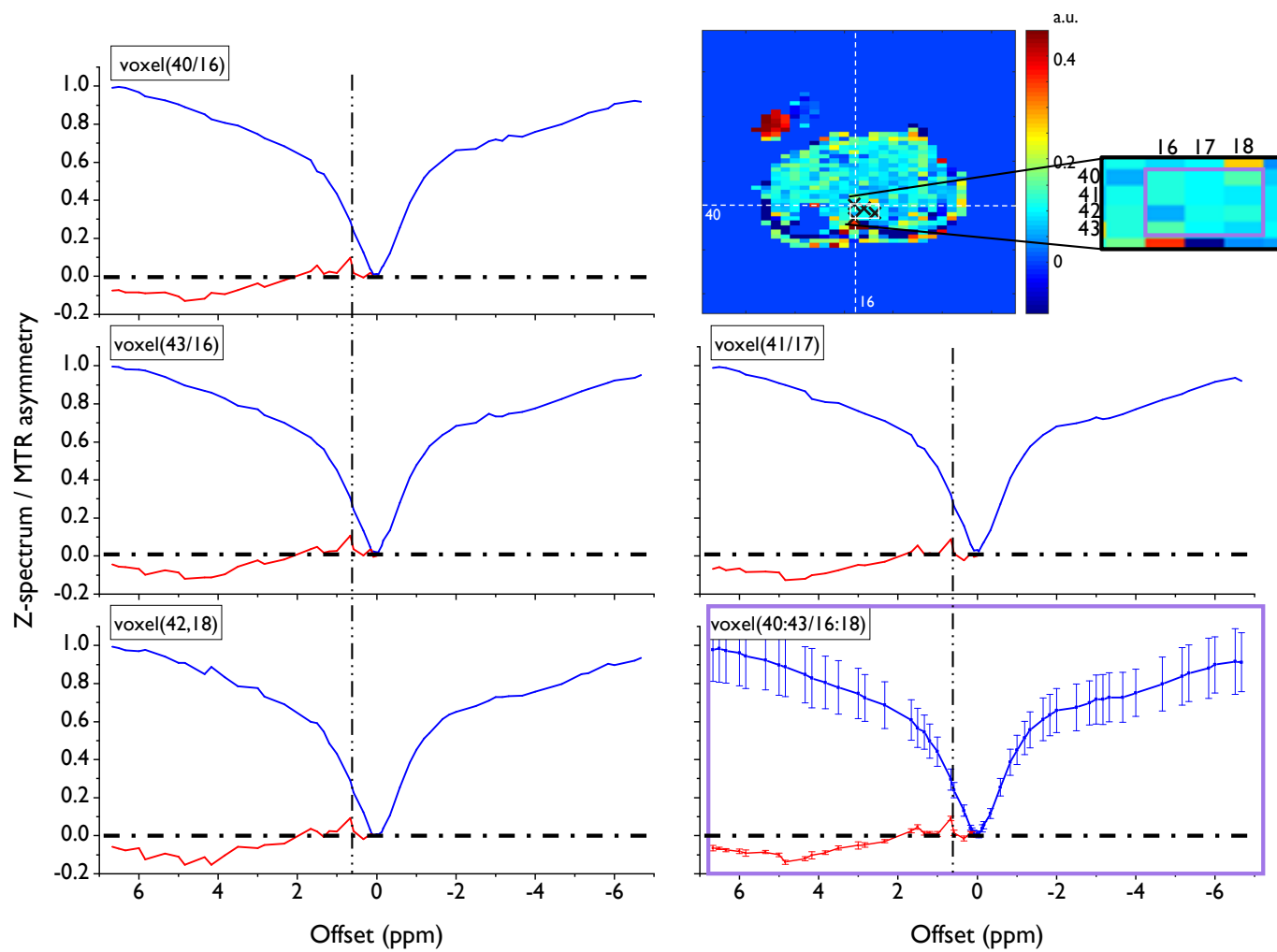


Figure 6.8: GlycoCEST map acquired from an *in vivo* rat thigh. Z-spectra and MTR asymmetry of four different voxel in muscle with mean and standard deviation over 12 voxel (**bottom right**). Vertical line at offset of glycoCEST resonance to guide the eye.

The confirmation experiment displayed a flat MTR asymmetry curve of voxels within the water phantom, confirming that no erroneous CEST effect was observed in the absence of exchanging metabolite protons. Furthermore, the 50 mM glycogen phantom used as reference in the *in vivo* experiment exhibited strong CEST effect at the expected resonance around 1 ppm (Figure 6.9).

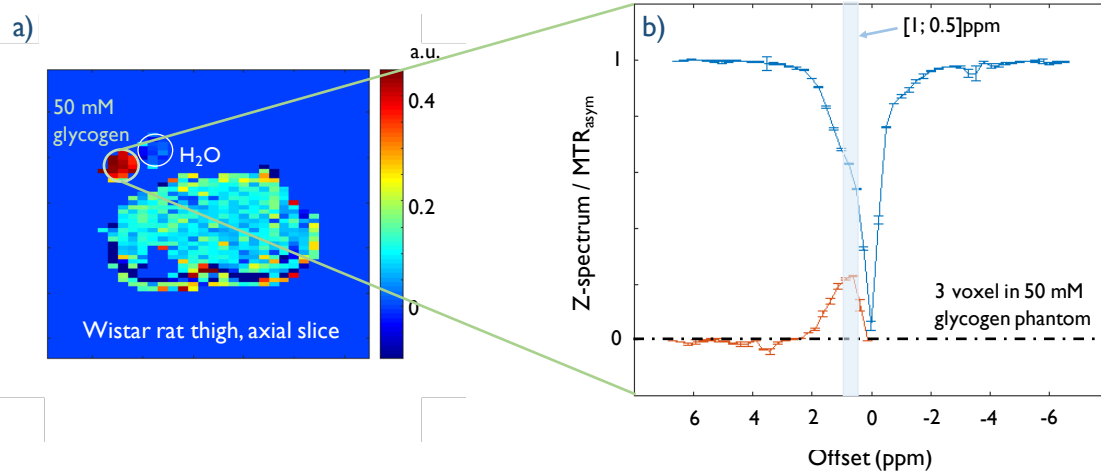


Figure 6.9: GlycoCEST control samples scanned concurrently with *in vivo* glycoCEST imaging (a). The two control samples (i) distilled H₂O and (ii) 50 mM glycogen from bovine liver were scanned next to the rat thigh to acquire glycoCEST reference scans. b) Mean and standard deviation of Z-spectrum and MTR_{asym} within the 50 mM glycogen phantom. A strong MTR asymmetry signal around 1 ppm was observed.

6.5 Discussion

This study showed that a single channel ¹H saddle coil can be an advantageous choice compared to an 8-leg ¹H quadrature birdcage coil in the context of MRI and MRS studies at 14.1 T. The saddle coil provided 20 % higher SNR, along with 54 % higher B_1^+ efficiency in a 190 mm³ VOI without suffering substantial loss in transmit field homogeneity compared to the 8-leg birdcage coil. These gains can benefit for example CEST imaging, especially if the solutes resonate close to the water frequency, as is the case for glycogen. This was illustrated above by glycoCEST imaging of a rat thigh muscle.

Electromagnetic field simulations demonstrated higher transmit field homogeneity for saddle coils (1) over central ROIs of various diameters and (2) over slices extended in axial

direction. Slightly asymmetric excitation patterns were observed for the saddle coil, as well as the birdcage coil in the transverse plane (Figure 6.6). Asymmetry effect of the birdcage coil displaying similar patterns have been reported in previous publications [260]. Those patterns identify areas of intrinsically reduced field homogeneity compared to a central ROI.

Transmit field patterns of phantom measurements were in qualitative agreement with simulations. They moreover confirmed good homogeneity over the investigated regions. The birdcage coil driven in quadrature mode, which is known to increase B_1^+ homogeneity [33, 261], yielded more homogeneous B_1^+ field maps than the saddle coil, unlike data obtained from simulations. Simulations deviated from empirical results in terms of their assumption of perfect angular symmetry, ideal current distribution throughout the rungs, no RF losses and balanced segmenting capacitors. Moreover, the saddle coil had to be segmented by chip capacitors of slightly different nominal values (2.2 pF vs. 1.8 pF, see Figure 6.2) to achieve tuning to 600 MHz. Such a compliance issue with manufacturer standards was not an issue in simulations. This unbalanced capacitor distribution entailed an asymmetric current distribution, therefore contributing to B_1^+ inhomogeneity.

A dielectric resonator design might yield even better B_1^+ homogeneity compared to a saddle coil [34]. Even though the study of Neuberger et al. (2008) was equally conducted at 600 MHz, their evaluated ROI was considerably smaller (with a 2 mm diameter and 5 mm long) [34]. It is therefore not straightforward to project their results to small-animal anatomy applications which require a considerable space availability within the coil. Yet, it is interesting to note that both, the dielectric resonator design and the saddle coil, profit from their simple design and small number of RF components when used in ultra-high field.

The corrected SNR indicated a better performance of the saddle coil in RX mode. This was also reflected in the 2.5x higher Q -factor ratio for the saddle coil ($Q_{ul} / Q_l = 2.7$). The ratio Q_{ul} / Q_l of 1.1 for the high-pass birdcage coil was consistent with previous publications [262]. It should be noted that decoupling between the two channels was -8.5 dB. The consideration that driving the birdcage coil in quadrature mode increases the SNR by a full factor of $\sqrt{2}$ (which was assumed for the SNR correction) was therefore a slight overestimation. However, the use of quadrature detection or decoupling are merely secondary factors contributing to the SNR unlike, for example, the filling or quality factors which play a primary role [31]. This was also reflected in the SNR obtained by the 16-leg birdcage coil (cf. Table C.2), which was not significantly different ($\mathcal{O}(10\ %)$) from the 8-leg birdcage coil SNR despite a much better decoupling of -20 dB [247].

The consistent power difference of 5 dB and 6 dB needed to generate a nominal 90° flip angle for both, localized and non-localized excitation indicated that the birdcage coil required about four times as much transmit power as the saddle coil. Even though the input power was subjected to losses between amplifier output and the coil, these losses were equivalent for both coils since the same RF chain was used. Those losses did therefore not bias the result. Both coils were mid-range coils, defined as diameter · frequency $\in [2 - 30]$ MHz·m [263], such that besides the sample, especially RF-components represented considerable sources of power loss [35, 264]. That losses were coil-dominated was also seen in the birdcage coil quality factor, where Q_{ul} was a mere 10 % higher than Q_l . The lower number of RF components on the saddle coil entailed that less power was dissipated in the lumped components. Furthermore, saddle coils do not necessitate shielding, whereas birdcage coils require shielding to reduce interaction between the RF coil and the scanner environment. Shielding adds conductive material (in the far field) such that the B_1^+ field suffers some inductive loss through energy dissipation in the shield. Shielding was shown to decrease B_1^+ amplitude as well as B_1^+ homogeneity [116]. To conclude, the saddle coil was also found to yield higher SNR as well as higher coil efficiency than the birdcage coil, which confirms the coherence of the experimental results according to the principle of reciprocity [31]. Hence, the saddle coil had also an advantage over the birdcage coil in TX mode. The saddle coil's high B_1^+ efficiency entails interesting advantages for MRS: High transmit field efficiency, providing the possibility to generate higher B_1^+ values with the same RF input power, enables the use of shorter pulses with larger bandwidth and/or a better pulse response profile for a given flip angle and it opens the way for short-TE MRS. In this respect, the saddle coil yields a considerable advantage for spectroscopic studies and whenever power limitations are encountered.

The saddle coil was successfully used to perform glycoCEST measurements despite the challenging proximity of the glycogen resonance to the water resonance. This demonstrated the capacity of the saddle coil to generate selective pulse profiles. Simultaneously, the resulting MTR asymmetry maps displayed highly homogeneous excitation over an axial slice. The two resonance groups observed in muscle at [2.1, 1.7] ppm and [1, 0.5] ppm, respectively, were allocated to the creatine amide resonance and the glycogen hydroxyl group and were found to be comparable to results reported in a previous study [163]. The observation of these peaks across the skeletal muscle as well as the small standard deviation of the MTR asymmetry further confirmed the consistency in the resulting glycoCEST map. *In vivo* imaging of the rat thigh muscle demonstrated the qualities of the saddle coil for small-animal imaging at ultra-high field in terms of image homogeneity. The good transmit field homo-

geneity together with the high transmit field efficiency encourages the use of saddle coils for *in vivo* experiments at ultra-high field, especially considering the facilitated positioning of the animal. A comparison of a 16-leg birdcage coil and the saddle coil for *in vivo* glycoCEST is illustrated in the appendix (Figure C.5).

Even though the 50 mM glycogen reference sample was convenient for confirming the seamless functioning of the acquisition-processing pipeline, it could not be used to directly determine the glycogen concentration in the muscle. Such a referenced quantification of the CEST effect was not possible since molecular environment, pH, temperature, proton exchange rates, etc. differ in the phantom and in muscle. One of the limitations becoming apparent from Figure 6.9 - apart from the lacking possibility of metabolite quantification, as is common - was a limited specificity. No significant regional variations in glycogen content were observed. Yet, based on tissue analysis, glycogen content in rat skeletal muscle was reported to differ considerably between anatomical regions [265]. Even though the trend was less pronounced, similar muscle fibre dependent glycogen storage was observed for human glycoCEST at 3 T (using 0 - 2 ppm AUC), indicating lower glycogen abundance in the soleus and higher abundance in the gastrocnemius [153].

Transmit field inhomogeneity also causes non-uniform electric field distribution. Such a non-uniformity entails locally increased (tissue) heating [266]. In extreme cases, local "hotspots" of high RF power deposition can emerge and eventually lead to tissue damage. Electromagnetic field simulations can provide information on the generated electric field. Yet, despite the growth of the specific absorption rate with B_0^2 , power deposition is not commonly evaluated for pre-clinical studies even at ultra-high magnetic field and MR safety protocols that define limitations on specific absorption rates (W/kg) are mainly destined for scan protocols involving human subjects [267]. Nevertheless, high local energy deposition can entail chemical and physical reactions, for instance causing resonance shifts in the sub-ppm range¹. Local hotspots are directly related to an increased risk of injury [270] so that reducing strong local gradients in pH or temperature, for instance, contributes to ensuring physiological stability. In general, improving a coil's transmit field inhomogeneity contributes to more reliable results in temperature-sensitive studies. An ideal coil design uses the RF power as efficiently as possible to convert it into magnetic energy for homogeneous RF excitation over the ROI.

¹The reported ¹H chemical shift dependence on temperature was found to be rather small with -0.01 ppm / K, allocated to the degree of excitation of hydrogen-bond-stretching vibrational modes [268, 269].

Last but not least, the inherently open and accessible design of the saddle coil allowed for easier handling of the animal. A further practical aspect related to the structural simplicity of the saddle coil concerned the fine tuning and matching. While this manual adjustment was not trivial for the birdcage coil due to coupling, multi-modal resonance spectra and splitting of degenerate modes, it was all the more straightforward in the case of a single-resonance saddle coil, which allowed for a higher degree of robustness throughout the measurements. While the birdcage coil provided overall more mechanical stability, the saddle coil fulfilled the sturdiness requirements imposed by the phantom and *in vivo* experiments.

6.6 Conclusion and Outlook

To conclude the present study, the presented saddle coil design can be beneficial regarding several aspects. Practically speaking, its inherently open design facilitated the general positioning of the animal and experimental set-up. It could more easily be built to tightly fit the region of interest and displayed higher SNR and Q -factor values than the birdcage coil. Since acquisition time increases with the square of SNR, the increased sensitivity of the saddle coil with respect to the birdcage coil offers opportunities for accelerating dynamic MRI or MRS studies, for which speed is pivotal. Combining these qualities with the higher saddle coil transmit field efficiency entails a major advantage for studies where MRI experiments are conducted conjointly with MRS acquisitions. The general performance of the saddle coil upon glycoCEST imaging, which relies not only on a homogeneous transmit field but also on highly frequency selective pulsing, was an encouraging example for its application. Conclusively, the saddle coil can be considered an interesting alternative to the birdcage coil at ultra-high field, especially for applications where short-TE ^1H -spectroscopy is combined with imaging techniques and increased pulse bandwidth and high transmit field homogeneity are needed.

Chapter 7

Conclusion, Perspectives, Outlook

7.1 Increasing Nuclear Polarization via Microwave Frequency Modulation

In this study, the method of microwave frequency modulation studied on a system of xenon spins embedded in different doped solvents, revealed a direct relationship between the electron spin lattice relaxation rate and an increase in ^{129}Xe polarization levels. The increase in xenon polarization achieved, is a step towards using a dissolution DNP polarizer for conducting solid state, *in vitro* or *in vivo* studies with hyperpolarized ^{129}Xe in the future. Overall, the encouraging results obtained from this study therefore motivated the application of this method to hyperpolarizing ^{13}C nuclei for cardiac MRS (chapter 5), with a positive impact on polarization levels.

The conclusions drawn from this study point towards the promising effects linked to modulating the microwave frequency for a vast range of future applications. For instance, dipolar coupling increases with the radical concentration (Equation 2.18), resulting in facilitated spreading of polarization across the ESR spectrum [271]. For a higher amount of electron spins involved in the polarization transfer, more nuclear spins in their vicinity can undergo direct triple spin flips with electron spins instead of relying on the extremely short-range nuclear-spin diffusion. Efficient DNP therefore relies on sufficiently high radical concentrations. However, depending on the sample composition, limiting solubility thresholds may exist. Samples with a sub-optimal amount of free radicals entail longer polarization times and often times lower achievable solid-state polarization. Theoretically, microwave frequency modulation represents a possible solution to counteract these drawbacks originating from higher radical concentrations by promoting electronic spectral spin diffusion owing to its equivalence to stronger electron dipolar coupling. An experimental indication supporting this is the 77 % increase in polarization achieved by frequency modulation for 60 mM of the ultra-narrow linewidth radical SA-BDPA, while no positive effect was observed at 120 mM SA-BDPA [184].

The method of microwave frequency modulation has the potential of increasing nuclear polarization without entailing any drawbacks and can especially be expected for large-linewidth radicals, for radicals with a short spin-lattice relaxation time T_{1S} , at high magnetic field, in case of ESR line over-saturation, for sub-optimal radical concentrations or when inefficient spin diffusion is encountered. Microwave frequency modulation is therefore a most versatile tool, beneficial to a broad range of nuclei, radicals and applications.

7.2 High ^{13}C Polarization for *in vivo* dDNP using Non-persistent Radical Precursors

To conclude, two novel endogenous radical precursors, namely αkV and αkB , were found. They generated a sufficiently high concentration of radicals ($> 50 \text{ mM}$) to be used in dDNP samples. The study therefore extended the method of radical-free dDNP to a sample containing only endogenously-occurring substances. Not only did they yield similar or higher ^{13}C polarization compared to using PA, but they were also successfully used to perform *in vivo* cardiac MRS, allowing for the detection of a wide range of metabolites. Using microwave frequency modulation, they hyperpolarized glucose up to 17 % and butyrate up to 13 %. This study yielded exciting results for the novel radical precursors and a few follow-up studies are suggested here.

While past studies motivated our interest in the α -keto acids αkV and αkB as potential radical precursors, it was not our aim to study their impact on *in vivo* cardiac metabolism. For their future use *in vivo*, it is necessary to more fully understand the pathways of and the enzyme affinities for αkV and αkB . Contrarily, metabolization of their molecular analogue PA is better understood. PA crosses from the blood into the cytoplasm through Monoarboxylate Transporters (MCT) and it is then transported into the mitochondrion through Mitochondrial Pyruvate Carriers (MPC) located inside the inner membrane, where it is metabolized by PDH. PDH-affinity experiments for αkB [221] were merely done *in vitro*, using soluble PDH and mitochondria. Therefore, experiments in biological systems have not been conducted to date so that there is no prior knowledge of whether MCT facilitates passive transport of αkV or αkB . A metabolism-focussed study design would be needed to determine how the three α -keto acids are metabolized and to assess their respective advantages for monitoring *in vivo* cardiac metabolism. It should also be noted that while glycerol may be an excellent glassing agent [195] and safe to use *in vivo*, it is also rapidly metabolized [272, 273]. As an alternative, trehalose was recently suggested as a metabolically-inert (upon IV-injection) substitute for glycerol to create a glassy matrix [190]. Exchanging glycerol for trehalose could potentially help to avoid injecting a non-inert glassing agent when investigating the effect of αkV and αkB on metabolism.

Another suggestion for a future study focus arose from observations related to structural stability of the beads upon UV-irradiation. Deviations from a glycerol: H_2O 1:1 (v/v) ratio resulted in pulverized beads mid-irradiation. This prevented reproducibility due to the bead-

size dependency of the radical generation rate, rendering the sample composition useless. The bead stability under UV-irradiation was found to deteriorate for lower glycerol concentrations. Interestingly, a recent study found that 20 % (vol) of trehalose generated higher polarization with a shorter build-up time than a corresponding sample with 60 % glycerol [190]. If the resistance of trehalose-based beads to long UV-irradiation is enhanced with respect to glycerol-based beads, then previous studies suggest that this would likely allow for a decrease of the glassing agent concentration, probably impacting the overall bead opacity and therefore the radical generation efficiency. It would be interesting to investigate the consistency of trehalose-based beads and the potential impact on precursor concentrations.

Further consideration could be given to a systematic optimization of concentration ratios and the UV-irradiation time versus bead size relationship. However, optimizing the sample matrix for minimal precursor concentrations does not necessarily result in maximal polarization and vice versa. Depending on the application, either one of the criteria should be fixed as primary aim. Overall, DNP using persistent radicals has profited from over a decade of research investigating sample compositions to steadily increase substrate polarization. One of the most efficient polarizing agents singled out during this process are trityls, narrow line-width radicals enabling impressive polarization levels. The glucose and butyrate polarization levels obtained in this study are being compared to studies that benefit from the choice of a polarizing agent which is *a priori* known to be excellent (cf. table 5.6). The fact that polarization levels obtained with the new α -keto precursors are approaching the range of state-of-the-art research on persistent radicals, in spite of lacking comprehensive sample (preparation) optimization, is encouraging.

7.3 Perspectives of a Versatile Coil Design

This study allowed to tackle the problem of power limitations encountered upon large flip angle pulsing in studies using the birdcage coil. The research led to the conclusion that the saddle coil yielded higher SNR and transmit field efficiency (*after* correcting for the different coil diameters) than the birdcage coil, with a nonetheless homogenous transmit field over a large ROI. Furthermore, a higher flip angle consistency was found over a thick slice (in axial direction) compared to the birdcage coil. The saddle coil can be considered an interesting alternative to the birdcage coil at ultra-high field, owing to a homogeneous transmit field and high sensitivity. It might particularly be beneficial for applications where short-TE ^1H -

spectroscopy is combined with imaging techniques and increased pulse bandwidth and high transmit field homogeneity are needed.

A concrete proposition for improved transmit field homogeneity concerns the coil design: Our saddle coil geometry resulted in a low length-to-diameter ratio l/d of 0.65 since it was tailored to image a rat thigh. Optimal B_1^+ homogeneity being achieved for l/d of 2 [113], such a low l/d ratio entails reduced homogeneity. In fact, calculations conducted by Bonetto et al. (2006) suggest that highest field homogeneity for a geometry characterized by $l/d = 0.65$ is achieved for an angular aperture α of $1.3537\pi/3 = 161^\circ$ [274]. This value differs notably from the chosen $\alpha = 120^\circ$. Future saddle coil designs can take this easily into account without complicating coil construction or being encumbering during the experimental set-up. By further customizing the saddle coil's angular aperture according to the application of interest, transmit field homogeneity improvements are likely possible beyond current results.

A suggested continuation of the work presented is the use of the ^1H saddle coil in MRS studies to quantify CEST metabolite maps. Furthermore, determination of the concentration limit for detectable lactate or glycogen CEST effect allows for moving towards *in vivo* metabolism studies. Now that an ultra-high field RF coil was thoroughly studied with promising NMR performance regarding several key parameters evaluated over a 190 mm^3 ROI, the rest of the pipeline can be optimized (data acquisition and post-processing for CEST). If the method can be refined sufficiently to detect concentrations down to a few mM, many possibilities for metabolic studies in the *in vivo* brain open up. Further developments include the following approaches. Applying 90° or 180° saturation pulses are expected to lead to more optimal saturation compared to the currently used 540° RF pulse, due to RF spill-over effect of DS [275]. Further, previously published results indicate that replacing the currently-used B_0 -correction scheme (B_0 -map created from dual-echoes due to TE differences) by WASSR [153], higher-order polynomial fitting [126] or Lorentzian fitting [149] is likely to yield more consistent results if dense sampling around the water frequency is applied [125]. WASSR is of particular use for solutes resonating close to the water resonance frequency, as is the case in glycoCEST. In this case, the Lorentzian CEST agent lineshape overlaps the direct water saturation, causing asymmetric broadening of the DS lineshape and unreliable w_0 calculations. WASSR uses short saturation times and small B_1 amplitudes, rendering contributions from CEST and MTC effect negligible, so that the Z-spectrum is governed by DS. The symmetry of the DS lineshape allows for a direct determination of w_0 with a sub-hertz accuracy on a voxel-wise basis [73]. Finally, disentangling the Z-spectrum architecture by modelling the system through simulations of the Bloch-McConnell equations or implementing corrections for

parasite contributions improves the sensitivity and accuracy of the CEST method. Further, accelerated CEST MRI would allow for dynamic imaging [140, 141, 276]. These suggestions only scratch the surface of the optimizations possible in CEST imaging. The vast amount of saturation patterns, imaging sequences and post-processing-correction approaches, which cater to the needs of the specific application, emphasize the potential for continuous work.

7.4 Overall Conclusion and Outlook of the Thesis

This thesis has provided solutions to enhance the NMR sensitivity of X-nuclei by using novel methods and studying underlying mechanisms, by deepening the knowledge of existing solutions and by contributing to advancing the field of DNP. Ideal experimental conditions to be able to capitalize maximally on the method of modulating the microwave frequency have been formulated. This was first demonstrated on the example of a ^{129}Xe DNP matrix, where nuclear polarization was increased by up to 220 %. The application of the frequency modulation method was then extended to other X-nuclei. Namely, it was applied to samples containing the novel non-persistent radical precursors αkV and αkB , thereby enhancing ^{13}C -labelled butyrate and glucose polarization levels in samples containing purely endogenous components. Those novel DNP radical precursors were found to be promising for translational DNP due to their efficiency as polarizing agents and their chemical shifts, which allowed for the detection of a wide range of downstream metabolites. In parallel to these results, a practical solution was found to obtain high sensitivity upon ^1H MR scans while simultaneously maximizing transmit field homogeneity and efficiency. The deepened knowledge of how existing RF coil designs compare at ultra-high field was used to propose a custom-designed solution to small-animal MRI studies at ultra-high magnetic field. The detailed characterization of the versatile saddle coil facilitates the choice of the coil design for future pre-clinical MR studies at ultra-high magnetic field.

Overall, the methodological developments have contributed to advancing and improving existing approaches in the fields of DNP and MRI. The identified advantages and drawbacks of two coil designs allow for a more complete picture. The methodological implementations and novel DNP samples worked towards facilitating translational DNP and increasing its efficiency. A natural continuation of the work consists of applying the developed strategies.

Appendix A

Hyperpolarizing ^{129}Xe matrices

Contribution

Contributions as declared in chapter [4](#).

A.1 ESR Spectra and T_{1S}

The T_{1S} of TEMPO in a protonated matrix of EtOH were found to be slightly shorter than in the deuterated matrix of EtOH- d_6 (Figure A.2, Table 4.1), in correspondence with results published previously [186]. A T_{1S} of TEMPO in a glass of protonated and deuterated ethanol was reported to be 80 ms and 140 ms, respectively, at 5 K and X-band (0.335 T) [72, 186]. However, T_{1S} increased exponentially with decreasing temperatures in the range between 5 – 80 K [72].

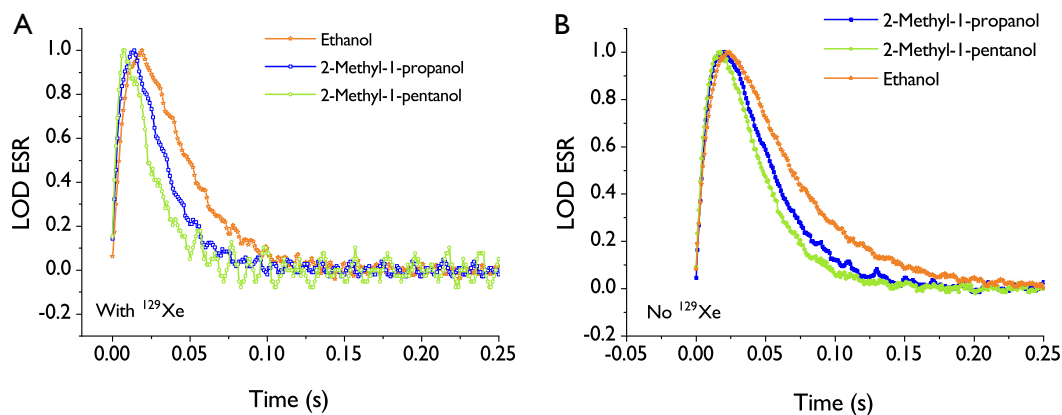


Figure A.1: Solvent-dependent LOD ESR with (A) and without (B) ^{129}Xe for protonated solvents.

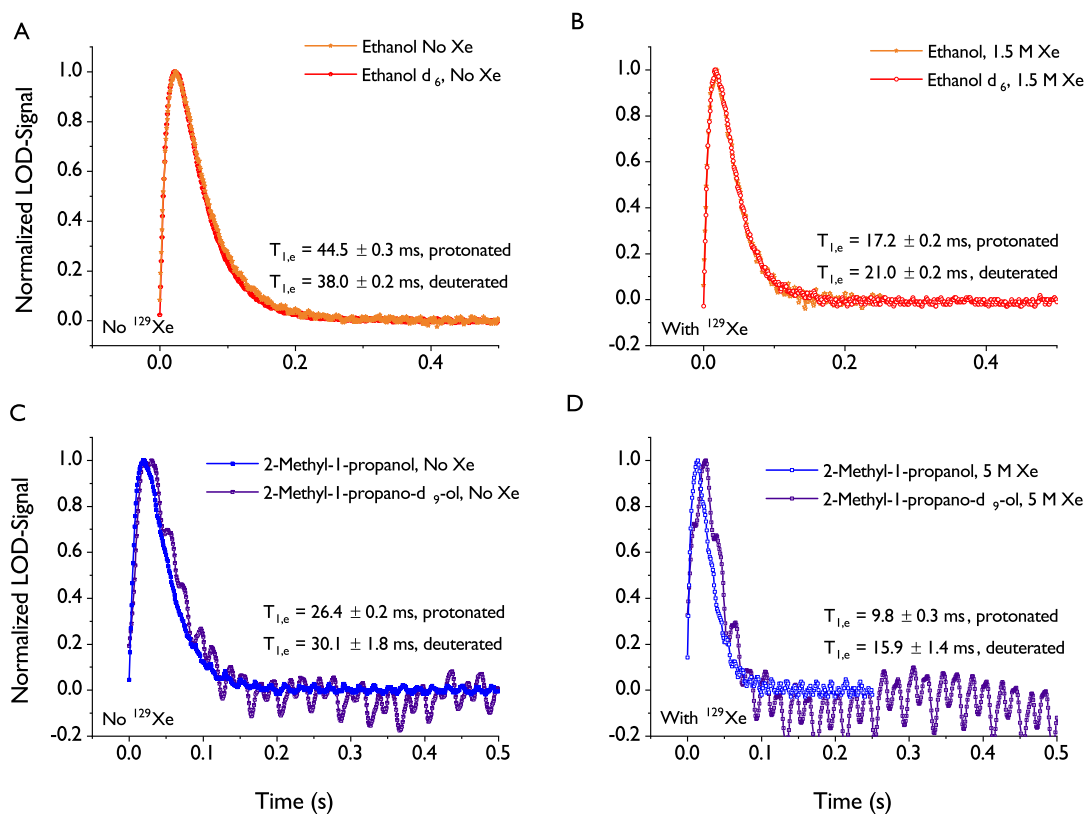


Figure A.2: Electron relaxation rates in protonated and deuterated matrices in the absence (A, C) and presence (B, D) of xenon.

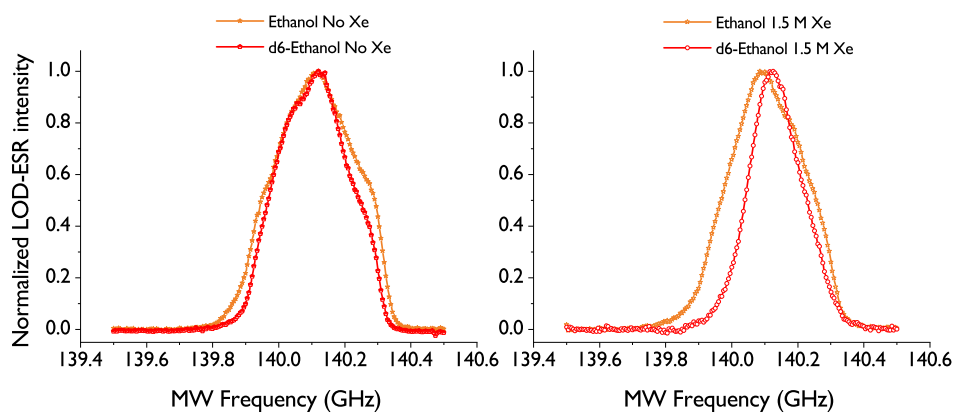


Figure A.3: ESR spectra for a radical embedded in a protonated versus deuterated ethanol solvent, with and without the addition of xenon to the matrix.

A.2 DNP Maxima and Frequency Modulation Parameters

The build-up times increases for microwave irradiation at the wings of the frequency sweep. In this region, DNP build-ups did therefore not reach the same proximity to their plateau values as build-ups close to the ideal irradiation frequencies. This phenomenon lead to an inaccurate narrowing of the resulting frequency sweep, thereby underlying the importance of planning sufficiently long sweeping steps, especially at low temperature. The optimal irradiation frequency depended on the amplitude of the modulation and generating a calibration curve for the modulation amplitude required individual sweeps (for optimal irradiation frequency determination) prior to the calibration. The polarization enhancement caused by modulation of the microwave frequency was increased for the positive DNP due to the ESR-line asymmetry of TEMPO. The steep slope of the ESR line at the negative DNP was more easily saturated. Therefore, monochromatic beams saturated a more substantial part of the ESR line if applied at the negative DNP maximum compared to the positive DNP maximum (Figure A.4).

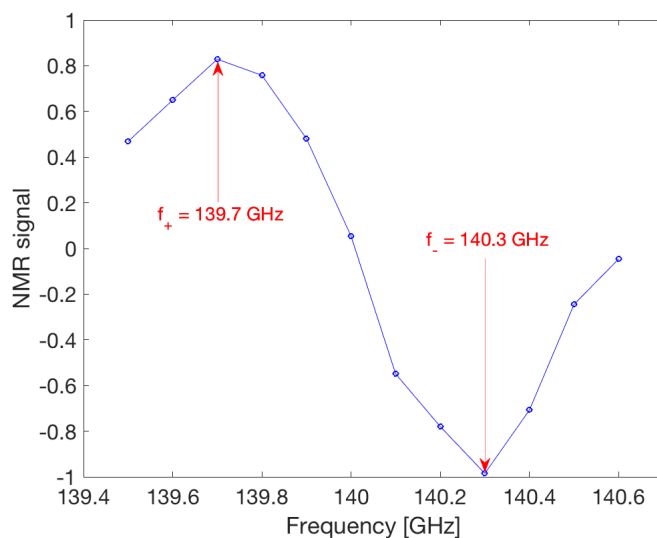


Figure A.4: Asymmetry of positive and negative DNP maxima in the frequency sweep with mono-chromatic microwave frequency. The NMR signal was normalized to the negative DNP maximum at 140.3 GHz, which showed $\sim 20\%$ higher absolute polarization values at 4.2 K compared to the positive DNP maximum at 139.7 GHz. A 5 M xenon in 2-methyl-1-propanol matrix doped with 50 mM TEMPO was used.

Consequently, the polychromatic nature of microwave modulated beams affected the polarization build-up at the positive DNP stronger (Figure A.6), therefore producing higher enhancement effects than at the negative DNP (Figure A.5).

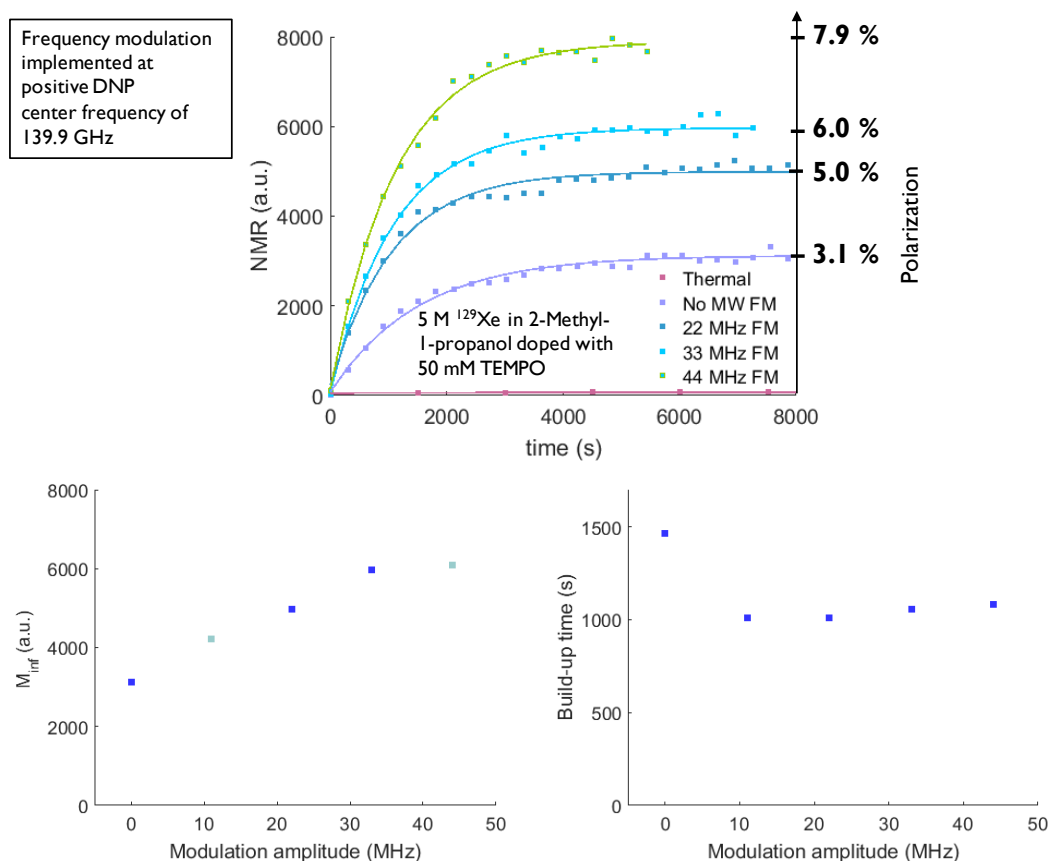


Figure A.5: Modulation amplitude calibration for increasing amplitudes between 7 MHz and 86 MHz conducted on a matrix of 5 M xenon in 2-methyl-1-propanol doped with 50 mM TEMPO. Frequency modulation was implemented around the positive DNP peak, center frequency set to 139.9 GHz. For the sake of clear visibility, the build-up curves (**top**) for 11 MHz and 44 MHz are not shown but their respective build-up times and maximal magnetization (M_{inf}) are shown (**bottom**).

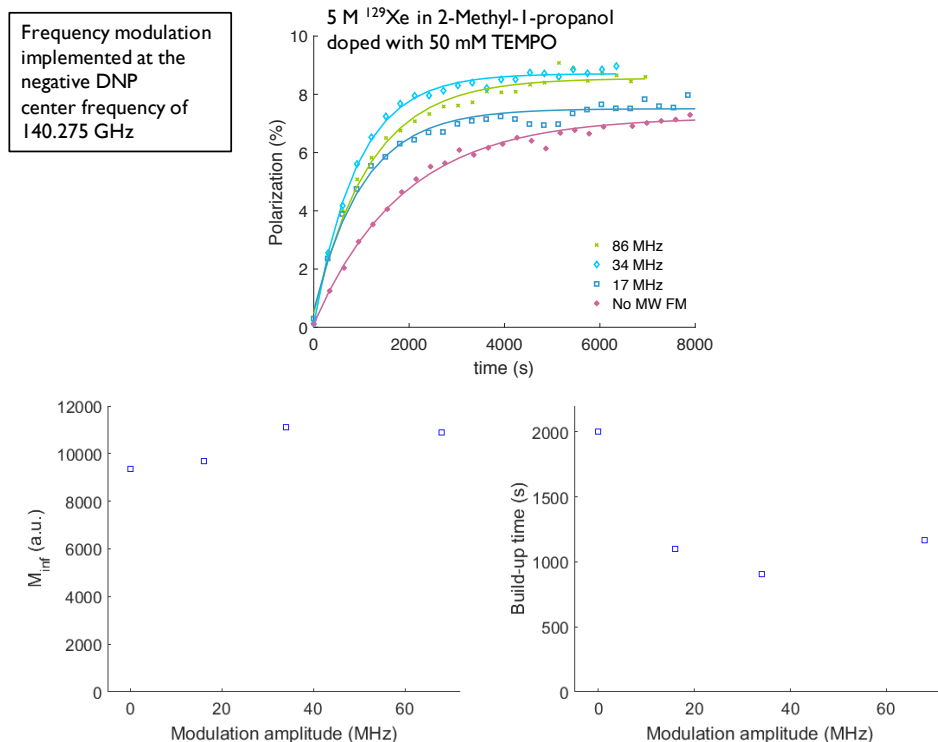


Figure A.6: Exemplary calibration of the modulation amplitude at the negative DNP peak, center frequency set to 140.275 GHz. Matrix of 5 M xenon in 2-methyl-1-propanol doped with 50 mM TEMPO. From the polarization build-up curves (**top**), the maximal magnetization (M_{inf}) and build-up times are extracted (**bottom**).

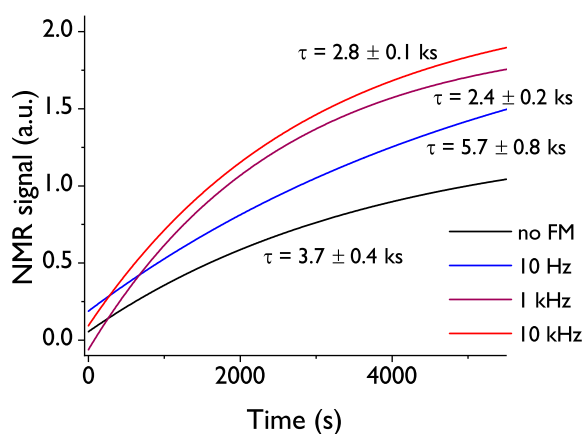


Figure A.7: Calibration of the rate of frequency modulation obtained from mono-exponential fits of the polarization build-up curves. The amplitude of modulation was kept constant at 40 MHz throughout all experiments. A 5 M xenon in 2-methyl-1-propanol matrix doped with 50 mM TEMPO was used.

A.3 Mixing Procedures

Figure A.8 shows xenon nuclear polarization build-up curves for different mixing procedures and hyperpolarization methods. A batch of doped (with 50 mM TEMPO radical) 2-methyl-

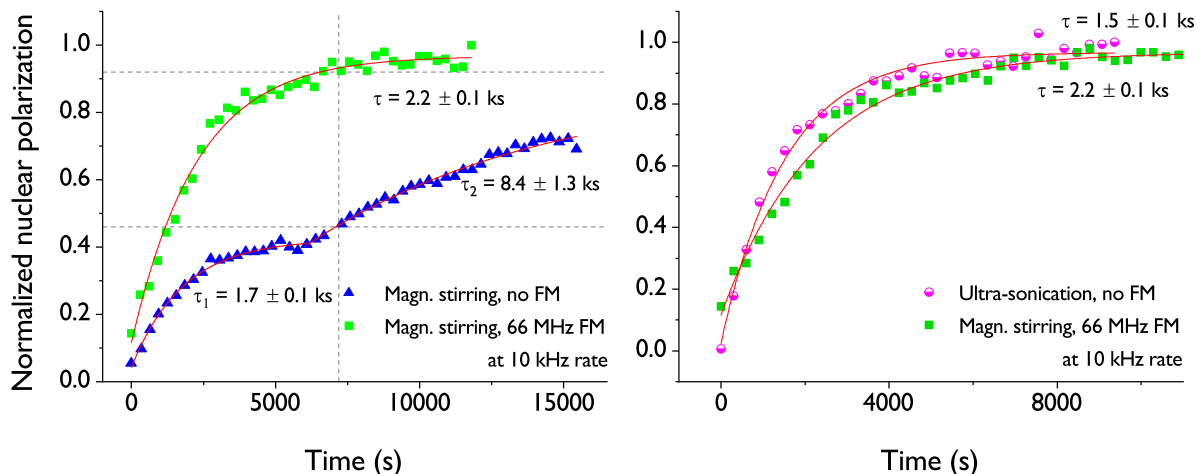


Figure A.8: Xenon nuclear polarization build-up curves for different mixing procedures and hyperpolarization methods. Values are normalized to the plateau value of the stirred sample when frequency modulation with 66 MHz amplitude at a rate of 10 kHz was applied. The mono- and bi-exponential build-up times τ are indicated. Dashed lines indicate the obtained normalized available magnetization of 0.46 and 0.92 without and with frequency modulation after the typical extraction time of 7.2 ks.

1-propanol solution was prepared and used to either embed xenon gas through cooling under constant *magnetic stirring* or through alternately cooling and *ultra-sonicating*. A mono-exponential build-up was observed for samples mixed by using ultra-sonication or in the case of applying microwave frequency modulation. The polarization evolution of the sample prepared via magnetic stirring and in the case that no frequency modulation was employed showed a bi-exponential build-up with a near linear behaviour after the initial faster hyperpolarization. Frequency modulation doubled the available polarization from 0.46 to 0.92 (normalized values) at the characteristic time of extraction ($t = 7200$ s).

The results indicate that both, ultra-sonication and microwave frequency modulation are methods that promote spectral diffusion by overcoming the previously discovered bottleneck arising from pure xenon cluster boundaries [185].

Appendix B

Residual B_0 -field Considerations for *ex situ* Sublimation DNP and *in situ* dDNP

Contribution

This chapter consists of two parts with the following contributions: Claudia C. Zanella planned and executed the B_0 -field mapping and conducted the hyperpolarized ^{129}Xe experiments.

Any experiments directly related to the ^{13}C measurements were conducted during a group project involving five PhD students contributing equally. Claudia C. Zanella contributed to experimental design, set-up planning and implementation, data acquisition and interpretation.

B.1 Motivation

In order to use ^{129}Xe as a non-endogenous tracer in MR studies, the hyperpolarized xenon has to be extracted and transported in its gaseous form. This method is known as sublimation DNP [29]. It is beneficial for the biomedical applications to maximally preserve ^{129}Xe polarization levels after extraction. High polarization can be maintained if fast adiabatic passage of the hyperpolarized gas at room temperature is ensured during transport between the polarizer and the MR scanner. Thus, in order to increase nuclear relaxation times $T_{1\rho}$ during extraction and collection of the gas, a magnetic field map of the 5 T polarizer, its stray fields and its environment was created. An advantageous positioning of the cryogen-free collection set-up was subsequently chosen accordingly. Finally, *ex vivo* proof of concept was given, demonstrating the ability to extract, temporarily store and transfer xenon gas whilst preserving sufficient polarization for MRS.

Furthermore, the knowledge obtained from mapping the 5 T stray magnetic field was applied to enhance dissolution DNP of $[1-^{13}\text{C}]$ -labelled substrates when transferred to the adjacent 14.1 T MR scanner. Finally, a perspective outlook regarding hard-ware implementations for using dissolution and sublimation DNP combined with MR studies at ultra-high magnetic field is given. These results are aimed at providing a basis for choosing appropriate set-up, dissolution protocol and for future *in vivo* or *in vitro* MR studies at either the 9.4 T or the 14.1 T MR scanner.

B.2 Introduction

At $B_0 = 5\text{ T}$ and $T = 1.1\text{ K}$ the electron spin polarization is close to $> 99\%$ (cf. Table 2.1) and nuclear polarization in the two-digit percentage range can be obtained using μW irradiation. Preserving this polarization throughout dissolution / sublimation and transfer to a delocalised MR scanner is a main concern during the DNP experiment.

One of the challenges when transferring dissolved or sublimated samples from one magnetic field to another is the earth magnetic field encountered in between them. Spins are transferred from a strong static magnetic field \mathbf{B}_0 in the order of Tesla to only a few dozen μT and back to $B_0 \sim \mathcal{O}(\text{T})$. Apart from \mathbf{B}_0 changing by several orders of magnitude, its orient-

ation changes as well. Spins are transferred from a vertical polarizer, through the randomly oriented earth magnetic field, into a horizontal bore MR magnet. Furthermore, the rapid dissolution / sublimation imposes a high temperature gradient on the nuclear spin system. Transfer through low magnetic fields at room temperature entails rapid nuclear relaxation T_{1I} of bulk magnetisation, thereby decreasing the duration of the hyperpolarized state and available polarization for MRI / MRS. Thus, magnetic field and temperature influence the nuclear spin-lattice relaxation rate $1/T_{1I}$. One way to tackle this bottleneck is to ensure fast adiabatic passage of the nuclear spins. Transferring polarized spin populations through reduced field gradients decreases the rate at which relaxation process occur, thus prolonging the lifetime of the hyperpolarized state. The following chapter therefore investigated two different experimental set-ups, one performing sublimation DNP of ^{129}Xe and the second one tackling dissolution DNP of ^{13}C , with the aim to improve available polarization in the MR scanner after transfer for future studies. This was done by mapping the magnetic fields around the polarizer and MR scanner and by putting several optimized transfer procedures in place.

B.3 Methods

B.3.1 Probing Magnetic Field Lines

B -mapping around the magnets was conducted to determine a convenient location for temporarily storing the hyperpolarized gas, to locate potential zero-field crossings (to be able to avoid them) and to determine a favourable transfer line path. The local magnetic field was measured using a Hall-probe (Hall Teslameter ETM-1 Metrolab, Emitec Messtechnik AG, Rotkreuz, Switzerland). The Hall probe used was a 3-axis Teslameter, which allowed for mapping not only magnetic field strength but also local magnetic field direction. A virtual grid of the room was pre-defined and the origin of the coordinate system was chosen on ground level, centred below the polarizer mantle. The magnetic field was probed at 40 grid points around the polarizer mantle (33.6 cm radius): the local magnetic field B_l was probed at 5 heights Above Ground Level (AGL): 13 cm, 50 cm, 80 cm, 110 cm and 120 cm, corresponding to the z -direction in [Figure B.5](#). B_l was probed at these 5 heights with 45° angular resolution. Furthermore, B_l at half a dozen positions along the transfer line and at the

position of the MW source (197 cm AGL) were measured. A 3D representation of the stray magnetic field around the 5 T polarizer and the adjacent 14.1 T MR scanner set-up shielded only by a Faraday cage was reconstructed by feeding grid positions and corresponding magnetic field strengths into MATLAB. The schematic representation constructed in MATLAB therefore represents distances and field strengths to scale unless otherwise indicated. The local magnetic field \vec{B}_l was indicated by arrows (at the position of arrow onset), equally true to scale and direction.

B.3.2 *Ex Situ* Sublimation DNP of ^{129}Xe

The term *ex situ* will in the following be used to describe de-localized sublimation DNP where gaseous ^{129}Xe is carried manually from the 5 T polarizer to the 9.4 T MR magnet. To perform sublimation DNP, a sample of 6.5 M ^{129}Xe embedded in an 2-methyl-1-propanol matrix containing 50 mM TEMPO radicals was hyperpolarized at 5 T and 1.2 ± 0.1 K. The time course (**top**) and schematics (**bottom**) of the major steps involved in ^{129}Xe sublimation DNP are illustrated in [Figure B.1](#). Embedding xenon gas homogeneously in a solid state matrix followed the procedure explained previously (cf. [chapter 4](#)). Microwave irradiation was applied at the frequency of the negative DNP maximum at 5 T (140.3 GHz). The polarization build-up was monitored using 5° flip angles in 5 minutes intervals. After the polarization reached its plateau, sublimation followed by propelling 5.5 ml of D_2O pressurized to 12 bar onto the frozen, hyperpolarized sample.

The classical extraction procedure is *cryo-collection*, which involves a liquid nitrogen cold trap. Xenon gas solidifies in the cold finger in which it is stored and transported until the spectroscopy measurement is imminent. This procedure was replaced by a cryogen-free procedure, equivalent to its use in SEOP [[278](#), [279](#)]. The dissolution line was connected to a spherical glass flask with a 3-way luer lock (cf. [Figure B.1](#)). Before sublimation initiation, the tubing system, including the glass vessel, was pumped to get rid of O_2 which is a fatal source for longitudinal relaxation [[280](#)]. The gas was momentarily stored in the glass vessel flask at room temperature. A sphere being the optimal geometry for minimizing the surface to volume ratio, this temporary storage was chosen to maximally reduce wall relaxation processes and slow down longitudinal spin relaxation [[281](#)]. The sublimation procedure followed the same steps described previously [[29](#)].

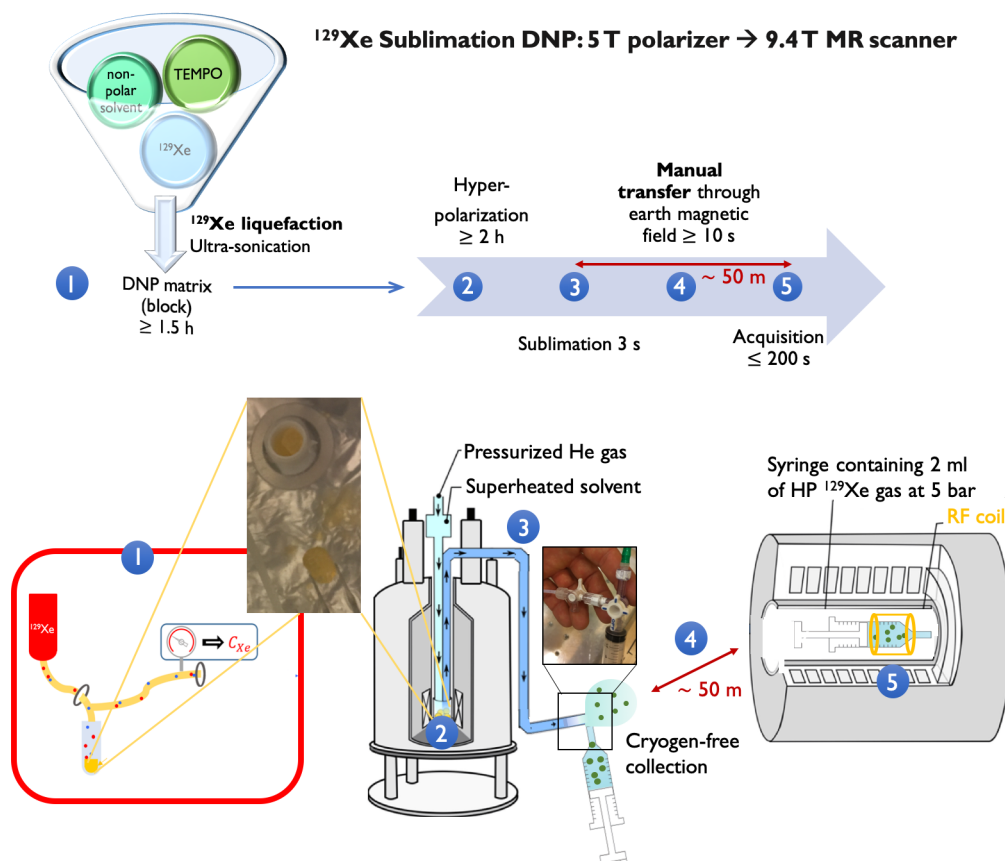


Figure B.1: Time course (**top**) and schematics (**bottom**) of the major steps involved in a ^{129}Xe sublimation DNP experiment with subsequent hyperpolarized MRS on a de-localized 9.4 T scanner. (1) 6.5 M ^{129}Xe is admixed to a non-polar matrix of 2-methyl-1-propanol containing 50 mM TEMPO radical. (2) Hyperpolarization inside the sample space of a 5 T polarizer at 1.15 K. (3) Extraction of the noble gas via sublimation. (4) Cryogen-free collection and manual transfer to the 9.4 T MR system located at a distance approximately 40 m away. (5) Hyperpolarized and thermally polarized MRS at 9.4 T and room temperature. Magnet schematics adapted from [277] with permission.

To measure the obtainable polarization in its gaseous state, two different locations were chosen where the spherical glass flask was set-up and where the hyperpolarized ^{129}Xe gas was collected to then be transferred to the MR scanner. One position was chosen close to the polarizer mantle and a second one approximately 2 m away from the isocenter of the polarizer (cf. Figure B.2). Subsequent MRS measurements of the hyperpolarized gas were conducted for collection of the gas in either of the two positions. Flip angle calibration MRS at the remotely-located and actively shielded 9.4 T MR scanner was first conducted on a phantom containing ^{129}Xe gas pressurised to 9 bar. The longitudinal relaxation time of the gas phantom was determined via saturation recovery neglecting relaxation due to RF pulse excitation. A 90° angle was calibrated using $TR = 5 \cdot T_{1I}$. After sublimation, the hyperpolarized gas was collected from the spherical glass flask using a 10 ml syringe. The hyperpolarized gas inside the syringe was compressed to 5 bar occupying a volume of 2 ml and

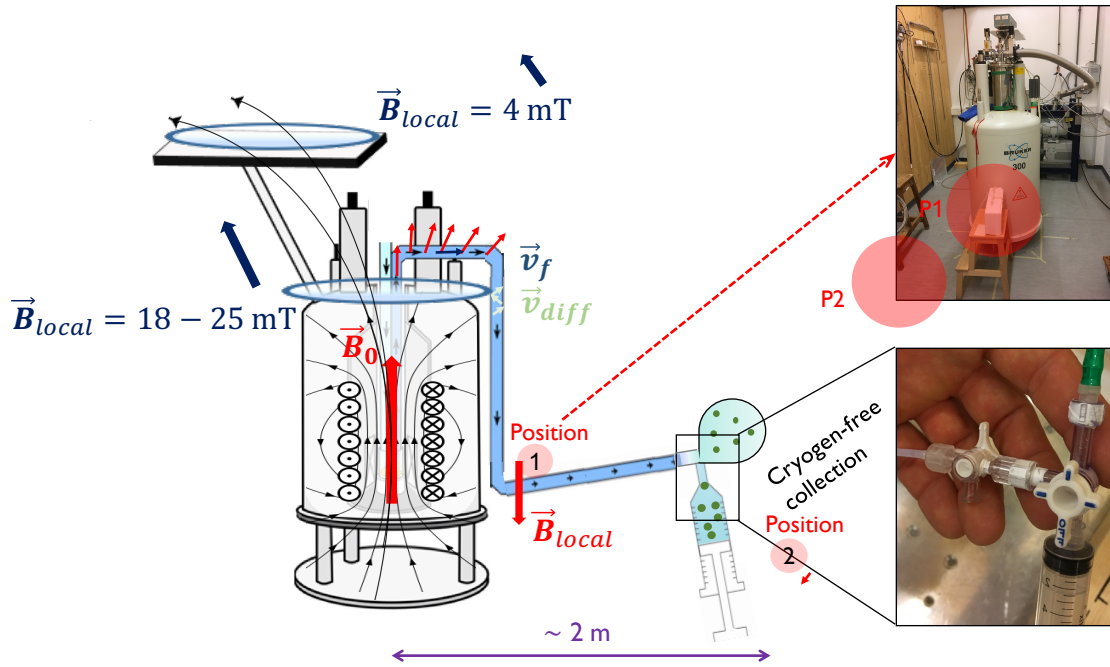


Figure B.2: Schematic illustration of the polarizer set-up and insights gained from Hall-probe measurements (cf. Figure B.5). Directions of local magnetic field \vec{B}_l (red arrows), diffusion and flow velocity, $\vec{v}_{diff}/|\vec{v}_{diff}|$ and $\vec{v}_f/|\vec{v}_f|$, are indicated. The dissolution line was connected to a spherical glass flask with a 3-way luer lock. Upon sublimation, the hyperpolarized gas was collected inside the glass flask. The two different sites at which hyperpolarized xenon gas was collected are also indicated (red circles). The first location is placed right next to the polarizer mantle (35 cm from the isocenter, ~ 50 cm AGL) and the second location is approximately 1.65 m further away (~ 20 cm AGL). Coil size and magnetic field line orientation are not to scale.

then manually carried to the 9.4 T horizontal bore MR magnet where MRS was conducted using an Alderman-Grant coil [167]. The enhancement ϵ was calculated as the ratio between integrated signal intensities of the hyperpolarized and the thermally polarised state. MR spectroscopy of the hyperpolarized gas was acquired using single pulses α of 6° and duration τ of $5 \mu\text{s}$, with a TR of 3 s. The thermal signal was acquired with the same 6° RF pulse, using 500 averages and a TR of 1 s.

B.3.3 *In Situ* dDNP of $[1-^{13}\text{C}]$ Pyruvate

The *in situ* sample transfer was set up to enable hyperpolarized *in vivo* MRS at the 14.1 T MR scanner adjacent to the 5 T polarizer (Figure B.3). In this case, *in situ* refers to a automated sample transfer process which delivered the dissolved sample directly from the polarizer into the MR scanner via a transfer line without manual transfer of the hyperpolarized liquid.

Sample compositions: 5 sample compositions were prepared in total. First, a reference sample of 3 M sodium acetate was used to calibrate the carbon insert. The polarization and



Figure B.3: *In situ* set-up for conducting hyperpolarized MRS at 14.1 T (MR scanner behind the filter panel cavity) after having transferred the sample from the adjacent 5 T polarizer (in the foreground).

$T_{1\rho}$ of four samples were then tested at 14.1 T, namely (1) 2.7 M sodium pyruvate with 45 mM TEMPOL, (2) as (1) but with addition of sodium ascorbate (vitamin C) to scavenge TEMPOL radicals, (3) 2.7 M sodium pyruvate with 15 mM of the trityl radical OX063, (4) 7 M pyruvic acid whereas UV-radical were generated by irradiating the sample during 1 h with UV light (cf. [Table B.1](#)).

Solid state confirmation experiments on the 5 T polarizer were conducted to confirm the positive DNP at 140.4 GHz, as found using a frequency sweep for 40 mM TEMPOL at 5 T [[282](#)].

Liquid state polarization measurements were conducted to determine the sample yielding the highest liquid state polarization, which was subsequently used to quantify solid state polarization, optimize transfer parameters and quantify the effect of microwave frequency modulation. Liquid state data was acquired inside the separator using single loop coils (^1H and ^{13}C). Hyperpolarized spectra were obtained using 4.5 μs hard pulses calibrated for 10° flip angles, and a TR of 3 s. Thermal state measurements for sample (1) were conducted using 400 averages and a TR of 110 s. In order to decrease the repetition time, 5 μl of 0.5 M gadolinium was admixed to the relaxed solution and thermal spectra of samples (2)-(4) were acquired with a 10° flip angle every TR = 5 s with 1024 averages. Subsequent polarization levels were corrected for the amount of averages acquired to ensure comparability.

***In vivo* hyperpolarized MR** was conducted to determine if the newly optimized set-up yielded enough sensitivity to allow for detecting metabolism. Hyperpolarized spectra were acquired from a male Wistar rat after automatic infusion using a syringe pump (Oxford instruments), programmed to start 9 s after dissolution, was completed. A quadrature ^1H and ^{13}C surface coil was positioned on top of the liver. Data was acquired with non-localized spectroscopy and a 30° adiabatic RF excitation pulses (BIR-4) [[230](#)] and a TR of 3 s. The SNR was calculated as the maximum signal intensity over the standard deviation of the noise (region without resonances). A total of 13 MR scans were added.

B.4 Results

B.4.1 $|\vec{B}_0|$ -mapping

The main magnetic fields B_0 were found to point towards the ceiling (+ z-direction) and towards the polarizer (+ y-direction) for the 14.1 T scanner and the 5 T polarizer, respectively. The residual magnetic field of the 14.1 T MR scanner never exceeded 2 T and dropped towards ~ 25 mT at the position where the transfer line crossed the panel (Figure B.4). B_z

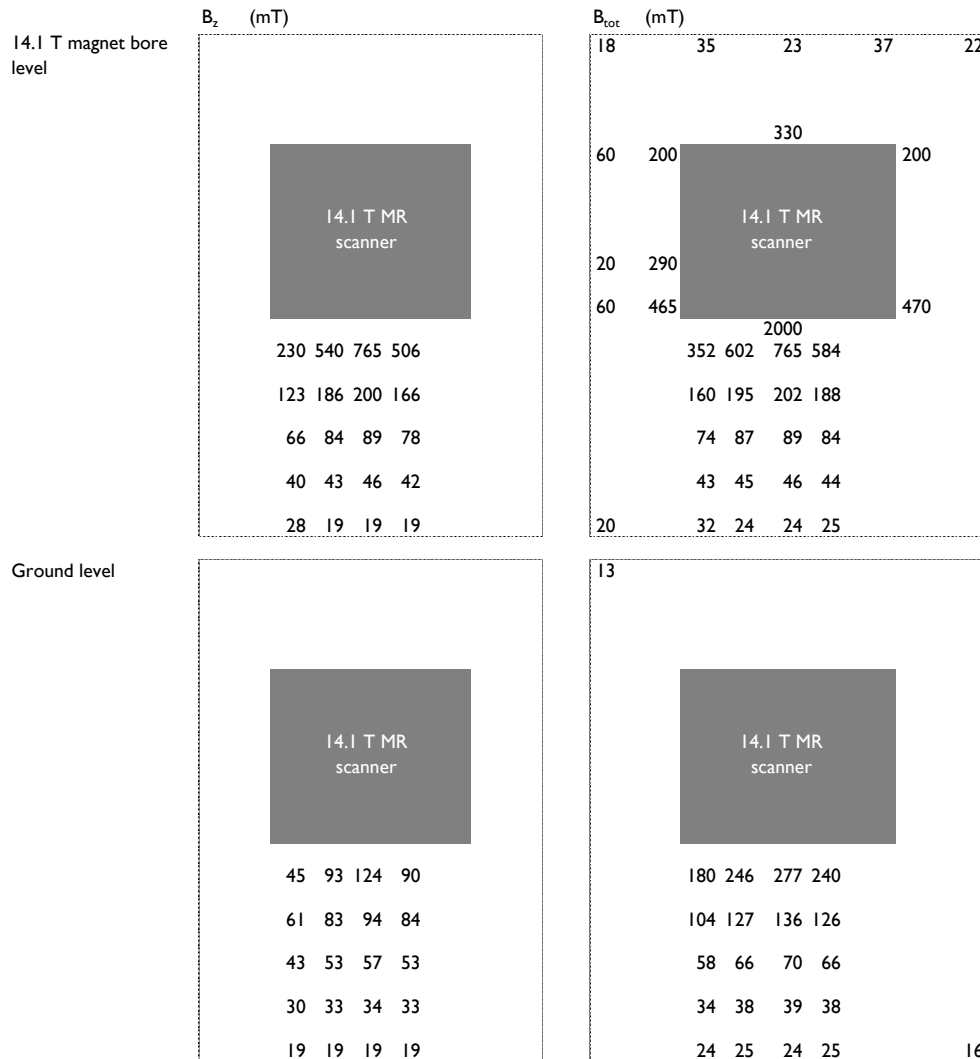


Figure B.4: Magnetic field mapping of the 14.1 T MR scanner at EPFL. B_0 field strength in z-direction ($|\vec{B}_0|$) and total $|\vec{B}_0|$ field at the level of the magnet bore center (**top**) and at ground level (**bottom**). Data given in mT. Data represented by and acquired with the help of Nicolas Kunz.

and B_{tot} largely coincided for locations along the symmetry axis of the scanner, as expected. The absolute value of the local magnetic field $|\vec{B}_l|$ never deviated by more than 3 % at all 8 angular directions at a given height AGL. This isotropic field distribution indicated a negligible residual magnetic field of the ultra-high field MR scanner at the site of the polarizer.

$|\vec{B}_l|$ at the position of the MW source (on top of the polariser, 197 cm AGL) was measured to be 4 mT. The top part of the cryostat mantle (at 120 cm AGL) was found to have a residual $|\vec{B}_l|$ of 18 - 25 mT. Maximal residual field along the polarizer mantle was 82 mT, 50 cm AGL (Figure B.2). Extraction location (1), 50 cm AGL, was within the influence of the residual magnetic field of the polarizer and ~ 30 mT strong. However, \vec{B}_l was oriented in the opposite direction (pointing towards $-\vec{e}_z$) of the center field. Only a weak residual field $< 1 \mu\text{T}$ was detected at extraction location (2). A transfer line for dissolution DNP passing through the filter panel has been put in place previously [283]. Note that $\vec{v}_f = \vec{v}_f(x)$ in Figure B.5

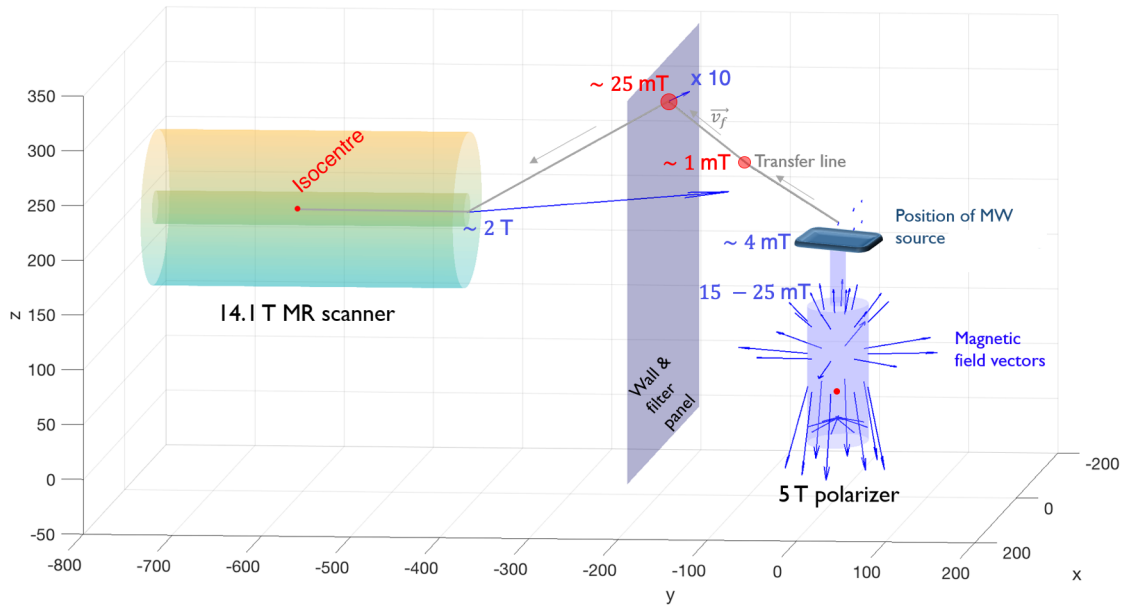


Figure B.5: 3D representation of 5 T polarizer and 14.1 T MR scanner set-up at our laboratory. Distances and field strengths are to scale unless otherwise indicated. Arrows (blue) indicate the local magnetic field (at the position of arrow onset), true to scale and direction. The ultra-high field magnet of 14.1 T in the isocentre displayed a strong stray magnetic field of ~ 2 T at the bore entrance. Isocentres (red dots) of polarizer and MR scanner were ~ 6 m apart in y-direction and separated by a filter panel. A transfer line set-up used in dissolution DNP was already in place to transfer hyperpolarized liquid state samples through a hole in the filter panel [283]. Upon dissolution, the hyperpolarized samples were pushed through the transfer line (grey).

only represents the direction of flow within the transfer line (grey) and does not mirror spin orientation within the local magnetic field.

B.4.2 ^{129}Xe MRS at 9.4 T

Each dissolution allowed for the extraction of 80 ml of hyperpolarized gas in total. No hyperpolarized signal was detectable after the gas was extracted in the designated position (1), located right next to the cryostat mantle (Figure B.6 C). In case of placing the spherical glass flask at position (2) (cf. Figure B.2), the first data acquisition yielded an enhancement ϵ of 4.8k. This corresponds to a ^{129}Xe polarization of 4.4 % (Figure B.6 B). Fitting the MRS decay curve to a mono-exponential function yielded a nuclear longitudinal relaxation time T_{1f} of 62 s at 9.4 T. The SNR of the first hyperpolarized acquisition and of the thermally polarized spectrum were 1921 and 8, respectively.

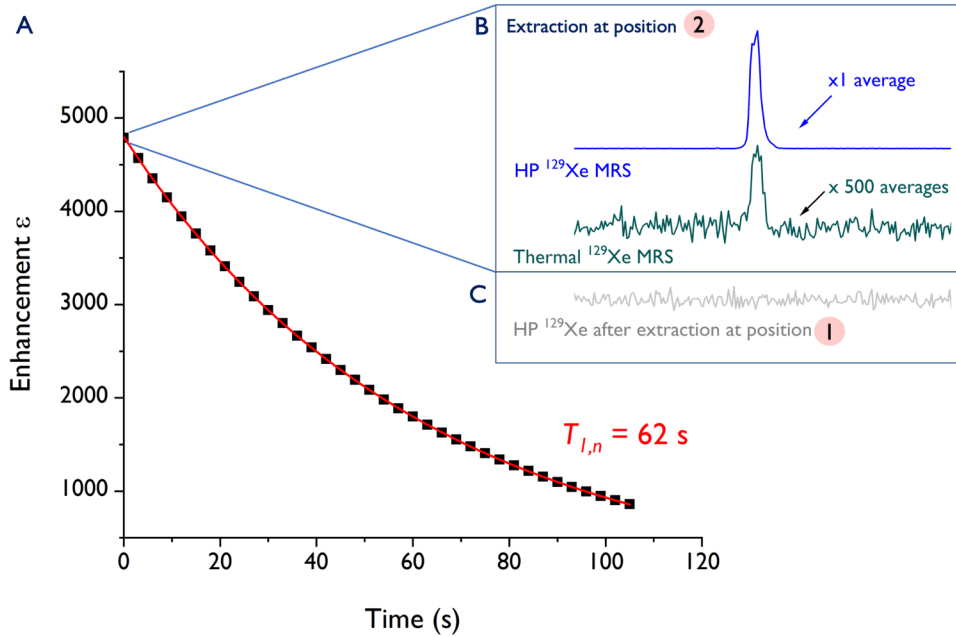


Figure B.6: *Ex vivo* hyperpolarized ^{129}Xe MRS at 9.4 T after cryogen-free extraction. **A)** After extracting the hyperpolarized gas in location (2) (cf. Figure B.2), the first acquisition yielded an enhancement ϵ of 4.8k, corresponding to a ^{129}Xe polarization of 4.4 %. **B)** Hyperpolarized ^{129}Xe MRS acquired using $\alpha = 6^\circ$, $TR = 3 \text{ s}$ on a syringe containing 2 ml hyperpolarized ^{129}Xe gas at 5 bar. The thermal signal was acquired with the same $\alpha = 6^\circ$, 500 averages and TR of 1 s. **C)** No hyperpolarized signal was observed after collecting the hyperpolarized ^{129}Xe gas in position (1), located right next to the cryostat mantle.

B.4.3 ^{13}C MRS at 14.1 T

Out of the four sample compositions tested, the highest liquid state polarization and longest T_{1f} were measured for sample (2) (cf. Table B.1) with 10.7 % polarization and a T_{1f} of 41.3 s. Sample (2) was therefore subsequently chosen to perform microwave frequency modulation experiments, yielding the same nuclear solid state polarization in about a sixth of the time (Figure B.7). The characteristic build-up time τ_p was reduced to 770 s with frequency modulation compared to 5000 s when no frequency modulation was applied. Out of a dozen attempts, a solid state polarization of 14.6 ± 1.6 % could be calculated from three successful attempts.

Several locations where the transfer line crossed through the filter panel of the 14.1 T MR scanner, which separated the two magnets, were investigated. Results obtained from the B_0 field mappings were used to ensure that the transfer path to the 14.1 T MR magnet was chosen in a way to avoid zero-field crossings. Resulting liquid state polarizations were between 11.5 ± 3.6 % and 15.3 ± 6.8 % (Figure B.8). Liquid state nuclear relaxation times were about half a minute, irrespective of the sample. No statistically significant polarization differences were observed for the transfer line passage through different filter panel holes such that the most convenient passage, location (2) in Figure B.8, was chosen for subsequent measurements. At the location where the transfer line crossed through the filter panel into the 14.1 T scanner room $|\vec{B}_l|$ was measured to be 25 mT.

Table B.1: Liquid state ^{13}C polarization P_{LS} and characteristic nuclear relaxation time T_{1f} at 14.1 T. Polarization values were corrected for number of averages. Reference measurement to test the carbon insert of the polarizer were conducted with Sodium acetate (NaOAc). UV radicals were created by irradiating the sample during 1 h with UV light.

No	Substrate	Solvent	Radical	P_{LS}	LS $T_{1f,n}$ (s)
*	3 M $[1-^{13}\text{C}]\text{NaOAc}$	$\text{D}_2\text{O} : \text{d}_8\text{-glycerol}$ 0.8:1 (v/v)	50 mM TEMPOL	n.a.	n.a.
1	2.7 M $[1-^{13}\text{C}]\text{NaPyr}$	$\text{D}_2\text{O} : \text{d}_8\text{-glycerol}$ 3.2 : 1 (v/v)	45 mM TEMPOL	6.7 %	26.2
2	2.7 M $[1-^{13}\text{C}]\text{NaPyr}$	$\text{D}_2\text{O} : \text{d}_8\text{-glycerol} : \text{NaAsc}$ 3.2 : 1 : 1.3 (v/v/v)	45 mM TEMPOL	10.7 %	41.3
3	2.7 M $[1-^{13}\text{C}]\text{NaPyr}$	$\text{H}_2\text{O} : \text{glycerol}$ 3.2 : 1 (v/v)	15 mM OX063	7.6 %	36.7
4	7 M $[1-^{13}\text{C}]\text{PA}$	$\text{H}_2\text{O}:\text{PA}$ 1:1 (v/v)	UV radical	8.3 %	36.6

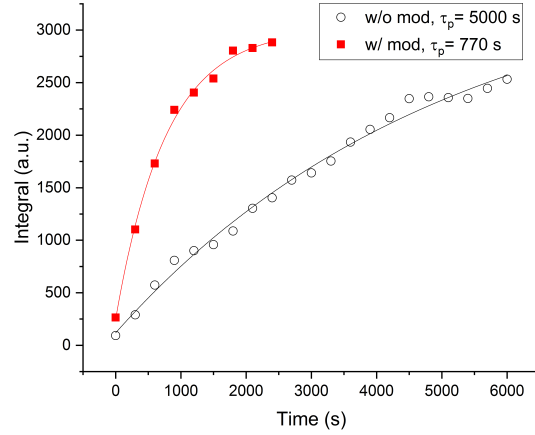
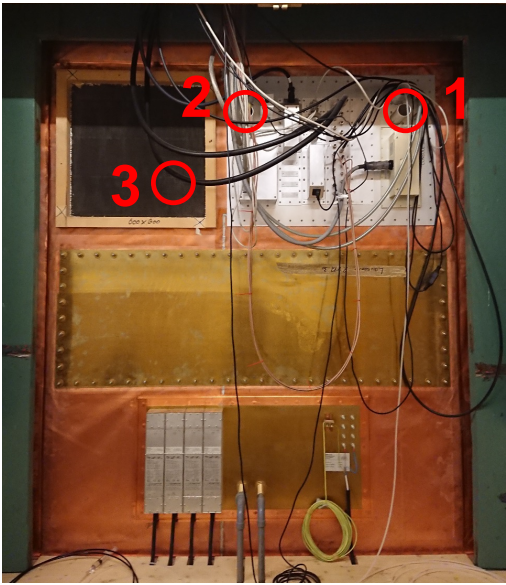


Figure B.7: Nuclear enhancement with (squares) and without (circles) microwave frequency modulation of a 2.7 M $[1-^{13}\text{C}]\text{NaPyr}$ sample containing 45 mM TEMPOL. Experiments conducted at 5 T, 1.1 K.

Prior to *in vivo* MRS, the transfer path was optimized by shortening the transfer line from 9.90 m to 7.50 m, which allowed for a reduction of the pushing time from 5 s to 3 s while transferring the same volume of 2.2 ± 0.05 ml. Even though this length still exceeded the transfer line length of the 7 T polarizer to the 9.4 T MR scanner, which was 5.60 m, the same pushing time of 3 s could be set. Furthermore, triggering the start of the acquisition sequence was put in place. Implementation of these optimizations lead to a $[1-^{13}\text{C}]\text{PA}$ liquid state po-



Hole	P_{LS}	LS $T_{1\rho}$ at 14.1 T	n
1	$11.5 \pm 3.6 \%$	33.3 ± 1.3 s	3
2	$15.3 \pm 6.8 \%$	29.3 ± 3.7 s	3
3	$12.7 \pm 1.8 \%$	32.8 ± 1.9 s	3

Figure B.8: Possible transfer line crossings through the 14.1 T MR scanner filter panel with liquid state polarization P_{LS} and $T_{1\rho}$ subsequently measured in the separator. Samples were hyperpolarized without microwave frequency modulation.

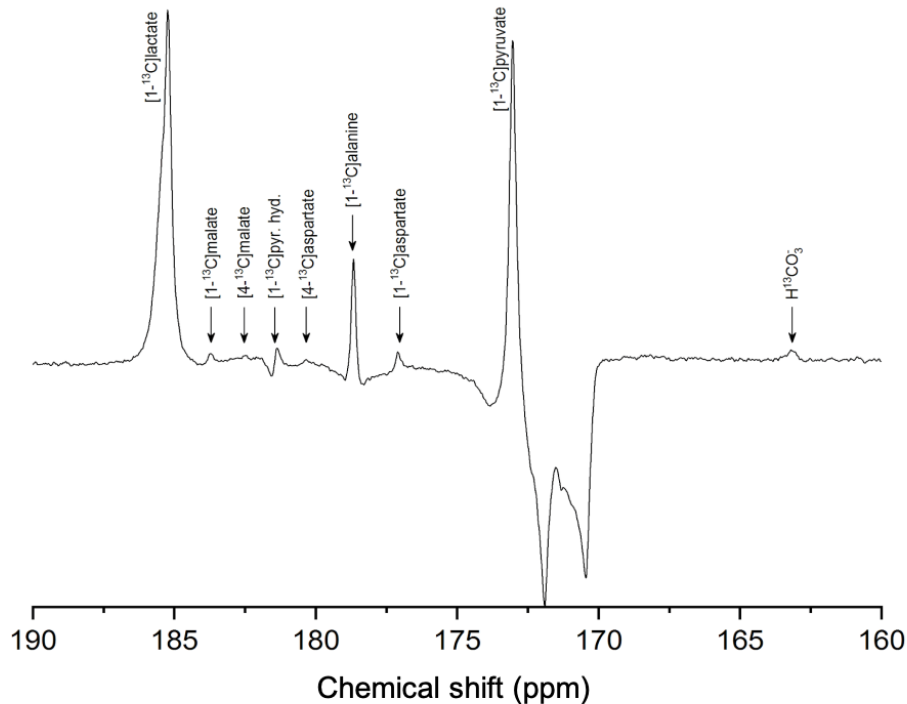


Figure B.9: *In vivo* MR spectrum of rat liver acquired at 14.1 T after *in situ* transfer of hyperpolarized sodium pyruvate from the 5 T polarizer. Spectrum shows the sum of 13 scans. Lactate was visible for 60 s.

larization of $23.3 \pm 1.7 \%$, $n = 3$, for the sample containing 15 mM of the trityl radical OX063.

In vivo metabolism in the rat liver could be measured after the injection of hyperpolarized $[1-^{13}\text{C}]\text{NaPyr}$. Apart from the injected $[1-^{13}\text{C}]\text{pyruvate}$, the resonance peaks of $[1-^{13}\text{C}]\text{lactate}$, $[1-^{13}\text{C}]\text{malate}$, $[4-^{13}\text{C}]\text{malate}$, $[1-^{13}\text{C}]\text{pyruvate hydroxide}$, $[4-^{13}\text{C}]\text{aspartate}$, $[1-^{13}\text{C}]\text{alanine}$ and $[1-^{13}\text{C}]\text{aspartate}$ were visible. A maximum SNR of 164 was measured. Lactate was detectable for 60 seconds.

B.5 Discussion

The glass flask, where hyperpolarized ^{129}Xe gas was collected, was initially placed in position (1) in order to take advantage of stray field of the polarizer. The idea was to decrease the magnetic field gradient during transfer and to avoid the almost vanishing and randomly oriented earth magnetic field for the short-lived storage of the gas. The flask was thus set up

close to the center field. However, extractions of the ^{129}Xe gas at position (1) resulted in undetectable hyperpolarized MR signal at the 9.4 T scanner. Only after having conducted the B -mapping of the polarizer, it became clear that extracting the gas at position (1) implied a zero-field crossing during transfer, since the local magnetic field at the position at the flask was oriented opposite to the B_0 -field used to hyperpolarize the nuclear spins ($B_l \sim -30$ mT, 50 cm AGL). Hence, cryogen-free collection was conducted at the newly-chosen position (2) where no such zero-field crossing had to be overcome. This location profited from a weak residual magnetic field which sheltered the spins from the randomly oriented earth magnetic field. And indeed, the hyperpolarized ^{129}Xe signal could be preserved for subsequent MRS measurements, indicating an improved adiabatic passage [284]. The measured T_{1I} of 62 s compared well with previous results [180, 285]. The measured polarization, however, was much lower than polarization levels obtained with the gold standard for hyperpolarizing ^{129}Xe gas, that is SEOP [43, 45]. However, those experiments were conducted prior to the implementation of microwave frequency modulation, which was shown to potentially boost ^{129}Xe polarization considerably (chapter 4). One advantage sublimation DNP has over SEOP is that it can be performed without dedicated hardware. ^{129}Xe spins can be hyperpolarized using a conventional DNP polarizer since it is most versatile with respect to the nuclear species, requiring but a few hardware modifications.

Experiments conducted later on with the broad-line radical TEMPOL profited as expected from the implemented microwave frequency modulation in a major way, especially in terms of the build-up rate. The decrease in build-up time by about a factor of 6 upon frequency modulation indicated that the initial radical concentration was rather low. By using microwave frequency modulation, an increase in radical concentration could be avoided. This was advantageous since this would have, in turn, affected the relaxation time of the nuclei. Even before having applied frequency modulation or having optimized the transfer path, several ^{13}C -labelled sample compositions have achieved 7 - 10 % polarization using affordable nitroxyl radicals. The final 23 % of ^{13}C polarization obtained (even though the expensive trityl radical OX063 had to be used) as well as the metabolic profile acquired *in vivo* demonstrated the feasibility for conducting subsequent hyperpolarized studies on the 5 T polarizer coupled to the 14.1 T MR scanner.

B.6 Conclusion and Perspectives

Magnetic field lines inside and around the polarizer influenced the state of the spin system. Creating conditions under which the state spin system underwent minimal changes helped conserve bulk magnetization. No hyperpolarized ^{129}Xe signal was initially measured after transport to the remotely-located 9.4 T MR scanner. Detailed knowledge of the residual B_0 field and subsequent optimization of the extraction procedure allowed for conservation of the hyperpolarized state, resulting in a 4.4 % ^{129}Xe polarization measured in gaseous state at the MR scanner. Adiabatic passage could, for instance, be further improved during transport by confining the hyperpolarized gas inside a home-build transportation system of small but constant magnetic field. Such a set-up could in the simplest form merely consisting of a Helmholtz coil and a source of electricity [286]. This set-up would to a certain extent counterbalance the strong field gradient caused by an almost vanishing and randomly oriented earth magnetic field encountered upon extraction.

A possible perspective tailored to the laboratories at EPFL could be to drive ^{129}Xe sublimation DNP towards *in vivo* MR applications at ultra-high field. The laboratory's ultra-high field MR scanner (14.1 T) being located in the room adjacent to the 5 T polarizer, renders it an interesting alternative to the more remotely located 9.4 T MR scanner. Hardware-based modifications to the existing system could include building a magnetic tunnel between polarizer and MR magnet in order to approximate adiabatic passage between the systems, as was demonstrated at other EPFL facilities [287]. Xenon gas could possibly be pushed through the transfer line using pressurised helium gas (as is the case in the current set-up) but then only be collected it in front of the 14.1 T magnet bore. In this case, collecting the gas could be implemented within the influence of the magnet's magnetic field, which is still strong at the bore entrance with ~ 330 mT.

So far, implemented improvements of the polarizer hardware included the addition of (i) a butterfly valve for manual helium flow regulation and (ii) a helium transfer line extension to counteract excessive helium consumption of the 5 T polarizer (cf. [Appendix D](#)). Further, the extraction transfer path was optimized, reducing the transfer time and hence polarization loss during said transfer. Microwave frequency modulation enhanced the solid state polarization ([chapter 4](#)) and B_0 mapping allowed for reduced polarization loss upon sample extraction. The implemented optimizations resulted in a small loss of polarization during transfer and polarization levels measured were sufficiently high to conduct *in vivo* studies.

Appendix C

Expanding the Saddle Coil <> Birdcage Coil Comparison: Considering a High-pass 16-leg Quadrature ^1H Birdcage Coil

Contribution

Contribution as declared in [chapter 6](#).

C.1 Motivation

In addition to the research conducted in [chapter 6](#), a follow-up question was investigated. Namely, how a 16-leg birdcage coil would compare to the 8-leg birdcage and the saddle coil at ultra-high magnetic field. The interest arose since a higher symmetry can theoretically be achieved thanks to an increased number of rungs N . The higher the number of rungs, the lower the importance of fluctuations in current distribution. Therefore, more homogeneous B_1^+ coverage could *a priori* be expected. It was shown through finite-difference time-domain (FDTD) calculations that increasing the number of rungs from $N = 8$ to $N = 16$ increased B_1^+ homogeneity and B_1^+ efficiency while simultaneously decreasing power deposition [288]. These calculations hold at 200 MHz, 300 MHz and 500 MHz and the same trend was observed for increasing N to 32, 64 and 128, with the highest improvement achieved for increasing N from 8 to 16. Since the 8-leg birdcage coil was found to display significantly lower transmit field efficiency than the saddle coil design (cf. [chapter 6](#)), it seemed of interest to see whether a coil design with higher intrinsic symmetry performed better.

C.2 Methods

The 16-leg ^1H quadrature birdcage coil was constructed by a previous PhD student, Masoumeh Dehghani (2016) [247]. Both birdcage coils have the same dimensions except for unavoidable decreased rung width W and inter-rung spacing s (cf. [Table C.1](#)). They also differ from each other in the chosen material: the main body was constructed out of ertalyte for the 8-leg birdcage coil and out of a plastic tube for the 16-leg coil.

To study the impact of this slightly refined coil geometry at 600 MHz, the same methodology, simulations and experiments mentioned in [chapter 6](#) were applied to the 16-leg ^1H quadrature birdcage coil. All experimental parameters were equally kept the same as previously described, unless otherwise mentioned. Data shown for the saddle coil and the 8-leg birdcage coil are identical to previously given data and were repeated here in graphs and tables to allow for a direct comparison between the three coils.

Additionally to the afore-mentioned SNR calculations, RF transmit power requirements, electromagnetic field simulations, saline phantom experiments and *in vivo* glycoCEST imaging, B_1^+ homogeneity maps were acquired on phantoms useful for subsequent CEST imaging (10 mM glucose and 50 mM glycogen syringes). The effect on the MTR_{asym} of applying a

Table C.1: Data sheet containing lengths and fixed / variable capacitor values for constructing ^1H volume coils at 600 MHz. Dimensions of inner rung length l , rung width W , endring width W_r and inter-rung spacing s are given. C_m and C_t denote the matching and tuning capacitors. Schematics to scale are illustrated in [Figure 6.2](#) for the 8-leg birdcage coil (BC) and the saddle coil.

	W (mm)	l (mm)	C_u , fix (pF)	C_m , fix (pF)	C_t , tunable (pF)	W_r (mm)	s (mm)	Coil diameter (mm)	Shield radius (mm)	Shield length (mm)
8-leg BC coil	9	27	4.3	4.3	1-9	3	11	50.6	50	68
16-leg BC coil	2	27	8.2	12	1-9	3	8	50.6	50	68
Saddle coil	1.5	22	2x1.8, 2x2.2	-	-	-	-	34	No shield	-

B_1^+ correction map was plotted to demonstrate the increased CEST contrast coherence over a perfectly homogeneous sample. As another supplementary parameter, the MTR_{asym} coefficient of variation was calculated before and after B_1^+ correction maps were applied to the MTR_{asym} map. Corresponding experimental data for the saddle coil was calculated from [Figure C.4 \(f\)](#)). *In vivo* glycogen content was mapped in skeletal muscle via CEST imaging of a Wistar rat thigh.

C.3 Results

To evaluate transmit and receive characteristics, SNR and transmit power requirements were measured ([Table C.2](#)). After having applied corrections for number of channels and filling factor, an SNR of 0.7 ± 0.1 was found (normalized value with respect to the saddle coil SNR). The system-dependent transmit powers required to generate a 90° pulse were 63 dB for localized STEAM acquisition, respectively 28.4 dB for non-localized single block pulse acquisition.

To ascertain that a higher number of rungs entailed indeed a higher homogeneity, electromagnetic field simulations were conducted for the 16-leg birdcage coil. Transmit field non-uniformity throughout 14 mm of slices in axial direction was $NU = 2.04 \pm 0.02 \%$ (over ROI_{11}) ([Figure C.1](#)). For the largest analyzed ROI (13.7 mm in diameter), the relative uniformity RU was 98.1 %.

Table C.2: For the relative SNR: Comparison of SNR using a single slice GE sequence with $TR / TE = 10 \text{ s} / 2.6 \text{ ms}$, $\alpha = 0^\circ$, respectively 30° , FOV of $25 \times 25 \text{ mm}^2$ and resolution of 64×64 . The statistics includes a cylindrical ROI of 11 mm diameter and 2 mm slice thickness which consists of 611 voxel. The input power was calibrated for localized (voxel size of $11.2 \times 11.2 \times 3 \text{ mm}^3$) and non-localized acquisitions (full coil FOV), using a Stimulated Echo Acquisition Mode pulse sequence ($500 \mu\text{s}$ asymmetric 90° pulses, $TE = 2.8 \text{ ms}$, $TR = 4 \text{ s}$) [32, 257] and a single block pulse ($20 \mu\text{s}$ hard pulse), respectively.

	Relative SNR, corrected	Transmit power, localized acquisition (dB)	Transmit power, non-localized acquisition (dB)
Saddle coil	1 ± 0.1	58	23.5
8-leg BC coil	0.8 ± 0.1	63	29.5
16-leg BC coil	0.7 ± 0.1	63	28.4

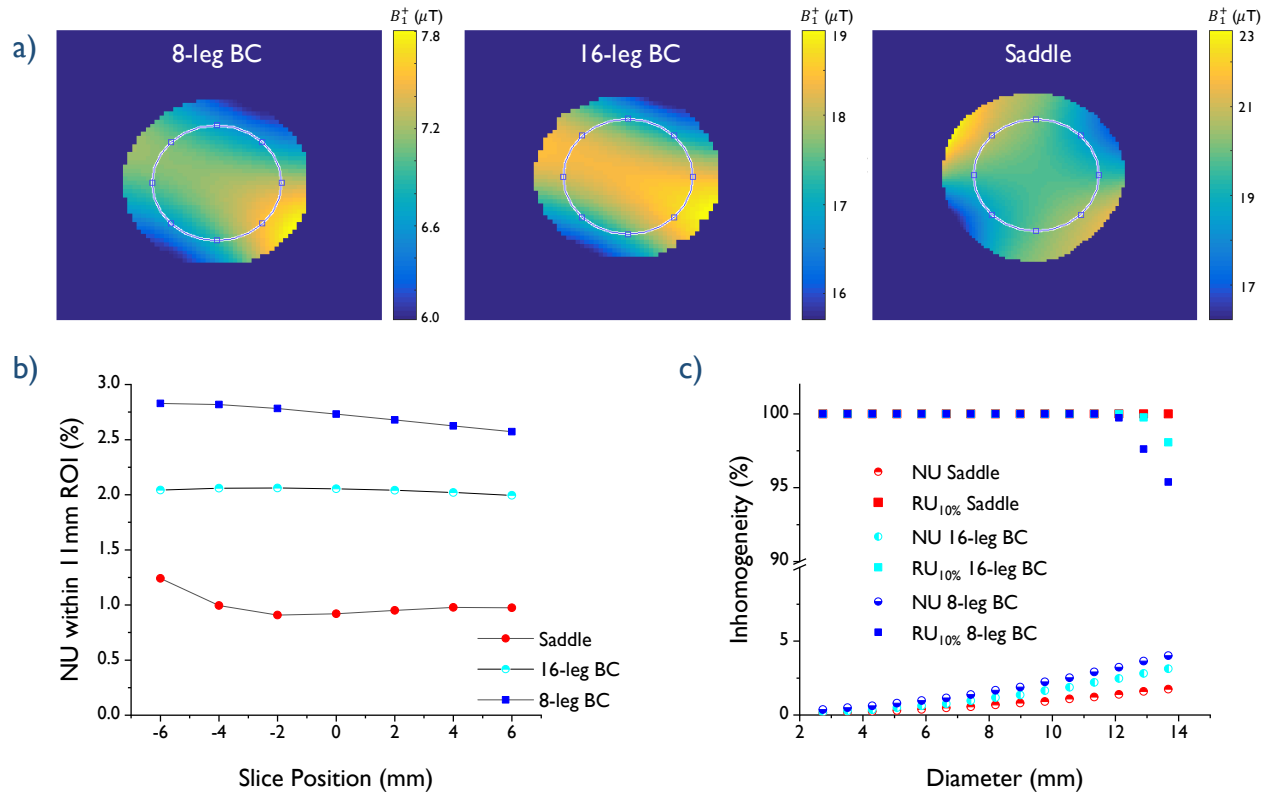


Figure C.1: Simulation of B_1^+ maps with slice- and ROI-dependent homogeneity analysis. **a)** B_1^+ maps simulated in a 0.9 % saline phantom for 1 W input power. **b)** Dependence of Non-uniformity (NU) on the slice position from the isocenter. Statistics within a 11 mm diameter ROI (encircled in a). **c)** NU and Relative Uniformity (RU) of the B_1^+ maps depending on the ROI diameter.

Following the simulations, experiments were conducted to estimate the effectively generated B_1^+ map inside the 0.9 % saline phantom. Homogeneity calculations yielded $NU = 5$ % and $RU = 92$ % at ROI_{11} (Figure C.2). The transmit field generated by the 8-leg birdcage coil was most homogeneous, with the other two coils creating similarly less homogeneous B_1^+ maps. The same trend was observed independently of the phantom composition.

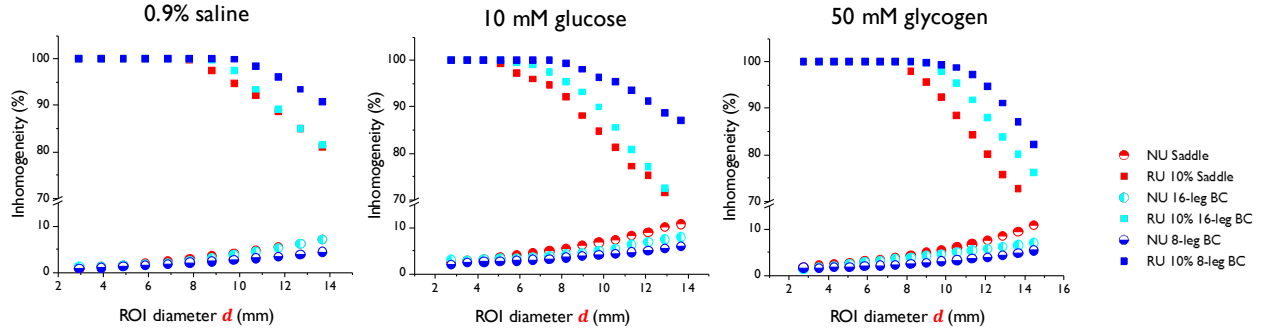


Figure C.2: B_1^+ homogeneity over increasing ROIs in phantoms generating CEST contrast and in a 0.9 % saline phantom. Homogeneity is evaluated using 10 % Relative Uniformity (RU 10 %) and Non-uniformity (NU).

To ensure that both coil designs created homogeneous CEST contrast over an isotropic sample, the MTR_{asym} map was calculated (Figure C.4), and the effect of applying a B_1^+ correction map was illustrated (Figure C.4 e,f). Quantitative analysis showed a decrease in MTR variation due to B_1^+ field corrections by 39 %, 35 % and 42 % for the saddle coil, the 8-leg and the 16-leg birdcage coils, respectively (Figure C.3). *In vivo* MTR_{asym} maps of a rat thigh demonstrated the feasibility to detect the glycoCEST effect in the range [1; 0.5] ppm (Figure C.5). The creatine CEST effect was equally detectable around [1.7; 1.2] ppm.

Figure C.3: MTR asymmetry coefficient of variation calculated before and after B_1^+ correction maps were applied. Normalized standard deviation of the MTR asymmetry of a 50 mM glycogen phantom in a predefined region of 375 central voxels. Corresponding experimental data for the saddle coil is displayed in Figure C.4.

	MTR_{asym} variation, uncorrected (%)	MTR_{asym} variation, corrected (%)
8-leg BC coil	4.0	2.6
16-leg BC coil	7.1	4.1
Saddle coil	7.3	5.2

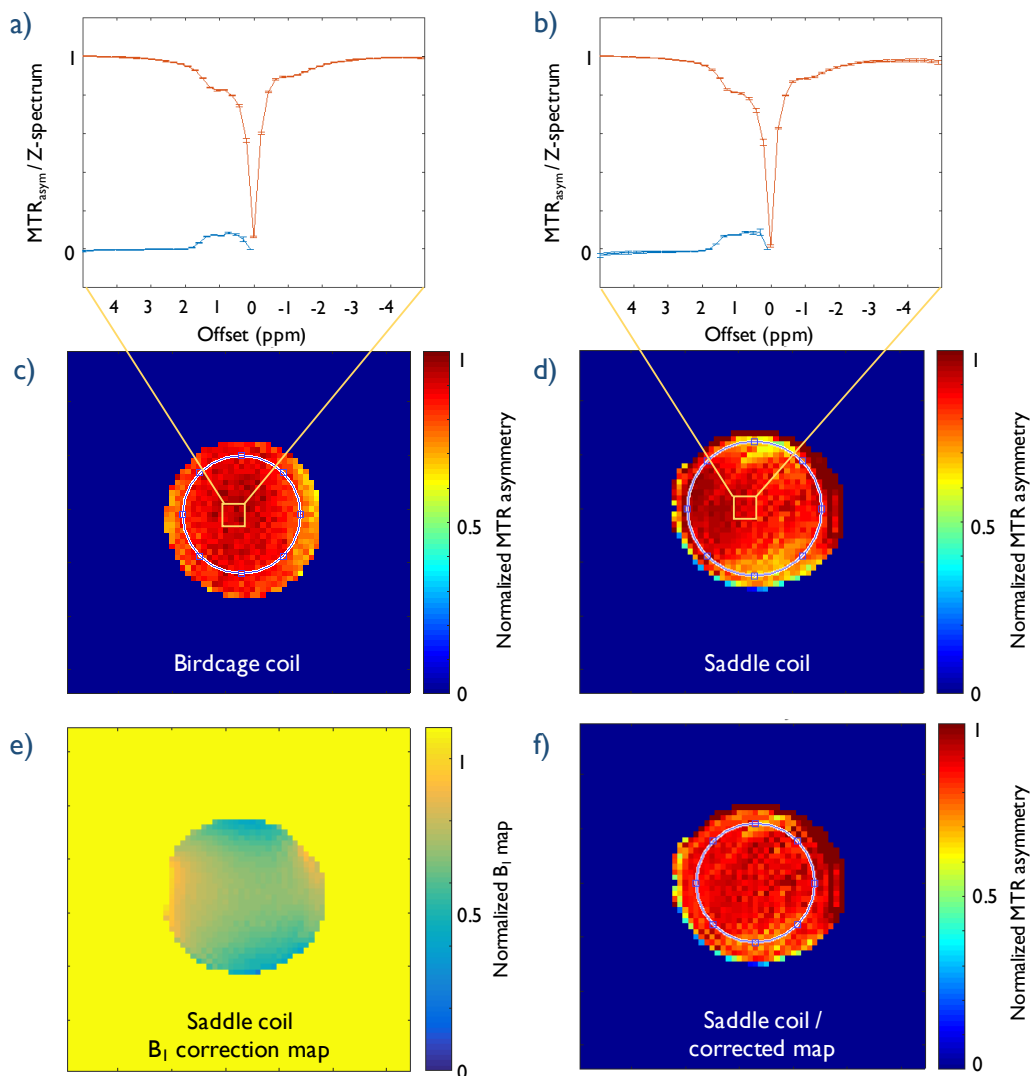


Figure C.4: MTR asymmetry and Z-spectra of a 50 mM glycogen phantom at pH = 7.16, room temperature. MTR asymmetry maps (uncorrected) obtained from **c)** a **16-leg birdcage coil** and **d)** a **saddle coil**. MTR asymmetry maps were obtained from voxel-wise summation of the MTR over [1; 0.5] ppm, sampling step size of 0.2 ppm, and normalized with respect to brightest point in image to account for possible nominal flip angle discrepancies. CEST measurements were conducted using $t_S = 6$ s, FOV = 35 x 35 mm², resolution of 64 x 64, imaging flip angle of 20°. **a), b)** Z-spectra with corresponding MTR asymmetries averaged over 25 central voxel (yellow square in c) and d) as well as their standard deviations. **e)** B_1 correction map for saddle coil experiment. **f)** MTR asymmetry map corrected for transmit field inhomogeneity. The corresponding statistics for CEST effect homogeneity acquired from 375 voxels within a cylindrical volume of 11 mm diameter and 2 mm thickness (encircled region) can be found in [Figure C.3](#).

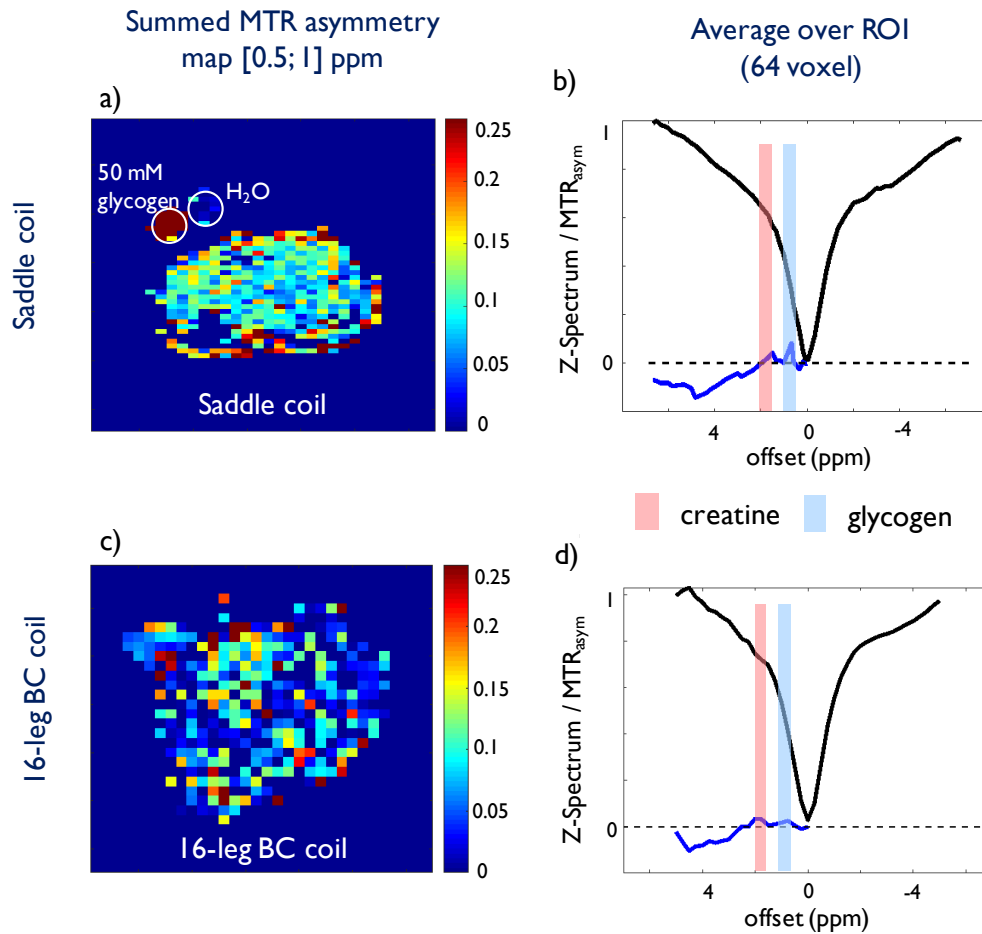


Figure C.5: *In vivo* glycoCEST MTR asymmetry maps of female Wistar rat thigh muscles with corresponding mean Z-spectra within 64 center voxels. The glycogen (blue bar) and creatine (red bar) CEST ranges are indicated around [1; 0.5]ppm and [1.7; 1.2]ppm, respectively. **a), b) Saddle coil.** Acquisition parameters: FOV = 30 x 30 mm², t_S = 10 s using a train of 345 pre-saturation pulses of 29 ms, resolution = 32 x 64. **c), d) 16-leg birdcage coil.** Acquisition parameters: FOV = 27 x 27 mm², t_S = 8 s using 276 saturation pulses of 29 ms, resolution = 32 x 32.

C.4 Discussion and Conclusion

The power required to generate a 90° pulse upon non-localized acquisition was 30 % lower for the 16-leg birdcage coil than for the 8-leg birdcage coil but still required $>3x$ as much power as the saddle coil. This higher B_1^+ efficiency when increasing the number of rungs N was to be expected from previous publications [288]. While the electromagnetic field simulations confirm increased transmit field homogeneity for a higher number of rungs, phantom experiments deviated from the theory. This indicated a decreased symmetry of the actual 16-leg birdcage coil. A possible causes for this asymmetry was identified as the deformation of the outer casing of the 16-leg birdcage coil. The deformation of the plastic casing was likely to have been caused by heating due to repetitive high power pulsing. Thus, the PCB of the 16-leg birdcage coil no longer matched a perfect cylindrical shape. With it, the current distribution along the rungs and the symmetry of the capacitors in space were subjected to deviations from an ideal distribution, leading to asymmetry in the transmit field intrinsic to the coil geometry. Meanwhile, the ertalyte casing of the 8-leg birdcage coil withstood deformations, possibly owing to the high heat resistance and structural rigidity of the material. Consistent with these results was the higher MTR_{asym} coefficient of variation for the 16-leg birdcage coil.

The performance of the coils was comparable when used for CEST imaging, given the low standard deviation over a FOV as large as 1 cm^2 , especially after B_1^+ correction was applied. Investing additional time to acquire a B_1^+ correction map (eg. 2×5 min for a 32×32 resolution map using the double angle method) allowed for decreasing deviations for real CEST contrast below $\sim 5\%$ in all cases. Previous publications motivate the implementation of other transmit field correction methods to further decrease this bias [125]. *In vivo* glycoCEST displayed higher sensitivity with respect to the exchanging protons of creatine and glycogen for the saddle coil. Higher SNR and B_1^+ efficiency aid in detecting small metabolite concentrations that resonate close to the water resonance frequency reliably. In future glycoCEST experiments, the integration range for exchanging hydroxyl could be expanded to cover the full $[1.5;0.5]$ ppm range [121, 289]. This might increase the sensitivity of the CEST contrast since the hydroxyl peak was found to shift towards 1.5 ppm for high-amplitude pulsing compared to the 0.8 ppm for low amplitude pulsing [159].

Appendix D

5 T Polarizer Hardware Optimisations & Extensions

Contribution

Claudia C. Zanella contributed to the troubleshooting and implementation of the debugging solutions.

This chapter aims at documenting a few hardware optimizations and extensions that were implemented for the 5 T polarizer. It describes the changes conducted, the reasons for doing so and the specifications of the modified hardware. The aim was to record the state of the home-build polarizer for the future. A detailed description of the 5 T polarizer state as it was before the alterations described in this chapter was provided previously [283].

D.1 Excessive Helium Consumption

Several hardware issues occurred early on; a major one was related to excessive helium consumption with up to 100 l liquid helium in less than 48 hours. Apart from the obvious budget issues this also lead to limited scan time for solid state measurements at 1.1 K, well below 4 hours, rendering thermal measurements and microwave frequency sweeps difficult or even impossible. Several measures were put in place to counteract the excessive helium usage. First, the current transfer line extension was replaced by a custom-made extension of reduced mass to decrease the thermal load within the helium dewar (Figure D.1). Replacing the double-walled insulating extension line with a single-walled one was possible since no thermal insulation against ambient atmosphere was needed at the last 20 cm at the bottom of the helium dewar.

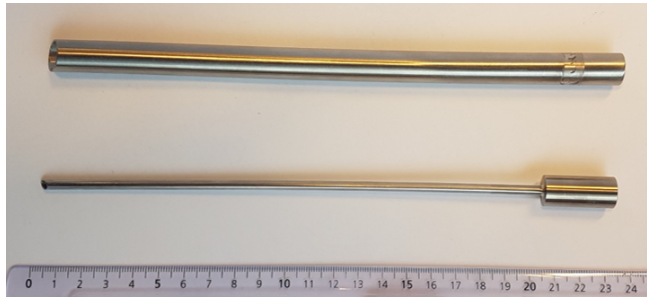


Figure D.1: The double-walled (**top**) transfer line extension was replaced by a single-walled (**bottom**) extension of only 4 mm outer \varnothing and a wall thickness of 1 mm to reduce the head load and thus the helium consumption.

Further, insufficient vacuum of transfer line of merely $\sim 10^{-3}$ mbar was identified as main cause of icing of the dewar clamp, safety valves, delivery port and the upper neck within minutes upon cooldown. This source of additional heat load was eliminated by repetitive pumping of the transfer line down to $10^{-6} - 10^{-7}$ mbar.

Moreover, pressures of up to 800 mbar were encountered during cool-down and filling procedures, despite the nominal pressure being set to 400 mbar. This led to uncharacteristically slow and uncontrolled cooling of the separator and sample space. Thus, manual flow control was implemented by adding an adjustable butterfly valve in front of the primary pump for pressure control.

The filling procedure was further complicated by the helium level probe being defective. Without this feedback loop, no indication of the level of helium inside the sample space was available and typical filling times based on prior experience did not apply due to the overly high filling pressure of 800 mbar. This led to either overfilling or insufficient filling, further reducing the time window of measurement at 1.1 K. After having replaced the helium level probe of the polarizer (Twickenham Scientific Instruments Ltd., SS-1250-650-7M-21, total length of 1250 mm, active length of 650 mm), to ensure reading of the helium level down to approximately 4 K ($p > 50$ mbar), a second stainless steel helium level probe was put in place to equally keep track of the dewar helium level. The second cryogenic probe of 550 mm active length, 1200 mm total length and 2.1 mm diameter (Cryogenic limited Ltd, UK, HLP-

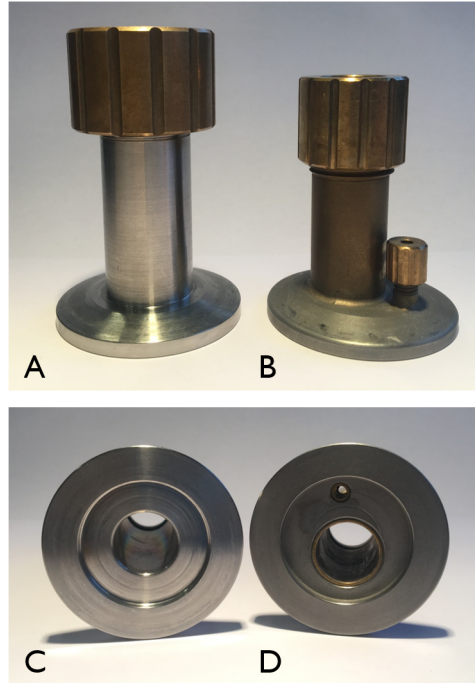


Figure D.2: The original helium dewar connector joining the transfer line to the helium reservoir (**A,C**) was replaced by a custom-made dewar connection piece equipped with a helium level probe inlet to monitor permanent the remaining helium level (**B,D**). Connector pieces viewed from the side (**top**) and from below (**bottom**).

AL550-TL1250) allowed for prompt liquid helium level measurements. The connection piece joining the transfer line to the helium reservoir was replaced by a custom-made connection piece with a supplementary inlet for the helium level probe (Figure D.2). A 2-channel HDI reader (Twickenham Scientific Instruments Ltd.) served as console.

D.2 Further Testing, Repairs and New Implementations

The MW power supply unit as well as the microwave source itself did not perform as requested. Power calibration tests confirmed that the microwave source (high power voltage controlled oscillator ELVA-1 VCOM-06/140/0.5/50-DD, L-1006/70, frequency range [139.5;140.5] GHz) only supplied a tenth of its set output power (Figure D.3). Also, a broken fuse holder of the power supply unit and arching circuits of the power supply unit were fixed.

A broken capacitor for remote tuning and matching of the saddle coil was replaced by a 1.5 - 250 pF piston trim (CTP-V1949, Surplus sales of Nebraska). Furthermore, the 90° bend connecting the microwave source to the waveguide was twisted by as much as 15°, reducing optimal power transmission efficiency (Figure D.4). The deformation with respect to the E-plane caused some power to be reflexed due to distorted beam pathway. A new WR-6 to WR-6 E-plane bend (Elmika, BE90D-02E, $\varnothing = 1 \times 1$ inch, brass/copper with gold plating) was put in place. A maximal insertion loss of 0.5 dB, and as little as 0.4 ± 0.02 dB at 140 ± 0.5 GHz, was guaranteed for the new connector.

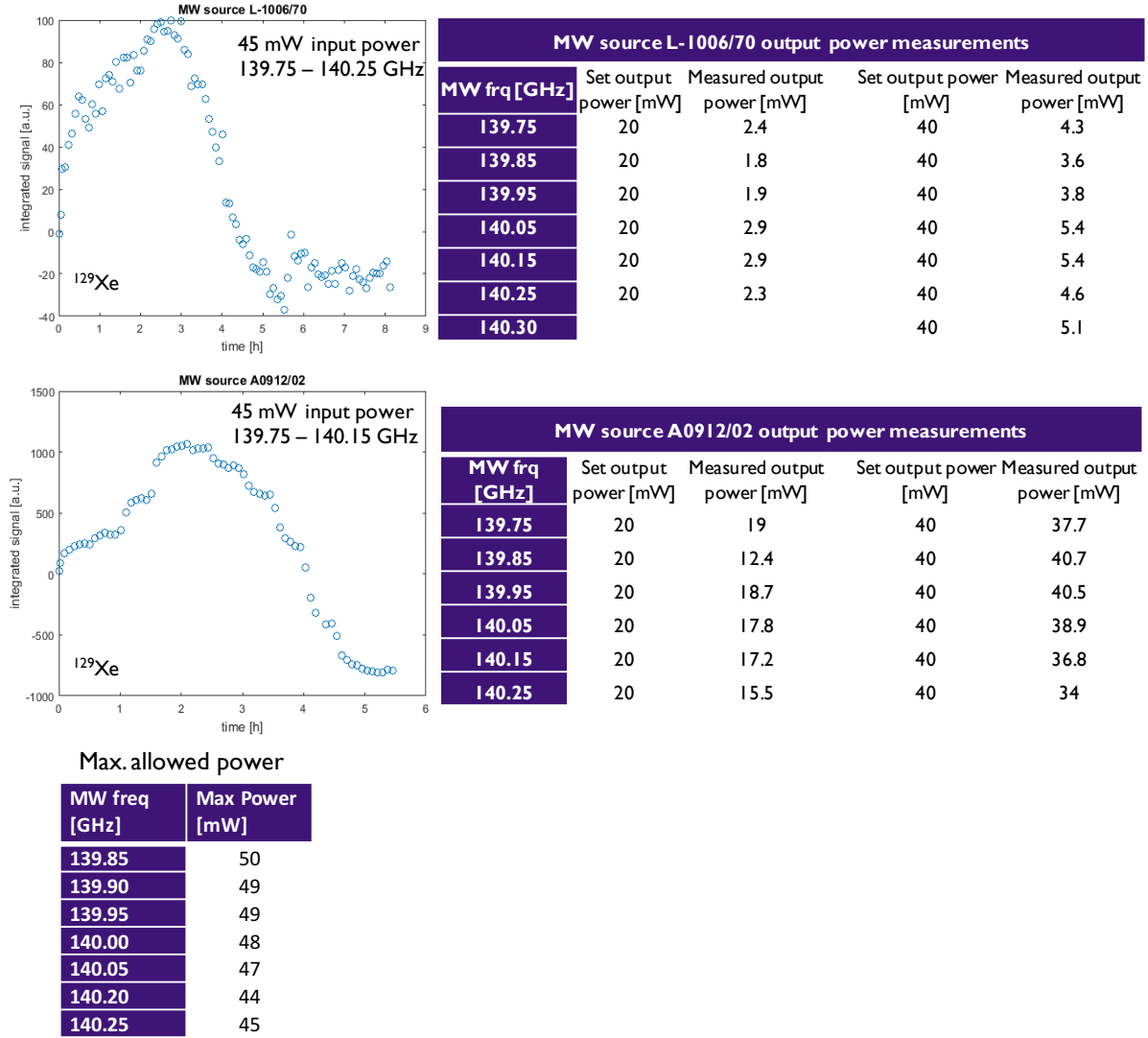


Figure D.3: Microwave source power calibration and power limitation performed on one ^{129}Xe sample confirming that the microwave source L-1006/70 supplied but a 10^{th} of its nominal output power.

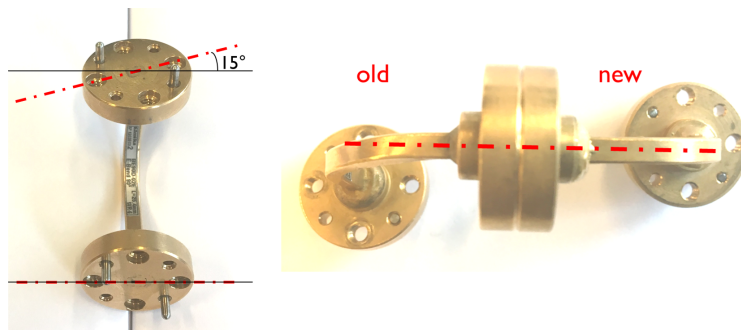


Figure D.4: The old 90° E-plane bend connector was replaced by a new one due to deformation by as much as 15° to ensure optimal microwave power transmission.

Bibliography

- [1] Robin A De Graaf. *In vivo NMR spectroscopy: principles and techniques*. John Wiley & Sons, 2019.
- [2] Jan-Henrik Ardenkjaer-Larsen, Gregory S Boebinger, Arnaud Comment, Simon Duckett, Arthur S Edison, Frank Engelke, Christian Griesinger, Robert G Griffin, Christian Hilty, Hidaeki Maeda, et al. Facing and overcoming sensitivity challenges in biomolecular NMR spectroscopy. *Angewandte Chemie International Edition*, 54(32):9162–9185, 2015.
- [3] Albert W Overhauser. Polarization of nuclei in metals. *Physical Review*, 92(2):411, 1953.
- [4] Tom R Carver and Charles P Slichter. Polarization of nuclear spins in metals. *Physical Review*, 92(1):212, 1953.
- [5] Jan H. Ardenkjær-Larsen, Björn Fridlund, Andreas Gram, Georg Hansson, Lennart Hansson, Mathilde H. Lerche, Rolf Servin, Mikkel Thaning, and Klaes Golman. Increase in signal-to-noise ratio of $> 10,000$ times in liquid-state NMR. *Proceedings of the National Academy of Sciences*, 100(18):10158–10163, 2003.
- [6] Klaes Golman and Mikkel Thaning. Real-time metabolic imaging. *Proceedings of the National Academy of Sciences*, 103(30):11270–11275, 2006.
- [7] Thomas R Eykyn, Richard Southworth, and Sebastian Kozerke. Dynamic nuclear polarization and mri for the study of cardiac metabolism. *Heart and metabolism*, (55):13–17, 2012.
- [8] Kevin M. Brindle. Imaging metabolism with hyperpolarized ^{13}C -labeled cell substrates. *Journal of the American Chemical Society*, 137(20):6418–6427, 2015.
- [9] Hikari AI Yoshihara, Jessica AM Bastiaansen, Corinne Berthonneche, Arnaud Comment, and Juerg Schwitter. An intact small animal model of myocardial ischemia-

- reperfusion: Characterization of metabolic changes by hyperpolarized ^{13}C MR spectroscopy. *American Journal of Physiology-Heart and Circulatory Physiology*, 309(12):H2058–H2066, 2015.
- [10] James T Grist, Jack J Miller, Fulvio Zaccagna, Mary A McLean, Frank Riemer, Tomasz Matys, Damian J Tyler, Christoffer Laustsen, Alasdair J Coles, and Ferdia A Gallagher. Hyperpolarized ^{13}C mri: A novel approach for probing cerebral metabolism in health and neurological disease. *Journal of Cerebral Blood Flow & Metabolism*, 40(6):1137–1147, 2020.
 - [11] Arnaud Comment. Dissolution DNP for in vivo preclinical studies. *Journal of Magnetic Resonance*, 264:39–48, 2016.
 - [12] Jessica AM Bastiaansen, Matthew E. Merritt, and Arnaud Comment. Measuring changes in substrate utilization in the myocardium in response to fasting using hyperpolarized $[1-^{13}\text{C}]$ butyrate and $[1-^{13}\text{C}]$ pyruvate. *Scientific reports*, 6(1):1–11, 2016.
 - [13] Mor Mishkovsky and Arnaud Comment. Hyperpolarized MRS: New tool to study real-time brain function and metabolism. *Analytical biochemistry*, 529:270–277, 2017.
 - [14] Sarah J. Nelson, John Kurhanewicz, Daniel B. Vigneron, Peder EZ Larson, Andrea L. Harzstark, Marcus Ferrone, Mark Van Criekinge, Jose W. Chang, Robert Bok, and Ilwoo Park. Metabolic imaging of patients with prostate cancer using hyperpolarized $[1-^{13}\text{C}]$ pyruvate. *Science translational medicine*, 5(198):198ra108–198ra108, 2013.
 - [15] Craig R. Malloy, Matthew E. Merritt, and A. Dean Sherry. Could ^{13}C MRI assist clinical decision-making for patients with heart disease? *NMR in Biomedicine*, 24(8):973–979, 2011.
 - [16] Charles H. Cunningham, Justin YC Lau, Albert P. Chen, Benjamin J. Geraghty, William J. Perks, Idan Roifman, Graham A. Wright, and Kim A. Connelly. Hyperpolarized ^{13}C metabolic MRI of the human heart: initial experience. *Circulation research*, 119(11):1177–1182, 2016.
 - [17] Rahul Aggarwal, Daniel B. Vigneron, and John Kurhanewicz. Hyperpolarized 1- $[^{13}\text{C}]$ -pyruvate magnetic resonance imaging detects an early metabolic response to androgen ablation therapy in prostate cancer. *European urology*, 72(6):1028, 2017.

- [18] Vesselin Z. Miloushev, Kristin L. Granlund, Rostislav Boltyanskiy, Serge K. Lyashchenko, Lisa M. DeAngelis, Ingo K. Mellinshoff, Cameron W. Brennan, Vivian Tabar, T. Jonathan Yang, and Andrei I. Holodny. Metabolic imaging of the human brain with hyperpolarized ^{13}C pyruvate demonstrates ^{13}C lactate production in brain tumor patients. *Cancer research*, 78(14):3755–3760, 2018.
- [19] Z. I. Cleveland, A. S. Bdaiwi, M. M. Hossain, L. L. Walkup, R. P. Thomen, K. Ruppert, H. Wang, M. Willmering, J. P. Clancy, and J. C. Woods. Hyperpolarized ^{129}Xe diffusion MRI in cystic fibrosis lung disease: Evidence for pathological alveolar enlargement. In *A108. Pathophysiology in diffuse parenchymal lung diseases*, pages A2568–A2568. American Thoracic Society, 2019.
- [20] Lloyd Lumata, S James Ratnakar, Ashish Jindal, Matthew Merritt, Arnaud Comment, Craig Malloy, A Dean Sherry, and Zoltan Kovacs. BDPA: an efficient polarizing agent for fast dissolution dynamic nuclear polarization NMR spectroscopy. *Chemistry–A European Journal*, 17(39):10825–10827, 2011.
- [21] F Kurdzesau, B van den Brandt, A Comment, P Hautle, S Jannin, JJ van der Klink, and JA Konter. Dynamic nuclear polarization of small labelled molecules in frozen water–alcohol solutions. *Journal of Physics D: Applied Physics*, 41(15):155506, 2008.
- [22] Lloyd Lumata, Matthew E. Merritt, Craig R. Malloy, A. Dean Sherry, and Zoltan Kovacs. Impact of Gd^{3+} on DNP of $[1-^{13}\text{C}]$ pyruvate doped with trityl OX063, BDPA, or 4-oxo-TEMPO. *The journal of physical chemistry A*, 116(21):5129–5138, 2012.
- [23] Jan Henrik Ardenkjær-Larsen, Sean Bowen, Jan Raagaard Petersen, Oleksandr Rybalko, Mads Sloth Vinding, Marcus Ullisch, and Niels Chr Nielsen. Cryogen-free dissolution dynamic nuclear polarization polarizer operating at 3.35 T, 6.70 T, and 10.1 T. *Magnetic resonance in medicine*, 81(3):2184–2194, 2019.
- [24] A. Comment, B. vd van den Brandt, K. Uffmann, F. Kurdzesau, S. Jannin, J. A. Konter, P. Hautle, W. Th Wenckeback, R. Gruetter, and J. J. Van Der Klink. Design and performance of a DNP prepolarizer coupled to a rodent MRI scanner. *Concepts in magnetic resonance part B: Magnetic resonance engineering*, 31(4):255–269, 2007.
- [25] Andrea Capozzi, Tian Cheng, Giovanni Boero, Christophe Roussel, and Arnaud Comment. Thermal annihilation of photo-induced radicals following dynamic nuclear polarization to produce transportable frozen hyperpolarized ^{13}C -substrates. *Nature communications*, 8(1):1–7, 2017.

- [26] Pascal Miéville, Puneet Ahuja, Riddhiman Sarkar, Sami Jannin, Paul R. Vasos, Sandrine Gerber-Lemaire, Mor Mishkovsky, Arnaud Comment, Rolf Gruetter, and Olivier Ouari. Scavenging free radicals to preserve enhancement and extend relaxation times in NMR using dynamic nuclear polarization. *Angewandte Chemie International Edition*, 49(35):6182–6185, 2010.
- [27] John P. Mugler III and Talissa A. Altes. Hyperpolarized ^{129}Xe MRI of the human lung. *Journal of Magnetic Resonance Imaging*, 37(2):313–331, 2013.
- [28] Xin Zhou, Yanping Sun, Mary Mazzanti, Nils Henninger, Joey Mansour, Marc Fisher, and Mitchell Albert. MRI of stroke using hyperpolarized ^{129}Xe . *NMR in Biomedicine*, 24(2):170–175, 2011.
- [29] Arnaud Comment, Sami Jannin, J-N Hyacinthe, Pascal Miéville, Riddhiman Sarkar, Puneet Ahuja, Paul R Vasos, Xavier Montet, François Lazeyras, J-P Vallée, et al. Hyperpolarizing gases via dynamic nuclear polarization and sublimation. *Physical review letters*, 105(1):018104, 2010.
- [30] Aurélien Bornet, Jonas Milani, Basile Vuichoud, Angel J. Perez Linde, Geoffrey Bodenhausen, and Sami Jannin. Microwave frequency modulation to enhance dissolution dynamic nuclear polarization. *Chemical Physics Letters*, 602:63–67, 2014.
- [31] David I Hoult and RE Richards. The signal-to-noise ratio of the nuclear magnetic resonance experiment. *Journal of Magnetic Resonance (1969)*, 24(1):71–85, 1976.
- [32] Ivan Tkáč, Z. Starčuk, I.-Y. Choi, and R. Gruetter. In vivo ^1H NMR spectroscopy of rat brain at 1 ms echo time. *Magnetic Resonance in Medicine*, 41(4):649–656, 1999.
- [33] Cecil E. Hayes, William A. Edelstein, John F. Schenck, Otward M. Mueller, and Matthew Eash. An efficient, highly homogeneous radiofrequency coil for whole-body NMR imaging at 1.5 T. *Journal of Magnetic Resonance*, 63(3):622–628, 1985.
- [34] Thomas Neuberger, V Tyagi, E Semouchkina, M Lanagan, A Baker, K Haines, and AG Webb. Design of a ceramic dielectric resonator for NMR microimaging at 14.1 tesla. *Concepts in Magnetic Resonance Part B: Magnetic Resonance Engineering*, 33(2):109–114, 2008.
- [35] Xiaozhong Zhang and Andrew Webb. Design of a capacitively decoupled transmit/receive NMR phased array for high field microscopy at 14.1 T. *Journal of Magnetic Resonance*, 170(1):149–155, 2004.

- [36] Peter J Hore. *Nuclear magnetic resonance*. Oxford University Press, USA, 2015.
- [37] Filip Jiru. Introduction to post-processing techniques. *European journal of radiology*, 67(2):202–217, 2008.
- [38] Matthew L Hirsch, Neal Kalechofsky, Avrum Belzer, Melanie Rosay, and James G Kempf. Brute-force hyperpolarization for NMR and MRI. *Journal of the American Chemical Society*, 137(26):8428–8434, 2015.
- [39] EV Krjukov, JD ONeill, and JR Owers-Bradley. Brute force polarization of ^{129}Xe . *Journal of low temperature physics*, 140(5-6):397–408, 2005.
- [40] W Happer, E Miron, S Schaefer, D Schreiber, WA Van Wijngaarden, and X Zeng. Polarization of the nuclear spins of noble-gas atoms by spin exchange with optically pumped alkali-metal atoms. *Physical Review A*, 29(6):3092, 1984.
- [41] Thad G Walker and William Happer. Spin-exchange optical pumping of noble-gas nuclei. *Reviews of modern physics*, 69(2):629, 1997.
- [42] Panayiotis Nikolaou, Aaron M Coffey, Laura L Walkup, Brogan M Gust, Nicholas Whiting, Hayley Newton, Scott Barcus, Iga Muradyan, Mikayel Dabaghyan, Gregory D Moroz, et al. Near-unity nuclear polarization with an open-source ^{129}Xe hyperpolarizer for NMR and MRI. *Proceedings of the National Academy of Sciences*, 110(35):14150–14155, 2013.
- [43] IC Ruset, S Ketel, and F William Hersman. Optical pumping system design for large production of hyperpolarized Xe ^{129} . *Physical review letters*, 96(5):053002, 2006.
- [44] G Norquay, G Collier, O Rodgers, and J. Wild. High-performance portable spin-exchange optical pumping polarizer for hyperpolarized ^{129}Xe MRI. In *Proceedings of the 26th Annual Meeting of ISMRM, Paris, France*, 2018.
- [45] Panayiotis Nikolaou, Aaron M Coffey, Kaili Ranta, Laura L Walkup, Brogan M Gust, Michael J Barlow, Matthew S Rosen, Boyd M Goodson, and Eduard Y Chekmenev. Multidimensional mapping of spin-exchange optical pumping in clinical-scale batch-mode ^{129}Xe hyperpolarizers. *The Journal of Physical Chemistry B*, 118(18):4809–4816, 2014.
- [46] C Russell Bowers and Daniel P Weitekamp. Parahydrogen and synthesis allow dramatically enhanced nuclear alignment. *Journal of the American Chemical Society*, 109(18):5541–5542, 1987.

- [47] Louis-S Bouchard, Scott R Burt, M Sabieh Anwar, Kirill V Kovtunov, Igor V Koptug, and Alexander Pines. NMR imaging of catalytic hydrogenation in microreactors with the use of para-hydrogen. *Science*, 319(5862):442–445, 2008.
- [48] EI Bunyatova. Free radicals and polarized targets. *Nuclear Instruments and Methods in Physics Research Section A: Accelerators, Spectrometers, Detectors and Associated Equipment*, 526(1-2):22–27, 2004.
- [49] Lloyd Lumata, Zoltan Kovacs, A Dean Sherry, Craig Malloy, Stephen Hill, Johan Van Tol, Lu Yu, Likai Song, and Matthew E Merritt. Electron spin resonance studies of trityl OX063 at a concentration optimal for DNP. *Physical Chemistry Chemical Physics*, 15(24):9800–9807, 2013.
- [50] Ralph E Hurd, Yi-Fen Yen, Albert Chen, and Jan Henrik Ardenkjaer-Larsen. Hyperpolarized ^{13}C metabolic imaging using dissolution dynamic nuclear polarization. *Journal of Magnetic Resonance Imaging*, 36(6):1314–1328, 2012.
- [51] Ta-Chung Ong, Melody L Mak-Jurkauskas, Joseph J Walish, Vladimir K Michaelis, Björn Corzilius, Albert A Smith, Andrew M Clausen, Janet C Cheetham, Timothy M Swager, and Robert G Griffin. Solvent-free dynamic nuclear polarization of amorphous and crystalline ortho-terphenyl. *The Journal of Physical Chemistry B*, 117(10):3040–3046, 2013.
- [52] Hikari AI Yoshihara, Emine Can, Magnus Karlsson, Mathilde H. Lerche, Juerg Schwit-ter, and Arnaud Comment. High-field dissolution dynamic nuclear polarization of $[1-^{13}\text{C}]$ pyruvic acid. *Physical Chemistry Chemical Physics*, 18(18):12409–12413, 2016.
- [53] Jan Henrik Ardenkjær-Larsen. On the present and future of dissolution-DNP. *Journal of Magnetic Resonance*, 264:3–12, 2016.
- [54] T. Kumada, Y. Noda, T. Hashimoto, and S. Koizumi. Dynamic nuclear polarization study of UV-irradiated butanol for hyperpolarized liquid NMR. *Journal of Magnetic Resonance*, 201(2):115–120, 2009.
- [55] Irene Marco-Rius, Tian Cheng, Adam P. Gaunt, Saket Patel, Felix Kreis, Andrea Capozzi, Alan J. Wright, Kevin M. Brindle, Olivier Ouari, and Arnaud Comment. Photogenerated radical in phenylglyoxylic acid for in vivo hyperpolarized ^{13}C MR with photosensitive metabolic substrates. *Journal of the American Chemical Society*, 140(43):14455–14463, 2018.

- [56] Tim R. Eichhorn, Yuhei Takado, Najat Salameh, Andrea Capozzi, Tian Cheng, Jean-Noël Hyacinthe, Mor Mishkovsky, Christophe Roussel, and Arnaud Comment. Hyperpolarization without persistent radicals for in vivo real-time metabolic imaging. *Proceedings of the National Academy of Sciences*, 110(45):18064–18069, 2013.
- [57] Jessica AM Bastiaansen, Hikari AI Yoshihara, Andrea Capozzi, Juerg Schwitter, Rolf Gruetter, Matthew E. Merritt, and Arnaud Comment. Probing cardiac metabolism by hyperpolarized ^{13}C MR using an exclusively endogenous substrate mixture and photo-induced nonpersistent radicals. *Magnetic resonance in medicine*, 79(5):2451–2459, 2018.
- [58] Aleksander Jablonski. Efficiency of anti-stokes fluorescence in dyes. *Nature*, 131(3319):839–840, 1933.
- [59] Marcelo I Guzman, Agustin J Colussi, and Michael R Hoffmann. Photogeneration of distant radical pairs in aqueous pyruvic acid glasses. *The Journal of Physical Chemistry A*, 110(3):931–935, 2006.
- [60] Peter A Leermakers and George F Vesley. The photochemistry of α -keto acids and α -keto esters. I. Photolysis of pyruvic acid and benzoylformic acid. *Journal of the American Chemical Society*, 85(23):3776–3779, 1963.
- [61] Lalitha J Mittal, JP Mittal, and E Hayon. Photo-induced decarboxylation of aliphatic acids and esters in solution. Dependence upon state of protonation of the carboxyl group. *The Journal of Physical Chemistry*, 77(12):1482–1487, 1973.
- [62] Matthieu Cavaillès, Aurélien Bornet, Xavier Jaurand, Basile Vuichoud, David Baudouin, Mathieu Baudin, Laurent Veyre, Geoffrey Bodenhausen, Jean-Nicolas Dumez, Sami Jannin, et al. Tailored microstructured hyperpolarizing matrices for optimal magnetic resonance imaging. *Angewandte Chemie*, 130(25):7575–7579, 2018.
- [63] T E Daraï, D Montarnal, S Cousin, A Ferrari, D Gajan, M Ceillier, O Cala, and S Jannin. Generating, storing and transporting hyperpolarization with HYPOP (hyperpolarizing porous polymers). In *Proceedings of the 60th Experimental Nuclear Magnetic Resonance Conference (ENC), CA, US*, 2019.
- [64] W Tom Wenckebach. *Essentials of Dynamic Nuclear Polarization*. Spindrift Publications, 2016.
- [65] JH Van Vleck. The dipolar broadening of magnetic resonance lines in crystals. *Physical Review*, 74(9):1168, 1948.

- [66] Andrea Capozzi, Christophe Roussel, Arnaud Comment, and Jean-Noël Hyacinthe. Optimal glass-forming solvent brings sublimation dynamic nuclear polarization to ^{129}Xe hyperpolarization biomedical imaging standards. *The Journal of Physical Chemistry C*, 119(9):5020–5025, 2015.
- [67] R de L Kronig. On the mechanism of paramagnetic relaxation. *Physica*, 6(1):33–43, 1939.
- [68] JH Van Vleck. Paramagnetic relaxation times for titanium and chrome alum. *Physical Review*, 57(5):426, 1940.
- [69] CBP Finn, R Orbach, and WP Wolf. Spin-lattice relaxation in cerium magnesium nitrate at liquid helium temperature: a new process. *Proceedings of the Physical Society*, 77(2):261, 1961.
- [70] C Hess, J Herick, A Berlin, W Meyer, and G Reicherz. Measurement of electron spin-lattice relaxation times in radical doped butanol samples at 1 K using the NEDOR method. *Nuclear Instruments and Methods in Physics Research Section A: Accelerators, Spectrometers, Detectors and Associated Equipment*, 694:69–77, 2012.
- [71] Anatole Abragam and Maurice Goldman. Nuclear magnetism: order and disorder. 1982.
- [72] Marina Kveder, Dalibor Merunka, Milan Jokić, and Boris Rakvin. Low-temperature electron-spin relaxation in the crystalline and glassy states of solid ethanol. *Physical review B*, 77(9):094202, 2008.
- [73] Peter CM van Zijl, Wilfred W Lam, Jiadi Xu, Linda Knutsson, and Greg J Stanisiz. Magnetization transfer contrast and chemical exchange saturation transfer MRI. Features and analysis of the field-dependent saturation spectrum. *Neuroimage*, 168:222–241, 2018.
- [74] Ionel Solomon. Relaxation processes in a system of two spins. *Physical Review*, 99(2):559, 1955.
- [75] A Abragam. Overhauser effect in nonmetals. *Physical Review*, 98(6):1729, 1955.
- [76] Aany Sofia Lilly Thankamony, Johannes J Wittmann, Monu Kaushik, and Bjoern Corzilius. Dynamic nuclear polarization for sensitivity enhancement in modern solid-state NMR. *Progress in Nuclear Magnetic Resonance Spectroscopy*, 102:120–195, 2017.

- [77] Alfred G Redfield. Nuclear magnetic resonance saturation and rotary saturation in solids. *Physical Review*, 98(6):1787, 1955.
- [78] BN Provotorov. A quantum statistical theory of cross relaxation. *Sov. Phys. JETP*, 15(3):611–614, 1962.
- [79] Michel Borghini. Spin-temperature model of nuclear dynamic polarization using free radicals. *Physical Review Letters*, 20(9):419, 1968.
- [80] Benedikt Preckel, Nina C Weber, Robert D Sanders, Mervyn Maze, and Wolfgang Schlack. Molecular mechanisms transducing the anesthetic, analgesic, and organ-protective actions of xenon. *The Journal of the American Society of Anesthesiologists*, 105(1):187–197, 2006.
- [81] JP Coles. Imaging after brain injury. *British journal of anaesthesia*, 99(1):49–60, 2007.
- [82] Katie Harris, Scott P Armstrong, Rita Campos-Pires, Louise Kiru, Nicholas P Franks, and Robert Dickinson. Neuroprotection against traumatic brain injury by xenon, but not argon, is mediated by inhibition at the N-methyl-D-aspartate receptor glycine site. *Anesthesiology: The Journal of the American Society of Anesthesiologists*, 119(5):1137–1148, 2013.
- [83] Ecem Esencan, Simge Yuksel, Yusuf Berk Tosun, Alexander Robinot, Ihsan Solaroglu, and John H Zhang. Xenon in medical area: emphasis on neuroprotection in hypoxia and anesthesia. *Medical gas research*, 3(1):4, 2013.
- [84] Rita Campos-Pires, Scott P Armstrong, Anne Sebastiani, Clara Luh, Marco Gruss, Konstantin Radyushkin, Tobias Hirnet, Christian Werner, Kristin Engelhard, Nicholas P Franks, et al. Xenon improves neurological outcome and reduces secondary injury following trauma in an in vivo model of traumatic brain injury. *Critical care medicine*, 43(1):149, 2015.
- [85] Siyuan P Sheng, Beilei Lei, Michael L James, Christopher D Lascola, Talaighair N Venkatraman, Jin Yong Jung, Mervyn Maze, Nicholas P Franks, Robert D Pearlstein, Huaxin Sheng, et al. Xenon neuroprotection in experimental strokeinteractions with hypothermia and intracerebral hemorrhage. *Anesthesiology: The Journal of the American Society of Anesthesiologists*, 117(6):1262–1275, 2012.
- [86] J Lavaur, Marc Lemaire, J Pype, D Le Nogue, EC Hirsch, and Patrick Pierre Michel. Xenon-mediated neuroprotection in response to sustained, low-level excitotoxic stress. *Cell death discovery*, 2:16018, 2016.

- [87] Tuo Yang, Yang Sun, and Feng Zhang. Anti-oxidative aspect of inhaled anesthetic gases against acute brain injury. *Medical gas research*, 6(4):223, 2016.
- [88] James R Trudell, Donald D Koblin, and Edmond I Eger. A molecular description of how noble gases and nitrogen bind to a model site of anesthetic action. *Anesthesia & Analgesia*, 87(2):411–418, 1998.
- [89] Eric Honoré. The neuronal background K⁺ 2P channels: focus on TREK1. *Nature reviews neuroscience*, 8(4):251, 2007.
- [90] Scott P Armstrong, Paul J Banks, Thomas JW McKittrick, Catharine H Geldart, Christopher J Edge, Rohan Babla, Constantinos Simillis, Nicholas P Franks, and Robert Dickinson. Identification of two mutations (f758w and f758y) in the n-methyl-d-aspartate receptor glycine-binding site that selectively prevent competitive inhibition by xenon without affecting glycine binding. *Anesthesiology: The Journal of the American Society of Anesthesiologists*, 117(1):38–47, 2012.
- [91] Paul D Leeson and Leslie L Iversen. The glycine site on the nmda receptor: structure-activity relationships and therapeutic potential. *Journal of medicinal chemistry*, 37(24):4053–4067, 1994.
- [92] Robert Dickinson, Brian K Peterson, Paul Banks, Constantinos Simillis, Juan Carlos Sacristan Martin, Carlos A Valenzuela, Mervyn Maze, and Nicholas P Franks. Competitive inhibition at the glycine site of the n-methyl-d-aspartate receptor by the anesthetics xenon and isoflurane: evidence from molecular modeling and electrophysiology. *The Journal of the American Society of Anesthesiologists*, 107(5):756–767, 2007.
- [93] Ludovic Sauguet, Zeineb Fourati, Thierry Prangé, Marc Delarue, and Nathalie Colloc’h. Structural basis for xenon inhibition in a cationic pentameric ligand-gated ion channel. *PLoS One*, 11(2):e0149795, 2016.
- [94] Michael T McMahon and Assaf A Gilad. Cellular and molecular imaging using chemical exchange saturation transfer (CEST). *Topics in magnetic resonance imaging: TMRI*, 25(5):197, 2016.
- [95] Andrea Cherubini and Angelo Bifone. Hyperpolarised xenon in biology. *Progress in Nuclear Magnetic Resonance Spectroscopy*, 42(1):1–30, 2003.
- [96] Débora B Vieira and Lionel F Gamarra. Getting into the brain: liposome-based strategies for effective drug delivery across the blood–brain barrier. *International journal of nanomedicine*, 11:5381, 2016.

- [97] David ML Lilburn, Galina E Pavlovskaya, and Thomas Meersmann. Perspectives of hyperpolarized noble gas mri beyond 3he. *Journal of Magnetic Resonance*, 229:173–186, 2013.
- [98] Haidong Li, Xiuchao Zhao, Yujin Wang, Xin Lou, Shizhen Chen, He Deng, Lei Shi, Junshuai Xie, Dazhong Tang, Jianping Zhao, et al. Damaged lung gas exchange function of discharged covid-19 patients detected by hyperpolarized 129xe mri. *Science advances*, 7(1):eabc8180, 2021.
- [99] CFM Clewett and T Pietra β . 129Xe and 131Xe NMR of gas adsorption on single-and multi-walled carbon nanotubes. *The Journal of Physical Chemistry B*, 109(38):17907–17912, 2005.
- [100] Ana-Maria Oros and N Jon Shah. Hyperpolarized xenon in NMR and MRI. *Physics in medicine and biology*, 49(20):R105–R153, 2004.
- [101] Thomas Meersmann and Eike Brunner. *Hyperpolarized xenon-129 magnetic resonance: concepts, production, techniques and applications*. Number 4. Royal Society of Chemistry, 2015.
- [102] Danila A Barskiy, Aaron M Coffey, Panayiotis Nikolaou, Dmitry M Mikhaylov, Boyd M Goodson, Rosa T Branca, George J Lu, Mikhail G Shapiro, Ville-Veikko Telkki, Vladimir V Zhivonitko, et al. NMR hyperpolarization techniques of gases. *Chemistry*, 23(4):725, 2017.
- [103] Zackary I. Cleveland, Gary P. Cofer, Gregory Metz, Denise Beaver, John Nouns, S. Sivaram Kaushik, Monica Kraft, Jan Wolber, Kevin T. Kelly, and H. Page McAdams. Hyperpolarized 129Xe MR imaging of alveolar gas uptake in humans. *PloS one*, 5(8), 2010.
- [104] Zaiyi Liu, Tetsuro Araki, Yuka Okajima, Mitchell Albert, and Hiroto Hatabu. Pulmonary hyperpolarized noble gas MRI: recent advances and perspectives in clinical application. *European journal of radiology*, 83(7):1282–1291, 2014.
- [105] Neil J Stewart, General Leung, Graham Norquay, Helen Marshall, Juan Parra-Robles, Philip S Murphy, Rolf F Schulte, Charlie Elliot, Robin Condliffe, Paul D Griffiths, et al. Experimental validation of the hyperpolarized 129Xe chemical shift saturation recovery technique in healthy volunteers and subjects with interstitial lung disease. *Magnetic Resonance in Medicine*, 74(1):196–207, 2015.

- [106] Madhwesha R Rao, Neil J Stewart, Paul D Griffiths, Graham Norquay, and Jim M Wild. Imaging human brain perfusion with inhaled hyperpolarized ^{129}Xe MR imaging. *Radiology*, 286(2):659–665, 2018.
- [107] Madhwesha Rao, Neil J Stewart, Graham Norquay, Paul D Griffiths, and Jim M Wild. High resolution spectroscopy and chemical shift imaging of hyperpolarized ^{129}Xe dissolved in the human brain in vivo at 1.5 tesla. *Magnetic resonance in medicine*, 75(6):2227–2234, 2016.
- [108] Francis T Hane, Tao Li, Jennifer-Anne Plata, Ayman Hassan, Karl Granberg, and Mitchell S Albert. Inhaled xenon washout as a biomarker of alzheimers disease. *Diagnostics*, 8(2):41, 2018.
- [109] Leif Schröder, Thomas J Lowery, Christian Hilty, David E Wemmer, and Alexander Pines. Molecular imaging using a targeted magnetic resonance hyperpolarized biosensor. *Science*, 314(5798):446–449, 2006.
- [110] L. Schröder. Xenon Biosensor HyperCEST MRI. In *Hyperpolarized and Inert Gas MRI*, pages 263–277. Elsevier, 2017.
- [111] Anatole Abragam. *The principles of nuclear magnetism*. Number 32. Oxford university press, 1961.
- [112] Andrew Webb. Increasing the sensitivity of magnetic resonance spectroscopy and imaging. *Analytical Chemistry*, 84(1):9–16, 2012. PMID: 21978101.
- [113] D. M. Ginsberg and Melvin J. Melchner. Optimum geometry of saddle shaped coils for generating a uniform magnetic field. *Review of Scientific Instruments*, 41(1):122–123, 1970.
- [114] Peter Mansfield. *NMR imaging in biomedicine: Supplement 2 advances in magnetic resonance*, volume 2. Elsevier, 1982.
- [115] James Tropp. The theory of the bird-cage resonator. *Journal of Magnetic Resonance (1969)*, 82(1):51–62, 1989.
- [116] Mark C. Leifer. Resonant modes of the birdcage coil. *Journal of Magnetic Resonance*, 124(1):51–60, 1997.
- [117] I. Jo Mispelter, Mihaela Lupu, and Andr Briguët. *NMR probeheads for biophysical and biomedical experiments: theoretical principles & practical guidelines*. Imperial college press, 2006.

- [118] James Tropp. The theory of an arbitrarily perturbed bird-cage resonator, and a simple method for restoring it to full symmetry. *Journal of Magnetic Resonance* (1969), 95(2):235–243, 1991.
- [119] KM Ward, AH Aletras, and Robert S Balaban. A new class of contrast agents for mri based on proton chemical exchange dependent saturation transfer (CEST). *Journal of magnetic resonance*, 143(1):79–87, 2000.
- [120] Peter CM Van Zijl and Nirbhay N. Yadav. Chemical exchange saturation transfer (CEST): what is in a name and what isn’t? *Magnetic resonance in medicine*, 65(4):927–948, 2011.
- [121] Elena Vinogradov, a Dean Sherry, and Robert E Lenkinski. CEST: from basic principles to applications, challenges and opportunities. *Journal of magnetic resonance*, 229:155–72, apr 2013.
- [122] Feliks Kogan, Hari Hariharan, and Ravinder Reddy. Chemical exchange saturation transfer (CEST) imaging: description of technique and potential clinical applications. *Current radiology reports*, 1(2):102–114, 2013.
- [123] Moritz Zaiss and Peter Bachert. Chemical exchange saturation transfer (CEST) and MR Z-spectroscopy in vivo: a review of theoretical approaches and methods. *Physics in Medicine & Biology*, 58(22):R221, 2013.
- [124] Peter CM van Zijl and Akansha Ashvani Sehgal. Proton chemical exchange saturation transfer (CEST) MRS and MRI. *eMagRes*, pages 1307–1332, 2007.
- [125] Adrienne N Dula, Seth A Smith, and John C Gore. Application of chemical exchange saturation transfer (CEST) MRI for endogenous contrast at 7 Tesla. *Journal of Neuroimaging*, 23(4):526–532, 2013.
- [126] Jinyuan Zhou, Jean-Francois Payen, David A Wilson, Richard J Traystman, and Peter CM Van Zijl. Using the amide proton signals of intracellular proteins and peptides to detect pH effects in MRI. *Nature medicine*, 9(8):1085, 2003.
- [127] Nirbhay N Yadav, Craig K Jones, Jiadi Xu, Amnon Bar-Shir, Assaf A Gilad, Michael T McMahon, and Peter CM van Zijl. Detection of rapidly exchanging compounds using on-resonance frequency-labeled exchange (FLEX) transfer. *Magnetic resonance in medicine*, 68(4):1048–1055, 2012.

- [128] Moritz Zaiss, Junzhong Xu, Steffen Goerke, Imad S Khan, Robert J Singer, John C Gore, Daniel F Gochberg, and Peter Bachert. Inverse Z-spectrum analysis for spillover-MT-, and T1-corrected steady-state pulsed CEST-MRI-application to pH-weighted MRI of acute stroke. *NMR in biomedicine*, 27(3):240–252, 2014.
- [129] Harden M McConnell. Reaction rates by nuclear magnetic resonance. *The Journal of Chemical Physics*, 28(3):430–431, 1958.
- [130] Steven D Wolff and Robert S Balaban. Magnetization transfer contrast (MTC) and tissue water proton relaxation in vivo. *Magnetic resonance in medicine*, 10(1):135–144, 1989.
- [131] Sture Forsén and Ragnar A Hoffman. Study of moderately rapid chemical exchange reactions by means of nuclear magnetic double resonance. *The Journal of Chemical Physics*, 39(11):2892–2901, 1963.
- [132] Donald E Woessner, Shanrong Zhang, Matthew E Merritt, and A Dean Sherry. Numerical solution of the Bloch equations provides insights into the optimum design of PARACEST agents for MRI. *Magnetic Resonance in Medicine*, 53(4):790–799, 2005.
- [133] Phillip Zhe Sun. Simplified and scalable numerical solution for describing multi-pool chemical exchange saturation transfer (CEST) MRI contrast. *Journal of magnetic resonance*, 205(2):235–241, 2010.
- [134] K Herz, K Scheffler, and M Zaiss. CEST Simulations: Toolbox for Bloch-McConnell equations with arbitrary number of pools. In *36th Annual Scientific Meeting of the European Society for Magnetic Resonance in Medicine and Biology (ESMRMB 2019)*, page 422, 2019.
- [135] Kenya Murase and Nobuyoshi Tanki. Numerical solutions to the time-dependent Bloch equations revisited. *Magnetic resonance imaging*, 29(1):126–131, 2011.
- [136] Evelyne Baguet and Claude Roby. Off-resonance irradiation effect in steady-state NMR saturation transfer. *Journal of Magnetic Resonance*, 128(2):149–160, 1997.
- [137] Phillip Zhe Sun, Christian T Farrar, and A Gregory Sorensen. Correction for artifacts induced by B0 and B1 field inhomogeneities in pH-sensitive chemical exchange saturation transfer (CEST) imaging. *Magnetic Resonance in Medicine*, 58(6):1207–1215, 2007.

- [138] Jinyuan Zhou, David A Wilson, Phillip Zhe Sun, Judith A Klaus, and Peter CM Van Zijl. Quantitative description of proton exchange processes between water and endogenous and exogenous agents for WEX, CEST, and APT experiments. *Magnetic Resonance in Medicine*, 51(5):945–952, 2004.
- [139] Jinyuan Zhou and Peter C Van Zijl. Chemical exchange saturation transfer imaging and spectroscopy. *Progress in Nuclear Magnetic Resonance Spectroscopy*, 48(2-3):109–136, 2006.
- [140] Hye-Young Heo, Yi Zhang, Dong-Hoon Lee, Shanshan Jiang, Xuna Zhao, and Jinyuan Zhou. Accelerating chemical exchange saturation transfer (cest) mri by combining compressed sensing and sensitivity encoding techniques. *Magnetic resonance in medicine*, 77(2):779–786, 2017.
- [141] Grzegorz Kwiatkowski and Sebastian Kozerke. Accelerating cest mri in the mouse brain at 9.4 t by exploiting sparsity in the z-spectrum domain. *NMR in Biomedicine*, 33(9):e4360, 2020.
- [142] Jonathan Grad and Robert G Bryant. Nuclear magnetic cross-relaxation spectroscopy. *Journal of Magnetic Resonance (1969)*, 90(1):1–8, 1990.
- [143] A Dean Sherry and Mark Woods. Chemical exchange saturation transfer contrast agents for magnetic resonance imaging. *Annu. Rev. Biomed. Eng.*, 10:391–411, 2008.
- [144] Susumu Mori, Scott M Eleff, Ulrich Pilatus, Noriko Mori, and Peter CM Van Zijl. Proton NMR spectroscopy of solvent-saturable resonances: a new approach to study pH effects in situ. *Magnetic resonance in medicine*, 40(1):36–42, 1998.
- [145] Peter CM Van Zijl, Jinyuan Zhou, Noriko Mori, Jean-Francois Payen, David Wilson, and Susumu Mori. Mechanism of magnetization transfer during on-resonance water saturation. A new approach to detect mobile proteins, peptides, and lipids. *Magnetic Resonance in Medicine*, 49(3):440–449, 2003.
- [146] Craig K Jones, Alan Huang, Jiadi Xu, Richard AE Edden, Michael Schär, Jun Hua, Nikita Oskolkov, Domenico Zacà, Jinyuan Zhou, Michael T McMahon, et al. Nuclear overhauser enhancement (NOE) imaging in the human brain at 7 T. *Neuroimage*, 77:114–124, 2013.
- [147] V Guivel-Scharen, T Sinnwell, SD Wolff, and RS Balaban. Detection of proton chemical exchange between metabolites and water in biological tissues. *Journal of Magnetic Resonance*, 133(1):36–45, 1998.

- [148] Ingolf Sack and Tobias Schaeffter. *Quantification of biophysical parameters in medical imaging*. Springer, 2018.
- [149] Moritz Zaiss, Benjamin Schmitt, and Peter Bachert. Quantitative separation of cest effect from magnetization transfer and spillover effects by lorentzian-line-fit analysis of z-spectra. *Journal of magnetic resonance*, 211(2):149–155, 2011.
- [150] Michael T McMahon, Assaf A Gilad, Jeff WM Bulte, and Peter CM Van Zijl. *Chemical Exchange Saturation Transfer Imaging: Advances and Applications*. CRC Press, 2017.
- [151] Zhongliang Zu, Ke Li, Vaibhav A Janve, Mark D Does, and Daniel F Gochberg. Optimizing pulsed-chemical exchange saturation transfer imaging sequences. *Magnetic resonance in medicine*, 66(4):1100–1108, 2011.
- [152] Patrick Schuenke, Johannes Windschuh, Volkert Roeloffs, Mark E Ladd, Peter Bachert, and Moritz Zaiss. Simultaneous mapping of water shift and B1 (WASABI) Application to field-inhomogeneity correction of CEST MRI data. *Magnetic resonance in medicine*, 77(2):571–580, 2017.
- [153] Mina Kim, Joseph Gillen, Bennett A Landman, Jinyuan Zhou, and Peter CM van Zijl. Water saturation shift referencing (WASSR) for chemical exchange saturation transfer (CEST) experiments. *Magnetic resonance in medicine*, 61(6):1441–1450, 2009.
- [154] Anup Singh, Mohammad Haris, Kejia Cai, Victor B Kassey, Feliks Kogan, Damodar Reddy, Hari Hariharan, and Ravinder Reddy. Chemical exchange saturation transfer magnetic resonance imaging of human knee cartilage at 3 T and 7 T. *Magnetic resonance in medicine*, 68(2):588–594, 2012.
- [155] Rudolf Stollberger and Paul Wach. Imaging of the active B1 field in vivo. *Magnetic Resonance in Medicine*, 35(2):246–251, 1996.
- [156] EK Insko. Mapping of the radiofrequency field. *J Magn Reson A*, 103:82–85, 1993.
- [157] Li-Hsin Zang, Douglas L Rothman, and Robert G Shulman. ^1H NMR visibility of mammalian glycogen in solution. *Proceedings of the National Academy of Sciences*, 87(5):1678–1680, 1990.
- [158] Wei Chen, Xiao Hong Zhu, Malcolm J Avison, and Robert G Shulman. Nuclear magnetic resonance relaxation of glycogen H1 in solution. *Biochemistry*, 32(36):9417–9422, 1993.

- [159] Daniel James Clark, Alex K Smith, Richard D Dortch, Michael V Knopp, and Seth A Smith. Investigating hydroxyl chemical exchange using a variable saturation power chemical exchange saturation transfer (vCEST) method at 3 T. *Magnetic resonance in medicine*, 76(3):826–837, 2016.
- [160] Gizeaddis Lamesgin Simegn, Ali Alhamud, Frances Robertson, and Andre JW van der Kouwe. Chemical exchange saturation transfer MRI optimal continuous wave RF irradiation parameters for glycogen (glycoCEST) detection. *Applied Magnetic Resonance*, 51(7):621–640, 2020.
- [161] Min Deng, Shu-Zhong Chen, Jing Yuan, Queenie Chan, Jinyuan Zhou, and Yi-Xiáng J Wáng. Chemical exchange saturation transfer (CEST) MR technique for liver imaging at 3.0 Tesla: an evaluation of different offset number and an after-meal and over-night-fast comparison. *Molecular imaging and biology*, 18(2):274–282, 2016.
- [162] Peter CM Van Zijl, Craig K. Jones, Jimin Ren, Craig R. Malloy, and A. Dean Sherry. MRI detection of glycogen in vivo by using chemical exchange saturation transfer imaging (glycoCEST). *Proceedings of the National Academy of Sciences*, 104(11):4359–4364, 2007.
- [163] Elise Marie Catherine Vinckenbosch. *Ultra high magnetic field for glial contribution into brain metabolism studied by MR spectroscopy and CEST methods for molecular imaging of glycogen*. PhD thesis, EPFL, Lausanne, 2018.
- [164] Panayiotis Nikolaou, Aaron M Coffey, Michael J Barlow, Matthew S Rosen, Boyd M Goodson, and Eduard Y Chekmenev. Temperature-ramped ^{129}Xe spin-exchange optical pumping. *Analytical chemistry*, 86(16):8206–8212, 2014.
- [165] JN Hyacinthe. Beyond Spin Exchange Optical Pumping : Hyperpolarization of Xe via Sublimation Dynamic Nuclear Polarization. (4):442–452, 2015.
- [166] A Comment, J Rentsch, F Kurdzesau, S Jannin, K Uffmann, RB Van Heeswijk, P Hautle, JA Konter, B Van den Brandt, and JJ Van der Klink. Producing over 100 ml of highly concentrated hyperpolarized solution by means of dissolution DNP. *Journal of magnetic resonance*, 194(1):152–155, 2008.
- [167] Andrea Capozzi, Jean Noël Hyacinthe, Tian Cheng, Tim R. Eichhorn, Giovanni Boero, Christophe Roussel, Jacques J. Van Der Klink, and Arnaud Comment. Photoinduced Nonpersistent Radicals as Polarizing Agents for X-Nuclei Dissolution Dynamic Nuclear Polarization. *Journal of Physical Chemistry C*, 119(39):22632–22639, 2015.

- [168] Christian Østergaard Mariager, Steffen Ringgaard, Jan Henrik Ardenkjær-Larsen, and Christoffer Laustsen. Hyperpolarized xenon by d-DNP using the clinical GE SpinLab polarizer system. In *ISMRM 25th Annual Meeting & Exhibition*, 2017.
- [169] Y. Hovav, A. Feintuch, S. Vega, and D. Goldfarb. Dynamic nuclear polarization using frequency modulation at 3.34 T. *Journal of Magnetic Resonance*, 238:94–105, 2014.
- [170] B. Adeva and et al. Large enhancement of deuteron polarization with frequency modulated microwaves. *Nuclear Instruments and Methods in Physics Research Section A: Accelerators, Spectrometers, Detectors and Associated Equipment*, 372(3):339–343, April 1996.
- [171] Kent R Thurber, Wai-Ming Yau, and Robert Tycko. Low-temperature dynamic nuclear polarization at 9.4 T with a 30 mW microwave source. *Journal of Magnetic Resonance*, 204(2):303–313, 2010.
- [172] A Ajoy, R Nazaryan, K Liu, X Lv, B Safvati, G Wang, E Druga, JA Reimer, D Suter, C Ramanathan, et al. Enhanced dynamic nuclear polarization via swept microwave frequency combs. *Proceedings of the National Academy of Sciences*, 115(42):10576–10581, 2018.
- [173] MC Cassidy, HR Chan, BD Ross, PK Bhattacharya, and Charles M Marcus. In vivo magnetic resonance imaging of hyperpolarized silicon particles. *Nature nanotechnology*, 8(5):363–368, 2013.
- [174] Akiva Feintuch, Daphna Shimon, Yonatan Hovav, Debamalya Banerjee, Ilia Kaminker, Yaacov Lipkin, Koby Zibzener, Boris Epel, Shimon Vega, and Daniella Goldfarb. A dynamic nuclear polarization spectrometer at 95 GHz/144 MHz with EPR and NMR excitation and detection capabilities. *Journal of Magnetic Resonance*, 209(2):136–141, 2011.
- [175] Daphna Shimon, Yonatan Hovav, Akiva Feintuch, Daniella Goldfarb, and Shimon Vega. Dynamic nuclear polarization in the solid state: a transition between the cross effect and the solid effect. *Physical Chemistry Chemical Physics*, 14(16):5729–5743, 2012.
- [176] Josef Granwehr, James Leggett, and Walter Köckenberger. A low-cost implementation of EPR detection in a dissolution DNP setup. *Journal of Magnetic Resonance*, 187(2):266–276, 2007.

- [177] Arthur C Pinon, Andrea Capozzi, and Jan Henrik Ardenkjær-Larsen. Hyperpolarized water through dissolution dynamic nuclear polarization with UV-generated radicals. *Communications Chemistry*, 3(1):1–9, 2020.
- [178] A Comment, B Van Den Brandt, K Uffmann, F Kurdzesau, S Jannin, JA Konter, P Hautle, W Th Wenckebach, R Gruetter, and JJ Van Der Klink. Principles of operation of a dnp prepolarizer coupled to a rodent mri scanner. *Applied Magnetic Resonance*, 34(3-4):313–319, 2008.
- [179] Andrea Capozzi, Magnus Karlsson, Jan Raagaard Petersen, Mathilde Hauge Lerche, and Jan Henrik Ardenkjær-Larsen. Liquid-state ^{13}C polarization of 30% through photoinduced nonpersistent radicals. *The Journal of Physical Chemistry C*, 122(13):7432–7443, 2018.
- [180] Andrea Capozzi, Jan-Hendrik Ardenkjær-Larsen, and Jean-Noël Hyacinthe. Xe-129 gas hyperpolarized via sublimation DNP at 6.7 T and 1.1 K using a reusable purpose built fluid path. In *European magnetic resonance meeting (EUROMAR), Berlin, DE*, page 800, 2019.
- [181] Andrea Capozzi. *Methods to hyperpolarize nuclear spins via dissolution and sublimation DNP at high magnetic field*. PhD thesis, EPFL, Lausanne, 01 2016.
- [182] Andrea Capozzi, Saket Patel, W Thomas Wenckebach, Magnus Karlsson, Mathilde H Lerche, and Jan Henrik Ardenkjær-Larsen. Gadolinium effect at high-magnetic-field dnp: 70% ^{13}C polarization of [U- ^{13}C] glucose using trityl. *The journal of physical chemistry letters*, 10(12):3420–3425, 2019.
- [183] Thach V Can, Ralph T Weber, Joseph J Walish, Timothy M Swager, and Robert G Griffin. Frequency-swept integrated solid effect. *Angewandte Chemie*, 129(24):6848–6852, 2017.
- [184] Alice Radaelli, Hikari AI Yoshihara, Hiroshi Nonaka, Shinsuke Sando, Jan Henrik Ardenkjaer-Larsen, Rolf Gruetter, and Andrea Capozzi. ^{13}C Dynamic Nuclear Polarization using SA-BDPA at 6.7 T and 1.1 K: Coexistence of Pure Thermal Mixing and Well-Resolved Solid Effect. *The Journal of Physical Chemistry Letters*, 11(16):6873–6879, 2020.
- [185] NN Kuzma, M Pourfathi, H Kara, P Manasseh, RK Ghosh, JH Ardenkjær-Larsen, SJ Kadlecsek, and RR Rizi. Cluster formation restricts dynamic nuclear polarization of xenon in solid mixtures. *The Journal of Chemical Physics*, 137(10):104508, 2012.

- [186] Marina Kveder, Dalibor Merunka, Milan Jokić, Janja Makarević, and Boris Rakvin. Electron spin-lattice relaxation in solid ethanol: Effect of nitroxyl radical hydrogen bonding and matrix disorder. *Physical review B*, 80(5):052201, 2009.
- [187] Malcolm D Cook and Brian P Roberts. Liquid xenon as a solvent for esr studies. *Journal of the Chemical Society, Chemical Communications*, (6):264–266, 1983.
- [188] JR Morton, KF Preston, SJ Strachb), FJ Adrian, and AN Jette. Anisotropic hyperfine interactions of rare-gas nuclei near trapped hydrogen atoms. *The Journal of Chemical Physics*, 70(6):2889–2893, 1979.
- [189] M. Karlsson et al. Development of dissolution dnp-mr substrates for metabolic research. *Appl. Magn. Reson.*, 43:223, 2012.
- [190] Jeffrey R Brender, Shun Kishimoto, Gareth R Eaton, Sandra S Eaton, Yu Saida, and Murali C Krishna. Trehalose as an alternative to glycerol as a glassing agent for in vivo dnp mri. *BioRxiv*, page 866665, 2019.
- [191] Emmanuelle MM Weber, Giuseppe Sicoli, Hervé Vezin, Ghislaine Frebourg, Daniel Abergel, Geoffrey Bodenhausen, and Dennis Kurzbach. Sample ripening through nanophase separation influences the performance of dynamic nuclear polarization. *Angewandte Chemie International Edition*, 57(18):5171–5175, 2018.
- [192] M Pourfathi, NN Kuzma, H Kara, RK Ghosh, H Shaghaghi, SJ Kadlecsek, and RR Rizi. Propagation of dynamic nuclear polarization across the xenon cluster boundaries: Elucidation of the spin-diffusion bottleneck. *Journal of Magnetic Resonance*, 235:71–76, 2013.
- [193] Asif Equbal, Yuanxin Li, Tarnuma Tabassum, and Songi Han. Crossover from a solid effect to thermal mixing ^1H dynamic nuclear polarization with trityl-OX063. *The Journal of Physical Chemistry Letters*, 11(9):3718–3723, 2020.
- [194] Hanjiao Chen, Alexander G Maryasov, Olga Yu Rogozhnikova, Dmitry V Trukhin, Victor M Tormyshev, and Michael K Bowman. Electron spin dynamics and spin-lattice relaxation of trityl radicals in frozen solutions. *Physical Chemistry Chemical Physics*, 18(36):24954–24965, 2016.
- [195] Alisa Leavesley, Christopher B Wilson, Mark Sherwin, and Songi Han. Effect of water-glycerol polymorphism on dynamic nuclear polarization. *Physical Chemistry Chemical Physics*, 20(15):9897–9903, 2018.

- [196] Kong Ooi Tan, Michael Mardini, Chen Yang, Jan Henrik Ardenkjær-Larsen, and Robert G Griffin. Three-spin solid effect and the spin diffusion barrier in amorphous solids. *Science advances*, 5(7):eaax2743, 2019.
- [197] Armen Sarvazyan and Lev Ostrovsky. Stirring and mixing of liquids using acoustic radiation force. *The Journal of the Acoustical Society of America*, 125(6):3548–3554, 2009.
- [198] Andrea Capozzi, Jan-Hendrik Ardenkjær-Larsen, and Jean-Noël Hyacinthe. LOD-ESR investigation of trityl doped Xe-129 DNP samples at 6.7 T and 1.1 K. In *Hyperpolarized magnetic resonance (HYP-18)*, Southampton, UK, page 76, 2018.
- [199] Mehrdad Pourfathi, Justin Clapp, Stephen J. Kadlecsek, Caroline D. Keenan, Rajat K. Ghosh, Nicholas N. Kuzma, and Rahim R. Rizi. Low-temperature dynamic nuclear polarization of gases in frozen mixtures. *Magnetic Resonance in Medicine*, 76(3):1007–1014, 2016.
- [200] Sami Jannin, Arnaud Comment, and JJ Van der Klink. Dynamic nuclear polarization by thermal mixing under partial saturation. *Applied Magnetic Resonance*, 43(1-2):59–68, 2012.
- [201] Andrea Capozzi, Jean-Noël Hyacinthe, Tian Cheng, Tim R. Eichhorn, Giovanni Boero, Christophe Roussel, Jacques J. van der Klink, and Arnaud Comment. Photoinduced nonpersistent radicals as polarizing agents for X-nuclei dissolution dynamic nuclear polarization. *The Journal of Physical Chemistry C*, 119(39):22632–22639, 2015.
- [202] Andrea Capozzi, Saket Patel, Christine Pepke Gunnarsson, Irene Marco-Rius, Arnaud Comment, Magnus Karlsson, Mathilde H. Lerche, Olivier Ouari, and Jan Henrik Ardenkjær-Larsen. Efficient hyperpolarization of U-13C-Glucose using narrow-line UV-generated labile free radicals. *Angewandte Chemie International Edition*, 58(5):1334–1339, 2019.
- [203] Arthur C. Pinon, Andrea Capozzi, and Jan Henrik Ardenkjær-Larsen. Hyperpolarized water through dissolution dynamic nuclear polarization with UV-generated radicals. *Communications Chemistry*, 3(1):1–9, 2020.
- [204] Robert E. Olson. Effect of pyruvate and acetoacetate on the metabolism of fatty acids by the perfused rat heart. *Nature*, 195(4841):597–599, 1962.

- [205] Karlos X. Moreno, Scott M. Sabelhaus, Matthew E. Merritt, A. Dean Sherry, and Craig R. Malloy. Competition of pyruvate with physiological substrates for oxidation by the heart: implications for studies with hyperpolarized [1- ^{13}C] pyruvate. *American Journal of Physiology-Heart and Circulatory Physiology*, 298(5):H1556–H1564, 2010.
- [206] Alain Grynberg and Luc Demaison. Fatty acid oxidation in the heart. *Journal of cardiovascular pharmacology*, 28:11–17, 1996.
- [207] Gary D. Lopaschuk, John R. Ussher, Clifford DL Folmes, Jagdip S. Jaswal, and William C. Stanley. Myocardial fatty acid metabolism in health and disease. *Physiological reviews*, 90(1):207–258, 2010.
- [208] Jessica AM Bastiaansen, Tian Cheng, Mor Mishkovsky, João MN Duarte, Arnaud Comment, and Rolf Gruetter. In vivo enzymatic activity of acetylCoA synthetase in skeletal muscle revealed by ^{13}C turnover from hyperpolarized [1- ^{13}C] acetate to [1- ^{13}C] acetylcarnitine. *Biochimica et Biophysica Acta (BBA)-General Subjects*, 1830(8):4171–4178, 2013.
- [209] Jessica AM Bastiaansen, Tian Cheng, Hongxia Lei, Rolf Gruetter, and Arnaud Comment. Direct noninvasive estimation of myocardial tricarboxylic acid cycle flux in vivo using hyperpolarized ^{13}C magnetic resonance. *Journal of molecular and cellular cardiology*, 87:129–137, 2015.
- [210] Jonas Steinhauser, Patrick Wespi, Grzegorz Kwiatkowski, and Sebastian Kozerke. Production of highly polarized [1- ^{13}C] acetate by rapid decarboxylation of [2- ^{13}C] pyruvate—application to hyperpolarized cardiac spectroscopy and imaging. *Magnetic resonance in medicine*, 82(3):1140–1149, 2019.
- [211] Daniel R. Ball, Ben Rowlands, Michael S. Dodd, Lydia Le Page, Vicky Ball, Carolyn A. Carr, Kieran Clarke, and Damian J. Tyler. Hyperpolarized butyrate: a metabolic probe of short chain fatty acid metabolism in the heart. *Magnetic resonance in medicine*, 71(5):1663–1669, 2014.
- [212] Cornelius von Morze, Robert A. Bok, Michael A. Ohliger, Zihan Zhu, Daniel B. Vigneron, and John Kurhanewicz. Hyperpolarized [^{13}C] ketobutyrate, a molecular analog of pyruvate with modified specificity for LDH isoforms. *Magnetic resonance in medicine*, 75(5):1894–1900, 2016.
- [213] Desiree Abdurrachim, Xing Qi Teo, Chern Chiuh Woo, Sing Yee Ong, Nurul Farhana Salleh, Janise Lalic, Ru-San Tan, and Philip Teck Hock Lee. Cardiac metabolic mod-

- ulation upon low-carbohydrate low-protein ketogenic diet in diabetic rats studied in vivo using hyperpolarized ^{13}C pyruvate, butyrate and acetoacetate probes. *Diabetes, Obesity and Metabolism*, 21(4):949–960, 2019.
- [214] Alessandra Flori, Giulio Giovannetti, Maria Filomena Santarelli, Giovanni Donato Aquaro, Daniele De Marchi, Silvia Burchielli, Francesca Frijia, Vincenzo Positano, Luigi Landini, and Luca Menichetti. Biomolecular imaging of ^{13}C -butyrate with dissolution-DNP: Polarization enhancement and formulation for in vivo studies. *Spectrochimica Acta Part A: Molecular and Biomolecular Spectroscopy*, 199:153–160, 2018.
- [215] Hikari AI Yoshihara, Jessica AM Bastiaansen, Magnus Karlsson, Mathilde H. Lerche, Arnaud Comment, and Juerg Schwitter. Detection of myocardial medium-chain fatty acid oxidation and tricarboxylic acid cycle activity with hyperpolarized $[1-^{13}\text{C}]$ octanoate. *NMR in Biomedicine*, page e4243, 2020.
- [216] Mor Mishkovsky, Brian Anderson, Magnus Karlsson, Mathilde H. Lerche, A. Dean Sherry, Rolf Gruetter, Zoltan Kovacs, and Arnaud Comment. Measuring glucose cerebral metabolism in the healthy mouse using hyperpolarized ^{13}C magnetic resonance. *Scientific reports*, 7(1):1–8, 2017.
- [217] Jessica AM Bastiaansen, Hikari AI Yoshihara, Yuhei Takado, Rolf Gruetter, and Arnaud Comment. Hyperpolarized ^{13}C lactate as a substrate for in vivo metabolic studies in skeletal muscle. *Metabolomics*, 10(5):986–994, 2014.
- [218] Yuhei Takado, Tian Cheng, Jessica AM Bastiaansen, Hikari AI Yoshihara, Bernard Lanz, Mor Mishkovsky, Sylvain Lengacher, and Arnaud Comment. Hyperpolarized ^{13}C magnetic resonance spectroscopy reveals the rate-limiting role of the blood-brain barrier in the cerebral uptake and metabolism of l-lactate in vivo. *ACS chemical neuroscience*, 9(11):2554–2562, 2018.
- [219] Simon Hu, Minhua Zhu, Hikari AI Yoshihara, David M. Wilson, Kayvan R. Keshari, Peter Shin, Galen Reed, Cornelius von Morze, Robert Bok, and Peder EZ Larson. In vivo measurement of normal rat intracellular pyruvate and lactate levels after injection of hyperpolarized $[1-^{13}\text{C}]$ alanine. *Magnetic resonance imaging*, 29(8):1035–1040, 2011.
- [220] David S. Wishart, Yannick Djoumbou Feunang, Ana Marcu, An Chi Guo, Kevin Liang, Rosa Vázquez-Fresno, Tanvir Sajed, Daniel Johnson, Carin Li, and Naama Karu. HMDB 4.0: the human metabolome database for 2018. *Nucleic acids research*, 46(D1):D608–D617, 2018.

- [221] J. Bremmer. Pyruvate dehydrogenase, substrate specificity and product inhibition. *European journal of biochemistry*, 8(4):535–540, 1969.
- [222] Wendy A Withycombe, DT Plummer, and JH Wilkinson. Organ specificity and lactate-dehydrogenase activity. Differential inhibition by urea and related compounds. *Biochemical Journal*, 94(2):384–389, 1965.
- [223] Antonio Blanco, Carlos Burgos, NM Gerez de Burgos, and EE Montamat. Properties of the testicular lactate dehydrogenase isoenzyme. *Biochemical Journal*, 153(2):165–172, 1976.
- [224] Mahn Joo Kim and George M Whitesides. L-lactate dehydrogenase: substrate specificity and use as a catalyst in the synthesis of homochiral 2-hydroxy acids. *Journal of the American Chemical Society*, 110(9):2959–2964, 1988.
- [225] Helen M Wilks, David J Halsall, Tony Atkinson, William N Chia, Anthony R Clarke, and J John Holbrook. Designs for a broad substrate specificity keto acid dehydrogenase. *Biochemistry*, 29(37):8587–8591, 1990.
- [226] Tian Cheng, Andrea Capozzi, Yuhei Takado, Riccardo Balzan, and Arnaud Comment. Over 35% liquid-state ^{13}C polarization obtained via dissolution dynamic nuclear polarization at 7 T and 1 K using ubiquitous nitroxyl radicals. *Physical Chemistry Chemical Physics*, 15(48):20819–20822, 2013.
- [227] Tian Cheng, Mor Mishkovsky, Jessica AM Bastiaansen, Olivier Ouari, Patrick Hautle, Paul Tordo, Ben Van den Brandt, and Arnaud Comment. Automated transfer and injection of hyperpolarized molecules with polarization measurement prior to in vivo NMR. *NMR in biomedicine*, 26(11):1582–1588, 2013.
- [228] Fabian Jähnig, Grzegorz Kwiatkowski, Alexander Däpp, Andreas Hunkeler, Beat H Meier, Sebastian Kozerke, and Matthias Ernst. Dissolution dnp using trityl radicals at 7 t field. *Physical Chemistry Chemical Physics*, 19(29):19196–19204, 2017.
- [229] A. J. Shaka, James Keeler, Tom Frenkiel, and R. A. Y. Freeman. An improved sequence for broadband decoupling: WALTZ-16. *Journal of Magnetic Resonance (1969)*, 52(2):335–338, 1983.
- [230] R. Scott Staewen, Anton J. Johnson, Brian D. Ross, Todd Parrish, Hellmut Merkle, and Michael Garwood. 3-D FLASH imaging using a single surface coil and a new adiabatic pulse, BIR-4. *Investigative radiology*, 25(5):559–567, 1990.

- [231] Mark E Ladd, Peter Bachert, Martin Meyerspeer, Ewald Moser, Armin M Nagel, David G Norris, Sebastian Schmitter, Oliver Speck, Sina Straub, and Moritz Zaiss. Pros and cons of ultra-high-field MRI/MRS for human application. *Progress in nuclear magnetic resonance spectroscopy*, 109:1–50, 2018.
- [232] Shigeyoshi Saito, Yusuke Takahashi, Akiko Ohki, Yasunori Shintani, and Takahiro Higuchi. Early detection of elevated lactate levels in a mitochondrial disease model using chemical exchange saturation transfer (CEST) and magnetic resonance spectroscopy (MRS) at 7T-MRI. *Radiological physics and technology*, 12(1):46–54, 2019.
- [233] Kejia Cai, Rong-Wen Tain, Xiaohong Joe Zhou, Frederick C Damen, Alessandro M Scotti, Hari Hariharan, Harish Poptani, and Ravinder Reddy. Creatine CEST MRI for differentiating gliomas with different degrees of aggressiveness. *Molecular imaging and biology*, 19(2):225–232, 2017.
- [234] Ronald Ouwerkerk, Yee Kai Tee, and Craig K Jones. Glycogen chemical exchange effects in 1H-MRS and glyco-CEST at 3T and 7T. In *Proceedings of the International Society of Magnetic Resonance Medicine, 21st Scientific Meeting (ISMRM), Sydney, Australia*, page 1990, 2013.
- [235] RLW Tain, S Yang, XJ Zhou, et al. Separated quantification of creatine and phosphocreatine based on a novel proton MR method combining 1H-MRS and CEST MRI. *Process Intl Soc Magn Reson Med*, 23:3352, 2015.
- [236] Stephen J Bawden, Olivier Mougin, Karl Hunter, Luca Marciani, and Penny Gowland. Simultaneously measuring glycogen and lipid levels using localized CEST spectroscopy at 3T. In *Proceedings of the International Society of Magnetic Resonance Medicine, 21st Scientific Meeting (ISMRM), Sydney, Australia*, page 3159, 2014.
- [237] Maike Höfemann. *Optimizing acquisition and quantitative evaluation in 1H Magnetic Resonance Spectroscopy*. PhD thesis, University of Bern, Bern, 2020.
- [238] Simon Walker-Samuel, S Peter Johnson, Barbara Pedley, Mark F Lythgoe, and Xavier Golay. Extracranial measurements of amide proton transfer using exchange-modulated point-resolved spectroscopy (EXPRESS). *NMR in Biomedicine*, 25(6):829–834, 2012.
- [239] TB Price, DL Rothman, MJ Avison, P Buonamico, and RG Shulman. ^{13}C -NMR measurements of muscle glycogen during low-intensity exercise. *Journal of Applied Physiology*, 70(4):1836–1844, 1991.

- [240] Jesper Franch, Rune Aslesen, and Jørgen Jensen. Regulation of glycogen synthesis in rat skeletal muscle after glycogen-depleting contractile activity: effects of adrenaline on glycogen synthesis and activation of glycogen synthase and glycogen phosphorylase. *Biochemical Journal*, 344(1):231–235, 1999.
- [241] J Jensen, R Aslesen, JL Ivy, and O Brors. Role of glycogen concentration and epinephrine on glucose uptake in rat epitrochlearis muscle. *American Journal of Physiology-Endocrinology And Metabolism*, 272(4):E649–E655, 1997.
- [242] Peter M Tiidus, A Russell Tupling, and Michael E Houston. *Biochemistry primer for exercise science*. Human Kinetics, 2018.
- [243] Gulin Oz, Elizabeth R Seaquist, Anjali Kumar, Amy B Criego, Luke E Benedict, Jyothi P Rao, Pierre-Gilles Henry, Pierre-Francois Van De Moortele, and Rolf Gruetter. Human brain glycogen content and metabolism: implications on its role in brain energy metabolism. *American Journal of Physiology-Endocrinology and Metabolism*, 292(3):E946–E951, 2007.
- [244] Hongxia Lei and Rolf Gruetter. Effect of chronic hypoglycaemia on glucose concentration and glycogen content in rat brain: a localized ^{13}C NMR study. *Journal of neurochemistry*, 99(1):260–268, 2006.
- [245] Gülin Öz, Nolawit Tesfaye, Anjali Kumar, Dinesh K Deelchand, Lynn E Eberly, and Elizabeth R Seaquist. Brain glycogen content and metabolism in subjects with type 1 diabetes and hypoglycemia unawareness. *Journal of Cerebral Blood Flow & Metabolism*, 32(2):256–263, 2012.
- [246] Gunamony Shajan, Jens Hoffmann, Dávid Z. Balla, Dinesh K. Deelchand, Klaus Scheffler, and Rolf Pohmann. Rat brain MRI at 16.4 T using a capacitively tunable patch antenna in combination with a receive array. *NMR in Biomedicine*, 25(10):1170–1176, 2012.
- [247] Masoumeh Dehghani Moghadam. *Proton diffusion spectroscopy and modeling of brain metabolism at 14.1 T*. PhD thesis, EPFL, Lausanne, 2016.
- [248] Thomas Neuberger and Andrew Webb. Radiofrequency coils for magnetic resonance microscopy. *NMR in Biomedicine: An International Journal Devoted to the Development and Application of Magnetic Resonance In vivo*, 22(9):975–981, 2009.

- [249] Julia R Krug, Remco van Schadewijk, Frank J Vergeldt, Andrew G Webb, Huub JM de Groot, A Alia, Henk Van As, and Aldrik H Velders. Assessing spatial resolution, acquisition time and signal-to-noise ratio for commercial microimaging systems at 14.1, 17.6 and 22.3 T. *Journal of Magnetic Resonance*, page 106770, 2020.
- [250] A Macor, E de Rijk, G Annino, S Alberti, and J-Ph Ansermet. THz-waves channeling in a monolithic saddle-coil for dynamic nuclear polarization enhanced NMR. *Journal of Magnetic Resonance*, 212(2):440–449, 2011.
- [251] Chunqi Qian, Ihssan S. Masad, Jens T. Rosenberg, Malathy Elumalai, William W. Brey, Samuel C. Grant, and Peter L. Gor’kov. A volume birdcage coil with an adjustable sliding tuner ring for neuroimaging in high field vertical magnets: ex and in vivo applications at 21.1 T. *Journal of Magnetic Resonance*, 221:110–116, 2012.
- [252] Chih-Liang Chin, Christopher M Collins, Shizhe Li, Bernard J Dardzinski, and Michael B Smith. Birdcagebuilder: design of specified-geometry birdcage coils with desired current pattern and resonant frequency. *Concepts in Magnetic Resonance: An Educational Journal*, 15(2):156–163, 2002.
- [253] F. D. Doty, T. J. Connick, X. Z. Ni, and M. N. Clingan. Noise in high-power, high-frequency double-tuned probes. *Journal of Magnetic Resonance*, 77(3):536–549, 1988.
- [254] Rolf Gruetter. Automatic, localized in vivo adjustment of all first-and second-order shim coils. *Magnetic resonance in medicine*, 29(6):804–811, 1993.
- [255] Rolf Gruetter and Ivan Tkáč. Field mapping without reference scan using asymmetric echo-planar techniques. *Magnetic Resonance in Medicine*, 43(2):319–323, 2000.
- [256] Carlos Ernesto Garrido Salmon, Edson Luiz Géa Vidoto, Mateus José Martins, and Alberto Tannús. Optimization of saddle coils for magnetic resonance imaging. *Brazilian Journal of Physics*, 36(1A):4–8, 2006.
- [257] Jens Frahm, Klaus-Dietmar Merboldt, and Wolfgang Hänicke. Localized proton spectroscopy using stimulated echoes. *Journal of Magnetic Resonance (1969)*, 72(3):502–508, 1987.
- [258] Yasuo Amano, Atsushi Nozaki, and Tatsuo Kumazaki. Effects of view ordering and dummy pulse rate on two-dimensional and three-dimensional steady-state free precession imaging. *Academic radiology*, 10(8):901–907, 2003.

- [259] Bonnie Tocher Clause. The Wistar rat as a right choice: Establishing mammalian standards and the ideal of a standardized mammal. *Journal of the History of Biology*, 26(2):329–349, 1993.
- [260] Andrew G. Webb. Challenges for high field clinical MRI. In *2010 IEEE International Symposium on Biomedical Imaging: From Nano to Macro*, pages 575–578. IEEE, 2010.
- [261] Alexander Novikov. Advanced theory of driven birdcage resonator with losses for biomedical magnetic resonance imaging and spectroscopy. *Magnetic resonance imaging*, 29(2):260–271, 2011.
- [262] Tian Cheng, Arthur W. Magill, Arnaud Comment, Rolf Gruetter, and Hongxia Lei. Ultra-high field birdcage coils: A comparison study at 14.1 T. In *2014 36th Annual International Conference of the IEEE Engineering in Medicine and Biology Society*, pages 2360–2363. IEEE, 2014.
- [263] F David Doty, George Entzminger Jr, Cory D Hauck, and John P Staab. Practical aspects of birdcage coils. *Journal of magnetic resonance*, 138(1):144–154, 1999.
- [264] F. David Doty, George Entzminger, Jatin Kulkarni, Kranti Pamorthy, and John P. Staab. Radio frequency coil technology for small-animal MRI. *NMR in Biomedicine*, 20(3):304–325, 2007.
- [265] B Op ’t Eijnde, EA Richter, JC Henquin, Bente Kiens, and Peter Hespel. Effect of creatine supplementation on creatine and glycogen content in rat skeletal muscle. *Acta physiologica Scandinavica*, 171(2):169–176, 2001.
- [266] TS Ibrahim, AM Abduljalil, BA Baertlein, R Lee, and PML Robitaille. Analysis of B1 field profiles and SAR values for multi-strut transverse electromagnetic RF coils in high field MRI applications. *Physics in Medicine & Biology*, 46(10):2545, 2001.
- [267] MRI Faruque, MT Islam, and MAM Ali. A new design of metamaterials for SAR reduction. *Measurement Science Review*, 13(2):70–74, 2013.
- [268] Norbert Muller and Richard C Reiter. Temperature dependence of chemical shifts of protons in hydrogen bonds. *The Journal of Chemical Physics*, 42(9):3265–3269, 1965.
- [269] Norbert Muller. Concerning structural models for water and chemical-shift data. *The Journal of Chemical Physics*, 43(7):2555–2556, 1965.

- [270] Y Ishihara, H Watanabe, K Okamoto, T Kanamatsu, and Y Tsukada. Temperature monitoring of internal body heating induced by decoupling pulses in animal ^{13}C -mrs experiments. *Magnetic resonance in medicine*, 43(6):796–803, 2000.
- [271] Ting Ann Siaw, Matthias Fehr, Alicia Lund, Allegra Latimer, Shamon A Walker, Devin T Edwards, and Song-I Han. Effect of electron spin dynamics on solid-state dynamic nuclear polarization performance. *Physical Chemistry Chemical Physics*, 16(35):18694–18706, 2014.
- [272] Robert C Tao, Robert E Kelley, Norman N Yoshimura, and Floyd Benjamin. Glycerol: its metabolism and use as an intravenous energy source. *Journal of Parenteral and Enteral Nutrition*, 7(5):479–488, 1983.
- [273] Toshiyuki Hibuse, Norikazu Maeda, Azumi Nagasawa, and Tohru Funahashi. Aquaporins and glycerol metabolism. *Biochimica et Biophysica Acta (BBA)-Biomembranes*, 1758(8):1004–1011, 2006.
- [274] F Bonetto, E Anoardo, and M Polello. Saddle coils for uniform static magnetic field generation in NMR experiments. *Concepts in Magnetic Resonance Part B: Magnetic Resonance Engineering: An Educational Journal*, 29(1):9–19, 2006.
- [275] Phillip Zhe Sun, Enfeng Wang, Jerry S Cheung, Xiaoan Zhang, Thomas Benner, and A Gregory Sorensen. Simulation and optimization of pulsed radio frequency irradiation scheme for chemical exchange saturation transfer (CEST) MRI - demonstration of pH-weighted pulsed-amide proton CEST MRI in an animal model of acute cerebral ischemia. *Magnetic resonance in medicine*, 66(4):1042–1048, 2011.
- [276] Kyle M Jones, Alyssa C Pollard, and Mark D Pagel. Clinical applications of chemical exchange saturation transfer (cest) mri. *Journal of Magnetic Resonance Imaging*, 47(1):11–27, 2018.
- [277] Jessica Bastiaansen. *In vivo metabolic studies in skeletal and cardiac muscle using ^{13}C magnetic resonance spectroscopy*. PhD thesis, EPFL, Lausanne, 2013.
- [278] Theodore Hughes-Riley, Joseph S Six, David ML Lilburn, Karl F Stupic, Alan C Dorkes, Dominick E Shaw, Galina E Pavlovskaya, and Thomas Meersmann. Cryogenics free production of hyperpolarized ^{129}Xe and ^{83}Kr for biomedical MRI applications. *Journal of Magnetic Resonance*, 237:23–33, 2013.

- [279] Joseph S. Six, Theodore Hughes-Riley, Karl F. Stupic, Galina E. Pavlovskaya, and Thomas Meersmann. Pathway to Cryogen Free Production of Hyperpolarized Krypton-83 and Xenon-129. *PLoS ONE*, 7(11), 2012.
- [280] Cynthia J Jameson, A Keith Jameson, and Joseph K Hwang. Nuclear spin relaxation by intermolecular magnetic dipole coupling in the gas phase. ^{129}Xe in oxygen. *The Journal of chemical physics*, 89(7):4074–4081, 1988.
- [281] BC Anger, G Schrank, A Schoeck, KA Butler, MS Solum, RJ Pugmire, and B Saam. Gas-phase spin relaxation of Xe ^{129} . *Physical Review A*, 78(4):043406, 2008.
- [282] Andhika Kiswandhi, Bimala Lama, Peter Niedbalski, Mudrekh Goderya, Joanna Long, and Lloyd Lumata. The effect of glassing solvent deuteration and Gd ^{3+} doping on ^{13}C DNP at 5 T. *RSC advances*, 6(45):38855–38860, 2016.
- [283] Riccardo Balzan. *Methods for Molecular Magnetic Resonance Imaging and Magnetic Resonance Spectroscopy using Hyperpolarized Nuclei*. PhD thesis, EPFL, Lausanne, 2013.
- [284] JG Powles. The adiabatic fast passage experiment in magnetic resonance. *Proceedings of the Physical Society*, 71(3):497, 1958.
- [285] Jean-Noël Hyacinthe. *Développements méthodologiques en RMN du ^{129}Xe hyperpolarisé en vue d’applications à la mesure de la perfusion cérébrale chez le petit animal*. PhD thesis, Université Joseph Fourier (Grenoble), 2004.
- [286] Hong Shang, Timothy Skloss, Cornelius von Morze, Lucas Carvajal, Mark Van Criekinge, Eugene Milshteyn, Peder EZ Larson, Ralph E Hurd, and Daniel B Vigneron. Handheld electromagnet carrier for transfer of hyperpolarized carbon-13 samples. *Magnetic resonance in medicine*, 75(2):917–922, 2016.
- [287] Jonas Milani, Basile Vuichoud, Aurélien Bornet, Pascal Miéville, Roger Mottier, Sami Jannin, and Geoffrey Bodenhausen. A magnetic tunnel to shelter hyperpolarized fluids. *Review of Scientific Instruments*, 86(2):024101, 2015.
- [288] Jeung-Hoon Seo, Sang-Doc Han, and Kyoung-Nam Kim. Investigation of the B1 field distribution and RF power deposition in a birdcage coil as functions of the number of coil legs at 4.7 T, 7.0 T, and 11.7 T. *Journal of the Korean Physical Society*, 66(12):1822–1826, 2015.

- [289] B Wu, G Warnock, M Zaiss, C Lin, M Chen, Z Zhou, L Mu, D Nanz, R Tuura, and G Delso. An overview of CEST MRI for non-MR physicists. *EJNMMI physics*, 3(1):19, 2016.

Acronyms

AGL Above Ground Level.

AUC Area Under Curve.

BA Butyric Acid.

CEST Chemical Exchange Saturation Transfer.

cw continuous wave.

dDNP dissolution Dynamic Nuclear Polarization.

diaCEST diamagnetic CEST.

DNP Dynamic Nuclear Polarization.

DS Direct Saturation.

ESR Electron Spin Resonance.

ETL Echo Train Length.

FF Far Field.

FM Frequency Modulation.

FOV Field Of View.

FWHM Full Width Half Maximum.

Glc Glucose.

glycoCEST glycogen CEST.

LDH Lactate Dehydrogenase.

LOD Longitudinal Detection.

MCT Monoarboxylate Transporter.

MPC Mitrochondrial Pyruvate Carrier.

MRI Magnetic Resonance Imaging.

MRS Magnetic Resonance Spectroscopy.

MTC Magnetization Transfer Contrast.

MTR Magnetisation Transfer Ratio.

NF Near Field.

NMDA N-methyl-D-aspartate.

NMR Nuclear Magnetic Resonance.

NOE Nuclear Overhauser Effect.

OX063 tris(8-carboxyl-2,2,6,6-benzo(1,2-d:4,5-d)-bis(1,3)dithiole-4-yl)methyl sodium salt.

PA Pyruvic Acid.

paraCEST paramagnetic CEST.

PCB Printable Circuit Board.

PDH Pyruvate Dehydrogenase.

ppm parts per million.

PRESS Point RESolved Spectroscopy.

PTR Proton Transfer Ratio.

RF Radiofrequency.

ROI Region Of Interest.

RX Receive mode.

SE Solid Effect.

SEOP Spin Exchange Optical Pumping.

SNR Signal to Noise Ratio.

TEMPO (2,2,6,6-Tetramethylpiperidin-1-yl)oxyl.

TX Transmit mode.

UV Ultra-Violet.

UV-Vis Ultra-Violet-Visible.

VCO Voltage Controlled Oscillator.

VOI Volume Of Interest.

WASABI Simultaneous mapping of water shift and B_1 .

WASSR Water Saturation Shift Referencing.

I expected the climb to be long and challenging.

I just never expected it to be this steep.

A path so concealed and camouflaged that I have mistaken the abyss for the peak.

”A chiunque, almeno una volta nella vita, sorge spontanea la questione dell’esistenza di un percorso già scritto.

E non vi si trova risposta.”

Federico Gnesutta
*The Timeless Hours*¹

¹Unpublished, reproduced with permission from the author.

Acknowledgements

Rolf, you have given me free reign throughout every step of my way. The liberty to choose any path and govern any decision is rarely conceded so amply and I grew on the responsibility.

It started with an open door. Thank you, Carole, for being my compass and pointing me into the right direction.

Starting to work with you, Bernard, turned my PhD around. You have my deepest gratitude. It has been such a pleasure et je te remercie pour tout. J'ai adoré nos conversations sur les vignes et le Valais, la culture et la politique. J'espère qu'elles continueront.

Every day that I got to work with you, Jessica, I considered myself lucky. You have been a mentor and role model. I admire how you handle any situation and it has been my privilege to learn from you on so many occasions.

Thanks to Andrea and Jean-Noël for your availability to discuss science and contemplate puzzling observations. And thank you Andrea for being so involved in the final stretches of the dissertation. The same goes for my colleagues Hikari, Mor, Yves, Daniel and Thanh.

I thank my office mates Emma, Jérémie and Radek for sharing puns and stories. Jérémie, je te remercie d'avoir rendue la première minute de chaque matinée un moment de joie. Le plus grand merci à Nasreen, pour ta gentillesse et pour nos conversation; ton sourire a amélioré chacune de mes journées. To Lillian and Anh for the support you have been to me in more than one way.

I would like to thank my committee members, Jan, Chris and Sebastian, for taking the time to thoughtfully engage with my work amidst the pandemic. Sebastian, I thank you for your support throughout my path starting five years ago; I was honoured that you were part of my jury.

Alice, you held a special place in the past four years. I thank you for being the optimist that you are and for sharing your calm with me, teaching me the most important lesson of them all. Our travels have been delightful and relaxing, in spite of road tripping at the verge of a pandemic and nocturnal emergency alerts.

A heartfelt mention to my fellows at CDI. Your high spirits and genuine affection were a source of inexhaustible motivation and energy. You gave me the strength to make it through the final months and beyond. Thank you for making every day spent with you detoxifying and restful. A special thank you to Fra, Ludo and Fede for gifting me a beautiful memory. It meant the world to me.

To my good friends Caroline and Christian, Sonia, Elise, Emile, Val, Augu, Robin, mon ami Sami, Guillaume, Leo and Sherif. For hours and days spent in Sat, for introducing me to Belgian beer and for long evenings of Jass and Seven Wonders. For much needed coffee breaks and pep talks. Pour les marches épiques. For being you, and being there.

My final thanks are to my family.

To Xenia and Jönn, for fun game nights, spontaneous pancake breakfasts and your unconditional friendship. To Cora, Torsten, Herbert and Lore for welcoming me so openly to your home and family. Both were a shelter in turbulent times.

Ferd Mama und dr Papa. Merci fer dassi mine Wäg immer ha chännu frii wähle. Fer die ganzu Jahr woner mi mit Züelose, Rat und Ziit unnerstützt heit. Fer dassi mi immer cha freuu heim z cho, entspannendi Wuchenend z geniessu und di Batterie bim Brunchu obudir iner Morgusunna üfzlade. Fer z Wissu, dasser mis Schweschterhärzji und mich immer gärü heit, wie eu immer wier ischers Läbu läbe.

To my sis, you who have always been there for me. Thank you for having shown me what is of true importance in life. You are the constant in my life that keeps me from tumbling. It is soothing to know you will always be close even when you are far away.

To a person without whom I would not have made it. No matter how rough my day, a moment spent with you made up for it all. Je te remercie Tarek. For being at my side when times were most difficult and for keeping me balanced. Not just for supporting me wherever I chose to go, but for going with me.

Communications

Journal Articles

- Zanella, C.C., Capozzi, A., Yoshihara, H.A.I., Radaelli, A., Arn, L.P., Grütter, R., Bastiaansen, J.A.M. (2020). Radical-free Hyperpolarized MRI using Endogenously-occurring Pyruvate Analogues and UV-induced Nonpersistent Radicals. *arXiv preprint*, arXiv:2006.14408. Manuscript in revision at NMR in biomedicine.
- Zanella, C.C., Clément, J., Wenz, D., Lanz, B., Grütter, R. The Saddle Coil Design as Advantageous Solution for Preclinical MRI and MRS at Ultra-high Magnetic Field. Manuscript in preparation for submission to MAGMA.
- Zanella, C.C., Lê, T.P., Radaelli, A., Hyacinthe, J.-N., Grütter, R., Capozzi, A. Microwave Frequency Modulation Enhances Solid-state ^{129}Xe Polarization in Ultra-short Radical T_{1,e^-} Matrices. (Tentative title). Manuscript in preparation.

Oral Communications

- Zanella C.C. (2019). Molecular Magnetic Resonance Imaging - Introduction to Clinical Applications of CEST Imaging. For Medical Radiologic Technologists. *Haute Ecole de Santé Genève (HES-SO)*. Guest lecture.
- Zanella, C.C., Capozzi, A., Lê, T.P., Grütter, R., Hyacinthe, J.-N. (2018). Boosting ^{129}Xe DNP Efficiency using Ultrasonic Sample Mixing and Microwave Frequency Modulation. *International Conference on Nuclear Hyperpolarization (HYP18)*. Talk.

- Zanella, C.C., Winckenbosch, E., Grütter, R. (2018). Mapping Lactate Concentrations Via CEST Magnetic Resonance Imaging. *Lausanne Integrative Metabolism Nutrition Alliance Symposium (LIMNA)*. Best poster price preselection.

Peer Reviewed Conference Proceedings²

- Zanella, C.C., Capozzi, A., Yoshihara, H., Radaelli, A., Arn, L., Grütter, R., Bastiaansen, J. (2020). Radical-free and Metal-free Hyperpolarized MRI using Endogenous Pyruvate Analogues. *International Society for Magnetic Resonance in Medicine (ISMRM)*. Accepted abstract, poster presentation.
- Zanella, C.C., Clément, J., Wenz, D., Lanz, B., Grütter, R. (2020). A Preclinical Saddle Coil Design as a Favorable Alternative to the Birdcage Coil for Combined B_1^+ Homogeneity and Efficiency at 14.1 T. *International Society for Magnetic Resonance in Medicine (ISMRM)*. Accepted abstract, poster presentation.
- Zanella, C.C., Capozzi, A., Yoshihara, H., Grütter, R., Bastiaansen, J. (2020). Exploring Pyruvate Analogues as Non-persistent Endogenous Radical Precursors for Dissolution DNP. *Experimental Nuclear Magnetic Resonance Conference (ENC)*. Accepted abstract, poster presentation.
- Zanella, C., Capozzi, A., Lê, T.P., Radaelli, A., Grütter, R., Hyacinthe, J.N. (2019). Solvent-dependent DNP of Embedded ^{129}Xe upon Microwave Frequency Modulation *Experimental Nuclear Magnetic Resonance Conference (ENC)*. Accepted abstract, poster presentation.
- Zanella, C.C., Vinckenbosch, E., Clément, J., Dehghani, M., Lanz, B., Grütter, R. (2019). A Custom-designed ^1H Saddle Coil for CEST Imaging at 14.1 Tesla. *International Society for Magnetic Resonance in Medicine (ISMRM)*. Accepted abstract, digital poster presentation.
- Arn, L.P., Zanella, C.C., Lê, T.P., Capozzi, A., Bastiaansen, J.A.M. (2018). Boosting the Dynamical Nuclear Polarization of $[1-^{13}\text{C}]$ butyrate with Microwave Frequency Modulation. *International Conference on Nuclear Hyperpolarization (HYP18)*. Accepted abstract, poster presentation.

²For ISMRM abstracts: 20-30% rejection rate, ismrm.org/about/ampc-faq/

- Zanella, C.C., Capozzi, A., Lê, T.P., Grütter, R., Hyacinthe, J.-N. (2018). Boosting ^{129}Xe DNP Efficiency using Ultrasonic Sample Mixing and Microwave Frequency Modulation. *International Conference on Nuclear Hyperpolarization (HYP18)*. Accepted abstract, poster presentation.

Extracurricular Scientific Activities

- Introduction to Leadership for Early Career Researchers, EPFL, Switzerland, January 2020.
- Zanella, C.C., Capozzi, A., Yoshihara, H., Radaelli, A., Arn, L., Grütter, R., Bastiaansen, J. (2019). Translational Hyperpolarized MRI with Radical-free, Metal-free Endogenous Contrast Agents. *CIBM research day*. Poster presentation.
- RESAL Module 1: Introductory Course in Laboratory Animal Science / Education and Training of Persons Conducting Animal Experiments, UNIL, Switzerland, June 2018.
- LabView Core 1, EPFL, Switzerland, July 2018.
- Co-organizer of a 2-days DNP workshop hosting Tom Wenckebach - in collaboration with Alice Radaelli, EPFL, Switzerland, March 2018.

CV - Zanella Claudia

Gliserallee 45
3902 Brig-Glis (VS)
Switzerland

c.zanella@epfl.ch

Tel.: +41 79 245 20 64



01.07.1992
Swiss, unmarried

Education

- 11.16 – today **PhD candidate at EPFL Lausanne**
- 09.14 – 08.16 **Master of Science in Physics ETH Zürich**
- 03.15 – 07.15 **EPFL Exchange semester**
- 09.11 – 09.14 **Bachelor of Science in Physics ETH Zürich**
- 08.07 – 07.11 **Swiss Federal Maturity**

Project Experience

- 01.2020-today **External relations officer** *The Consulting Society*
- 09.2017 **Scientific workshop Host and Organizer EPFL** Initiation and execution of a specialised seminar on Dynamic Nuclear Polarization
- 09.15 – 01.16 **Internship in Financial Project Controlling VW in Germany**, controlling of long-term projects in research and development
- 09.15 – 01.16 **Project leader Femtec Innovation Workshop**, Leading a team of 14 engineers and scientists; development of pioneering solutions for sustainable fuel production for the refinery BP Lingen

Teaching & Mentoring Responsibilities

- 02.17 – today **Assistantship at EPFL** *Physics, Biomedical Imaging Master class*
- 02.16 – 06.16 **Assistantship at ETHZ** *Analysis for computer scientists*
- 05.13 – 07.13 **College substitute teacher** *Kantonsschule Wettingen (AG)*

Scholarships

- 09.2018 **HYP Travel Bursary** awarded by the scientific HYP committee
- 03.15 – 07.15 **Mobility Scholarship** Swiss Federal Institutes of Technology
- 07.14 – 03.16 **Femtec Careerbuilding Program** *Berlin, 2 Year Scholarship*

Computer Science Skills

Programming: MATLAB, rudimentary LABVIEW

Project Management tools: Redmine, Trello

Data Analysis & Scientific reporting: ORIGINLAB, L^AT_EX, Microsoft Office

Languages

Swiss German

Mother tongue

French

Full professional proficiency

English

Full professional proficiency

Italian

Limited Working Proficiency

Extracurricular Activities

Nordic ski / Via Ferrata / Horse Riding / Hiking

2019/20 **Company First Aider** *Formamed*

2019/20 **Assessment Center Jury** *Femtec.Alumnae e.V.*

